## ABSTRACT

GU, CHUNZHI (JITTY). SIMS Quantification of Matrix and Impurity Species in III-Nitride Alloys. (Under the direction of Dr. Phillip E. Russell and Dr. Dieter P. Griffis)

New applications in optoelectronic devices and high power electronic devices continue to be developed using III-Nitride. In the case of $Al_xGa_{1-x}N$, the quantification of matrix and impurity species is essential for matrix composition analysis, dopant control, and impurity control. Dynamic SIMS quantification in $Al_xGa_{1-x}N$ is challenging because of matrix and charging effects. The secondary ion yield of matrix and impurity species varies in $Al_xGa_{1-x}N$ with different AlN mole fraction (x). $Al_xGa_{1-x}N$ also shows charging effects when the material becomes more insulating with increasing AlN mole fraction.

In this work, a SIMS quantification method is developed for the $Al_xGa_{1-x}N$ system over the range of x = 0 to 1. A set of $Al_xGa_{1-x}N$ films prepared on SiC or sapphire substrates with AlN mole fraction ranging from 0 to 0.58 were implanted with $^{16}O$, $^{24}Mg$ and $^{29}Si$. Very high Al concentration $Al_xGa_{1-x}N$ samples were created using high dose ion implantation of Ga into AlN. With these samples, calibration curves of matrix ion intensity ratio for quantification of Ga and Al matrix constituents, Relative Sensitivity Factors (RSF) for impurity species, and sputter rate as a function of AlN mole fraction were obtained. Using these calibration curves, the matrix and impurity concentrations of an unknown $Al_xGa_{1-x}N$ sample can be determined, and the elemental composition of multi-layer $Al_xGa_{1-x}N$ samples can be measured. Electron beam charge neutralization methods for high Al content $Al_xGa_{1-x}N$ are shown. The calibration curves in $Al_xGa_{1-x}N$ using $O_2^+$ bombardment with positive secondary ion detection, using $Cs^+$ bombardment with negative secondary ion

detection and $MCs^+$ detection are developed.  The ionization mechanisms under these conditions are rationalized.

Using the sputtering conditions stated above, the sputter yield decreases with AlN mole fraction in $Al_xGa_{1-x}N$ and the rate of decrease in the sputter rate versus x declines as x increases.   In the range of $0 \leq x \leq 0.58$, the matrix ion intensity ratios of Al-containing ions over Ga-containing ions appear to increase linearly with the corresponding matrix mole fraction ratio or AlN mole fraction.   For higher x, the inverse plots of the ratio of Ga-containing ions over Al-containing ions as a function of GaN mole fraction or mole fraction ratio appear to increase linearly in the range of $0.39 \leq x \leq 1$.   The RSF's for Si and Mg normalized to the appropriate Ga-containing matrix ions decrease exponentially with x in the range of $0 \leq x \leq 0.58$; those normalized to the N-containing matrix ions have smaller variation with x in the range of $0 \leq x \leq 0.58$.  The exponential correlation of RSF's with x is consistent with that of ion yield with the surface work function.

Based on the calibration curves developed in this work at multiple analysis conditions, the matrix elements in $Al_xGa_{1-x}N$ can be quantified in the range of $0 \leq x \leq 1$, and the impurity species can be quantified over $0 \leq x \leq 0.58$.  The technique can be employed for impurity control, composition and growth rate determination, as well as structural analysis of the finished optoelectronic and electronic devices.

The ionization yields of both positive and negative ions are studied when x is changed in $Al_xGa_{1-x}N$.  The yield variation is mainly caused by the increase of surface concentration of primary species due to the sputter yield reduction as x is increased.

# SIMS Quantification of Matrix and Impurity Species in III-Nitride Alloys

By
**CHUNZHI (JITTY) GU**

A dissertation submitted to the graduate faculty of
North Carolina State University
in partial fulfillment of the
requirements for the Degree of
Doctor of Philosophy

**MATERIALS SCIENCE AND ENGINEERING**

Raleigh
2005

APPROVED BY

Carlton Osburn

Mark A L Johnson

Fred A. Stevie

Dieter P. Griffis
Co-Chair of Advisory Committee

Phillip E. Russell
Chair of Advisory Committee

## DEDICATION

To my parents, my husband and my children…

For your love and support…

## BIOGRAPHY

Chunzhi (Jitty) Gu was born in Henan Province, China and grew up in her hometown until she graduated from high school. She went to Naikai University in Tianjin, China in 1988 and graduated with a Bachelor of Science degree in Electronics Information Systems in 1992. Following graduation, Jitty started the graduate studies in Nankai University. In 1995, she graduated with a Masters of Science degree in Semiconductor Physics and Devices.

Right after graduation in 1995, Jitty joined Motorola as a failure analysis engineer. Her job duties included analyzing samples from the Si wafer fabrication production line using Scanning Electron Microscopy (SEM), Energy Dispersive Spectrometry (EDS) and Focused Ion Beam (FIB), for the purpose of process improvement and yield enhancement.

In January 2002, Jitty started Ph.D program under the direction of Dr. Russell and Dr. Griffis, working on SIMS quantification in III-Nitride semiconductors.

## ACKNOWLEDGEMENTS

I would like to express my sincere gratitude and appreciation to my advisors, Dr. Phil Russell and Dr. Dieter Griffis, for providing me with the opportunity to work in the Analytical Instrumentation Facility research group and guiding me through the course of the research. Without their guidance and support, this research would not have been possible.

Special thanks go to Fred Stevie for his expert guidance and mentorship, and for his encouragement and support. I deeply appreciate the thought provoking ideas.

I would like to thank Dr. Carl Osburn and Dr. Mark Johnson for being my committee members, for taking the time to evaluate my work and advising me in the development of this research.

My thanks also go to Dr. Frank Zhu and the staff of AIF I have known, Roberto Garcia, Dale Batchelor, Chuck Mooney and Rich Fiore for all their help in many ways during my journey in the group; to all the students of AIF, Curt Progl, Mike Salmon, Chad Parish, Anthony Garetto, Kristin Bunker for discussion and sharing experience.

In addition, I would like to thank Cree Inc. and Photonics Research Center for providing the samples utilized in this research.

Last, but not least, I would like to thank my husband, Yongjun Lei, for his understanding, support and encouragement during the past few years; My parents, Linbo Gu and Shaoying Dong, for their believing in me and for their endless love.

## TABLE OF CONTENTS

**LIST OF FIGURES** ............................................................ ix

**LIST OF TABLES** ............................................................ xiv

**LIST OF EQUATIONS** ............................................................ xv

**LIST OF SYMBOLS** ............................................................ xx

**LIST OF ACRONYMS** ............................................................ xxii

**1. Introduction and Overview** ............................................................ 1

1.1 Structure of the Dissertation ............................................................ 1
1.2 Research Motivation and Objective ............................................................ 1
1.3 III-Nitride Materials System ............................................................ 3
1.3.1 Nomenclature ............................................................ 3
1.3.2 III-Nitride Semiconductor Materials System ............................................................ 3
1.4 Secondary Ion Mass Spectrometry (SIMS) ............................................................ 8
1.4.1 Introduction ............................................................ 8
1.4.2 Mass Analyzers Commonly Used For SIMS ............................................................ 11
1.4.3 Sensitivity and Depth Resolution ............................................................ 18
1.5 References ............................................................ 22

**2 Quantification Using Magnetic Sector (MS) SIMS** ............................................................ 24

2.1 Introduction ............................................................ 24
2.2 Theoretical Review: Secondary Ion Emission ............................................................ 26
2.2.1 Bond-breaking Model ............................................................ 26
2.2.2 Electron-tunneling Model ............................................................ 28
2.2.3 Local Thermal Equilibrium (LTE) Model ............................................................ 30
2.2.4 Other Secondary Ion Emission Models ............................................................ 32
2.2.5 Summary ............................................................ 38

2.3 Quantification Approaches ........ 39
2.3.1 Semi-theoretical Model Approach ........ 39
2.3.2 Empirical Calibration Approach ........ 40
2.4 Issues in Quantification of Matrix and Impurities in $Al_xGa_{1-x}N$ ........ 43
2.4.1 Matrix Effects ........ 43
2.4.2 Sample Charging Effects ........ 45
2.5 References ........ 49

**3 Instrumentation and Experimental Method ........ 52**

3.1 Introduction ........ 52
3.2 Instrumentation ........ 53
3.2.1 CAMECA Magnetic Sector SIMS Instrument IMS-6f ........ 53
3.2.2 Tencor P-20 stylus profilometer ........ 63
3.3 The $Al_xGa_{1-x}N$ Sample Set ........ 64
3.4 Fabrication of High Al Content AlGaN Samples ........ 67
3.5 Electron Beam Charge Neutralization ........ 69
3.5.1 Positive Mode Charging Neutralization ........ 70
3.5.2 Negative Mode Charging Neutralization ........ 72
3.6 Analysis Conditions ........ 74
3.7 References ........ 75

**4 Quantification of Matrix and Impurity Species in $Al_xGa_{1-x}N$ under $O_2^+$ Bombardment with Positive Ion Detection ........ 78**

4.1 Introduction ........ 78
4.2 Oxygen Incorporation and Positive Secondary Ion Emission Enhancement ........ 79
4.3 Experimental Method ........ 80
4.4 Results and Discussion ........ 83
4.4.1 Sputter Rate ........ 83
4.4.2 Matrix Ion Intensity Ratio ........ 84
4.4.3 Impurity RSF's ........ 88
4.5 Secondary Ion Emission Mechanism in $Al_xGa_{1-x}N$ under $O_2^+$ Primary Beam ........ 90

4.5.1 Trend of the Secondary Ion Yield of Matrix and Impurity Species ............ 90
4.5.2 Secondary Ion Emission Mechanism in $Al_xGa_{1-x}N$ under $O_2^+$ Primary Beam ........ 97
4.6 Summary ........ 98
4.7 References ........ 100

**5 Quantification of Matrix and Impurity Species in $Al_xGa_{1-x}N$ under $Cs^+$ Bombardment with Negative Ion Detection ........ 102**

5.1 Introduction ........ 102
5.2 Cs Incorporation and Negative Secondary Ion Yield Enhancement ........ 102
5.3 Experimental Method ........ 103
5.4 Results and Discussion ........ 105
5.4.1 Sputter Rate ........ 105
5.4.2 Matrix Ion Intensity Ratio ........ 106
5.4.3 Impurity RSF's ........ 107
5.5 Secondary Ion Emission Mechanism in $Al_xGa_{1-x}N$ under $Cs^+$ Primary Beam ... 110
5.5.1 Trend of the Secondary Ion Yield of Matrix and Impurity Species ........ 110
5.5.2 Negative Secondary Ion Emission Mechanism in $Al_xGa_{1-x}N$ under $Cs^+$ Primary Ion Beam Bombardment ........ 112
5.6 Summary ........ 117
5.7 References ........ 119

**6 Quantification of Matrix and Impurity Species in $Al_xGa_{1-x}N$ using the $MCs^+$ Technique ........ 121**

6.1 $MCs^+$ Technique ........ 121
6.2 $MCs^+$ and $MCs_2^+$ Secondary Ion Formation ........ 122
6.3 Previous Studies on III-nitrides using $MCs^+$ Technique ........ 125
6.4 Experimental ........ 126
6.5 Results and Discussion ........ 130
6.5.1 Sputter Rate ........ 130
6.5.2 Matrix Ion Intensity Ratio ........ 131

6.5.3 Impurity RSF's ........ 133
6.5.4 Secondary Ion Formation Mechanism in $Al_xGa_{1-x}N$ Using $MCs^+$ Method ........ 139
6.6 Summary ........ 144
6.7 References ........ 146

**7 Comparison of SIMS Quantification Techniques for $Al_xGa_{1-x}N$ ........ 148**

7.1 Introduction ........ 148
7.2 Quantification in $Al_xGa_{1-x}N$ ........ 148
7.2.1 Sputter Yield ........ 148
7.2.2 Quantification of Matrix Species ........ 152
7.2.3 Quantification of Impurity Species ........ 153
7.3 Uncertainty Analysis ........ 155
7.3.1 Sample Composition Measurement ........ 155
7.3.2 Sputter Rate Error Analysis ........ 156
7.3.3 Matrix Ion Intensity Ratio and RSF Error Analysis ........ 157
7.3.4 Ion Yield Error Analysis ........ 165
7.3.5 Summary of Experimental Uncertainty ........ 165
7.4 References ........ 167

**8 Conclusions and Future Work ........ 169**

8.1 The Contribution ........ 169
8.2 Recommendations for Future Work ........ 170
8.2.1 Further Study using Better Quality $Al_xGa_{1-x}N$ Samples ........ 170
8.2.2 Study of InGaN ........ 171
8.2.3 Thin Layer Quantification ........ 172
8.3 References ........ 174

## LIST OF FIGURES

Figure 1-1. Typical structure of III-Nitride ($Al_xGa_{1-x}N/In_xGa_{1-x}N$) optoelectronic device for multi-layer quantification.......... 2

Figure 1-2. Energy bandgap versus lattice constant for III-nitrides and selected substrate materials.......... 5

Figure 1-3. Schematic of Secondary Ion Mass Spectrometry.......... 9

Figure 1-4. Collision cascades after primary ions impinge sample surface .......... 10

Figure 1-5. Schematic of magnetic sector double focusing mass analyzers, including electrostatic analyzer (ESA) and mass spectrometer (MS).......... 13

Figure 1-6. Schematic of quadrupole mass spectrometer .......... 15

Figure 1-7. Operation of a time-of-flight (TOF) mass spectrometer with a reflectron.......... 17

Figure 1-8. Monte Carlo simulation of oxygen and cesium incorporation into GaN at different energies. .......... 20

Figure 2-1. Variation of RSF's in Si matrix under $O_2^+$ and $Cs^+$ bombardment.......... 25

Figure 2-2. Potential energy curves of NaCl for (a) the NaCl molecule in gas phase and (b) an Na atom leaving the NaCl crystal phase in solid phase.......... 27

Figure 2-3. Potential energy curves for $Si^+$ emission from localized $SiO_x$ complexes at the sputtered surface.......... 28

Figure 2-4. Schematic drawing of energy diagram of an atom leaving a metal surface.......... 29

Figure 2-5. The simple graphical illustration of the perturbation model.......... 33

Figure 2-6. Band-structure model for oxygen enhancement of positive and negative ions .. 35

Figure 2-7. Illustration of molecular model – sputtering of a transient M-O molecule and possible level crossing processes during the dissociation of this entity.......... 36

Figure 2-8. Illustration of surface excitation model.......... 37

Figure 2-9. Calibration curve - the relationship between impurity secondary ion intensity and impurity concentration .......... 42

Figure 2-10. Optical image shows severe sample damages from charging.......... 46

Figure 3-1. Illustration of duoplasmatron plasma ionization source .......... 54

Figure 3-2. Schematic of the Accel/Decel system for IMS-6F duoplasmatron source ......... 55

Figure 3-3. Schematic drawing of Microbeam Cesium surface ionization source ................ 57

Figure 3-4. Trajectory of ions with different energies ........................................................ 58

Figure 3-5. Mass separation of ions with the same energy but different trajectories ............ 59

Figure 3-6. Illustration of Faraday cup in CAMECA IMS-6F ............................................. 60

Figure 3-7. Schematic of an electron multiplier .................................................................. 60

Figure 3-8. Principle of post acceleration system in electron multiplier .............................. 61

Figure 3-9. Schematic of electron beam charge neutralization by normal incidence electron gun ........................................................................................................ 63

Figure 3-10. Principle of LEXES measurement .................................................................. 66

Figure 3-11. Depth profiles of high dose Ga in AlN and Al in GaN .................................... 68

Figure 3-12. Electron beam position is adjacent to raster area in positive electron compensation ........................................................................................................ 71

Figure 3-13. Electron cloud formation above sample surface in negative mode charge neutralization........................................................................................................ 73

Figure 4-1. Depth profile of matrix and impurity species in $Al_xGa_{1-x}N$ where x= 0.58 under $O_2^+$ with positive ion detection ......................................................................... 82

Figure 4-2. Sputter rate of $Al_xGa_{1-x}N$ as a function of AlN mole fraction under $O_2^+$ bombardment ........................................................................................................ 83

Figure 4-3. Comparison of sputter rate of $Al_xGa_{1-x}N$ as a function of AlN mole fraction (x) at high and low impact energies under $O_2^+$ primary ion bombardment... 84

Figure 4-4. Matrix ion intensity ratio $Al^+/Ga^+$ ratio as a function of AlN mole fraction (x) with x<0.4 ($O_2^+$ ion impact energy 5.5 keV) .......................................... 85

Figure 4-5. Matrix ion intensity ratio $Al^+/Ga^+$ ratio as a function of AlN mole fraction (x) with wide range of x ($0 \leq x < 1$) with $O_2^+$ ion impact energy 5.5 keV ........ 86

Figure 4-6. Matrix ion intensity ratio $Al^+/Ga^+$ ratio as a function of AlN and GaN mole fraction ratio x/(1-x)........................................................................................ 86

Figure 4-7. Inverse plot of figure 4-6: Matrix ion intensity ratio $Ga^+/Al^+$ ratio as a function of GaN and AlN mole fraction ratio (1-x)/x ................................................ 87

Figure 4-8. Comparison of matrix ion intensity ratio with high and low impact energies .... 88

Figure 4-9. $Mg^+$ RSF (normalized to $Ga^+$) as a function of AlN mole fraction (x) at high and low impact energies ........ 89

Figure 4-10. $Si^+$ RSF (normalized to $Ga^+$) as a function of AlN mole fraction (x) at high and low impact energies ........ 89

Figure 4-11. Useful ion yield of $Ga^+$ as a function of x using $O_2^+$ bombardment and detecting positive secondary ions with impact energy 5.5 keV ........ 92

Figure 4-12. The energy distribution of $Al^+$ and $Ga^+$ from conductive and non-conductive samples ........ 93

Figure 4-13. Relative ion yield of $Al^+$ ($1/RSF_{Al}$) to that of $Ga^+$ as a function of x in $Al_xGa_{1-x}N$ under $O_2^+$ primary beam with 5.5 keV impact energy ........ 95

Figure 4-14 Relative ion yield of $Si^+$ and $Mg^+$ to that of $Ga^+$ as a function of x in $Al_xGa_{1-x}N$ under $O_2^+$ primary beam with 5.5 keV impact energy ........ 96

Figure 5-1. Comparison of sputter rate of $Al_xGa_{1-x}N$ under $Cs^+$ bombardment with negative ion extraction at high and low impact energies. ........ 106

Figure 5-2. Matrix ion intensity ratio $AlN^-/GaN^-$ as a function of AlN mole fraction (x) with $x \leq 0.58$ at impact energy of 6.0 keV and 14.5 keV ........ 106

Figure 5-3. Inverse plot of figure 5-3: Matrix ion intensity ratio $GaN^-/AlN^-$ ratio as a function of GaN mole fraction (1-x) in $Al_xGa_{1-x}N$ at 14.5 keV impact energy ........ 107

Figure 5-4. $MgN^-$ RSF (normalized to $GaN^-$) as a function of AlN mole fraction (x) at high and low impact energies ........ 108

Figure 5-5. $Si^-$ RSF (normalized to $GaN^-$) as a function of AlN mole fraction (x) at high and low impact energy ........ 109

Figure 5-6. $O^-$ RSF (normalized to $GaN^-$) as a function of AlN mole fraction (x) in $Al_xGa_{1-x}N$ at 14.5 keV and 6.0 keV impact energies ........ 110

Figure 5-7. Useful ion yield of negative ions in $Al_xGa_{1-x}N$ under $Cs^+$ primary ion bombardment ........ 111

Figure 5-8. Schematic drawing of the energy band gap of semiconductor showing the conduction band minimum ($E_c$), valence band maximum ($E_v$), the vacuum level $E_{vac}$, the Fermi energy $E_F$, the electron affinity $\chi$ and the work function $\phi$. ........ 113

Figure 5-9. Work function of n-type and p-type GaN as a function of Cs evaporation time at 130K ........ 114

Figure 5-10. The surface concentration of Cs atoms and the corresponding $GaN^-$ yield change with x in $Al_xGa_{1-x}N$ at 14.5 keV impact energy. ........ 115

Figure 5-11. Schematic energy diagram for a sputtered atom leaving solid surface........... 116

Figure 6-1. Compilation of the useful yields determined for the six analyzed species versus the corresponding sputtering yield............................................................... 125

Figure 6-2. Energy distribution of $GaCs^+$ after electron beam charge neutralization from the sample with the worst charging effect...................................................... 128

Figure 6-3. Depth profile of matrix and impurity species in $Al_xGa_{1-x}N$ with x=0.21 at 5.5 keV impact energy using $MCs^+$ technique.................................................... 129

Figure 6-4. Mass Spectrum of $Al_xGa_{1-x}N$ (x=0.21) at 5.5 keV energy using $MCs^+$ Technique.......................................................................................................... 130

Figure 6-5. Sputter rate (normalized to beam density) of $Al_xGa_{1-x}N$ as a function of AlN mole fraction (x) using $MCs^+$ at 5.5 keV and 1.25 keV impact energy............ 131

Figure 6-6. Matrix ion intensity ratio versus the matrix mole fraction ratio at 5.5 keV impact energies using $MCs^+$ technique..................................................................... 132

Figure 6-7. Inverse plot of matrix ion intensity ratio versus the matrix mole fraction ratio at 5.5 keV impact energies using $MCs^+$ technique.......................................... 132

Figure 6-8. Comparison of matrix ion intensity ratio with high and low impact energy using $MCs^+$ technique........................................................................................... 133

Figure 6-9. $MgCs^+$ RSF as a function of AlN mole fraction (x) at 1.25 and 5.5 keV impact energies ........................................................................................................ 134

Figure 6-10. $SiCs_2^+$ RSF as a function of AlN mole fraction (x) at high and low impact energies ................................................................................................................. 136

Figure 6-11. $OCs_2^+$ RSF as a function of AlN mole fraction (x). $OCs_2^+$ RSF generated by normalization to (a) $GaCs^+$, (b) $NCs^+$ and (c) $NCs_2^+$ ........................................ 138

Figure 6-12. Ion production of $Cs^+$ and $Cs_2^+$ ions at 5.5 keV and 1.25 keV impact energies ................................................................................................................. 140

Figure 6-13. The useful ion yield of $MCs^+$ versus AlN mole fraction (x) in $Al_xGa_{1-x}N$. (a) $GaCs^+$; (b) $AlCs^+$; (c) $MgCs^+$ and (d) $NCs^+$ ...................................................... 141

Figure 6-14. The useful ion yield of $MCs_2^+$ versus AlN mole fraction (x) in $Al_xGa_{1-x}N$. (a) $GaCs_2^+$; (b) $SiCs_2^+$ and (c) $NCs_2^+$...................................................................... 143

Figure 7-1. Sputter rate as a function of x in $Al_xGa_{1-x}N$ using $Cs^+$ and $O_2^+$ at different energies and different angle of incidence ............................................................... 150

Figure 7-2. Matrix ion intensity ratio versus mole fraction ratio or AlN mole fraction in $Al_xGa_{1-x}N$ under different analysis conditions........................................................ 152

Figure 7-3. The reverse plot of matrix ion intensity ratios vs. atomic concentration ratios ........ 153

Figure 7-4. The effect of electron beam intensity on the matrix ion intensity ratio in $Al_xGa_{1-x}N$ with x=0.39 using $O_2^+$ bombardment and positive secondary ion detection at 1.25 keV impact energy ........ 159

Figure 7-5. Comparison of O profile in $Al_xGa_{1-x}N$ film with x=0.49 before and after $^{16}O$ implantation using $Cs^+$ primary ion and negative secondary ion detection at 14.5 keV impact energy ........ 160

Figure 7-6. A typical 5-window holder for SIMS analysis ........ 161

Figure 7-7. The variation of secondary ion intensities and the calculated RSF's ........ 163

Figure 7-8. A modified 1-window holder for SIMS analysis.. ........ 164

Figure 8-1. Illustration of thin layer quantification with profile spreading by ion mixing... 173

## LIST OF TABLES

Table 1-1. The most common impurities in GaN materials system ....................................... 7

Table 2-1. Common methods to reduce charging effects ..................................................... 48

Table 3-1. AlGaN sample set used for the study ................................................................ 65

Table 3-2. Samples fabricated by high dose of implantation................................................ 69

Table 3-3. Analysis conditions in the project ...................................................................... 74

Table 4-1 Analysis conditions under $O_2^+$ primary ion bombardment.................................... 81

Table 4-2 bond enthalpies in gaseous diatomic species........................................................ 98

Table 5-1 Analysis conditions using $Cs^+$ primary ion with negative secondary ions detection ..................................................................................................... 104

Table 5-2. Electron affinity of Si, AlN, GaN, and MgN .................................................... 112

Table 6-1. Analysis conditions under $Cs^+$ primary ion bombardment with positive secondary ion ($MCs^+$) detection............................................................................ 127

Table 7-1. List of impurity and matrix secondary ions for the analysis conditions............. 154

Table 7-2. Estimation of the error of sputtering rate of $Al_xGa_{1-x}N$ with x=0.58 using $O_2^+$ beam at 1.25 keV and 50 nA beam current with raster area of 200µm by 200µm... 157

Table 7-3. Estimation of the error of sputtering rate of $Al_xGa_{1-x}N$ with x=0.18 using $Cs^+$ beam at 14.5 keV and 30 nA beam current with raster area of 180µm by 180µm... 157

Table 7-4. Comparison of nominal and measured dose after ion implantation .................. 159

Table 7-5. The variation of secondary ion intensity and the calculated RSF's using 5-window holder and bombarded with $Cs^+$ at 14.5 keV impact energy .................. 162

Table 7-6. Summary of experimental uncertainty ............................................................ 166

# LIST OF EQUATIONS


$E_g(Al_xGa_{1-x}N) = xE_g(AlN) + (1-x)E_g(GaN) - bx(1-x)$
$E_g(In_xGa_{1-x}N) = (1-x)E_g(InN) + xE_g(GaN) - bx(1-x)$ (Equation 1-1) ................. 4

$\frac{1}{2}mv^2 = qV$ (Equation 1-2) ................. 11

$\frac{mv^2}{r} = qvB$ (Equation 1-3) ................. 12

$\frac{m}{q} = \frac{B^2r^2}{2V}$ (Equation 1-4) ................. 12

$eV = \frac{1}{2}mv^2$ (Equation 1-5) ................. 16

$v = \frac{L}{t}$ (Equation 1-6) ................. 16

$\frac{m}{e} = \frac{2Vt^2}{L^2}$ (Equation 1-7) ................. 16

$t = L\sqrt{\frac{m}{e}\frac{1}{2V}}$ (Equation 1-8) ................. 16

$I_A = I_p \cdot Y \cdot P^{\pm} \cdot f \cdot C_A$ (Equation 2-1) ................. 24

$P^+ \approx \exp[-(I-\phi)/\varepsilon_0]$
$P^- \approx \exp[-(\phi-A)/\varepsilon_0]$ (Equation 2-2) ................. 29

$\varepsilon_0 = \frac{\hbar\gamma v_\perp}{C_1\pi}$ (Equation 2-3) ................. 30

$\frac{N_+}{N_0} \propto \exp(-\frac{I}{K})$ (Equation 2-4) ................. 30

$M^0 \longleftrightarrow M^+ + e^-$ (Equation 2-5) ................. 31

$K_+ = \frac{N_+N_e}{N_0}$ (Equation 2-6) ................. 31

$K_+ = (\frac{2\pi}{h^2}\frac{M_+M_e}{M_0}kT)^{3/2}\frac{B_+B_e}{B_0}\exp(-\frac{E}{kT})$ (Equation 2-7) ................. 31

$P^{+} = \frac{N_{+}}{N_0} = \frac{1}{N_e}(\frac{2\pi}{h^2}\frac{M_{+}M_e}{M_0}kT)^{3/2}\frac{B_{+}B_e}{B_0}\exp(-\frac{I}{kT})$ (Equation 2-8) ................................ 31

$\log(P^{+}) = 15.38 + \log\frac{2B_{+}}{B_0} + 1.5\log T - \frac{5040(I-\Delta E)}{T} - \log N_e$ (Equation 2-9) ................ 31

$P^{-} = \frac{N_{-}}{N_0} = N_e(\frac{2\pi}{h^2}\frac{M_{-}M_e}{M_0}kT)^{3/2}\frac{g_0 g_e}{g_{-}}\exp(-\frac{A}{kT})$ (Equation 2-10) ................................ 31

$MO \rightarrow M^{+} + O^{-}$ (Equation 2-11) ................................ 36

$n_{+} = nP_e$, $n_0 = nP_f$ (Equation 2-12) ................................ 37

$P_f = 1 - P_e$ (Equation 2-13) ................................ 38

$\frac{n_{+}}{n_0} = \frac{P_e}{1-P_e}$ (Equation 2-14) ................................ 38

$P_e = [1 + \exp(-\frac{\Delta E}{kT_e})]^{-1}$ (Equation 2-15) ................................ 38

$\frac{n_{+}}{n_0} = \exp(-\frac{\Delta E}{kT_e})$, where $\Delta E = I - E_T$ (Equation 2-16) ................................ 38

$\log(P^{+}) = 15.38 + \log\frac{2B_{+}}{B_0} + 1.5\log T - \frac{5040(I-\Delta E)}{T} - \log N_e$ (Equation 2-17) ................ 39

$\frac{I_m}{C_m} = RSF_i\frac{I_i}{C_i}$ (Equation 2-18) ................................ 40

$RSF = C_m RSF_i = \frac{I_m}{I_i}C_i$ (Equation 2-19) ................................ 40

$C_i = \frac{I_i}{I_m}RSF$ (Equation 2-20) ................................ 40

$RSF = \frac{\phi I_m t}{d\int I_i}$ (Equation 2-21) ................................ 41

$[O]\ \text{or}\ [Cs] \propto \frac{1}{1+Y}$ (Equation 2-22) ................................ 44

$$P^{+} = \frac{n^{+}}{n^{0}} \propto \left[\frac{1}{S_{1}}\right]^{c^{+}} \propto [O]_{v}^{c^{+}}$$
$$P^{-} = \frac{n^{-}}{n^{0}} \propto \left[\frac{1}{S_{1}}\right]^{c^{-}} \propto [Cs]_{v}^{c^{-}}$$
(Equation 2-23) ........ 44

$Q = q_p - q_s$ (Equation 2-24) ........ 46

$Q = q_p + q_s + q_e$ (Equation 2-25) ........ 47

$P \propto \exp(\frac{e(\phi - I)}{KT})$ (Equation 3-1) ........ 56

$\frac{N - N_C}{N} = \frac{N * \tau}{1 + N * \tau}$ (Equation 3-2) ........ 62

$\text{Instantaneous count rate} = \text{apparent count rate} \times \frac{\text{raster area}}{\text{analyzed area}}$ (Equation 3-3) ........ 62

$C_{MAX} = \frac{\Phi}{\sqrt{2\pi}\Delta R_P}$ (Equation 3-4) ........ 68

$x = \frac{\text{Al peak concentration}}{\text{Atomic density of GaN}} * 2$ for Al implant into GaN (Equation 3-5) ........ 68

$x = 1 - \frac{\text{Ga peak concentration}}{\text{Atomic density of AlN}} * 2$ for Ga implant into AlN (Equation 3-6) ........ 69

$R_{KO} = \frac{0.0276 W E_0^{1.67}}{Z^{0.89}\rho}$ (Equation 3-7) ........ 70

$\frac{\text{new electron source HV}}{2\,\text{kV}} = \frac{\text{new sample bias}}{4.5\text{kV}}$ (Equation 3-8) ........ 72

$\tau_{Ga} = \frac{I_{Ga} t}{C_{Ga} dA_{detect}}$ (Equation 4-1) ........ 91

$RSF = C_m RSF_i = \frac{I_m}{I_i} C_i$ (Equation 4-2) ........ 94

$RSF_i = \frac{RSF}{C_{Ga}}$ (Equation 4-3) ........ 94

$C_{Ga} = (1 - x) * \frac{N_{AlGaN}}{2}$ (Equation 4-4) ........ 94

$\tau_i = \frac{\int I_i}{\Phi A_{detect}}$ (Equation 4-5) ........ 94

$\tau_m = \frac{I_m t}{C_m dA_{detect}}$ . (Equation 4-6) ........ 95

$\frac{\tau_i}{\tau_m} = \frac{\int I_i}{\Phi A_{detect}} / \frac{I_m t}{C_m dA_{detect}} = \frac{d * \int I_i}{\Phi I_m t} * C_m = \frac{C_m}{RSF}$ (Equation 4-7) ........ 95

$\frac{1}{RSF_i} = \frac{C_m}{RSF} = \frac{\tau_i}{\tau_m}$ (Equation 4-8) ........ 95

$P^- \propto \exp[(A - \phi)/\varepsilon_0]$ (Equation 5-1) ........ 103

$A_{MN} = Ln[Exp(A_M) + Exp(A_N)]$ (Equation 5-2) ........ 112

$\phi = \chi + (E_c - E_F)$ (Equation 5-3) ........ 112

$\phi = \chi + \frac{E_g}{2}$ (Equation 5-4) ........ 113

$S = \frac{\text{linear sputter rate (nm/sec)}}{\text{sputter area } (\mu m^2)} * 1E-3\ (\mu m/nm)$ (Equation 5-5) ........ 115

$Y = \frac{S\ (\mu m^3/s)}{I_P * 6.24E9\ \text{atoms/s}} * N_{AlGaN}\ (\text{atoms/cm}^3) * 1E\text{-}12 (cm^3/\mu m^3)$ (Equation 5-6) ... 115

$[Cs] = \frac{1}{1+Y} * N_{AlGaN}$. (Equation 5-7) ........ 115

$M^0 + Cs^+ \rightarrow MCs^+$ (Equation 6-1) ........ 122

$M^0 + Cs_2^+ \rightarrow MCs_2^+$ (Equation 6-2) ........ 122

$MCs^0 + Cs^+ \rightarrow MCs_2^+$ (Equation 6-3) ........ 122

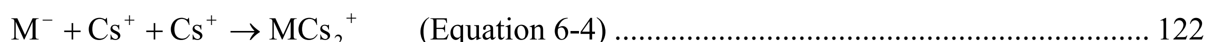
$M^- + Cs^+ + Cs^+ \rightarrow MCs_2^+$ (Equation 6-4) ........ 122

$I(MCs^+) = I_P \cdot Y^2 \cdot C_M \cdot C_{Cs} \cdot P_{Cs^+} \cdot \gamma_{M^0-Cs^+} \cdot \eta_{MCs^+}$ (Equation 6-5) ........ 123

$\tau = \frac{\text{number of detected ions}}{\text{number of sputted atoms}}$ (Equation 6-6) ........ 123

$n(M) = \int_0^{t_{final}} \frac{I_P}{e} \cdot Y \cdot C_M(t) dt = \frac{I_P}{e} \cdot Y \cdot \int_0^{t_{final}} C_M dt$ (Equation 6-7) ........ 123

$\tau(MCs^+) = k_1 \cdot Y \cdot C_{Cs} \cdot P_{Cs^+}$ (Equation 6-8) ........ 123

$\tau(MCs_2^+) = k_2 \cdot Y^2 \cdot C_{Cs}^2 \cdot P_{Cs^+}$ (Equation 6-9) ........ 124

$\tau(MCs_2^+) = k_3 \cdot Y^2 \cdot C_{Cs}^2 \cdot P_{Cs^+}^2 \cdot \varepsilon$ (Equation 6-10) ........ 124

$\tau(MCs_2^+) = k_4 \cdot Y^2 \cdot C_{Cs}^2 \cdot P_{Cs^+}^2 \cdot \beta_{M^-}$ (Equation 6-11) .................................................. 124

$C_{Cs_x^+} = \frac{I_{Cs_x^+} * t}{d * A_{detect}}$ (Equation 6-12) .................................................................... 139

$1\,\mu m^3/(s.nA) = \frac{1E-12\,cm^3}{6.24E19\,ions} * N_{AlGaN} = 14.68\,atoms/ion$ (Equation 7-1) ....................... 149

$Y_t = \sum Y_i$ (Equation 7-2) ............................................................................................ 151

## LIST OF SYMBOLS

| | |
|---|---|
| $A$ | Electron affinity of elements |
| $A_{detect}$ | Area from which secondary ions are collected |
| $C_A$ | Fractional concentration of element A |
| $C_i$ | Concentration of element i |
| $C_m$ | Concentration of matrix element |
| $d$ | Crater depth |
| $\varepsilon_0$ | Parameter proportional to the escape velocity of the ions |
| $E_c$ | Conduction band minimum |
| $E_F$ | Fermi energy |
| $E_g$ | Energy band gap |
| $E_{vac}$ | Vacuum energy |
| $f$ | Instrument transmission factor |
| $\phi$ | Work function |
| $\Phi$ | Implant dose in standards |
| $I$ | First ionization potential of elements |
| $I_A$ | Secondary ion intensity of element A |
| $I_i$ | Secondary ion intensity of element i |
| $I_p$ | Primary ion current |
| $I_m$ | Secondary ion intensity of matrix element |
| $I_R$ | Secondary ion intensity of reference element R |
| $\chi$ | Electron affinity of solid surface |
| $M^0$ | Neutral atom of element M |
| $M^{\pm}$ | Positive/negative ion of element M |
| $N_{AlGaN}$ | Atomic density of AlGaN |
| $N$ | True secondary ion count |
| $N_C$ | Measured pulse rate on detector |
| $P^{\pm}$ | Positive/negative ionization probability |
| RSF | Relative sensitivity factor |

| | |
|---|---|
| Rc | Crossing distance in Bond Breaking Model |
| $R_{KO}$ | Kanaya-Okayama range |
| ρ | Average density in g/cm$^3$ |
| S | Sputter rate |
| t | Sputter time |
| τ | Useful ion yield |
| W | Average atomic weight in g/mol |
| x | AlN mole fraction in $Al_xGa_{1-x}N$ |
| 1-x | GaN mole fraction in $Al_xGa_{1-x}N$ |
| Y | Sputter yield (atoms sputtered /incident ion) |
| Z | Average atomic number |
| Zc | Crossing distance in Electron-tunneling Model |
| [O] | Steady state surface concentration of oxygen atoms |
| [Cs] | Steady state surface concentration of Cs atoms |

# LIST OF ACRONYMS

| | |
|---|---|
| AlGaN | Aluminum Gallium Nitride |
| CL | Cathodoluminescence |
| DMCP | Dual Micro-Channel Plate detector |
| EBIC | Electron Beam Induced Conductivity |
| EM | Electron Multiplier |
| ESA | Electrostatic Analyzer |
| FC | Faraday Cup |
| GaN | Gallium Nitride |
| HEMT | High-Electron Mobility Transistor |
| LD | Laser Diode |
| LED | Light Emitting Diode |
| LEXES | Low energy Electron induced X-ray Emission Spectrometry |
| LTE | Local Thermal Equilibrium |
| LVDC | Linear Voltage Differential Capacitance |
| MBE | Molecular Beam Epitaxy |
| MOCVD | Metalorganic Chemical Vapor Deposition |
| MODFET | Modulation-Doped Field Effect Transistor |
| MQW | Multiple Quantum Well |
| NEG | Normal incidence Electron Gun |
| PL | Photoluminescence |
| RSF | Relative Sensitivity Factor |
| SIMS | Secondary Ion Mass Spectrometry |
| SRIM | Stopping and Range of Ions in Matter |
| TOF | Time-of-Flight |
| 2-DEG | 2-Dimensional Electron Gas |
| WDS | Wavelength Dispersive Spectrometers |
| XPS | X-ray Photoelectron Spectroscopy |

# 1. Introduction and Overview

## 1.1 Structure of the Dissertation

Chapter one describes the motivation and objective of this work and provides background information on the III-nitride semiconductor materials system and secondary ion mass spectrometry (SIMS). Chapter two reviews ion emission mechanisms and SIMS quantification related issues in $Al_xGa_{1-x}N$ materials. Chapter three gives a description of the experiments performed in this work. Chapters four through six discuss the quantification of matrix and impurity species in $Al_xGa_{1-x}N$ obtained using $O_2^+$ bombardment with positive ion detection and using $Cs^+$ bombardment with negative and $MCs^+$ ion detection. Chapter seven compares the quantification of matrix and impurity species in $Al_xGa_{1-x}N$ using the above analytical conditions including the analytical uncertainties inherent in these methods. Conclusions and future work are given in chapter eight.

## 1.2 Research Motivation and Objective

The motivation of this research is to provide analytical capabilities which will assist with the development of III-nitride semiconductors, specifically $Al_xGa_{1-x}N$'s, for use in optoelectronic and electronic devices. The concentration of alloys such as the ratio of Ga and Al in III-nitride semiconductors affects many parameters including their energy band gaps and lattice constants. The concentration and distribution of impurities in the materials affects their level of N or P type behavior, conductivity, and carrier density. The quantification of alloys and impurities in III-nitrides is essential for bandgap study, bandgap engineering, development of material growth techniques and device performance improvement.

Dynamic secondary ion mass spectrometry (SIMS) is an excellent characterization technique for this study because of its ability to provide elemental depth profiles with high sensitivity and good depth resolution.[1] In SIMS quantification of III-nitride semiconductors, two main issues exist which make the task of quantification challenging. One is matrix effects, i.e., the secondary ion yields of matrix and impurity elements vary with alloy composition because the changes in composition alter the chemical properties of the III-nitride material. A second issue is sample charging. Undoped $Al_xGa_{1-x}N$ alloys are generally insulating when $x>0.4$.[2,3] For $Al_xGa_{1-x}N$ with $x>0.4$, charging effects may become

sufficiently severe to preclude SIMS analysis especially when low energy primary ion bombardment is used.

To illustrate the challenges of SIMS quantification in III-Nitrides, figure 1-1 gives a typical structure of an optoelectronic device made of III-Nitride materials. It has a GaN layer, an AlGaN layer over which the mole fraction of Al may vary, and InGaN layers which are often only a few nm thick. This particular device is on a SiC substrate which requires an interfacial layer(s) of AlGaN to minimize the lattice mismatch between the SiC and GaN. The quantification of impurities such as the p-type dopant Mg in this type of structure is challenging because the Mg ion yield changes in GaN, $Al_xGa_{1-x}N$ and $Al_yGa_{1-y}N$, and the sputter rate at the same primary beam conditions varies in these layers. Without a sputter rate versus $Al_xGa_{1-x}N$ calibration curve which includes the range of $Al_xGa_{1-x}N$ encountered in this device, uniform sputter rate must be assumed and the Mg concentration must be approximated using GaN standard sample. Consequently, in the absence of such a calibration curve, the processed data indicating the thickness of the layers and the Mg concentration will not be accurate.

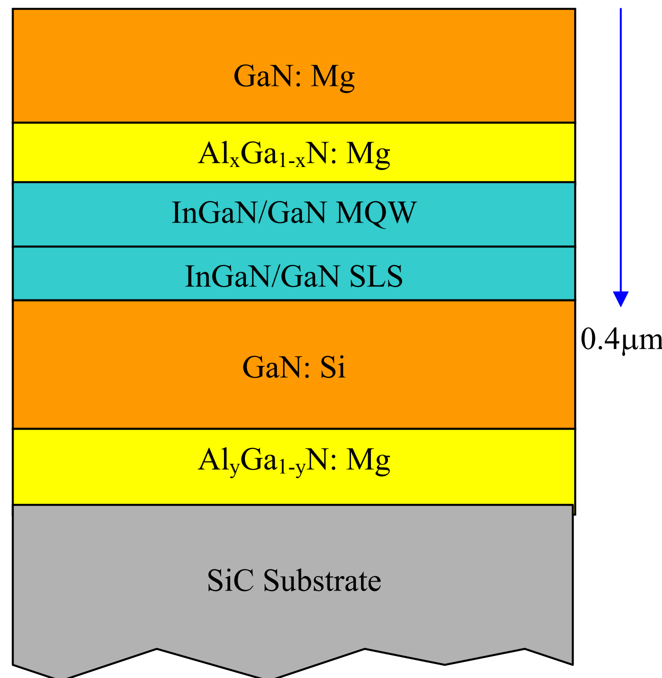


**Figure 1-1. Typical structure of III-Nitride ($Al_xGa_{1-x}N/In_xGa_{1-x}N$) optoelectronic device for multi-layer quantification**

To accurately quantify Mg in this type of structure, the AlN mole fraction in the $Al_xGa_{1-x}N$ and $Al_yGa_{1-y}N$ layers, the relative sensitivity factor (RSF) of Mg in GaN and in AlGaN layers, and the sputter rate in all layers must be determined. With that information, the depth scale of the depth profile can be corrected by applying the correct sputter rate to each layer, and the Mg concentration can be calculated using a point-by-point RSF correction referenced to a matrix species that tracks the change in Al concentration.

The objective of this study is to develop the methodologies required for accurate SIMS quantification of matrix and impurity species in III-Nitrides. Due to the availability of samples, quantification in $Al_xGa_{1-x}N$ will be studied. However, the experimental methods developed in this project can be used in the quantification of other III-nitride semiconductors such as InGaN and AlInGaN.

Comprehensive calibration curves under multiple analysis conditions will be developed in $Al_xGa_{1-x}N$ from GaN to AlN (over the range of $0 \le x \le 1$) which then must include quantitative analysis of both conducting to insulating materials. Based on the data obtained, the ionization mechanisms of matrix and impurity species in $Al_xGa_{1-x}N$ will be examined.

## 1.3 III-Nitride Materials System

### 1.3.1 Nomenclature

Various nomenclatures are used for III-Nitride materials. In the case of AlGaN, the Hill system formula of AlGaN with different Al concentration can be $Al_xGa_{1-x}N_1$, $Al_xGa_{0.5-x}N_{0.5}$, or $(Al_xGa_{1-x})_{0.5}N_{0.5}$. For $Al_xGa_{1-x}N$, x has been referred to as AlN mole fraction, Al mole fraction, AlN concentration, or Al concentration. To be consistent, the following name convention will be adapted in this work: AlGaN is written as $Al_xGa_{1-x}N$, with Hill system formula $Al_xGa_{1-x}N_1$, i.e. the sum of Al and Ga consists of 50% in atomic concentration, and N has 50%; x in $Al_xGa_{1-x}N$ is called AlN mole fraction, adapted from reference 4.

### 1.3.2 III-Nitride Semiconductor Materials System

The III-Nitride semiconductor materials system, including gallium nitride (GaN), aluminum nitride (AlN), indium nitride (InN) and their ternary and quaternary alloys, has

been attracting considerable attention due to wide applications in optoelectronic devices and in high power, high temperature electronic devices.[2-5] At ambient conditions the thermodynamically stable AlN, GaN and InN have wurtzite crystal structure which consists of two interpenetrating hexagonal close packed (HCP) sublattices, each with one type of atom, offset along the c-axis by 5/8 of the cell height.[6]

#### 1.3.2.1 Properties and Applications

In the GaN materials system, the incorporation of alloys such as aluminum (Al) and indium (In) can be used to control the band gap. The compositional dependence of energy band gap of $Al_xGa_{1-x}N$ and $In_xGa_{1-x}N$ may be expressed by eq. (1-1).[4]

$$\begin{aligned} E_g(Al_xGa_{1-x}N) &= xE_g(AlN) + (1-x)E_g(GaN) - bx(1-x) \\ E_g(In_xGa_{1-x}N) &= (1-x)E_g(InN) + xE_g(GaN) - bx(1-x) \end{aligned} \qquad \textbf{(Equation 1-1)}$$

Where $E_g(GaN)$ = 3.4 eV, $E_g(AlN)$ = 6.2 eV, $E_g(InN)$ = 1.9 eV, b is the bandgap bowing parameter. The energy band gap of the GaN materials system varies from 1.9eV to 6.2eV depending on the InN or AlN mole fraction.[4] In the more recent studies, the energy band gap if single crystal InN was found to be 0.9~1.4 eV,[7] or even down to ~0.7 eV as a result of improved quality of InN films grown using molecular beam epitaxy (MBE).[8,9] The wide range of band gap dependent on alloy composition allows potential emission wavelengths that cover nearly the entire visible spectrum range and extend into the ultraviolet (UV) region.

The lattice constant of these materials is also dependent on alloy composition. Figure 1-2 shows the energy band gap of III-Nitrides as a function of lattice constant.[10] Due to the difficulty of bulk growth, III-nitride semiconductors are typically deposited on a foreign substrate via epitaxial growth. A suitable substrate material should be lattice matched and have thermal expansion properties that are compatible with GaN. The most common substrates are sapphire ($Al_2O_3$) and silicon carbide (SiC).[11] Si is also used as the substrate material. The lattice constants of these three materials are shown in figure 1-2. Note that the lattice constant in the figure is "effective lattice constant". The III-nitrides generally grow on (0001) sapphire substrates with a 30° rotation about the c-axis with respect to the sapphire lattice, resulting in a smaller effective lattice constant which is $a_{sapphire}/\sqrt{3}$.[10] The (111) plane of Si substrate has the nearest match to (0001) GaN and has a lattice constant of 0.384 nm.

In all cases, lattice mismatch is large and a buffer layer is needed in order to confine most of the mismatch-induced lattice defects.

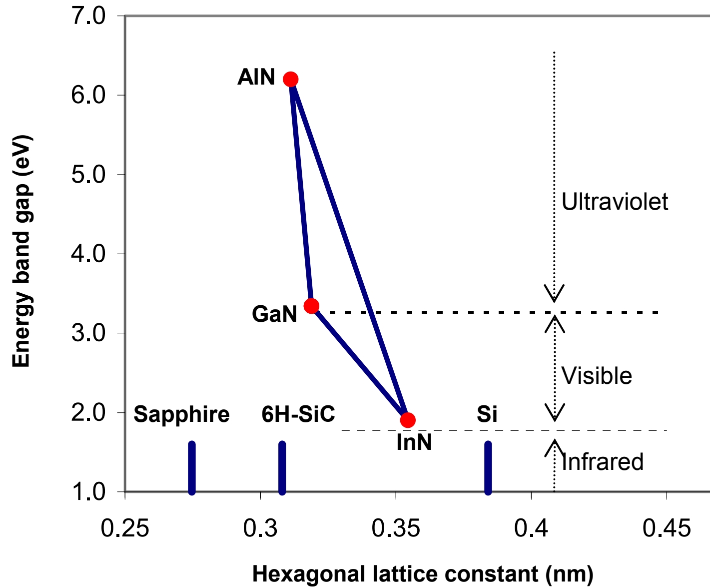


**Figure 1-2. Energy bandgap versus lattice constant for III-nitrides and selected substrate materials. (Data are from table 3 of reference 10. More recent data indicated a InN energy band gap of 0.7 eV [8,9])**

One of the most important properties of GaN is the wide range of the band gap which covers the visible spectrum as well as the near UV region. The band structure is direct which is most appropriate for optical devices with high emission efficiency. The strong chemical bonding in III-nitride materials system results in high electric field breakdown and high thermal / chemical stability making them suitable for high power, high temperature electronic devices.

The applications of III-nitride semiconductors are mainly in optoelectronic devices (both emitters and detectors) and high power/temperature electronic devices. III-nitride semiconductors are promising materials with the potential to reduce energy consumption by replacing conventional light sources such as incandescent or fluorescent lamps with solid state lighting.[12] Using III-nitride materials, highly efficient, long-lifetime solid-state light sources such as LED's (Light Electron Diodes) and LD's (Laser Diodes) may be fabricated. The nitride based LED's are very reliable and have found quick acceptance in display,

general illumination, indicator lighting, advertisement, and traffic sign/signal related applications.[13] Lasers are crucial for high density optical read and write technologies. Since the diffraction limited optical storage density increases as the laser wavelength is reduced, nitride-based coherent sources at wavelength approaching near UV are attracting much attention. III-nitrides, especially high Al content AlGaN, have been used for deep UV emitters for bio-chemical detection and for solar blind UV sensors with superior sensitivity for aircraft threat recognition.[14-16]

The large band gap, large electric field breakdown and good thermal/chemical capability of III-nitrides also make them promising materials for high power electronic devices.[17] Applications include electronic devices operating at high temperature and in harsh environments as well as low-cost compact amplifiers for earthbound and space applications.

#### 1.3.2.2 Common Impurities in III-Nitride Semiconductors

The properties of III-nitride materials are strongly influenced by impurites such as Si, Mg, O, Si, C and H.[18] Table 1-1 lists the most common impurities in GaN. Si and Mg are intentionally donor and acceptor dopants, respectively. The dopant source for Si is normally silane ($SiH_4$) or disilane ($Si_2H_6$). The dopant source for Mg is usually bis-cyclopentadienyl magnesium ($Cp_2Mg$). However, Si and Mg can be also residual impurities from contamination of the growth chamber. The typical impurity range for intentional doping of $Al_xGa_{1-x}N$'s with Si is from $10^{17}$ to $10^{20}$ atoms/cm$^{3}$. With Mg, intentional doping levels are usually approximately $10^{18}$ atoms/cm$^3$.[18]

**Table 1-1. The most common impurities in GaN materials system (data are from reference 18)**

| Impurities | Sources | Function | Level ($cm^{-3}$) |
|---|---|---|---|
| Si | Dopant from silane (SiH4) | n-type dopant | $10^{17}$~$10^{20}$ |
| Mg | Dopant from bis-cyclopentadienyl magnesium (Cp2Mg) | p-type dopant | ~$10^{18}$ |
| O | • Residual water vapor<br>• Oxygen impurities leached from the quartz containment vessel | unintentional doping shallow donor | $10^{16}$~$10^{19}$ |
| C | • Metal organic gallium precursor in MOCVD | amphoteric behavior | $10^{16}$~$10^{19}$ |
| H | • MOCVD: Metal organic sources, carrier gas, dopant sources | passivates acceptors | $10^{17}$~$10^{19}$ |

Oxygen acts as a shallow donor in GaN and can have strong influence on the background n-type conductivity. The source of oxygen is often the $NH_3$ precursor used in MOCVD (metal organic chemical vapor deposition) growth, the residual water vapor in MBE (molecular beam epitaxy) chamber or oxygen impurities leached from the quartz containment vessel often used in $N_2$ plasma sources. The typical concentration of oxygen varies from $10^{16}$ to $10^{19}$ atoms/$cm^3$. It is believed that the amount of residual oxygen depends on the Al content in $Al_xGa_{1-x}N$; the higher the AlN mole fraction the higher the amount of oxygen.[19,20]

Carbon can also be a major residual impurity in MOCVD nitrides. Its source is typically the metal organic gallium precursor.[21] Carbon is an amphoteric impurity in GaN and AlN,[22] with acceptor formation under some conditions and possible donor action in other cases. The carbon contamination is typically $10^{16}$ to $10^{19}$ atoms/$cm^3$.

Hydrogen is a component of most of the gases and liquids used in the growing, annealing and processing of semiconductors. Atomic hydrogen can exist as $H^0$, $H^+$ or $H^-$. It diffuses rapidly and can form neutral complexes with dopants. The hydrogen passivation results in the reduction in doping density in the near surface region and high resistivity of

GaN materials, especially p-type GaN. The hydrogen concentration in as-grown GaN samples is typically $10^{17}$ to $10^{19}$ atoms/cm$^3$.[18]

Secondary ion mass spectrometry (SIMS) is the technique of choice to measure these impurities at ppm (parts per million) and to obtain their depth distribution in the material, due to its high sensitivity (ppb or parts per billion) and good depth resolution (<2nm dependent on primary beam energy and the sputtering characteristics of the specimen). A description of the SIMS technique follows.

## 1.4 Secondary Ion Mass Spectrometry (SIMS)

### 1.4.1 Introduction

When a surface is bombarded with energetic primary ions, various atoms and molecules are sputtered from the surface. A small portion of the sputtered species are ionized and extracted by an electric field. These secondary ions are then mass separated and detected to determine the chemical composition of the sample surface. This is the basis of the Secondary Ion Mass Spectrometry (SIMS) technique. The incident ions are usually oxygen or cesium since these elements provide secondary ion yield enhancement of electropositive and electronegative elements, respectively.[21]

From the observation of the positive secondary ions by J.J. Thomson[23] in 1910 to the introduction of SIMS instruments in 1960s, the SIMS technique has made tremendous progress and has become a major technique for surface and thin-film analysis during the last 30 years. The basic components of a SIMS instrument include ion source, mass analyzer and detector. Figure 1-3 shows a schematic of a SIMS instrument.[24] In SIMS, the sample surface is bombarded with energetic primary ions. The collisions between primary ions and sample atoms produce particles including ions and neutrals as a result of what is termed a collision cascade discussed below. The secondary ions are extracted by the electric field, mass analyzed and detected. There are basically three types of SIMS data that can be obtained: mass spectra, depth profiles and secondary ion images. A mass spectrum contains secondary ion intensity as a function of mass-to-charge ratio thus providing an elemental and molecular survey of secondary ions obtained from the sputtered area. A depth profile provides the intensities of selected secondary ions as a function of time (or depth). Ion

images are formed when the monitored secondary ions are detected by an ion sensitive image amplifier such as a channel plate (ion microscope mode) or by mapping secondary ion intensity versus beam position (ion microscope mode). These images provide the lateral distribution of the selected secondary ion.

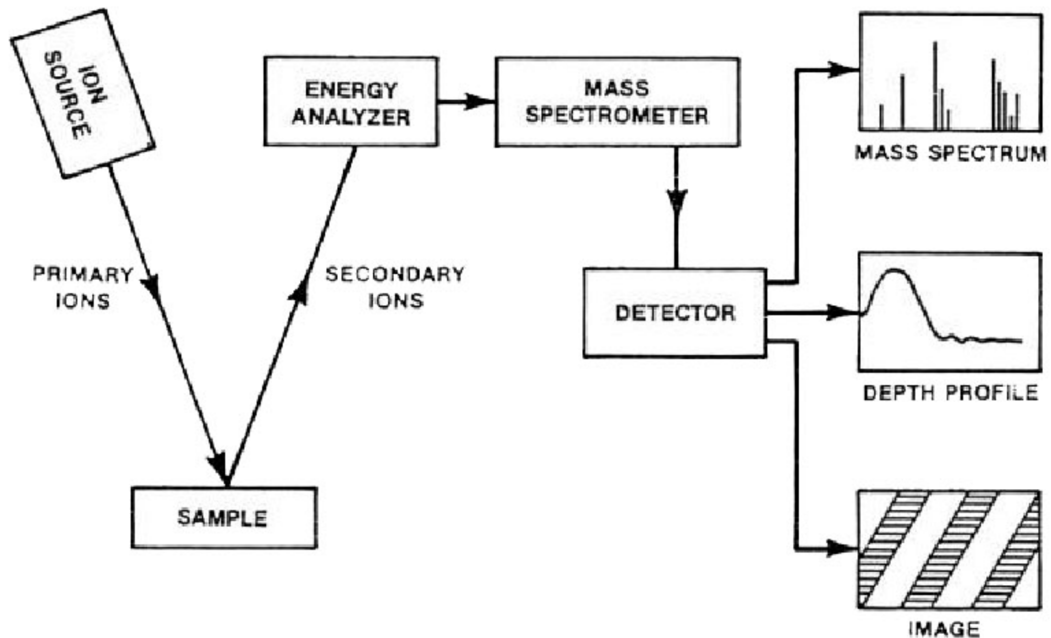


**Figure 1-3. Schematic of Secondary Ion Mass Spectrometry (Adapted from reference 24)**

When primary ions bombard the sample surface, they transfer kinetic energy to the target atoms via nuclear collisions. A target atom is set in motion by such a collision and this displaced atom may transfer a part of its energy to another target atom. A collision cascade is generated in this way. Figure 1-4 illustrates the formation of the collision cascade during primary ion/sample interaction.[25] During the collision, some of the target atoms in the near surface region receive sufficient momentum and energy to overcome the surface potential barrier and leave the target. Most of the sputtered species leave the surface with low energy (mainly in the 0~100 eV range) with a peak in the energy distribution at less than 10 eV. A small fraction of the emitted particles leave the sample surface in the ionized state, either positive or negative. These ions are then collected by the mass spectrometer and mass analyzed.

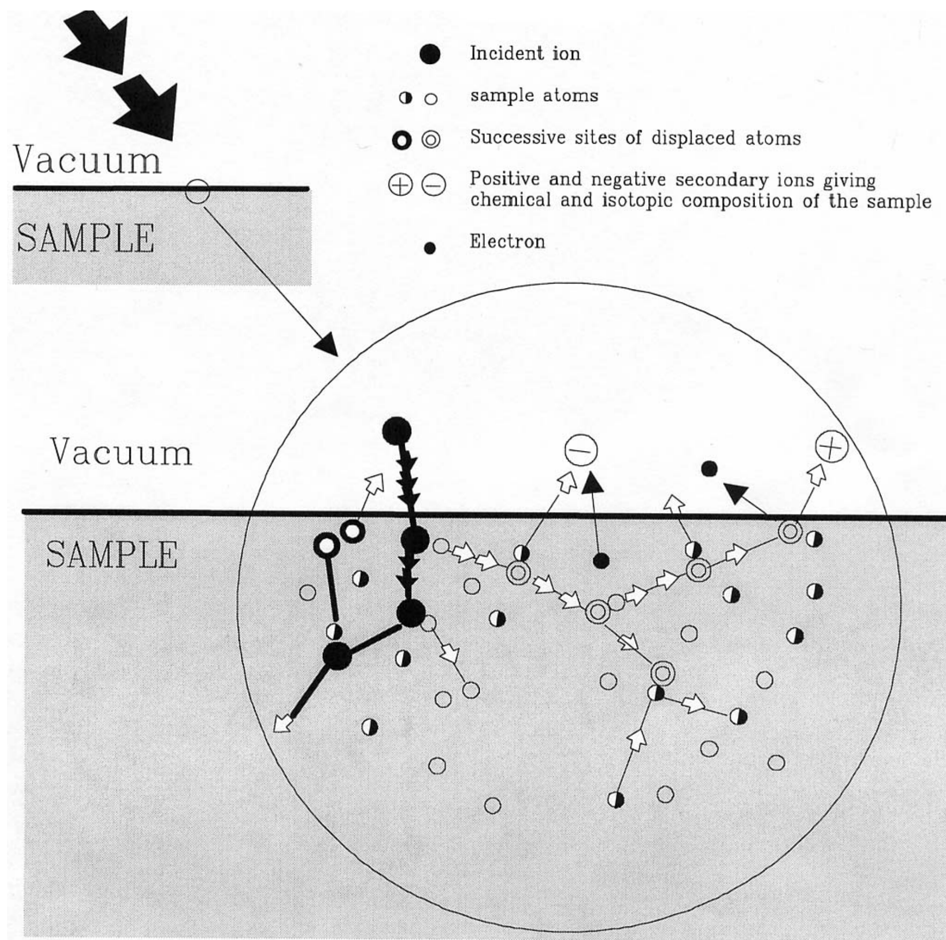


**Figure 1-4. Collision cascades after primary ions impinge sample surface (Adapted from reference 25)**

A typical SIMS instrument consists of the following basic components: ion sources to produce energetic primary ions such as $O_2^+$, $O^-$, $Cs^+$, $Ar^+$, $Ga^+$, etc.; ion optics to accelerate and focus the ions into the sample; a sample stage and exchange system to mount and transport samples; one or more energy filters to reduce energy dispersion of secondary ions; a mass filter to separate secondary ions according to their mass-to-charge ratio; and detectors to display or count secondary ions. Other components include apertures, slits, electronics, and high-vacuum system. The detail instrumentation of a CAMECA IMS SIMS will be described in chapter 3. In this section, different types of mass filters commonly used in SIMS are discussed in the following.

### 1.4.2 Mass Analyzers Commonly Used For SIMS

The secondary ions are selected and analyzed by mass analyzers. There are three basic types of mass analyzers in SIMS instrumentation, namely magnetic sector, quadrupole, and time-of-flight (TOF). Magnetic sector and quadrupole SIMS are often operated in a mode called “dynamic SIMS”.[21] In the “dynamic” mode, the sample surface can be eroded by scanning the ion beam in a raster pattern. Acquisition of the secondary ion intensities produced by a selected set of mass-to-charge ratios determined by elements for which information is desired, in a cyclic manner (the selected mass-to-charge ratio intensities are acquired and then the sequence is repeated as long as required to sputter to a desired depth) results in a depth profile. Although time-of-flight (TOF) instruments can also be used for depth profiling, it is typically utilized to provide top monolayer surface chemical analysis in the mode of operation called “static SIMS”.[26] In the “static” mode, a mass spectrum is obtained while the sample surface is sputtered very lightly, removing only a small fraction of the uppermost monolayers of the sample. The spectrum contains fragment ions or even intact molecular ions from the top monolayers, thus a thorough understanding of sample surface chemistry is possible. In Static TOF-SIMS, analyses are typically performed by employing a primary ion dose of less than $10^{12}$ ions/cm$^2$ in a pulse mode.[27] In the following sections, the three types of mass spectrometers are described in detail.

Magnetic Sector Analyzers

In a typical magnetic sector SIMS, e.g. CAMECA IMS 6F, the sample is maintained at a potential (adjustable from 0 to ±10 kV) and the immersion cover plate is grounded which is 4.5 mm above the sample. This setting results in a strong extraction field of secondary ions. The extracted secondary ions leaving the sample surface have kinetic energy given by eq. (1-2).

$$\frac{1}{2}mv^2 = qV \qquad \textbf{(Equation 1-2)}$$

Where m is the mass of the ion, v is its velocity, q is the charge of the ion and V is the secondary ion acceleration voltage.

The ions then pass through a magnetic sector flight tube in which the magnetic field (B) is applied in a direction perpendicular to the direction of ion motion. The ions are

deflected by the magnetic field. Only ions of mass-to-charge ratio that have equal centrifugal and centripetal forces pass through the flight tube as described by eq. (1-3).

$$\frac{mv^2}{r} = qvB \qquad \textbf{(Equation 1-3)}$$

Where r is the radius of curvature of the ion path.

From the above equations, the mass-to-charge ratio as a function of magnetic field and secondary ion acceleration voltage is obtained as shown in eq. (1-4).

$$\frac{m}{q} = \frac{B^2 r^2}{2V} \qquad \textbf{(Equation 1-4)}$$

By varying the magnetic field the magnetic sector spectrometer will separate ions of equal energy according to their mass-to-charge ratio. However, the resolution will be limited by the fact that ions leaving the ion source do not all have exactly the same energy and therefore do not have exactly the same velocity. This is analogous to the "chromatic aberration" in optical spectroscopy. To achieve better resolution, it is necessary to add an electrostatic sector that focuses ions according to their kinetic energy. Like the magnetic sector, the electrostatic sector applies a force perpendicular to the direction of ion motion.

Figure 1-5 is a schematic of a double focusing magnetic sector mass analyzer.[28] It consists of an electrostatic energy analyzer and a magnetic field mass spectrometer. Ion trajectory is illustrated by red (lower energy) and green colors (higher energy). The secondary ions extracted from the biased sample have an energy distribution up to hundreds of electron volts, with peak of ~10 eV. An electrostatic sector (ESA) is used to select the desired energy range of the secondary ions extracted from the sample surface. The selected secondary ion energy range can be further narrowed using an energy slit. Once a narrow range of secondary ion energies has been selected, a magnetic sector analyzer is used to select secondary ions according to their momentum which is equivalent to selecting for mass-to-charge ratio for monoenergetic secondary ions. In this arrangement using one electrostatic and one magnetic sector, the energy dispersion of the electrostatic sector can just compensate the energy dispersion of the magnet sector (see section 3.2.1.2), which reduces the chromatic aberrations and consequently produces higher mass resolution. This configuration of the magnetic sector instrument is typically called a double focusing instrument because it uses both direction and velocity (energy) focusing so that an ion beam initially diverging and

containing ions of different energies is brought into focus and separated according to the mass-to-charge ratio.[29]

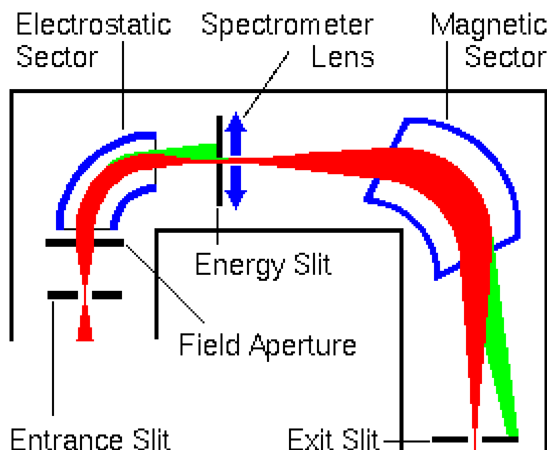


**Figure 1-5. Schematic of magnetic sector double focusing mass analyzers, including electrostatic analyzer (ESA) and mass spectrometer (MS) (Adapted from reference 28)**

The common operational mode of a magnetic sector mass spectrometer keeps the electrostatic sector at a constant potential and varies the magnetic field. A magnetic field scan can be used to cover a wide range of mass-to-charge ratios with constant ion transmission, i.e. ion transmission is essentially independent of the mass-to-charge ratio. The disadvantage of a magnetic field scan is that the magnetic field is subject to hysteresis and the mass switching speed is limited.

One alternative operation mode is to disperse ions over a detector array. Focal-plane (array) detectors can detect a range of masses simultaneously. This provides a multi-channel advantage that can improve the transmission efficiency for magnetic sectors. The array detectors for commercial magnetic sector mass spectrometers can only detect a portion of the entire mass range at any given instant.

The resolving power of a magnetic sector mass spectrometer is mainly determined by the slit widths (entrance slits, exit slits and energy slits). Higher resolution is obtained by decreasing these slit widths, however the number of ions that reach the detector will be decreased. Since secondary ion transmission decreases with increasing mass resolution, a typical effective mass resolution limit is about 4000 $m/\Delta m$ using the 10% valley definition.[30] In a special designed double focusing mass spectrometer with a large radius magnetic sector

(e.g. CAMECA IMS1280) the secondary ion optics has been optimized to work at full transmission up to 6000 mass resolution ($m/\Delta m$).[31]

Quadrupole Mass Analyzers

In a quadrupole SIMS, the sample is typically grounded. When energetic primary ions bombard a sample, the secondary ions ejected from sample surface are extracted by an extraction lens. The polarity of the voltage in extraction lens determines the polarity of the secondary ions that are extracted. Similar to the configuration of magnetic sector SIMS, an energy analyzer is typically used in combination with a quadrupole mass analyzer to reduce "chromatic aberrations". An energy filter passes ions that have a kinetic energy within a narrow range. All others, including neutrals are rejected by the analyzer. After the ions leave the energy filter, they are decelerated and focused in parallel onto the quadrupole mass spectrometer axis.[32] The ions are then separated by the quadrupole mass analyzer according to their mass-to-charge ratio. The ions having a specific mass-to-charge ratio are allowed to pass through the quadrupole and enter the detector, typically an electron multiplier which will be discussed in chapter 3 (section 3.2.1.3.2).

A typical quadrupole spectrometer consists of two pairs of conducting parallel rods 1 cm in diameter and 20 cm long. The rods are biased with direct and alternating potentials, as shown schematically in figure 1-6.[33] The alternating and direct voltages on the rods cause the ions to oscillate after entering the quadrupole. For a given set of voltages, ions with a certain mass-to-charge ratio undergo stable oscillations and traverse through the rods. All other ions have unstable oscillations and strike the rods. By varying the electrical signals to a quadrupole it is possible to vary the range of the mass-to-charge ratio transmitted. This makes spectral scanning possible.

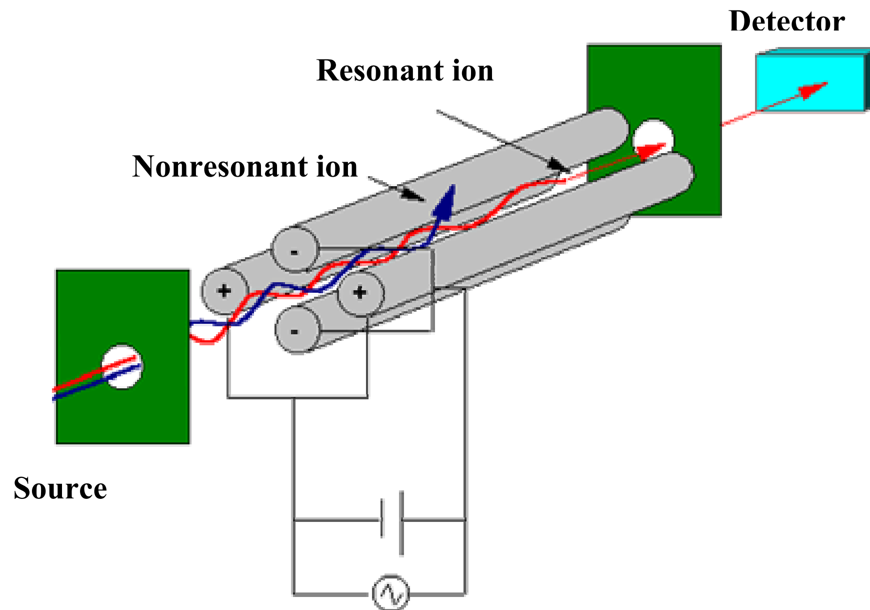


**Figure 1-6. Schematic of quadrupole mass spectrometer (Adapted from reference 33)**

The mass resolution that can be obtained with a quadrupole mass analyzer depends largely on the number of RF cycles that an ion undergoes when it penetrates the filter.[32] For optimum separation between mass peaks, the velocity of the ions should be very slow (only a few eV of energy) and the energy spread should be very small. For this purpose, the extraction field in quadrupole SIMS is usually small and the energy band pass of the system is narrow (typically 10 eV).

The low extraction fields typically used in quadrupole SIMS to extract secondary ions from the sample allow low energy ion bombardment which giving high depth resolution. It is also easier to do charge neutralization for the analysis of insulating materials because of the low extraction field and grounded sample. However, this system has limited mass resolution, with typical systems providing a resolution of about 300 using an m/Δm using the 10% valley definition.

Time-of-Flight (TOF) Mass Analyzers

In Time-of-Flight SIMS, pulsed primary ions, typically liquid metal ions such as $Ga^+$, or cluster ions such as $Au_n^+$, $Bi_n^+$, and $C_{60}^+$, are used to bombard the sample surface, causing the secondary elemental or cluster ions emit from the surface. The sample is biased to several kilovolts and an extraction field is formed above the sample surface. The secondary

ions are extracted and accelerated into a field-free drift region, separated by the time difference for the ions to flight from the ion source to the detector, and then detected by a dual microchannel plate (DMCP) detector.

Since a TOF mass spectrometer measures the time it takes ions of differing mass-to-charge ratios to move from the ion source to the detector, it requires that the starting time (the time at which the ions leave the ion source) is well-defined. This is typically achieved by pulsing the primary ion beam, which is different from quadrupole and magnetic sector SIMS instruments in which the primary beams typically operate in continuous mode.

The kinetic energy of an ion leaving the sample is:

$$eV = \frac{1}{2}mv^2 \qquad \textbf{(Equation 1-5)}$$

The ion velocity (v) is the length of the flight path (L) divided by the flight time (t):

$$v = \frac{L}{t} \qquad \textbf{(Equation 1-6)}$$

Substituting this expression into the kinetic energy relation, the working equation for the time-of-flight mass spectrometer can be derived:

$$\frac{m}{e} = \frac{2Vt^2}{L^2} \qquad \textbf{(Equation 1-7)}$$

Rearranging the equation to solve for the time of flight:

$$t = L\sqrt{\frac{m}{e}\frac{1}{2V}} \qquad \textbf{(Equation 1-8)}$$

The ions leaving the ion source of a time-of-flight mass spectrometer have neither exactly the same starting times nor exactly the same kinetic energies (similar to "chromatic aberrations"). Various time-of-flight mass spectrometer designs have been developed to compensate for these differences. To achieve the energy compensation, one way is to use electrostatic sector analyzer (ESA) as discussed in magnetic sector SIMS, the other way is to use an ion optic device called “reflectron” in which ions pass through a "mirror" or "reflectron" and their flight is reversed, as shown in figure 1-7.[30]

The reflector acts as an ion mirror, extending the flight length without increasing the instrument size. A linear-field reflectron allows ions with greater kinetic energies to penetrate deeper into the reflectron than ions with smaller kinetic energies. The ions that

penetrate deeper will take longer to return to the detector.  If a packet of ions of a given mass-to-charge ratio contains ions with varying kinetic energies, then the reflectron will decrease the spread in the ion flight times, and therefore improve the mass resolution of the time-of-flight mass spectrometer.  A curved-field reflectron ensures that the ideal detector position for the time-of-flight mass spectrometer does not vary with mass-to-charge ratio. This also results in improved resolution for time-of-flight mass spectrometers.

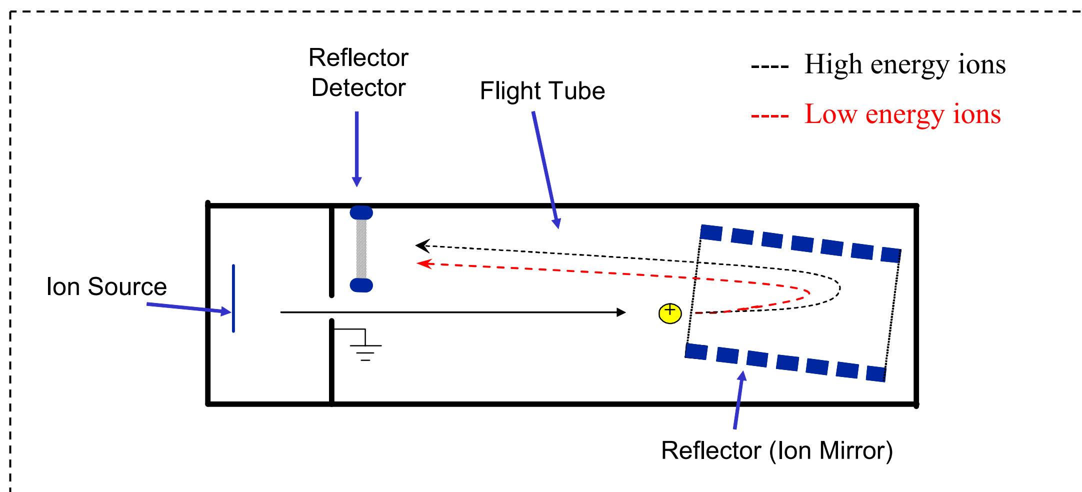


**Figure 1-7.  Operation of a time-of-flight (TOF) mass spectrometer with a reflectron (adapted from reference 30)**

The TOF mass spectrometer is a parallel detection analyzer.  It has high ion transmission (25%-90%), high mass resolution and the highest practical mass range of all SIMS analyzers.

For depth profiling, an ion gun is often operated in DC mode for sputtering, and the same ion gun or a second ion gun is operated in the pulsed mode for data acquisition.  For ultra-shallow depth profiling (a few nm) the ion gun can be operated in AC mode for sputtering.  Depth profiling by TOF-SIMS allows monitoring of all species of interest simultaneously, and with high mass resolution.[27]

During the drift time of the secondary ions, the extraction field can be switched off and low energy electrons can be directed toward the sample surface to compensate for any surface charging caused by primary or secondary particles. Thus all types of bulk insulators can be analyzed with minimal problems.

All three analyzers have their advantages and special applications. Magnetic sector and quadrupole SIMS are mainly used for depth profiling and TOF-SIMS for surface chemical analysis. Magnetic sector SIMS can achieve higher mass resolution than quadrupole SIMS, while quadrupole SIMS is suitable for depth profiling that requires constantly switch among masses due to the fast switching of electrical fields. Sample charge neutralization is simplified for both quadrupole and TOF based SIMS due to the low extraction field in quadrupole SIMS and pulsed extraction field in TOF SIMS. Table 1-2 summarizes the advantages/disadvantages and main applications of the three types of analyzers.

**Table 1-2. Comparison of three types of mass analyzers**

| Type | Advantages | Disadvantages | Main Application |
| --- | --- | --- | --- |
| Magnetic Sector | High mass resolution<br>High ion transmission<br>High dynamic range | Slow mass switching<br>Challenging charge neutralization | Depth profiling |
| Quadrupole | Fast mass switching<br>Easy charge neutralization | Low mass resolution<br>Low ion transmission<br>Narrow energy band pass | Depth profiling |
| Time-of-flight (TOF) | High mass resolution<br>High ion transmission<br>Parallel mass detection<br>High mass range<br>Easy charge neutralization | Limited dynamic range | Surface chemical analysis |

### 1.4.3 Sensitivity and Depth Resolution

Sensitivity and depth resolution are two important factors in III-nitride quantification, due to the requirement for the detection of low concentration impurities/contaminations and analysis of thin layers in real device structures. Non sample related parameters that affect sensitivity and depth resolution are primary beam species, primary beam energy, angle of incidence and other instrumentation factors.

Sensitivity is the minimum amount of an element which can be detected. SIMS can achieve detection sensitivity of less than 1E16 atoms/cm$^3$ for most elements. The major factors affecting the detection sensitivity are ionization efficiency, sputter rate, ion transmission of the analytical system, and detector efficiency. Ionization efficiency is affected not only by the detected species and the sample matrix, but also by the primary ion species. It has been determined that an electronegative species such as oxygen enhances the ion yield of electropositive species, and that very electropositive species such as cesium enhances the ion yield of electronegative species. Sputter rate of the material affects the secondary ion count rate. The faster the material sputters, the higher the secondary ion count rate. Thus increasing primary ion beam density increases sensitivity by increasing secondary ions emitted with respect to the constant dark current (the output of an electron multiplier based secondary ion detector when no secondary ions are striking it[28]). Transmission of the mass spectrometer, i.e. the ratio of the number of secondary ions reaching the detector to the number leaving the sample, can also limit detection. Mass spectrometer transmission factor is an instrumentation dependent parameter which varies with the configuration and type of mass analyzer used. High efficiency ion detectors are desirable for good detection sensitivity. The most widely used SIMS instruments have several types of detectors, including ion counting electron multiplier, Faraday cup and ion image detector. The ion counting electron multipliers are the most sensitive detectors, however the detection efficiency varies with the velocity of the impinging secondary particles determined by the mass and extraction voltage of the ions. When low extraction voltages have to be used, post acceleration of the secondary ions needs to be performed for efficient detection of low energy ions, which will be discussed in detail in chapter 3 (section 3.2.1.3.2). Other factors, such as mass interferences, residual gas in vacuum system, and memory effect also affect the sensitivity.

Depth resolution depends on the energy of the primary ion beam, the flatness of the crater bottom and the degree to which secondary ions originating from crater edges can be rejected. The primary beam transmits energy to the target atoms in a series of collisions via the collision cascade. Atoms from an outer monolayer can be driven into the sample resulting in surface mixing. The depth of the mixing region depends on the energy, the angle of impact and the species of the primary beam. Lower primary beam energies produce a shallower mixing region and thus higher depth resolution. Figure 1-8 is a Monte Carlo

simulation of oxygen and cesium implantation into GaN. Figure1-8 (a) and (b) can be used to compare the $O_2^+$ penetration at high (5.5 keV) and low (1.25 keV) impact energies , (b) and (c) compare $O_2^+$ and $Cs^+$ penetration at the same impact energy with angle of incidence of 48.5°. It is obvious that the penetration depth is deeper with high energy ion bombardment. At the same impact energy, the depth of the Cs mixing region is shallower than oxygen because of its larger atomic size. For higher depth resolution, a low energy $Cs^+$ ion beam will provide better results than $O_2^+$ at similar energy.

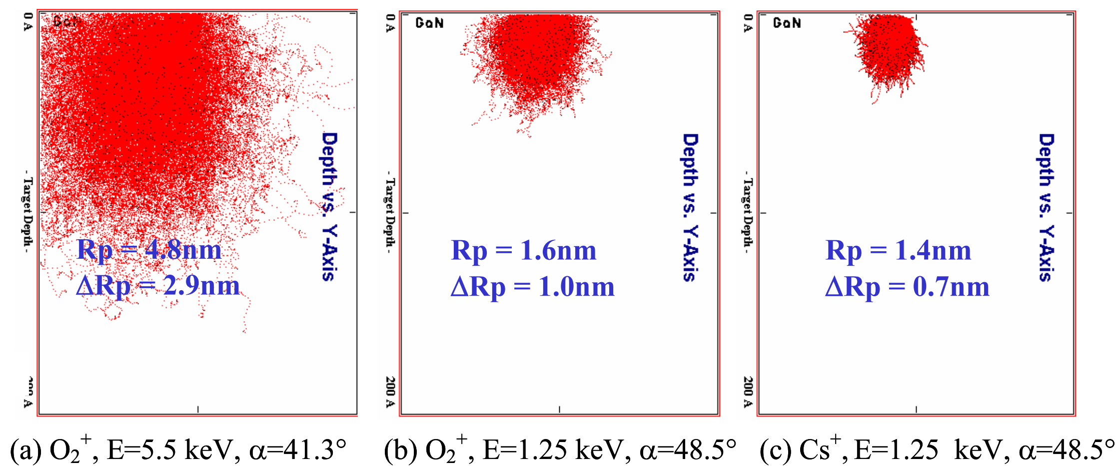


(a) $O_2^+$, E=5.5 keV, α=41.3° (b) $O_2^+$, E=1.25 keV, α=48.5° (c) $Cs^+$, E=1.25 keV, α=48.5°

**Figure 1-8. Monte Carlo simulation of oxygen and cesium incorporation into GaN at different energies. E is impact energy of primary ions, α is the angle of incidence.**

Crater bottom roughness and crater edge effects can also degrade depth resolution. A flat bottom crater is achieved by sweeping a finely focused primary beam in a uniform, overlapping raster pattern over a square region. In a CAMECA IMS-6f SIMS instrument, a field aperture in the path of the secondary ions allows extraction of the secondary ions leaving from a selected region of the crater bottom while rejecting ions from the crater edges.

The requirements of high sensitivity and high depth resolution are conflicting. Low energy ion bombardment provides better depth resolution but the inherently lower current obtainable with most primary columns tuned to low energy limits primary ion beam density. This lowered primary ion beam current density is often not sufficient to provide high sensitivity without requiring an inordinately long analysis time. In practice, the choice of analytical conditions employed must represent a compromise with respect to detection limit

and depth resolution. Depending on the need for yield enhancement of electropositive or electronegative elements and sensitivity and depth resolution requirements, analysis conditions with different primary species, primary ion energy and secondary ion extraction voltage must be chosen. In this project, SIMS analysis of III-nitrides using various primary species, primary ion energy and secondary ion extraction voltage will be studied.

## 1.5 References


[1] P. K. Chu, Y. Gao, and J. W. Erickson, J. Vac. Sci. Technol. B **16,** 197-203 (1998).

[2] S. N. Mohammad, A. A. Salvador, and H. Morkoc, Proceedings of the IEEE **83,** 1306-1355 (1995).

[3] H. Morkoc, S. Strite, G. B. Gao, M. E. Lin, B. Sverdlov, and M. Burns, Journal of Applied Physics **76,** 1363-1398 (1994).

[4] H. Morkoc, *Nitride Semiconductors and Devices* (Springer-Verlag Berlin Heidelberg, 1999).

[5] S. Strife and H. Morkoc, Journal of Vacuum Science & Technology B **10,** 1237-1266 (1992).

[6] S. J. Pearton, *GaN and related materials* (Gordon and Breach, New York, 1998).

[7] T. Inushima, V. V. Mamutin, V. A. Vekshin, S. V. Ivanov, T. Sakon, M. Motokawa, and S. Ohoya, Journal of Crystal Growth **227,** 481-485 (2001).

[8] J. Wu and W. Walukiewicz, Superlattices and Microstructures **34,** 63-75 (2004).

[9] J. Wu, W. Walukiewicz, K. M. Yu, J. W. Ager, E. E. Haller, H. Lu, and W. J. Schaff, Applied Physics Letters **80,** 4741-4743 (2002).

[10] P. Kung and M. Razeghi, Opto-Electronics Review **8,** 201-239 (2000).

[11] B. Monemar, Journal of Material Science: Materials in Electronics **10,** 227-254 (1999).

[12] S. Nakamura, S. J. Pearton, and G. Fasol, *The blue laser diode : the complete story* (Berlin ; New York : Springer, 2000).

[13] H. Morkoc, Properties of Nitrite Semiconductor, http://www.engineering.vcu.edu/fac/morkoc/learning/mahajan_short.pdf.

[14] J. C. Carrano, T. Li, D. L. Brown, P. A. Grudowski, C. J. Eiting, R. D. Dupuis, and J. C. Campbell, Electronics Letters **34,** 1779-1781 (1998).

[15] J. C. Carrano, T. Li, P. A. Grudowski, C. J. Eiting, D. Lambert, J. D. Schaub, R. D. Dupuis, and J. C. Campbell, Electronics Letters **34,** 692-694 (1998).

[16] M. Razeghi and A. Rogalski, Journal of Applied Physics **79,** 7433-7473 (1996).

[17] K. Zhu, M. L. Nakarmi, and K. H. Kim, Appl. Phys. Lett. **8,** 4669-4671 (2004).

[18] S. J. Pearton, J. C. Zolper, and R. J. Shul, Journal of Applied Physics **86,** 1-87 (1999).

[19] H. W. Jang, M. K. Lee, H. J. Shin, and J. L. Lee, Phys. Stat. Sol. (c) **0,** 2456-2459 (2003).

[20] S. P. Grabowski, M. Schneider, H. Nienhaus, W. Monch, R. Dimitrov, O. Ambacher, and M. Stutzmann, Applied Physics Letters **78,** 2503-2505 (2001).

[21] R. Zhang and T. F. Kuech, Applied Physics Letters **72,** 1611-1613 (1998).

[22] P. Boguslawski, E. L. Briggs, and J. Bernholc, Physical Review B **51,** 17255-17258 (1995).

[23] J. J. Thomson, Phil. Mag. **20,** 752 (1910).

[24] R. G. Wilson, F. A. Stevie, and C. W. Magee, *Secondary Ion Mass Spectrometry : a Practical Handbook for Depth Profiling and Bulk Iimpurity Analysis* (1989).

[25] CAMECA, IMS-6f user manual**,** 1-5 (1995).

[26] A. Benninghoven, F. G. Rudenauer, and H. E. Werner, *Secondary Ion Mass Spectrometry, Basic Concepts, Instrumental Aspects, Applications and Trends, p.290* (Wiley, New York, 1987).

[27] Phi, Our Techniques: TOF-SIMS, http://www.phi.com/genf.asp_Q_ID_E_283.

[28] R. Fleming, Secondary Ion Mass Spectrometry Theory Tutorial, http://www.eaglabs.com/cai/simstheo/caistheo.htm (1995).

[29] E_Source, Double-focusing Mass Spectrometer From Mass Spectrometry Terms, http://www.msterms.com/wiki/index.php?title=Double-focusing_Mass_Spectrometer.

[30] E_source, Atomic and Molecular Mass Spectrometry III, http://chz085.ust.hk/chem244/Lect13_0309Cao.ppt#1.

[31] CAMECA, Scientific Instruments, IMS 1280, http://www.cameca.fr/html/product_ims1280.html.

[32] ATOMICA, SIMS 4000 Service Manual, volume 3 section 24**,** 34 (1994).

[33] E_source, Characteristics of different mass analyzers, Fraunhofer-Institute for Process Engineering and Packaging IVV, http://www.ivv.fhg.de/ms/ms-analyzers.html.

# 2 Quantification Using Magnetic Sector (MS) SIMS

## 2.1 Introduction

Secondary Ion Mass Spectrometry (SIMS) has been widely used in material characterization, process control and new process development due to its high sensitivity and good depth resolution. Applications include both qualitative and quantitative analysis.

SIMS elemental quantification methods have been continually developed and improved over the last three decades. The purpose of SIMS quantification is to relate the measured secondary ion intensity $I_A$ of element A to its concentration $C_A$ in the sample. This relationship is given by the expression shown in eq. (2-1)[1]

$$I_A = I_p \cdot Y \cdot P^{\pm} \cdot f \cdot C_A \qquad \textbf{(Equation 2-1)}$$

where $I_A$ is the secondary ion intensity of element A, $I_p$ is primary ion current, Y is sputter yield, $P^{\pm}$ is the ionization probability of A, f is the instrument transmission factor (which includes secondary ion extraction efficiency, mass spectrometer transmission efficiency and detector efficiency for the measured mass–to-charge ratio), and $C_A$ is the fractional concentration of element A in the surface layer. In this expression, $I_P$, S and f can be measured or calculated, while the ionization probability is related not only to the element and the substrate matrix but also to the species of the primary ion in SIMS analysis. The complexity of the ionization probability leads to the diversity of secondary ion emission mechanisms which will be reviewed in section 2.2.

The difficulty of elemental quantification in SIMS results from the complexities of ionization. The secondary ion yields vary over six orders of magnitude from element to element across the periodic table as shown in figure 2-1 which illustrates the variation of relative sensitivity factor (RSF) in Si matrix under $O_2^+$ and $Cs^+$ bombardment.[2] Each element's ion yield is also affected by the matrix in which it is contained (matrix effects).

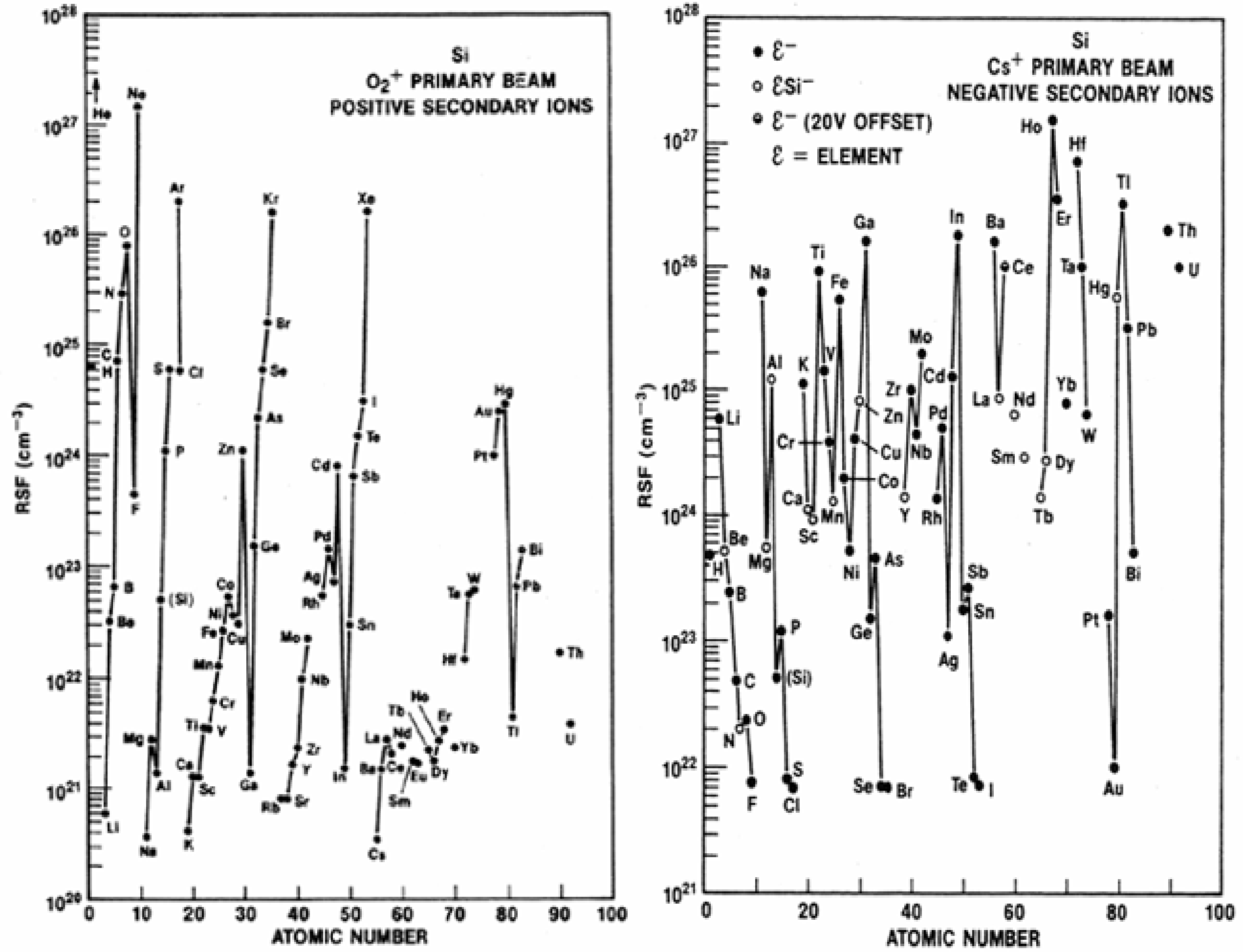


**Figure 2-1. Variation of RSF's in Si matrix under $O_2^+$ and $Cs^+$ bombardment (RSF is inversely proportional to the ion yield). (Adapted from reference 2)**

Although some semi-theoretical models and computer programs are available for SIMS quantification without a standard, quantification using standards is still the most accurate and widely used method. This chapter will review the theoretical models of secondary ion emission as well as quantification approaches in SIMS analysis in order to understand the ionization mechanism and quantification method in III-nitrides. Issues in quantification of matrix and impurities in $Al_xGa_{1-x}N$ will also be discussed.

## 2.2 Theoretical Review: Secondary Ion Emission

There are many fascinating phenomena in secondary ion formation These include the strong ion yield enhancement provided by oxygen for positive ion production from electropositive elements[3] and provided by cesium for negative ion production from electronegative species;[4] These secondary ion yield enhancements are directly influenced by the chemistry of the implanted primary ion species along with the influence of the exponential relationship of ionization probability to the ionization potential I, of electron affinity A, and of the emission velocity of the sputtered atom.[5] The negative ion yield enhancement of oxygen is also often a factor.[6] Although many efforts were made to develop the theory of secondary ion emission in order to explain these phenomena and to quantify the composition, the details of ion emission mechanisms remain unclear. There is still no general ion emission model that explains all ion yield phenomena on all types of surfaces.

A diversity of secondary ion emission models have been developed, each capable of rationalizing the data on which it was based. Excellent reviews on the models are available.[7-12] The models that attract most interest are bond-breaking, electron tunneling and local thermal equilibrium (LTE) models. These three models are reviewed in detail in this section. The physical background of other models is also briefly discussed.

### 2.2.1 Bond-breaking Model

The bond-breaking model was proposed by Slodzian and Henneyuin[3] to explain the extremely high positive ion yield of the cation species sputtered from ionic crystals, such as the alkali halides. A sputtered atom is ionized through the breaking of bond with an electronegative atom on the surface.

The electronic interaction of a departing cation with the solid surface is analogous to ion-pair dissociation in gas phase which was developed theoretically and experimentally by Laudau, Zener and Stuckelberg (LZS).[13-15] Figure 2-3a shows the potential energy curves for the NaCl molecule in gas phase,[9] where the covalent curve corresponds to an excited state of the molecule. The molecule is ionic at its equilibrium distance, stabilized by the Coulombic attraction of the ions. The initial dissociation is along the Coulombic potential curve leading to $Na^+$ and $Cl^-$ ions. Since the ionization potential of Na (5 eV) is greater than the electron affinity of Cl (3.5 eV), at infinite separation the ionic curve lies above the covalent curve by

~1.5 eV. If the ionic and covalent states did not interact (diabatic process), the two curves would cross at a specific distance, as shown by the solid curves. However, the two states do interact (adiabatic process) and the true result is that the curves do not truly intersect, as shown by the dotted curves. In the crossing region the state interaction results in a perturbation that can induce a transition and change the nature of the ground state curve from ionic to neutral through a resonant electron transfer from anion to cation.

The probability that the dissociating ions will survive without being neutralized is a function of the crossing distance Rc and the separation velocity. At a given velocity, the probability of ionic dissociation is related to Rc. The ionization probability ($P^+$) decreases very quickly as Rc decreases.

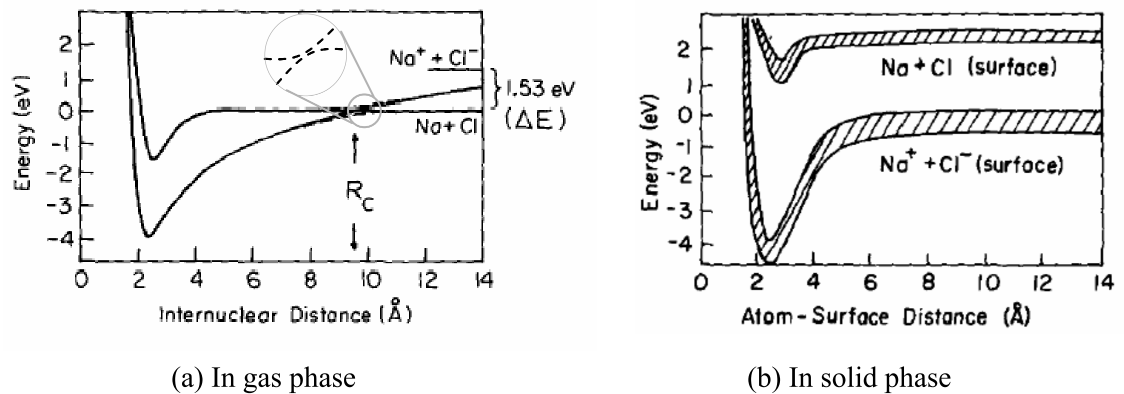


(a) In gas phase

(b) In solid phase

**Figure 2-2. Potential energy curves of NaCl for (a) the NaCl molecule in gas phase and (b) an Na atom leaving the NaCl crystal phase in solid phase (Adapted from reference 9)**

In the NaCl solid, the dissociation of $Na^+$ from crystal requires half the lattice energy or about 4 eV, while the removal of a neutral $Na^0$ requires an energy in the order of the band-gap energy (8.5 eV).[16] Thus the potential energy curves for the dissociation process of $Na^+$ and $Na^0$ do not have a crossing point, as indicated in figure 2-3b. At low energy (0.1 to a few keV) 100% emission of $Na^+$ is expected. Emission of neutral Na occurs when the collision energy is high enough for the system to reach crossing points on the repulsive portion of the potential energy curves.

This model was intended to rationalize the high ion yield formation of ionic solids. For oxides and other less polar compounds, the situation is more complex. However, as a

guideline, polar compounds with band gaps greater than half the lattice energy should have efficient positive ion yield at low primary ion impact energies (a few keV).

The positive ion yield enhancement resulting from surface oxygen incorporation can be explained by assuming that oxygen atoms create a local ionic lattice. The ionic character of the metal-oxygen bonds promotes direct emission of ions. In the case of Si, XPS (X-ray Photoelectron Spectroscopy) data shows that under oxygen adsorption or incorporation, the surface contains a mix of oxidation states with 1 to 4 oxygen atoms at nearest neighbor sites.[17] The result of such local $SiO_x$ formation can be visualized in a LZS (Laudau, Zener and Stuckelberg) model as shown in figure 2-3.[18] The formation of Si(IV) places Si in a more ionic environment, and consequently the energy of the Coulombic curve is lower and the crossing distance is larger, thus the positive ion yield of $Si^+$ is increased.

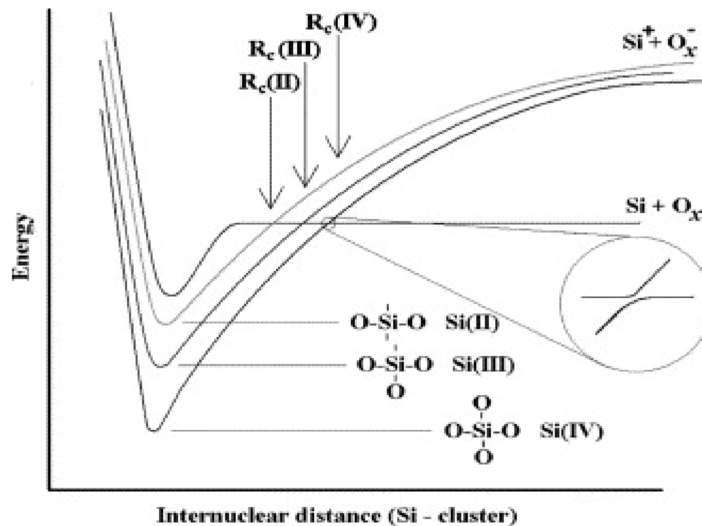


**Figure 2-3. Potential energy curves for $Si^+$ emission from localized $SiO_x$ complexes at the sputtered surface (Adapted from reference 18)**

### 2.2.2 Electron-tunneling Model

Yu[19] investigated the effect of Cs surface coverage on negative ion yield in 1978. His work showed that, with the increase of Cs coverage, the negative ion yield increased while the work function decreased. He correlated his results in terms of an electron tunneling model. This model assumes a free-electron-like metal surface which is characterized by Fermi level $E_F$. The work function is the difference between $E_F$ and the vacuum level. As a

sputtered atom leaves the surface, its energy level is shifted up or down due to the screening by the electrons in the metal. In the case of a positive ion leaving the surface (figure 2-4), the first ionization potential (I) is shifted up by an image potential inversely proportional to the separation between the atom and the surface.[20] When the energy level of the sputtered atom coincides with the occupied electronic levels in the metal (below Fermi level), the electron can tunnel between them via a resonant electron transfer process, hence neutralization of the outgoing ion can occur.[17]

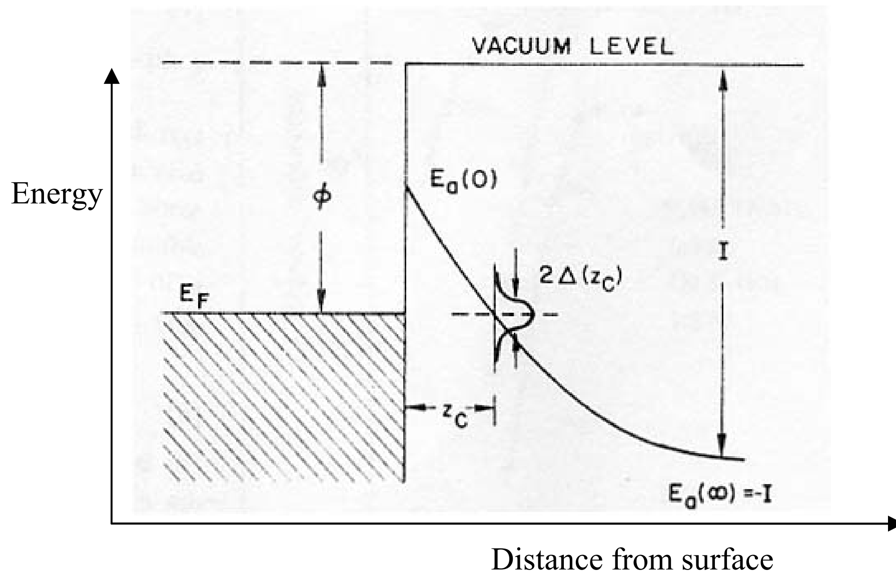


**Figure 2-4. Schematic drawing of energy diagram of an atom leaving a metal surface. $Z_C$ is the crossing distance when $E_a$=$E_F$ which is in the order of several bond lengths away from surface. (Adapted from reference 20)**

In figure 2-4, Zc is the separation between the atom and metal surface at the cross point where Ea = $E_F$, and Δ(Zc) is the half-width of atomic energy broadening due to the finite electron lifetime. The probability of atoms leaving the surface as an ion (ionization probability) is the function of the crossing point (Zc) and the separation velocity. Since the crossing point depends on work function ϕ which defines the position of $E_F$ and the ionization potential, the ionization probability can be reasonably approximated as eq. (2-2).[20, 21]

$$P^{+} \approx \exp[-(I-\phi)/\varepsilon_0]$$
$$P^{-} \approx \exp[-(\phi-A)/\varepsilon_0]$$

**(Equation 2-2)**

In this expression, $\phi$ is the work function of the surface, I is the first ionization potential for positive ionization, A is the electron affinity for negative ionization, $\varepsilon_0$ is a parameter proportional to the escape velocity of the ions as indicated in eq. (2-3).[21]

$$\varepsilon_0 = \frac{\hbar\gamma v_\perp}{C_1\pi} \qquad \textbf{(Equation 2-3)}$$

$\gamma$ and $C_1$ are parameters related to the electron configurations of the secondary ion-substrate combination as defined by Norskov and Lundqvist,[22] and $v_\perp$ is the normal component of the separation velocity of the atom.

This model provides a simple explanation of the work function and velocity dependences of the ionization probabilities observed in many experiments. $Cs^+$ is known to be chemisorbed on a metal surface which generates an electric dipole layer resulting in a lowered work function of the surface. The adsorption of $Cs^+$ thus enhances the ionization probability of negative ion yield. For oxygen, the surface polarization model (section 2.2.4.3) assumes that oxygen creates localized sites depending on whether the oxygen is adsorbed above or incorporated beneath the surface. Localized sites with adsorbed oxygen increase the photoelectron threshold (work function for metal) while incorporated oxygen lowers the photoelectron threshold. Thus the adsorption and incorporation of oxygen can enhance both positive and negative ion yields.

### 2.2.3 Local Thermal Equilibrium (LTE) Model

It was noted that the positive ion yield is inversely correlated to the ionization potential or electron affinity in the form of eq. (2-4). Anderson and Hinthorne[5] noted the similarity of eq. (2-4) with the Saha equations which arise from the application of Boltzmann statistics to ionization equilibrium in hot plasmas. Thus they stated that the sputtering region resembles a dense plasma in local thermal equilibrium.

$$\frac{N_+}{N_0} \propto \exp(-\frac{I}{K}) \qquad \textbf{(Equation 2-4)}$$

In this model, ions, electrons and neutral atoms in the plasma remain in thermodynamic equilibrium.[23] For positive ions, the ionization process can be described as a dissociation reaction between a neutral atom $M^0$, a positive ion $M^+$ and an electrons $e^-$ in eq. (2-5).

$$M^0 \longleftrightarrow M^+ + e^- \quad \textbf{(Equation 2-5)}$$

The dissociation constant of this reaction is given by eq. (2-6)

$$K_+ = \frac{N_+ N_e}{N_0} \quad \textbf{(Equation 2-6)}$$

where $N_+$, $N_e$ and $N_0$ are the densities of ions, electrons and atoms in plasma. $K_+$ has been calculated from the Saha-Eggert equation and can be expressed as

$$K_+ = (\frac{2\pi}{h^2}\frac{M_+ M_e}{M_0}kT)^{3/2}\frac{B_+ B_e}{B_0}\exp(-\frac{E}{kT}) \quad \textbf{(Equation 2-7)}$$

In this expression, h is Planck's constant, k is Bolzmann's constant, M is the mass, B the internal partition function, E the dissociation energy, in this case the ionization energy, and kT reflects the average energy of an atom in the collision cascade. The ionization probability, $P^+$, can be determined from eq. (2-6) and (2-7).

$$P^+ = \frac{N_+}{N_0} = \frac{1}{N_e}(\frac{2\pi}{h^2}\frac{M_+ M_e}{M_0}kT)^{3/2}\frac{B_+ B_e}{B_0}\exp(-\frac{I}{kT}) \quad \textbf{(Equation 2-8)}$$

Anderson and Hinthorne[5] gave a practical logarithmic form of eq. (2-8) as eq. (2-9).

$$\log(P^+) = 15.38 + \log\frac{2B_+}{B_0} + 1.5\log T - \frac{5040(I - \Delta E)}{T} - \log N_e \quad \textbf{(Equation 2-9)}$$

In this equation, 2B is the partition function of an electron, and ΔE is the ionization potential depression due to Coulomb interactions of the charged particles which can be calculated according to the Debye-Huckel model.

Similarly for negative ions, the ionization process can be described as an electron attachment process, and the ionization probability can be written as eq. (2-10).

$$P^- = \frac{N_-}{N_0} = N_e(\frac{2\pi}{h^2}\frac{M_- M_e}{M_0}kT)^{3/2}\frac{g_0 g_e}{g_-}\exp(-\frac{A}{kT}) \quad \textbf{(Equation 2-10)}$$

In this expression, g represents the statistic weight of the ground state of the atoms, negative ion or electron and A is the electron affinity of the atom. Other symbols are defined as before.

This model attempts to explain the oxygen or cesium enhancement of ion yields as follows. For an oxidized surface, the increase of electronic work function reduces the probability that an electron surmounts the potential barrier in the solid and neutralizes a

positive ion in the plasma. This results in a decrease of $N_e$ and an increase of $p^+$. Similarly, for a cesiated surface, the decreasing of work function causes $N_e$ to increase, which increases the negative ion emission.

Although the LTE model is the basis for a number of computer programs to provide standardless quantification, there is no evidence of the physical existence of plasma in local thermal equilibrium at the sputtering site. It is argued that the equilibrium can not be established in the short time period before the collision cascade begins to eject atoms or ions ($10^{-13}$ sec)[11] due to the inefficiency of the energy transfer through the nuclear collisions induced by the primary ion impact and electronic excitation.

### 2.2.4 Other Secondary Ion Emission Models

Other than the three models discussed in the previous sections, a few other ion emission models have been developed to rationalize the ion yield phenomena. Although some of these models are no longer attracting much attention, they describe the physical background and basic concepts of ion emission mechanisms. These models are reviewed briefly in this section.

#### 2.2.4.1 The Perturbation Model

The perturbation model can be illustrated simply by figure (2-5).[22] For an atom moving away from a metal surface, the excitation probability is a maximum closest to the surface where the atom-surface coupling is most strong. The strong atom-surface coupling also produces efficient de-excitation, thus the ion survival probability (P) is small. As the distance increases, the coupling is weaker and the ion survival probability begins to increase. Thus the probability of creating and observing an ion ($\Delta$P) reaches a maximum in a region a few angstroms from the surface.

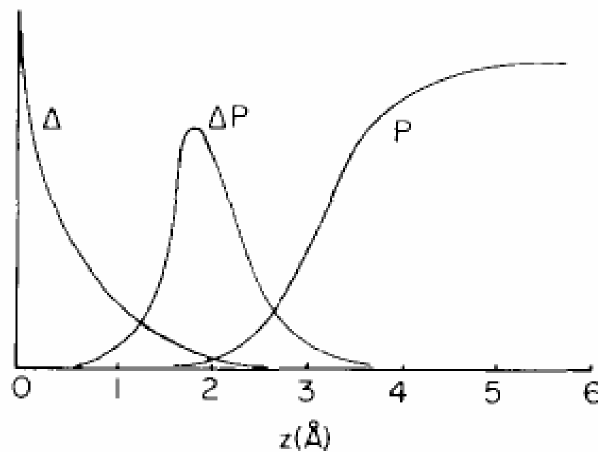


**Figure 2-5. The simple graphical illustration of the perturbation model. Δ is one electron level width which is a measure of the excitation probability, P is the ion survival probability. (Adapted from reference 22)**

This model was further developed by Yu[19] as the electron tunneling model (see above) which lead to a greater understanding of the exponential dependence of the ionization probability on surface work function, ionization potential (or electron affinity) and the ion escape velocity.

### 2.2.4.2 Work Function Model

A simple work function model was proposed by Anderson[24] to rationalize the ion yield modification by electropositive and electronegative species. He argued that the effect of oxygen was to increase the work function which would reduce the probability of electrons being excited thermionically over the potential barrier at the surface. The reduction by the surface oxygen of the availability of these electrons reduces the probability for neutralizing sputtered positive ions resulting in an increase in positive secondary ion production.

Evidence counter to this model came from the work by Blaise and Slodzian[25] on the work function change in situ using retarding potential measurement. For Mg metal, the measured work function is found to decrease with oxygen pressure while the ion yield of $Mg^+$ is still increased. In addition, oxygen can also enhance the negative ion yield.[6] Neither of these effects can be predicted by a simple work function model.

#### 2.2.4.3 Surface Polarization Model

In order to explain effects of oxygen on both positive and negative ion yields and the controversy with respect to the effect of oxygen on Mg metal, Williams[6] proposed a surface polarization model. He argued that the surface must be heterogeneous. Localized sites are created by the effect of oxygen which is either adsorbed onto or incorporated beneath the surface. For a substrate less electronegative than oxygen, localized sites having adsorbed oxygen create a dipole which increases photoelectron threshold and enhances positive ion yields. Incorporated oxygen results in a lower photoelectron threshold and enhanced negative ion yields. Local photoelectron threshold is the factor controlling ion formation instead of the surface average work function, which is the overall effect of oxygen on the surface.

This model differs from the bond-breaking model (section 2.2.1) and molecular model (section 2.2.4.5) in the mechanism of ion yield enhancement. In the two former models, the ionization probability of the atom bonded to oxygen is increased while, in the surface polarization model, the surface photoelectron threshold is changed by the oxygen and the ion yield of a third atom in the solid is enhanced.

#### 2.2.4.4 Band Structure Model

The concept of band structure was used by Van Der Weg and Bierman[26] in 1969 to rationalize the enhancement of sputtered excited-atom yields by oxygen. They argued that excited states were efficiently created in the sputtering collision. The excited atom moving away from a metal surface could de-excite through resonant detachment during which the excited electron tunneled into a vacant state above the Fermi level in the metal. When the surface is oxidized, the oxygenated surface has a wide band gap which prevents the resonant detachment of departing electrons with energies corresponding to states in the band gap.

The concept can be easily extended to explain the ion-yield effect. During the formation of the oxide, the electrons are move to the valence band where they have insufficient energy to undergo resonant transitions to neutralize most departing ion species.[27]

This model can explain both positive and negative ion phenomena by oxygen. Figure 2-6 illustrates the case of a Si ion departing a Si surface. The positive ion yield is enhanced because the electrons move to the valence band during oxidization where they are at a lower

energy level than the departing $Si^+$. A negative ion is assumed to be formed through the resonant attachment of an excited electron to a departing neutral atom. Thermalization of excited electrons to the bottom of conduction band is very rapid, so that most electrons in a clean Si surface have the energy level of the conduction band edge, which is not high enough energy to undergo attachment. However, oxidation raises the conduction band edge and electrons thermalized to this level are at about the correct energy to undergo attachment.

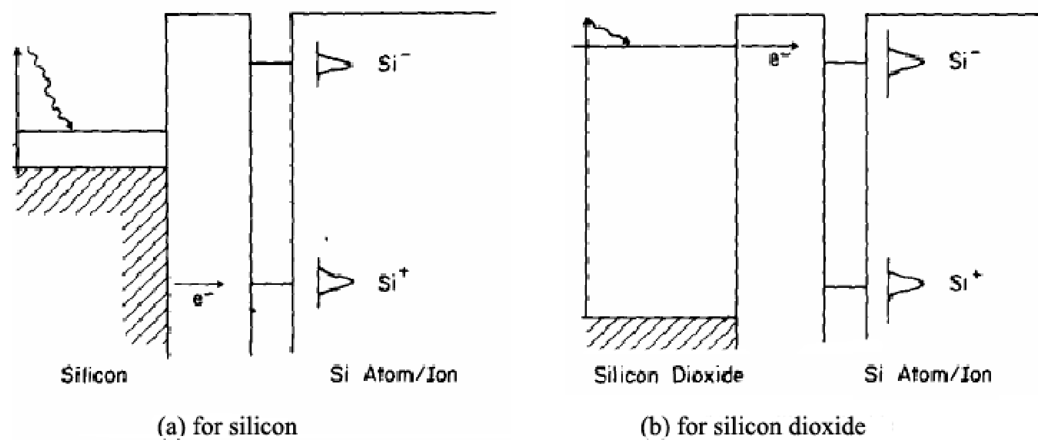


**Figure 2-6. Band-structure model for oxygen enhancement of positive and negative ions (Adapted from reference 9)**

The objections to the band structure model are concerned with the invalidity of band structure after the sputtering event. It is known that sputtering causes surface amorphization on semiconductors. At the experimental site, the model should predict discontinuities of the ionization probability, i.e., the yield of positive ions whose ionization potentials correspond to levels just above the valence band edge should be high, while those below the valence band edge the yield should be low, which is not observed experimentally.[28]

#### 2.2.4.5 Molecular Model

This Molecular Model was proposed by Thomas[29] in 1977 to explain the enhancement of ion yield by oxygen. Thomas suggested that no excited or ionized species formed at the surface can escape without de-excitation or neutralization because the electron

transition rates are very rapid ($10^{14}$-$10^{16}$ $s^{-1}$). Excited or ionized species can survive only if formed some distance away from the surface which can happen via level-crossing processes in dissociating sputtered molecular species.

The process is illustrated in figure 2-7. A surface atom (M) and an adsorbed atom (O) can receive enough energy to leave the surface. The transient sputtered molecule (MO) will dissociate through a level-crossing process.

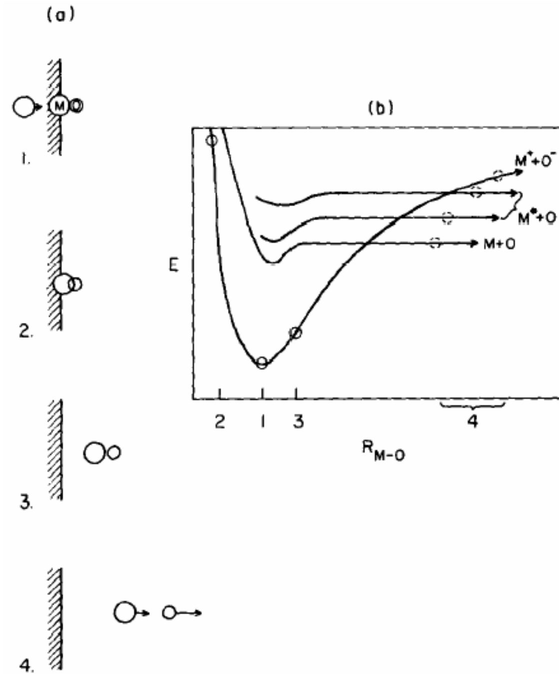


**Figure 2-7. Illustration of molecular model – sputtering of a transient M-O molecule and possible level crossing processes during the dissociation of this entity. The system is first compressed and moves up the repulsive wall of the potential well and then rebounds with enough energy to dissociate. (Adapted from reference 9)**

This model can easily explain positive ion enhancement because the ion-pair dissociation process shown in eq. (2-11) is very likely, but it is not so apparent for negative ion enhancement of oxygen.

$$MO \rightarrow M^{+} + O^{-}$$ **(Equation 2-11)**

#### 2.2.4.6 Surface Excitation Model

Williams[9] proposed that the charge state of the sputtered atom is determined by the state of excitation of the sputtering site. The sputtering site is electronically excited. The sputtered atom interacts electronically with the sputtering site as it departs, via resonant electron exchange process until a critical distance is reached. The probability of an atom leaving with an electron in any given level is equal to the probability that the level at the corresponding energy in the surface is occupied at the time interaction ceases.

The sputtering site contains a continuum of levels and electron excitation onto these levels is treated by Fermi-Dirac Statistics. In figure 2-8, at the level of ionization potential of the atom (I), the probability that the surface level is vacant is represented by $P_e$, and the probability that the level in the surface is filled is represented by $P_f$ (as shown in figure 2-8).

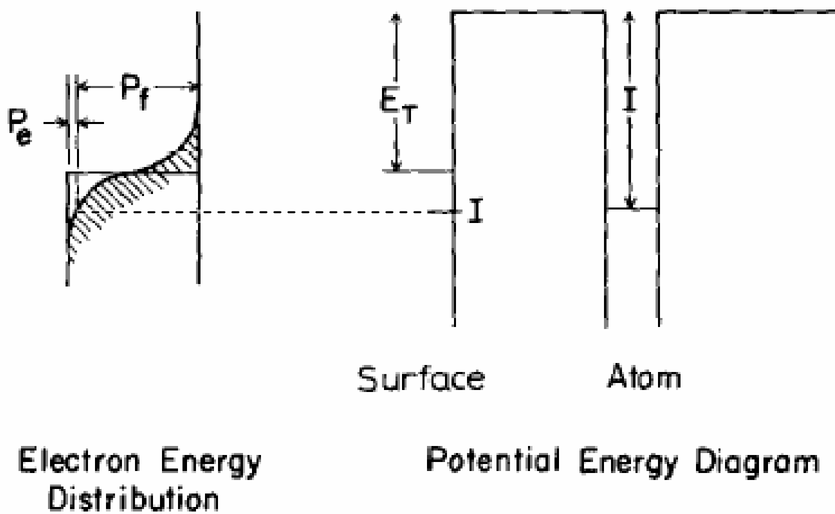


**Figure 2-8. Illustration of surface excitation model. $P_e$ is the probability that the surface level at level I is vacant, $P_f$ is the probability that the level in the surface at level I is filled. (Adapted from reference 9)**

Thus the positive ion and neutral flux can be written as eq. (2-12).

$$n_+ = nP_e$$
$$n_0 = nP_f \qquad \textbf{(Equation 2-12)}$$

Where n is the total flux. Since

$$P_f = 1 - P_e \qquad \textbf{(Equation 2-13)}$$

Then

$$\frac{n_+}{n_0} = \frac{P_e}{1 - P_e} \qquad \textbf{(Equation 2-14)}$$

Using Fermi-Dirac statistics, $P_e$ can be written as eq. (2-15).

$$P_e = [1 + \exp(-\frac{\Delta E}{kT_e})]^{-1} \qquad \textbf{(Equation 2-15)}$$

The ionization probability is then

$$\frac{n_+}{n_0} = \exp(-\frac{\Delta E}{kT_e}), \text{ where } \Delta E = I - E_T \qquad \textbf{(Equation 2-16)}$$

In this expression, $E_T$ is the photoelectron threshold, which is the work function in a metal or valence band edge in insulator or semiconductor. This is a similar ion yield expression to that produced by the electron-tunneling model or LTE model. Oxygen or Cs adsorption can vary the photoelectron threshold term $E_T$ and thus can affect the ion yield.

### 2.2.5 Summary

The formation of ions sputtered from a surface is a very complex process. For simplification only atomic collisions are considered. When the primary ions bombard a sample surface, they transfer kinetic energy to the target atoms and generate collision cascade. During the collision, some of the target atoms in the near surface region receive sufficient momentum and energy to overcome the surface potential barrier and leave the target. Despite of the atoms displacement deep into the bulk, most of the sputtered atoms are from the top mono atom layer. Greater than 80% of sputtered atoms come from surface atom layer for 15 keV primary ions, 100% for 1 keV primary ions.[30]

After the atomic collision, the atoms at the surface are in energetic motion which results in electronic excitation. As the excited atoms depart from a solid surface, charge transfer occurs which de-excites or neutralizes the departing ions. At a critical distance (a few Angstroms from the surface), the probability of charge transfer is reduced and ions can escape the surface.

## 2.3 Quantification Approaches

There are two main quantification approaches used in SIMS analysis: 1) semi-theoretical models and 2)empirical calibration.[31]

### 2.3.1 Semi-theoretical Model Approach

All semi-theoretical model quantification methods are based on secondary ion yield models which are calibrated using fitting parameters. Various computer programs based on different models were developed. The most widely used semi-theoretical model is the local thermal equilibrium (LTE) model (section 2.2.3). LTE model assumes dense plasma at thermal equilibrium formed in the sputtering site. The plasma can be described using a Saha-Eggert equation and the ionization probability can be simplified as eq. (2-17).

$$\log(P^+) = 15.38 + \log\frac{2B_+}{B_0} + 1.5\log T - \frac{5040(I - \Delta E)}{T} - \log N_e \qquad \textbf{(Equation 2-17)}$$

Where $P^+$ is the positive ionization probability, $B_+$ and $B_0$ are the internal partition function of positive ions and neutrals, I is the ionization potential, T is the electronic temperature, $\Delta E$ is the ionization potential depression due to Coulomb interactions of the charged particles which can be calculated according to the Debye-Huckel model, and $N_e$ is the electron density. In this expression, only two parameters are unknown, T and $N_e$. With two or more internal standards, these two parameters can be determined by computer fitting. Following determination of these parameters, the ionization probabilities of the unknown elements in the sample can be calculated and their elemental concentrations can be determined. Anderson and Hinthorne's computation program CARISMA[23] is base on the LTE model.

A number of simplified LTE modifications have been proposed. Other physical models were also presented (section 2.2). However, the semi-theoretical approach is not widely used in SIMS quantification to date due to its limitations. The secondary ion emission is a very complex many-body interaction problem and no one model defines all situations. There are many physically valid mechanisms for secondary ion emission and each one can become the dominant mechanism for a particular material and experimental regime. The semi-theoretical model also fails to include the effect of instrumental discrimination on the relative ion intensities. Semi-theoretical methods using fitting parameters in quantitative SIMS analysis can yield results only good to a factor of 2 or 3.[31]

### 2.3.2 Empirical Calibration Approach

Empirical approaches using calibration standards provide the best accuracy in quantitative SIMS analysis. There are two common used empirical calibration methods, by using a relative sensitivity factor (RSF) or by using a calibration curve. Both methods require external standard samples. Standards for impurity elements are typically made by ion implantation of the matrix of interest with a know dose of impurity or by doping the sample matrix of interest to a known concentration. For quantification of matrix species, a series of matrix standards having a known stoichiometry is used.

#### 2.3.2.1 Relative Sensitivity Factor (RSF)

The RSF technique is the most widely used calibration technique for quantitative analysis in SIMS if the impurity to be quantified is less than 1% of the total matrix concentration. Above 1%, care must be taken since the impurity concentration is no longer negligible with respect to the matrix concentration. In this situation, the presence of the impurity may have an impact on both impurity and matrix secondary ion yields. The sensitivity factor is defined according to eq. (2-18)

$$\frac{I_m}{C_m} = RSF_i \frac{I_i}{C_i} \qquad \textbf{(Equation 2-18)}$$

Where $I_m$ and $C_m$ are the secondary ion intensity and concentration of matrix element and $I_i$ and $C_i$ are the secondary ion intensity and concentration of element i. $RSF_i$ is the relative sensitivity factor of element i.

In trace element analysis, the matrix elemental concentration is assumed to be constant. The matrix concentration can be combined with the elemental $RSF_i$ to give a more convenient RSF.

$$RSF = C_m RSF_i = \frac{I_m}{I_i} C_i \qquad \textbf{(Equation 2-19)}$$

The RSF is a function of the element of interest and the sample matrix. If RSF is known for a particular matrix, the elemental concentration can be calculated from eq. (2-20).

$$C_i = \frac{I_i}{I_m} RSF \qquad \textbf{(Equation 2-20)}$$

An RSF for an impurity i can be calculated using an external standard sample with which has been implanted with a known dose known dose of this impurity. From an ion implanted standard, the RSF is determined from eq. (2-21)[2]

$$RSF = \frac{\phi I_m t}{d \int I_i} \qquad \textbf{(Equation 2-21)}$$

where $\phi$ is implanted dose of the impurity, $I_m$ is matrix secondary ion intensity in counts/sec, t is the total sputtering time, d is crater depth and $\int I_i$ is the integrated number of detected secondary ions over the depth profile.

RSF data have been published for a variety of matrices.[2, 32-34] One study showed the instrument dependence (the deviation in RSF within one instrument group) and time dependence (relative standard deviations over five years) can be less than ±50% using the RSF method.[35] Typical precision of quantification with the same instrument and analysis condition is less than 10%. However, very precise measurement can reach less than 1%, such as As in Si with NIST standards.[36, 37]

The standard samples can be made by ion implantation, using either implantation into a matrix which previously had none of the implanted impurity or a standard addition method in which case a higher level of impurity is implanted into a matrix already containing a lower level of the impurity.[38, 39] Implantation standards must meet the following requirements. First, sample and standard should match in matrix composition. The ion yield varies if the matrix composition of the sample and the standard are different (matrix effect), which generates errors in the quantification of species in the unknown sample. Secondly, matrices used for standards must be homogeneous to ensure the repeatability among different locations in the standard sample. Third, the ion implant dose and energy should be appropriately chosen. The dose should be high enough to obtain good counting statistics and low enough to avoid secondary ion yield change generally happens at atomic concentration higher than approximately 1%.[2] The energy should be high enough to place the implant peak deeper than the equilibrium depth and low enough to ensure at least 90% of the implanted ions in the layer of interest in the case of implanting thin layers.

#### 2.3.2.2 Calibration Curve Method

The relationship between impurity secondary ion intensity and impurity concentration is linear at low concentrations (generally below 1%), but this relationship may become non linear at higher impurity concentrations.[40] For high concentration elemental analysis, calibration curves are needed. In the calibration curve method the relationship between the concentration and intensity of an element (A) is determined empirically using a series of calibration samples containing the element A in various concentrations. The calibration curve provides information on the variation of ion yields with matrix composition.

Figure 2-9 illustrates the calibration curve method,[40] where $C_A$ is relative atomic concentration of element A in the matrix, $I_A$ is the detected ion current of A, and $I_R$ is the detected ion current of reference element R.

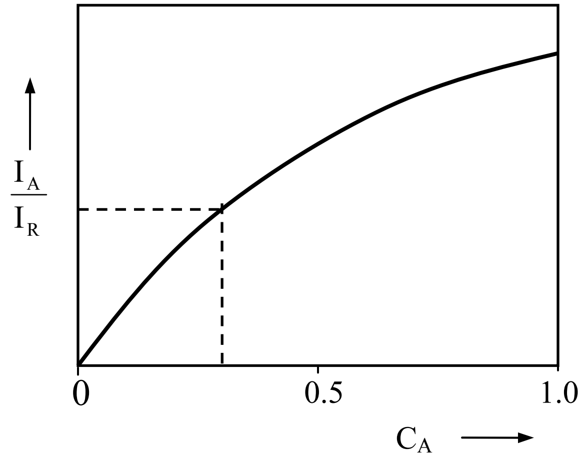


**Figure 2-9. Calibration curve - the relationship between impurity secondary ion intensity and impurity concentration (Adapted from reference 40)**

The calibration curve method can be extended to analyze trace elements in matrices with various concentrations of A. Since the ionization yield of trace element is different in matrices with differing concentrations of A (matrix effect), the relative sensitivity factor of trace element can not be directly used for a sample with unknown $C_A$. In this case, a calibration curve between the RSF of trace element i and $C_A$ needs to be generated.

To generate calibration curves, a series of calibration samples containing matrix element A in various concentrations and trace element i in known dose or known concentration are depth profiled under the same experimental conditions (instrument type, primary species, primary energy, sample bias, instrument transmission settings, etc.) until the

matrix ion counts reach a steady state for matrix compositional analysis and the impurity ion counts drop to the background level for implanted impurity analyses. The secondary ion intensity ratios of element A and reference element R, the RSF's of trace element relative to a matrix ion are computed and plotted as a function of $C_A$.

To quantitatively analyze the concentration of a trace element and/or a matrix species of an unknown sample, the calibration curve of matrix ion intensity ratio $I_A/I_R$ as a function of $C_A$ is first used to determine $C_A$ from the obtained matrix ion intensity ratio, then the calibration curve of RSF as a function of $C_A$ is used to determine the RSF of trace element for that matrix. Once the RSF and ion intensities are determined, the concentration of trace element can be calculated according to eq. (2-20).

## 2.4 Issues in Quantification of Matrix and Impurities in $Al_xGa_{1-x}N$

For SIMS quantification of matrix and impurity elements in $Al_xGa_{1-x}N$, two main issues affecting the analysis must be addressed: matrix effects and charging effects. Matrix effects are the result of chemical properties of $Al_xGa_{1-x}N$ which change with AlN mole fraction resulting in changes in the secondary ion yields of both the matrix and impurity elements. Charging effects occur because $Al_xGa_{1-x}N$ becomes more insulating as AlN mole fraction increases.

### 2.4.1 Matrix Effects

In SIMS, Matrix effects are changes in the secondary ion yields of matrix and impurity elements with changes in matrix. Secondary ion yield is dependent on the chemical composition of the sputtered surface of a matrix. Not all components of the sample play an equal role in affecting sputtered ion yields. By far the strongest effects arise from variations in the concentrations of those reactive species that enhance ion yields strongly, e.g. oxygen and the halogens for positive ions or the alkali metals for negative ions.[41]

In SIMS, matrix effects can be used as a great advantage through the use of secondary ion yield enhancing species. Oxygen and cesium are often used as primary species to enhance secondary ion yields in order to increase analytical sensitivity. The major cause of the matrix effect when ion yield enhancing primary ion species are used appears to be the variation in the concentration of implanted primary species in the sample surface which is

strongly affected by differences in the sputter yields of different matrices.[42, 43] The surface volume concentration of primary species is inversely proportional to the sputtering yield, as shown in eq. (2-22).

$$[\mathrm{O}]\ \mathrm{or}\ [\mathrm{Cs}] \propto \frac{1}{1+\mathrm{Y}} \qquad \textbf{(Equation 2-22)}$$

Where [O] or [Cs] represents O or Cs surface concentration, Y is the sputter yield defined as the substrate atoms ejected per primary atom. If the sputtered area and primary ion beam density are fixed, then the surface concentration of primary species is proportional to the linear sputtering rate. Simple relationships between the ion yields and sputtering rate as well as surface concentration of primary species are illustrated in eq. (2-23)[42]

$$\begin{aligned} P^{+} &= \frac{n^{+}}{n^{0}} \propto \left[\frac{1}{S_l}\right]^{c^{+}} \propto [\mathrm{O}]_v^{c^{+}} \\ P^{-} &= \frac{n^{-}}{n^{0}} \propto \left[\frac{1}{S_l}\right]^{c^{-}} \propto [\mathrm{Cs}]_v^{c^{-}} \end{aligned} \qquad \textbf{(Equation 2-23)}$$

where $S_l$ is the linear sputtering rate in Angstroms per second, $c^{\pm}$ are the factors may be characteristic of ionization cross section, which is between 2 and 3.[44]

Although matrix effect can be a great advantage in SIMS analysis by utilizing the strong positive and negative ion yield enhancement by oxygen and cesium, respectively, the ion yield variation in samples with varying matrices causes complexity and induces errors in quantitative SIMS analysis. Standard samples must be used for quantification in the presence of matrix effect. In the quantitative analysis of multilayer samples when standard samples for each layer do not exist, matrix effect has to be reduced in order to reduce errors.

To reduce matrix effect, one approach is to analyze the sputtered neutral atoms rather than the secondary ions (which is called secondary neutral mass spectrometry or SNMS). To achieve this, several techniques of post-ionization have been developed which consist of using a glow discharge, hot-electron gas, photons or lasers.[2] The low detection sensitivity and instrumentation complexity have limited the application form SNMS.

It is found that the secondary ions emitted from the sample surface with higher energy show a smaller matrix effects than those with low energy.[45] Thus the impact of matrix effects on an analysis can potentially be reduced by measuring high energy ions,[46, 47] which is

called the infinite velocity method.[48, 49] The drawback of the method is the reduced sensitivity.

Oxygen flooding which fully oxidizes the sample surface and $MCs^+$ technique which detects $MCs^+$ or $MCs_2^+$ clusters (M is the element of interest) under $Cs^+$ primary ion bombardments are also used to reduce matrix effect. It is reported[42, 43] that the secondary ion yields depend strongly on the near-surface concentration of primary species under the bombardment of oxygen or cesium. In the case of oxygen bombardment, the formation of ionic M-O bonds promotes the emission of positive ions (section 2.2.1). Higher surface concentration of oxygen results in higher degree of oxidation and increased positive ion yield. If the surface concentration of oxygen is high enough to fully oxidize the sample surface, then the ion yield variation among different matrices can be reduced. Several techniques, such as oxygen flooding and decreased impact angle of primary ions (with respect to surface normal) can be utilized for efficient oxidization of sample surface. $MCs^+$ cluster ions have less matrix effect in analogy to SNMS since $MCs^+$ ions are believed to be the combination of $M^0$ neutral and $Cs^+$ ion. The detail of $MCs^+$ technique will be described in chapter 6.

In $Al_xGa_{1-x}N$, changes in Al concentration result in variations in sputtering rate which changes the surface concentration of primary species and thus the ion yields. Materials with differing Al concentrations also have different levels of oxygen contamination due to differences in affinity for oxygen which also changes the ion yields. In the case where the Al concentration in a sample is unknown, the calibration curve of matrix ion intensity ratio versus AlN mole fraction must be used to determine the concentration of matrix elements, and the calibration curve of RSF versus AlN mole fraction can be used to determine the concentration of the impurity species being analyzed.

### 2.4.2 Sample Charging Effects

#### 2.4.2.1 Introduction

During SIMS analysis, primary ions impinge the sample surface, while secondary ions and/or secondary electrons leave the sample surface. If the ratio of the yield of secondary ions and electrons to primary ions are not equal to 1, a charge imbalance occurs and an excess of charge will accumulate in the sputtered area. If the sample has an intrinsic conductivity, the excess surface charge can be compensated by electrons flowing from

conductive sample holder and the potential of the sample surface will remain constant. If the sample is an insulator, the electrical charge will accumulate on the sample surface with deleterious results, such as non-stable or absent secondary ion signal and/or sample high voltage breakdown. When severe charging occurs, the potential of the sample will build up high enough to generate an arc and damage the sample. Figure 2-10 is an optical image of sample damage after a thick $SiO_2$ was bombarded with energetic (14.5 keV impact energy) $Cs^+$ ions.

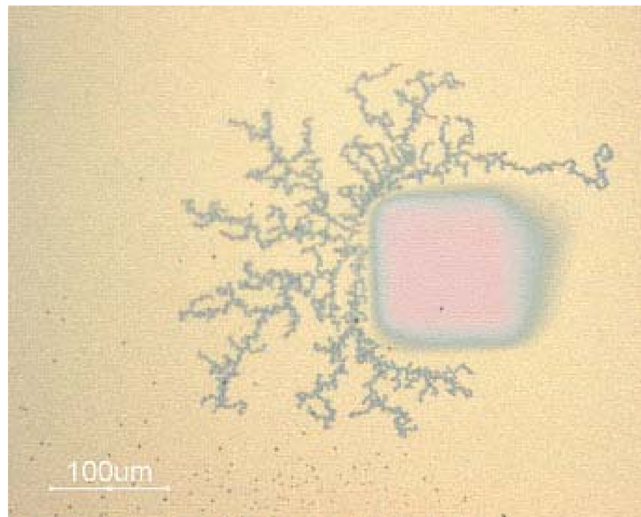


**Figure 2-10. Optical image shows severe sample damages from charging. Sample is 1.36μm $SiO_2$ under 14.5 keV impact energy of $Cs^+$ bombardment.**

#### 2.4.2.2 Charging Modes

In the case of the IMS-6f, samples must be biased either negatively or positively depending on the polarity of the secondary ion to be analyzed since the sample provided the secondary ion acceleration into the mass spectrometer. Depending on the bias of the sample, the charging can be classified as positive mode or negative mode. For positive mode sample charging, the sample is biased at positive potential. Only positive ions escape from the sample and leave behind negative charges. The net charge $Q^+$ on the sputtered area is the algebraic sum of the incoming primary ions and the secondary ions leaving the sample, as shown in eq. (2-24)[50]

$$Q = q_p - q_s \qquad \textbf{(Equation 2-24)}$$

where Q is total charge on sample surface, $q_p$ is charge due to primary ions, $q_s$ is charge due to positive secondary ions leaving the sample. When positive primary ion beam is used, i.e. $q_p$ is positive, eq. (2-26) resulting in a sample which always charges positively since the total ion yield is always less than 1, i.e. there are never enough positive secondary ions leaving to counterbalance the incoming positive primary ion beam. If a negative polarity primary ion beam is used such as $O^-$, the net positive charge accumulation on the sample can be reduced.

For negative mode sample charging, the sample is biased at a negative potential. Negative secondary ions and secondary electrons can escape from the sample leaving behind a net positive charge. The numbers of charges is then expressed by eq. (2-25).[50]

$$Q = q_p + q_s + q_e \qquad \textbf{(Equation 2-25)}$$

Where Q is the total charge on the sample surface, $q_p$ is charge due to primary ions, $q_s$ is charge due to negative secondary ions leaving the sample, $q_e$ is charge due to electrons leaving the sample. For positive primary ion beam bombardment e.g. $O_2^+$ or $Cs^+$, the sample always charges positively because all three components of Q add positive charges to the sample.

In summary, in either positive mode or negative mode of sample bias, a non-conductive sample always charges positively under positive primary ion bombardment. To neutralize the excess positive charges accumulated on sample surface, a flux of electrons can be introduced to the ion sputtering area.

#### 2.4.2.3 Charge Neutralization

Several approaches can be used to reduce or eliminate charging effects. The most commonly used methods involve the use of a conductive coating or a metal grid, $O^-$ primary ion bombardment, and electron beam charge neutralization. Table 2-1 lists the advantages and disadvantages of these common methods. Conductive layer coating is the easiest way to reduce charging effects. For very insulating material, charging still typically occurs after sputtering through the coating layer or grid. Although the $O^-$ primary ion beam available on the CAMECA IMS-6f and similar instruments has low beam density, this primary beam is still often used for charging reduction in geological applications. Charge compensation using an electron gun to provide an electron beam flux to neutralize charged samples is the most commonly used method and typically does not degrade the depth resolution and ion beam

intensity. A detailed description of the electron beam charge neutralization in CAMECA IMS 6F is given in section 3.5 of chapter 3 which describes the experimental methods used in this work.

**Table 2-1. Common methods to reduce charging effects**

| Common Methods for Charge Neutralization | Comments |
|---|---|
| Conductive layer coating | • Easy<br>• Degrades depth resolution<br>• Does not work for very insulating materials |
| Conductive grid | |
| $O^-$ primary ion beam | • Often used in geological applications<br>• Insufficient ion beam density for many applications |
| Electron beam flux | • The most commonly used method<br>• Used for both positive and negative secondary ion charge neutralization |

## 2.5 References


[1] J. C. Vickerman, A.Brown, and N. M. Beed, *Secondary Ion Mass Spectrometry: Principles and Applications* (Clarendon Press Oxford, 1989).

[2] R. G. Wilson, F. A. Stevie, and C. W. Magee, *Secondary Ion Mass Spectrometry : a Practical Handbook for Depth Profiling and Bulk Impurity Analysis* (John Wiley & Sons, 1989).

[3] G. Slodzian and J. F. Hennequin, Compt. Rend. Acad. Sci. B **263**, 1246 (1966).

[4] V. Krohn, Journal of Applied Physics **33**, 3523 (1962).

[5] C. A. Andersen and J. R. Hinthorne, Science **175**, 853 (1972).

[6] P. Williams and J. C.A Evans, Surface Science **78**, 324 (1978).

[7] P. Williams, Applied Surface Science **13**, 241 (1982).

[8] P. Williams, Annual Review of Materials Science **15**, 517 (1985).

[9] P. Williams, Surface Science **90**, 588 (1979).

[10] G. Blaise and A. Nourtier, Surface Science **90**, 495 (1979).

[11] P. Chakraborty, Pramana - Journal of Physics **50**, 617 (1998).

[12] P. Williams, *Secondary Ion Mass Spectrometry, SIMS VII, edited by A. Benninghoven, C. A. Evans, K. D. Mckeegan, H. A. Storms, and H. W. Werner, p.15* (Wiley, New York, 1990).

[13] L. Landau, Phys. V. Sowjetunion **2**, 46 (1932).

[14] E. C. G. Stuckelberg, Helv. Phys. Acta **5**, 369 (1932).

[15] C. Zener, Proceedings of the Royal Society of London. A, Mathematical and Physical Sciences **A 137**, 696 (1932).

[16] R. T. poole, J. Liesegang, R. C. G. Leckey, et al., Phys. Rev. B **11**, 5190 (1975).

[17] J. L. Alay and W. Vandervorst, Physical Review B **50**, 15015 (1994).

[18] K. Franzreb, J. Lorincik, and P. Williams, Surface Science **573**, 291 (2004).

[19] M. L. Yu, Phys. Rev. Lett. **40**, 574 (1978).

[20] M. L. Yu and N. D. Lang, Nucl. Instrum. Methods Phys. Res. Sect. **B14**, 403 (1986).

[21] M. L. Yu, Phys. Rev. Lett. **47**, 1325 (1981).

[22] J. K. Norskov and B. I. Lundqvist, Phys. Rev. B **19**, 5661 (1979).

[23] C. A. Andersen and J. R. Hinthorne, Analytical Chemistry **45**, 1421 (1973).

[24] C. A. Anderson, Int. J. Mass Spectrom. Ion Phys. **3**, 413 (1970).

[25] G. Blaise and G. Slodzian, Surface Science **40**, 708 (1973).

[26] W. F. vanDerWeg and D. J. Bierman, Physica **44**, 206 (1969).

[27] R. Kelly and C. B. Kerkdijk, Surface Science **46**, 537 (1974).

[28] A. E. Morgan and H. W. Wermer, L. Chem. Phys. **68**, 3900 (1978).

[29] G. E. Thomas, Radiation Effects **31**, 185 (1977).

[30] P. Williams, in *The 18th Annual Workshop on Secondary Ion Mass Spectrometry*, Hilton Head, South Carolina, 2005).

[31] G. H. Morrison, Secondary Ion Mass Spectrometry, SIMS III, edited by A. Benninghoven, J. Giber, J. Laszlo, M. Riedel and H.W. Werner, 244 (1981).

[32] G. E. Lux, F. A. Stevie, P. M. Kahora, et al., J. Vac. Sci. Technol. A **11**, 2373 (1993).

[33] P. M. Kahora and F. A. Stevie, Secondary Ion Mass Spectrometry, SIMS VII, edited by A. Benninghoven et al., Eds., Wiley, New York, 143 (1988).

[34] R. G. Wilson, Secondary Ion Mass Spectrometry, SIMS VII, edited by A. Benninghoven et al., Eds., Wiley, New York, 131 (1988).

[35] Y. Homma, Secondary Ion Mass Spectrometry, SIMS IX, edited by A. Benninghoven et al., Wiley, New York, 135 (1993).

[36] P. H. Chi, D. S. Simons, J. M. McKinley, et al., Journal of Vacuum Science & Technology A-Vacuum Surfaces and Films **20**, 688 (2002).

[37] NIST, Standard Reference Materials, SRM 2137, http://ts.nist.gov/ts/htdocs/230/232/232.htm.

[38] P. R. Boudewijn and H. W. Werner, Secondary Ion Mass Spectrometry, SIMS V, edited by A. Benninghoven et al., Wiley, New York, 270 (1986).

[39] G. P. Leta and G. H. Morrision, Analytical Chemistry **52**, 277 (1980).

[40] A. Benninghoven, F. G. Rudenauer, and H. E. Werner, *Secondary Ion Mass Spectrometry, Basic Concepts, Instrumental Aspects, Applications and Trends, p.290* (Wiley, New York, 1987).

[41] P. Williams, in *Practical Surface Analysis*, edited by D. Briggs and M. P. Seah (John Wiley & Sons, 1992), Vol. 2, p. 177.

[42] V. R. Deline, W. Katz, and C. A. Evans, Applied Physics Letters **33**, 832 (1978).

[43] V. R. Deline, C. A. Evans, and P. Williams, Applied Physics Letters **33**, 578 (1978).

[44] K. Wittmaack, Surface Science **112**, 168 (1980).

[45] Y. Gao, Applied Surface Science **32**, 420 (1988).

[46] Y. Gao, Applied Surface Science **32**, 420 (1988).

[47] Y. Gao, Y. Marie, F. Saldi, et al., International Journal of Mass Spectrometry and Ion Processes **143**, 11 (1995).

[48] K. Wittmaack, Surface Science **429**, 84 (1999).

[49] P. A. W. Vanderheide, M. Zhang, G. R. Mount, et al., Surface and Interface Analysis **21**, 747 (1994).

[50] CAMECA, IMS-6F User's Manual: Electrical Charging Effects, 6 (1996).

# 3 Instrumentation and Experimental Method

## 3.1 Introduction

Secondary ion mass spectrometry is considered one of the most important analytical techniques for elemental analysis. For trace and matrix level quantification in AlGaN, SIMS meets the requirements for high sensitivity, high mass resolution, and good depth resolution. The instrument used in this study is a CAMECA IMS-6f equipped as follows. Two types of ion sources are used in this study, a Duoplasmatron for $O_2^+$ and $Cs^+$ surface ionization source. The mass spectrometer is a double focusing electrostatic/magnetic sector analyzer. Detectors used are Faraday cup for high ion count rate and electron multiplier for low ion count rate (less than 2E6 counts/second). A post acceleration system is installed in the system for improved sensitivity at low energy analysis. For accurate quantitative analysis in AlGaN, charge compensation is required for many samples especially those having Al content higher than 0.4. A normal incidence electron gun (NEG) is used to provide charge neutralization. Crater depths are measured using a Tencor P-20 stylus profilometer reference and sputter rates were calculated assuming a linear sputter rate versus beam density.

The sample set used in this study consists of as-grown $Al_xGa_{1-x}N$ films with varying AlN mole fraction x on SiC or Sapphire substrates. The samples in the as-grown sample set were implanted with O, Si and Mg for the quantification of these impurities. The AlN mole fraction in the as-grown samples was determined using Low energy Electron induced X-ray Emission Spectrometry (LEXES). In addition to the as-grown samples described above, some high AlN mole fraction samples were fabricated using a high dose ion implantation method. The as-grown and implanted samples were then used to construct calibration curves of matrix ion intensity ratios, impurity RSF's and sputter yield as a function of AlN mole fraction for multiple analysis conditions. With these calibration curves, precise quantification of matrix and impurity elements in multiple layer AlGaN structure can be obtained over the mole fraction range of $0 \le x \le 1$.

Details of the above instrumentation, samples and experimental settings are described in the following sections.

## 3.2 Instrumentation

The SIMS instrumentation used in this research is a CAMECA IMS-6f Magnetic Sector SIMS for quantitative depth profiling. A Tencor P-20 stylus profilometer was used for crater depth measurement and sputter rate determination.

### 3.2.1 CAMECA Magnetic Sector SIMS Instrument IMS-6f

#### 3.2.1.1 Ion Sources

The CAMECA IMS-6f is equipped with a DuoPlasmatron which is a cold cathode plasma ionization source capable of producing either positive or negative ions and a with a surface thermal-ionization Cs microbeam source producing $Cs^+$ ions. $O_2^+$ ions produced by the DuoPlasmatron are used for positive secondary ion yield enhancement while $Cs^+$ produced from the surface ionization Cs source are used for negative secondary ion yield enhancement as well as the generation of $MCs^+$ cluster ions.

Duoplasmatron with Accel/Decel System

A schematic of the duoplasmatron source of the CAMECA IMS-6F is shown in figure 3-1.[1] The source consists of a cathode, an anode which is biased several hundred volts relative to the cathode and an intermediate electrode with a floating potential. A gas is introduced to the interior of the hollow cathode. The voltage difference between the hollow cathode and anode produces an arc which creates a plasma discharge. The discharge is maintained close to the center line axis of the source by a conical intermediate electrode at a floating potential. The plasma is concentrated close to the extraction hole (approximately 2 mm in diameter) in the anode by an electromagnetic coil produced magnetic field which is directed between the intermediate electrode and anode. A part of the plasma passes through the extraction hole and expands in a chamber due to the pressure difference between the duoplasmatron and the chamber of the gun. Primary ions are extracted from the plasma by a grounded extraction electrode (not shown in the figure). The source is called a duoplasmatron because the beam size is constricted by both the intermediate electrode and the action of the coil that surrounds the anode, intermediate electrode and cathode.

The duoplasmatron can furnish positive and negative ions according to the polarity of the extraction potential. The duoplasmatron on the CAMECA IMS-6F has the ability to

move the cathode in the y direction to take advantage of the greater density of positive ions emanating from the center of the cathode and negative ions form the edge. The most commonly used gas species is oxygen, which produces positive ($O_2^+$ or $O^+$) or negative ($O^-$ or $O_2^-$) ions. The minimum beam diameter obtainable with this source is 0.30 µm using 17.5 kV source bias and 5 kV sample bias.[2]

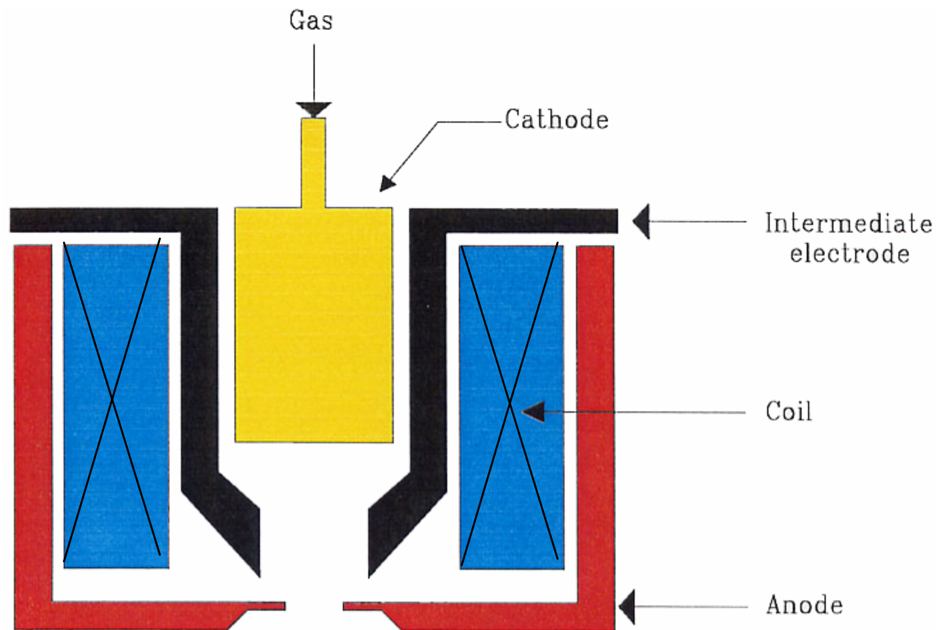


**Figure 3-1. Illustration of duoplasmatron plasma ionization source** [1]

For high depth resolution, a low energy primary beam is required. At low duoplasmatron extraction voltage, space charge effects reduce the source brightness and the primary beam density is no longer high enough to maintain reasonable sputter rate. In a magnetic sector SIMS instrument, the sample is biased in order to collect secondary ions more efficiently. Thus, low impact energies can be achieved even with a rather high extraction voltage on the duoplasmatron source by using a high sample bias. However, as the impact energy is reduced to low values this can lead to very large angles of incidence of the primary beam with respect to sample normal, which makes focusing the primary beam difficult. Moreover, large angles of incidence of the oxygen beam with respect to sample normal lead to ripple formation which deteriorates depth resolution.[3,4] An Accel/Decel system has been developed by CAMECA to overcome this limitation.[5,6]

The Accel/Decel system developed for the duoplasmatron source of the IMS-6F is schematically illustrated in figure 3-2. It operates by maintaining an extraction voltage on the duoplasmatron source high enough to avoid space charge effects and decelerating the primary ions at the entrance of the primary column such that ions reach the target with low impact energies. As shown in figure 3-2, the extraction electrode (EE) in duoplasmatron source is negatively biased instead of being grounded. An Einzel lens (L1) is added between the DUO source and Primary Beam Mass Filter (PBMF). Primary ions are accelerated between the DUO source anode (A) and the extraction electrode (EE), and then decelerated between EE and lens L1. L1 focuses the beam in order to increase the acceptance of the PBMF thus increasing the extraction efficiency. It has been shown that the maximum beam intensity can be increased by a factor of 1.4 to 2.5 with the Accel/Decel system when the duoplasmatron source voltage decreases from 10 to 1.5 kV.[6] It is possible to choose primary and secondary voltages to achieve an $O_2^+$ beam with impact energy as low as 500eV and yet maintain optimal incidence angle (40-50 degrees from normal).[6]

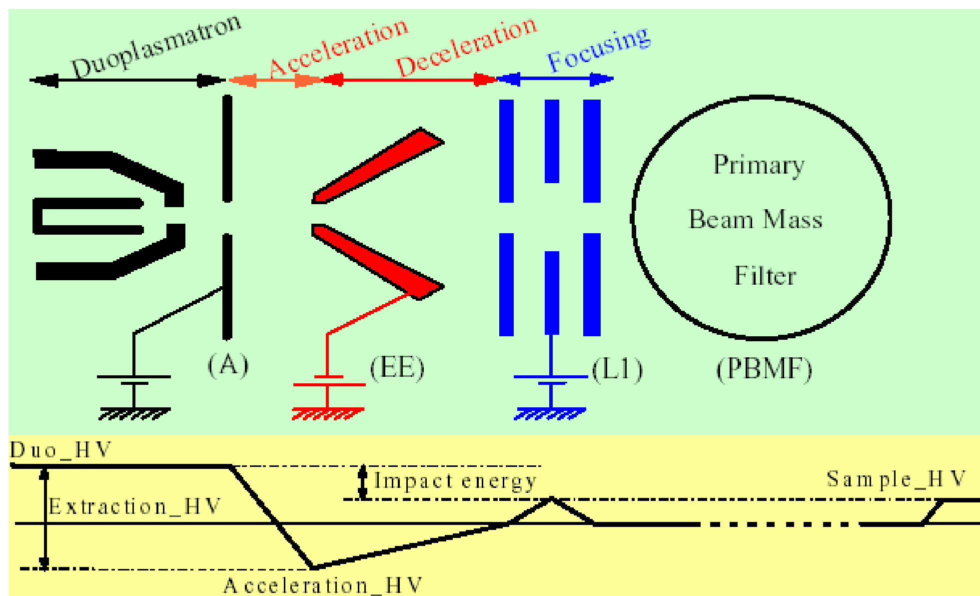


**Figure 3-2. Schematic of the Accel/Decel system for IMS-6F duoplasmatron source [5,6]**

<u>Cs Microbeam Source</u>

Ion sources based on the surface-ionization principle are generally characterized by a high degree of ion beam purity and a low energy spread, but this source is only viable for a

limited number of elements.[7] When an atom or molecule is near to or adsorbed on a hot metal surface, it can be thermally ionized. The positive ionization efficiency is given approximately by the Langmuir–Saha equation (eq. 3-1)[8]

$$P \propto \exp\left(\frac{e(\phi - I)}{KT}\right) \qquad \textbf{(Equation 3-1)}$$

where P is the ionization efficiency, e is the electronic charge, $\phi$ is the work function of the ionizing surface, I is the ionization potential of the species, K is the Boltzmann constant, and T is the absolute temperature. For efficient positive ionization, the work function of the metal must be high.

In the Cs microbeam surface ionization source in CAMECA IMS-6F SIMS, cesium carbonate tablet ($Cs_2CO_3$) is contained in a reservoir which is raised to 400°C to release cesium vapor. The cesium vapor comes into contact with the surface of a tungsten plate at a temperature of 1100°C and ionizes into Cs positive ions. The $Cs^+$ ions are extracted and accelerated when an electric field is applied between the surface of the tungsten plate and the extraction electrode. Figure 3-3 illustrates the layout and various parts of the Cs microbeam ionization source.[9] The minimum beam diameter obtainable with this source is 0.20 μm using 10 kV source bias and -5 kV sample bias.[2]

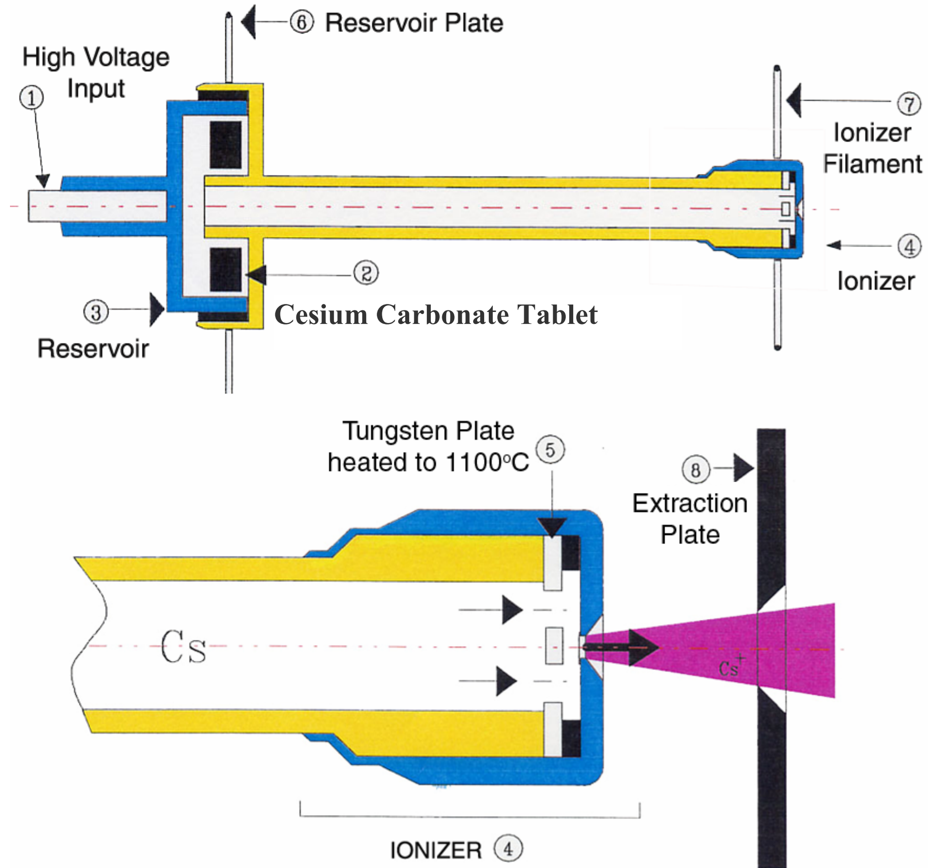


**Figure 3-3. Schematic drawing of Microbeam Cesium surface ionization source** [9]

### 3.2.1.2 The Mass Spectrometer

The mass spectrometer in the CAMECA IMS-6F is a double focusing magnetic sector mass spectrometer which uses both direction and velocity (energy) focusing. Due to the initial energy spread of the secondary ions, particles of a given mass will experience an additional dispersion in magnetic field. This is the equivalent of a "chromatic effect". This effect must be corrected in order to achieve better mass resolution.

In CAMECA IMS-6F, achromatic mass separation is achieved by coupling the magnetic prism with the electrostatic sector through an electrostatic lens (spectrometer lens). The setup is arranged in such a way that the energy dispersion produced by both prisms cancel each other (figure 3-4).[10]

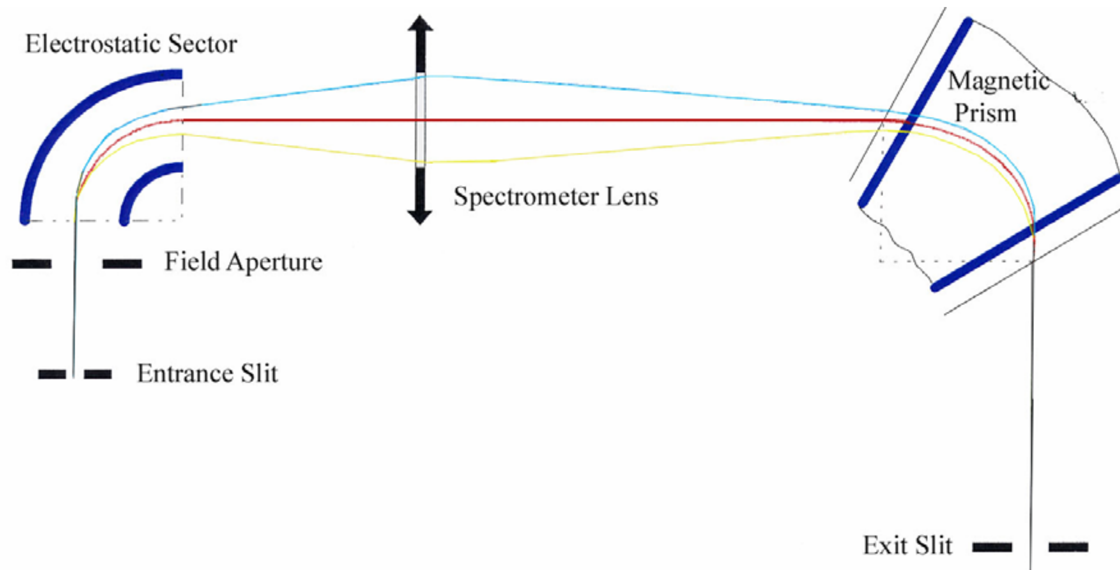


**Figure 3-4. Trajectory of ions with different energies. The energy dispersion produced by electrostatic sector and magnetic prism cancel each other. Blue, red, yellow colors refer to high, medium, low energies, respectively.[10]**

In figure 3-4, only the central ray with different energies is considered. Ions with different trajectories are also converted into one image point. In figure 3-5, yellow and blue lines refer to energy trajectories other than the central ray (red line). They are at the same energy and are brought into a common focus on the central ray by the electrostatic sector. The virtual image point produced by the lens will in turn play the part of an object point for the magnetic prism and be focused onto a real image point by the prism. Thus the entire beam is achromatic and not just one point on the central ray.[10]

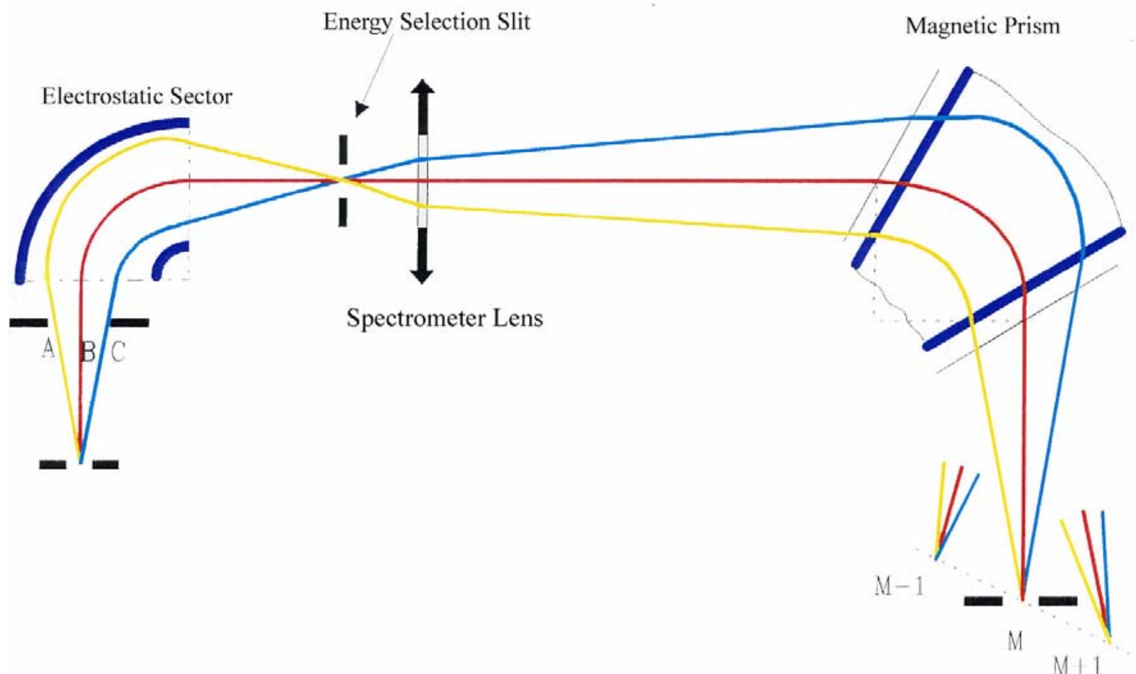


**Figure 3-5. Mass separation of ions with the same energy but different trajectories [10]**

#### 3.2.1.3 Secondary Ion Detection for Counting Mode

There are two types of detectors in the IMS-6F for secondary ion counting: a Faraday cup (FC) and an electron multiplier (EM). The electron multiplier is used to secondary ion count rates from 1E-1 to 2E6 counts/second, while the Faraday cup is used to measure count rates over the range of 1E5 to 2E9 counts/second. The combination of these two detectors provides a very high dynamic range for the secondary ion intensity measurement. Note that there is another detector, a channel plate/fluorescent screen combination which provides the capability to display images.

##### 3.2.1.3.1 Faraday Cup

The Faraday cup is a hollow cylinder with large length/diameter ratio. In order to prevent the escape of the secondary electrons produced by secondary ion bombardment of the Faraday cup walls, a negatively biased plate is placed in front of the Faraday cup. A schematic drawing of the IMS faraday cup is shown in figure 3-6.[11] The secondary ions are focused onto the Faraday cup and produce a current which is converted into a voltage by a high impedance amplifier. This voltage is sent to the input of a voltage/frequency converter.

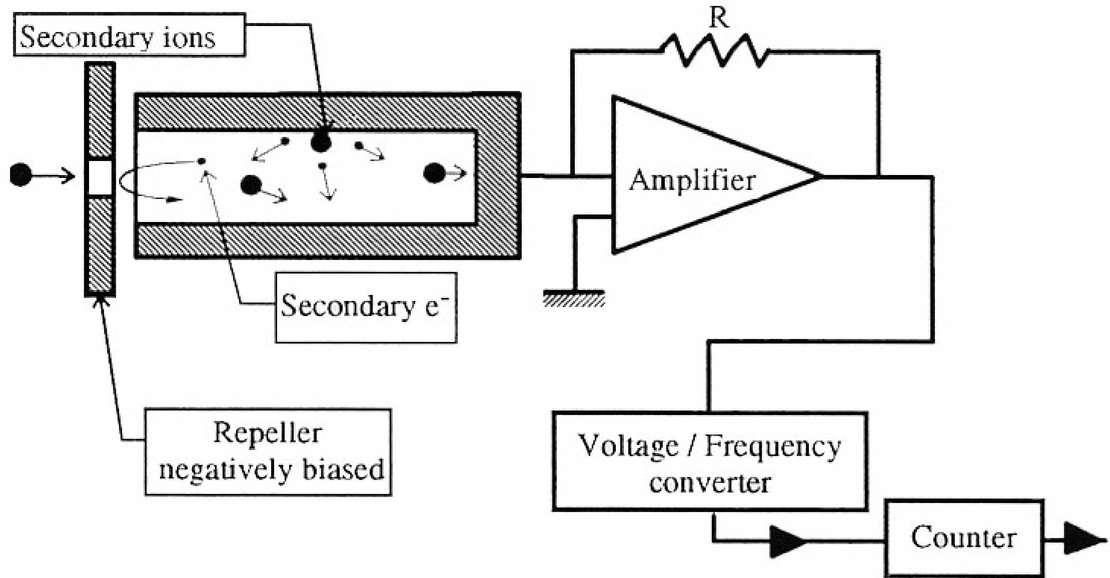


**Figure 3-6. Illustration of Faraday cup in CAMECA IMS-6F [11]**

### 3.2.1.3.2 Electron Multiplier with Post Acceleration System

The electron multiplier used consists of a series of electrodes called dynodes, each connected along a resistor string (see figure 3-7).[12] The signal output end of the resistor string attaches to positive high voltage. The other end of the string goes to the electron multiplier case and ground. The dynode potentials differ in equal steps along the chain. When a particle strikes the first dynode it produces secondary electrons. The secondary electrons are accelerated into the next dynode where each electron produces more secondary electrons. A cascade of secondary electrons ensues. The dynode acceleration potential controls the electron gain.

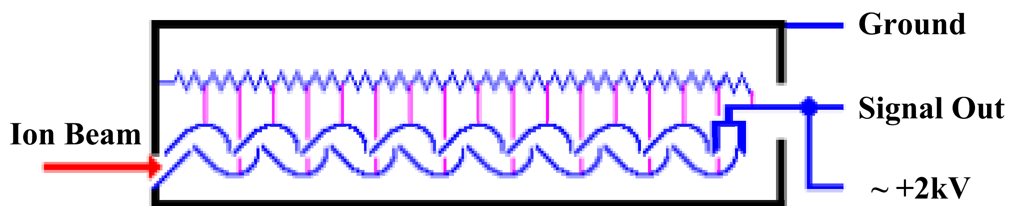


**Figure 3-7. Schematic of an electron multiplier [12]**

The ion / electron conversion efficiency of the first dynode of the electron multiplier varies with the velocity of the impinging secondary particles. The higher the velocity, the

higher the electron multiplier detection quantum efficiency. When the first dynode is grounded as with earlier CAMECA IMS instruments, the velocity of the secondary particles is fixed by both their mass and the secondary accelerating voltage. Thus, at the same extraction voltage, the sensitivity is lower for higher masses since velocity is inversely related to mass at constant energy. When low extraction voltages have to be used, the instrument sensitivity is reduced because of the decrease of the EM yield due to lower impact energy of the secondary particles onto the first dynode. This loss of electron multiplier performance can be reduced by post-accelerating the secondary particles just before they reach the electron multiplier first dynode.[13] Moreover, at a given secondary extraction voltage, post-acceleration minimizes the mass dependence of the electron multiplier efficiency. The post acceleration system in CAMECA IMS instruments has post acceleration voltage adjustable from -10 to +8 kV. The working principle is shown in figure 3-8.[13]

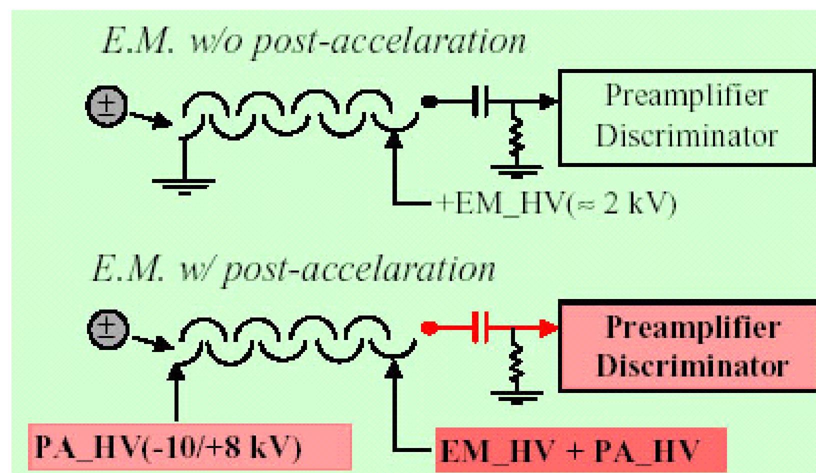


**Figure 3-8. Principle of post acceleration system in electron multiplier [13]**

#### 3.2.1.3.3 Instantaneous/Apparent Count Rate

Optical gating is typically used on the CAMECA IMS-6F to avoid signals from the crater wall for better depth resolution. When optical gating is used, i.e. the analyzed area is smaller than the rater size, it is important to be aware of the instantaneous count rate of the electron multiplier. All of the counts are obtained in the fraction of time that the beam passes over the optically gated detection region. Therefore the electron multiplier count limit may be reached while the apparent count rate measured appears much below the limit of 2E6

counts per second. When this count rate limit is passed, the accuracy of the ion intensity measurement will be deteriorated due to the detector dead time. The dead time of the pulse counting system is the time spent after each event before being able to detect the next one. For a dead time of $\tau$ and a true ion count of N, the error on the measured pulse rate ($N_C$) is:[14]

$$\frac{N - N_C}{N} = \frac{N * \tau}{1 + N * \tau} \quad \textbf{(Equation 3-2)}$$

For a given detector system with certain dead time, the higher the count rate, the higher the error on the measured ion intensity. The count rate limitation is determined by the dead time and accuracy of the detector system. The calculation of instantaneous count rate is shown in eq. (3-3).

$$\text{Instantaneous count rate} = \text{apparent count rate} \times \frac{\text{raster area}}{\text{analyzed area}} \quad \textbf{(Equation 3-3)}$$

In order to prevent the EM from count rate overloads, the software can be used to set up a transition such that the secondary beam is automatically switched into the Faraday cup if count rate reaches the preset value.

#### 3.2.1.4 Normal Incidence Electron Gun

As described in section 2.4.2, when positive primary ions, either $O_2^+$ or $Cs^+$, impinge on the sample surface, the sample always charges positively. To compensate for the excess positive charge during SIMS analysis, the typical method is to direct electron flux to the ion sputter area. In the CAMECA IMS-6F, the normal incidence electron gun (NEG) is used for electron beam charge neutralization.

Figure 3-9 is a schematic drawing that illustrates the configuration of the normal incidence electron gun. Electrons are generated from the tungsten filament and the electron beam is directed through the electron column. A magnetic sector (Bya) deflects the electron beam into the secondary ion optical axis through the immersion lens and towards the sample surface. The electron beam can be deflected along the x-direction or along the y-direction by Bya or Bx.

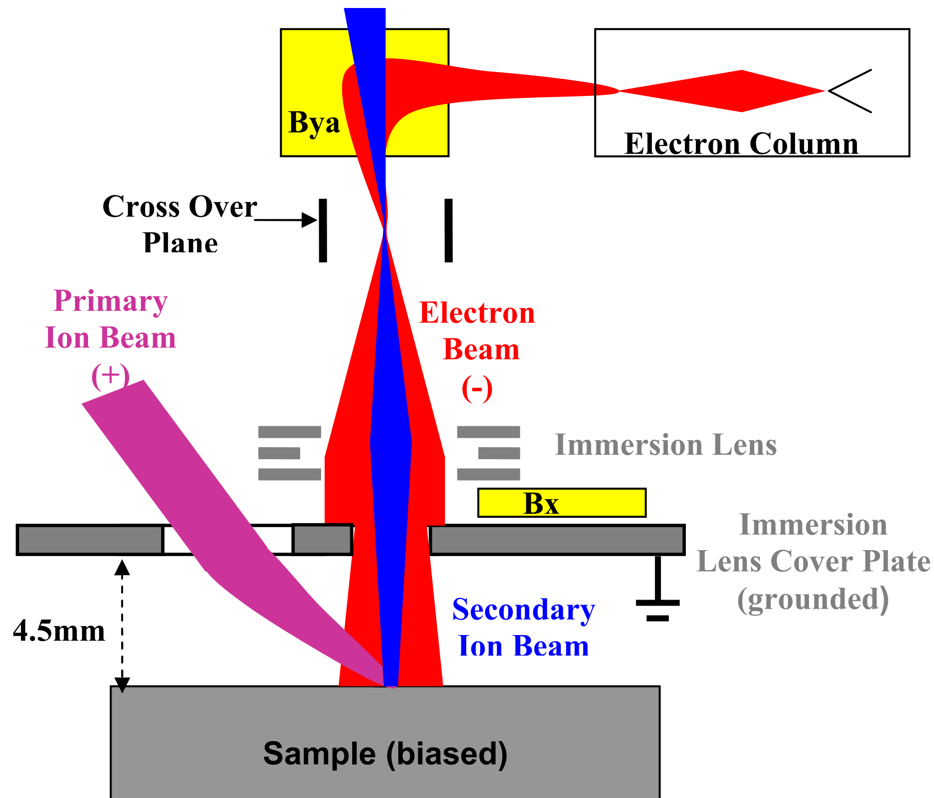


**Figure 3-9. Schematic of electron beam charge neutralization by normal incidence electron gun (drawing not to scale)**

### 3.2.2 Tencor P-20 stylus profilometer

In SIMS depth profiling, the raw data is in the form of secondary ion intensity versus sputter time. For a sample that is homogeneous and a primary beam that has constant density and current, it can be assumed the sputter rate is uniform during the analysis. The primary ion beam sputtered crater depth is measured using a stylus profilometer and the sputter rate is obtained by dividing the measured depth by the total sputter time. For a sample that is homogeneous with depth, the calculated sputter rate is then applied to the whole profile to convert the x-axis from sputter time to depth. If the sample has several layers, then an accurate depth scale requires knowledge of the sputtering rates of each layer. For crater depth larger than 10 nanometers, the craters can be measured using a stylus profilometer. Shallower craters should be measured using atomic force microscopy.

The stylus profilometer was first introduced by J.B. Williamson in 1967.[15] A stylus profilometer uses a diamond tip moved across a surface with very light pressure to provide information about surface topography. The KLA-Tencor P-20 profilometer uses Linear Voltage Differential Capacitance (LVDC) as a measurement device to detect the change in the topography of a sample.[16] The LVDC consists of two capacitor plates that are parallel to each other with a fixed separation distance. With a stylus attached on a center vane that floats between the two capacitor plates, the LVDC samples the surface area. By applying a continuous sinusoidal drive signal to the two capacitive plates, simulating a scan over a sample, the potential between the capacitive plates change in reference to the center vane. The LVDC measures the change in this potential to define the surface profile of the scanned sample. The analog signal is amplified, filtered, and converted to a digital sequence and processed by the computer system.

The KLA-Tencor P-20 profilometer is a programmable stylus profiler system that provides 0.25% precision above 0.4 μm for step height measurements.[17] It has a horizontal resolution of 0.01 μm at 1 μm/s scan speed and a vertical resolution of 0.5 angstrom with 3.25 μm step range.

### 3.3 The $Al_xGa_{1-x}N$ Sample Set

The samples in the $Al_xGa_{1-x}N$ sample set were selected to cover a wide range of Al content, from GaN to AlN. Samples in the sample set were obtained from several sources. Sample set 1 (SS1) were $Al_xGa_{1-x}N$ films grown on SiC substrate by MOCVD (Metal Organic Chemical Vapor Deposition) with x ranging from 0 to 0.18 as characterized by photoluminescence (PL). These samples were provided by Cree Inc.,[18] Sample set 2 (SS2) were $Al_xGa_{1-x}N$ film grown on Sapphire substrate by MOCVD with x is from 0.26 to 0.58 characterized by cathodluminescence (CL). These samples were provided by the Photonics Research Center in North Carolina State University. SS1 and SS2 were then implanted with $^{16}O$, $^{24}Mg$ and $^{29}Si$ with known dose to allow determination of the relative sensitivity sectors (RSF's) for these impurities. The doses and energies of these implants are listed in table 3.1. Sample set 3 (SS3) were fabricated using a high dose ion implant method described below.

Due to the difficulty of fabricating $Al_xGa_{1-x}N$ samples having x greater than 0.58 Al content with traditional MOCVD or MBE (molecular beam epitaxy) growth process, a novel approach was used to fabricate very high and very low Al content AlGaN by a high dose implantation method, which will be discussed in section 3.4. The validity of using high dose implants to generate low Al concentration samples was determined through comparison of SIMS data obtained from these samples with the as-grown low Al content samples. No comparison samples were available for the high AlN mole fraction (x) samples. The analysis and use of these samples is discussed in Chapter 4.

**Table 3-1. AlGaN sample set used for the study**

| Sample Set ID | Sources | Growth | x | Measure-met | Impurity Implantation | |
|---|---|---|---|---|---|---|
| | | | | | Species | Dose($cm^{-2}$)/ Energy (KeV) |
| SS1 | Cree Inc. | AlGaN film on SiC MOCVD | 0-0.21 | PL / LEXES | $^{16}O$<br>$^{24}Mg$<br>$^{29}Si$ | 5E14/70<br>2E14/100<br>5E14/110 |
| SS2 | Photonics Research Center | AlGaN film on Sapphire MOCVD | 0.23-0.58 | CL / LEXES | $^{16}O$<br>$^{24}Mg$<br>$^{29}Si$ | 5E15/140<br>2E14/120<br>1E15/150 |
| SS3 | High dose Ion Implantation | High dose Ga into AlN | 0.81*<br>0.98* | TRIM Simulation | NA | |
| | | High dose Al into GaN | 0.02*<br>0.22* | | | |

* Value at peak concentration of implant profile

The AlN mole fraction in the samples was characterized by the manufacturers using photoluminescence (PL) or cathodoluminescence (CL). Both PL and CL are commonly used in the industry to determine the alloy composition in III-nitrides. However, these are indirect composition measurement techniques which measure band gap by monitoring the light emission wavelength under photon or electron excitation. The alloy concentration is then calculated from the empirical relationship of band gap energy vs. AlN mole fraction (see eq.

1-1). The accuracy of these techniques is limited by uncertainties in the photon energy determination, ambient temperature and doping and defect levels.[19] There are no composition standards for III-nitrides and each industrial company or laboratory uses their own internal calibration standards. While these results may have high precision, there is no independent verification of measurement accuracy. In order to at least insure that a consistent set of measurement was available for SIMS quantification, AlN mole fractions were measured using wavelength dispersive electron induced x-ray emission spectroscopy (WDS) technique using the a commercially available Low energy Electron induced X-ray Emission Spectrometry (LEXES) system.

LEXES is a modified version of the multiple-spectrometer WDS technique. In LEXES, a solid sample is irradiated by a low energy electron beam and soft X-rays are emitted and analyzed, as shown in figure 3-10.[20] Because the X-rays are characteristic of the emitting elements, selective elemental analysis is achieved. The precise modeling of primary electron/matter interaction and of the absorption of the emitted soft X-rays allows accurate elemental quantification of the sampled depth over a wide range of concentration (from 100 at% down to tens parts per million). The matrix effects are small and well modeled.[21]

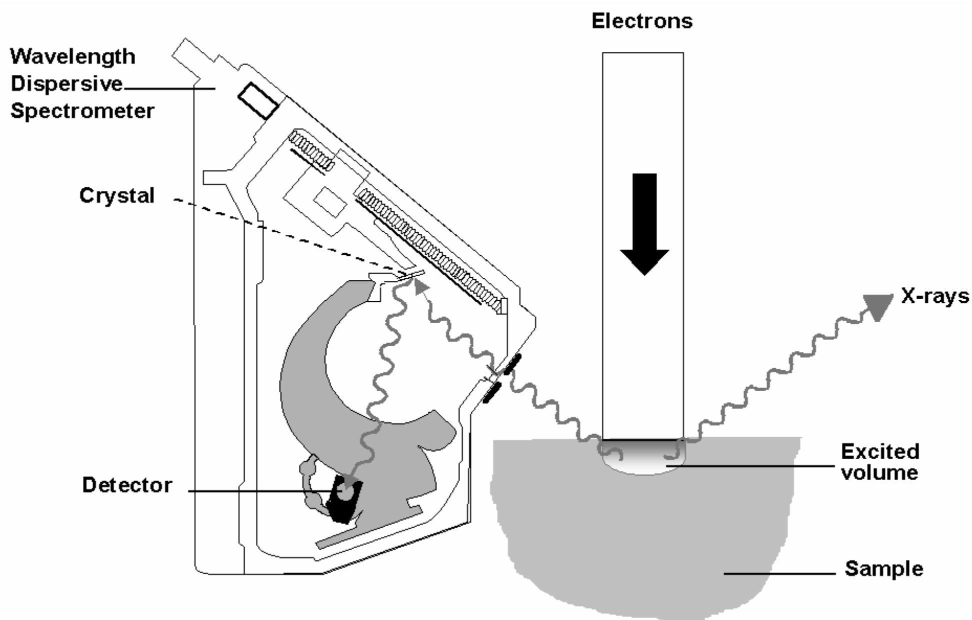


**Figure 3-10. Principle of LEXES measurement [20]**

The LEXES measurements in this study were performed by Full Wafer Analysis (http://www.fullwaferanalysis.com/home.htm) using a Shallow Probe 300 (SP300) manufactured by CAMECA Instruments (http://www.cameca.fr/html/lexes_technique.html). The instrument is equipped with a high current and low energy electron column (0.2 up to 10 keV), which permits study over the depth range 1–700 nm. The spot size is kept from 10 to 100 μm diameter while the current range extends from 0.5 nA to 100 μA. The instrument is equipped with three Wavelength Dispersive Spectrometers (WDS) designed by CAMECA.[22] With this arrangement, a typical accuracy of better than 5% in compositional analysis and a precision of 1-5% for a measurement time of 1 min can be achieved.[20]

### 3.4 Fabrication of High Al Content AlGaN Samples

AlGaN with high Al content has been attracting great attention in recently. High Al content AlGaN devices are desirable for deep UV (ultra-violet) emitters, solar-blind UV detectors, high speed high-electron mobility transistors (HEMT's), and high power Modulation-Doped Field Effect Transistor (MODFET).[23-29] In $Al_xGa_{1-x}N$, the energy band gap increases up to 6.2eV with the increase of AlN mole fraction. In order to obtain UV emitters or detectors in a shorter wavelength range, AlGaN-based devices with high Al concentration have to be developed. For an AlGaN/GaN MODFET or HEMT, the higher AlN mole fraction results in higher energy band gap and higher breakdown field. Also, the resultant higher conduction-band discontinuity (offset) improves the carrier confinement and allows a higher 2-dimensional electron gas (2-DEG) density which increases the power density of the devices.[23,29]

Al-rich AlGaN materials are very difficult to grow and to characterize. Although high quality crack-free Al-rich AlGaN has been demonstrated by several research groups, this material is not available commercially. In order to obtain high Al content AlGaN samples for this study for development of the methodology to quantify these materials using SIMS, a novel method was devised using high dose implantation of Ga into AlN.

Implantation has been used to make AlN film by ion implantation of nitrogen gas into an Al film.[30,31] In a recent report, Grigorov et al.[30] used broad energy nitrogen ion implantation and rapid thermal annealing to obtain a 150 nm thick continuous AlN layer. For SIMS quantification, a single energy ion implantation producing high Al content at the

implant peak position is sufficient. For this purpose, a high dose of Al was implanted into GaN to create a low Al content region, and a high dose of Ga was implanted to AlN to create a high Al content region. Ga depth profile in AlN and Al depth profile in GaN was acquired using SIMS analysis under 5.5 keV $O_2^+$ ion bombardment (see figure 3-11).

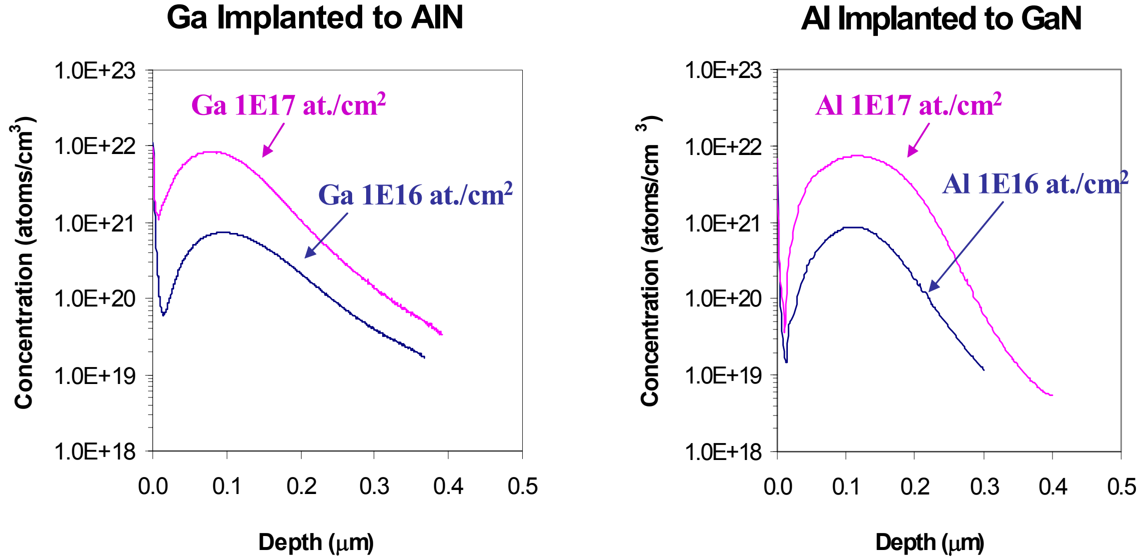


**Figure 3-11. Depth profiles of high dose Ga in AlN and Al in GaN**

The peak concentration of Ga and Al was obtained by simulation using an ion implantation predictive tool SRIM-2003 (http://www.srim.org). SRIM (Stopping and Range of Ions in Matter) is a group of programs calculating the stopping and range of ions into matter. From the dose and energy of the implantation used, the projected straggle $\Delta R_P$ is obtained from the simulation. The peak concentration of Al or Ga implantation can be calculated using eq. (3-4)[32] by assuming Gaussian distribution of the ion implantation.

$$C_{MAX} = \frac{\Phi}{\sqrt{2\pi}\Delta R_P} \quad \textbf{(Equation 3-4)}$$

Where $C_{MAX}$ is the peak concentration, $\Phi$ is the dose and $\Delta R_P$ is the straggle of the implantation.

From the peak concentration, the mole fraction x is calculated from eq. 3-5 or 3-6.

$$x = \frac{\text{Al peak concentration}}{\text{Atomic density of GaN}} * 2 \qquad \text{for Al implant into GaN} \qquad \textbf{(Equation 3-5)}$$

or

$$x = 1 - \frac{\text{Ga peak concentration}}{\text{Atomic density of AlN}} * 2 \qquad \text{for Ga implant into AlN} \qquad \textbf{(Equation 3-6)}$$

The atomic density of GaN is 8.83E22 atoms/cm$^3$ and of AlN is 9.49E22 atoms/cm$^3$. The four samples fabricated by this method are listed in table 3-2.

**Table 3-2. Samples fabricated by high dose of implantation**

| Implantation | Peak Concentration (atoms/cm3) | x value at peak position |
|---|---|---|
| Al→GaN 1E16 cm$^{-2}$/100keV | 9.97E20 | 0.02 |
| Al→GaN 1E17 cm$^{-2}$/100keV | 9.97E21 | 0.22 |
| Ga→AlN 1E16 cm$^{-2}$/150keV | 8.87E20 | 0.98 |
| Ga→AlN 1E17 cm$^{-2}$/150keV | 8.87E21 | 0.81 |

## 3.5 Electron Beam Charge Neutralization

Undoped $Al_xGa_{1-x}N$ alloys are generally insulating for x>0.4.[33,34] Even at lower AlN mole fraction, the material can have severe charging effects during SIMS analysis particularly when low primary beam energy is used. To reduce the charging effects, several methods can be used. For bulk insulators, an electron flood gun such as the NEG described above is generally used.[35] Other reported techniques include the use of negative ion primary beam,[36] use of a conducting grid, continuous evaporation of a metal layer, and heating of the insulator to increase the conductivity.[37]

In the CAMECA IMS-6f magnetic sector mass spectrometer, the use of the Normal incidence Electron Gun (NEG) for charging compensation is the most commonly employed method. Charge neutralization using the NEG typically does not degrade the depth resolution and secondary ion beam intensity. Depending on the polarity of the bias of the sample, the neutralization method can be positive mode charging compensation or negative mode charging compensation. The methods described in the following section are used in CAMECA IMS-6f magnetic sector design due to the special geometry of the instrument optics and high electric field which is on the order of kilovolts per mm over the 4.5mm

distance between the sample and the immersion lens cover plate. The electron-beam charge neutralization methods in quadrupole and time-of-flight SIMS are often easier to implement since the sample is grounded in the quadrupole and it can be zero biased in TOF-SIMS during electron pulse.

### 3.5.1 Positive Mode Charging Neutralization

The sample is positively biased in positive secondary ion mode, thus the electron impact energy is high since electrons are attracted to a positively biased sample. Depending on the thickness of the insulator, two approaches can be used for the charge neutralization.

Electron Penetration for Thin Layer Insulator on Conductive Substrate

Positive secondary ion analysis of thin insulators on conducting substrates is straightforward using a magnetic sector mass spectrometer. The electron beam impact energy is chosen such that electrons can penetrate the film and render the film conductive via electron beam induced conductivity (EBIC).

The electron impact energy has two components: the electron source high voltage and sample high voltage. The electron range is affected by the electron beam energy and the sample substrate properties. It can be estimated by Kanaya-Okayama range ($R_{KO}$) from eq. 3-7. [38]

$$R_{KO} = \frac{0.0276 W E_0^{1.67}}{Z^{0.89} \rho} \qquad \textbf{(Equation 3-7)}$$

Where $R_{KO}$ is the Kanaya-Okayama range in μm, $E_0$ is the incident beam energy in keV, W is the average atomic weight in g/mol, Z is the average atomic number, and ρ is the average density in g/cm$^3$. The electron beam impacts the sample surface at normal angle of incidence.

Electron Beam Adjacent to Ion Raster for Thick Film or Bulk Insulators

If the insulator is a thick film or bulk material, the electron beam can not penetrate through the insulator. In this case, achieving and maintaining a charge balance during SIMS analysis using a CAMECA IMS instrument has been very difficult. Pivovarov et al.[39] reported an electron beam based charge neutralization procedure for magnetic sector SIMS analysis of bulk insulators which allows the use of high $O_2^+$ primary ion currents and thus

high sputtering rates and which does not require careful and constant regulation of either the electron or ion beam current.

The method is best illustrated in figure 3-12 which shows the electron beam positioned adjacent to or just touching the ion beam raster. The electron beam shape was observed via the IMS-6f sample viewing light microscope by viewing the cathodoluminescence induced by electron beam impact in a Cu implanted $SiO_2$/Si sample. This image is the combination of cathodoluminescence (electron impinging area) and optical reflection image (all other areas). Cathodoluminescence resulting from electron beam bombardment of a Cu implanted $SiO_2$/Si sample provides the ability to observe both the position and the density (as indicated by variations in emission brightness) of the electron beam at the sample. Samples were sputter coated with approximately 20 nm gold.

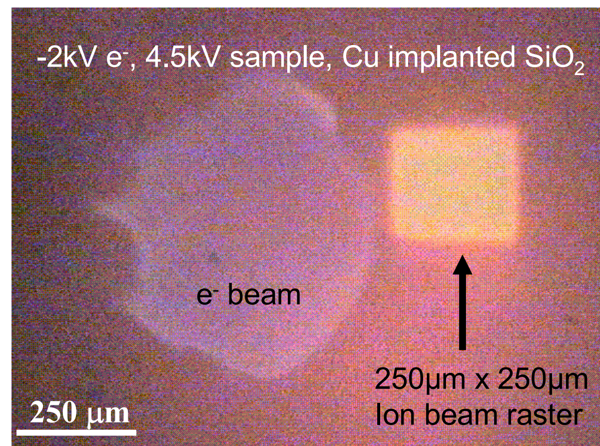


**Figure 3-12. Electron beam position is adjacent to raster area in positive electron compensation. The image is the combination of cathodoluminescence (electron impinging area) and optical reflection image (all other areas).**

The advantage of this method is the effective neutralization over a large range of primary ion beam currents, energies and raster sizes providing the ability to cover a wide range of analysis requirements such as differing sputter rates, depth resolutions and detection limits.

Because the electron beam size reaching the sample is defined by strength of the potential on the immersion lens, it is affected by the choice of the sample bias since the immersion lens potential must be increased to focus the secondary ions at the first cross over at the dynamic transfer plates. The higher the sample bias, the higher the immersion lens

setting, and the larger the electron beam size reaching the sample. The magnetic deflector, Bx in figure 3-9 can only deflect electron beam over a certain range limited by the excitation current in the magnet and the energy of the electrons. For a reasonable electron beam size and effective deflection from the center spot to the left of the raster area, an electron high voltage (HV) of -2 kV was used for a +4.5 kV sample bias. With other sample biases, the electron source HV has to be chosen according to eq. 3-8.

$$\frac{\text{new electron source HV}}{2\,\text{kV}} = \frac{\text{new sample bias}}{4.5\text{kV}} \qquad \textbf{(Equation 3-8)}$$

In the CAMECA IMS-6F, the electron beam density obtainable with electron source voltage setting less than 1 kV is too low for effective charge compensation. For the analysis with 1.75 kV sample bias, electron high voltage of 1 kV is used.

The use of the adjacent electron beam charge neutralization technique allows high sputter rate analysis of bulk insulating samples to be performed. Perhaps equally importantly, the process appears to be self-regulating in that no adjustment of either the primary ion beam or the electron beam current is required to maintain charge balance during the analysis.

### 3.5.2 Negative Mode Charging Neutralization

For negative secondary ion detection with a NEG, both electron source and sample are negatively biased to the same potential. When electrons reach the sample surface they have lost their momentum, so a “cloud” of very low energy electrons are formed above the sample as shown in figure 3-13. The availability of low energy electrons in the "cloud" provides self regulated charging compensation. If a region of the sample charges positively, electrons will be attracted to the positively charged region from the “cloud” as needed to compensate for the sample charging. Since a self balancing situation is established where electrons only impact the sample as needed for maintaining a charge balance, careful regulation of NEG electron beam current is not required. However, an excess of electrons above the sample surface is required, which requires that primary ion density be kept sufficiently low in order that sufficient electrons are available. In addition, due to the approximately 120µm diameter of the electron beam "cloud", the primary ion beam rastered area must be kept to approximately 100x100 $\mu m^2$.

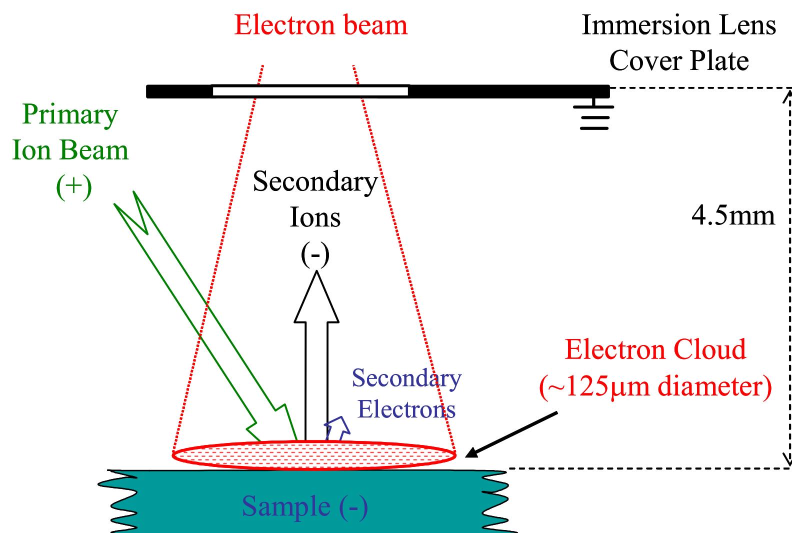


**Figure 3-13. Electron cloud formation above sample surface in negative mode charge neutralization**

During negative secondary ion insulator analysis, it is difficult to adequately determine the electron beam impact region utilizing the cathodoluminescent materials that can be used for NEG alignment for positive secondary ion analyses due to the low electron impact energy. Utilization of electron stimulated desorption of adsorbed species such as $H^-$ and $F^-$ is a commonly used method for NEG alignment, but this method of NEG beam visualization can make the NEG alignment difficult since the intensity of these electron desorbed secondary ion species is often not uniform and their intensity decreases with electron beam exposure time. To overcome this difficulty, a new technique has been developed that utilizes negative matrix ions, e.g. $Si^-$ from a silicon sample, for NEG alignment.[40] In this method, negative secondary matrix ion species produced from a sample surface are used to align the NEG both with respect to beam density and electron beam location with respect to the mass spectrometer secondary ion optical axis. The negative matrix ions appear to be produced by electron impact ionization of gaseous species. The detailed procedure is described in the reference,[40] but a brief summary is provided here. After Cs sputtering (implanting) the sample surface until the intensity of the matrix secondary ions reach steady state, the Cs ion source gate valve is closed (to stop any Cs neutrals impacting onto the sample surface and producing secondary ions) and NEG is turned on. The matrix negative ions then can be used to adjust the beam intensity of NEG.

### 3.6 Analysis Conditions

In the analysis of III-nitride materials, different requirements for sensitivity and depth resolution will be encountered. When high sensitivity of electropositive species (such as Al and Mg) is needed, $O_2^+$ primary bombardment and positive secondary potential are used. When high sensitivity of electronegative species (such as Si and O) is needed, $Cs^+$ primary bombardment and negative secondary potential are used. If both electropositive and electronegative species are needed at the same analysis, $MCs^+$ technique can be the choice (using $Cs^+$ source with $MCs^+$ cluster ion detection).

For high depth resolution, low primary beam energy is required. The CAMECA IMS-6F magnetic sector SIMS has provided a practical beam energy range from 200 eV to 22 keV. The lower the energy, the higher the depth resolution, but beam density and sputter rate are also reduced, which leads to a higher detection limit. Depending on the needs for good depth resolution or lower detection limit and reasonable sputter time, both high and low energies may be needed. Since the purpose of this study is to develop a quantification methodology as well as comprehensive calibration curves under multiple analysis conditions with high, low and medium energy, $O_2^+$ and $Cs^+$ species, positive and negative sample bias, a wide range of analytical conditions were used. Table 3-3 is the summary of analysis conditions employed in this project.

**Table 3-3. Analysis conditions in the project**

| Beam Sources | Secondary Ion Polarity | Primary Ion Impact Energy (keV) | Angle of Incidence | Projectile Range in GaN (nm) |
|---|---|---|---|---|
| $O_2^+$ | + | 5.5 | 41.3° | 7.7 nm |
| | | 1.25 | 48.5° | 2.6 nm |
| $Cs^+$ | - | 14.5 | 24.8° | 9.0 nm |
| | | 6.0 | 27.3° | 5.4 nm |
| | + | 5.5 | 41.3° | 4.6 nm |
| | | 1.25 | 48.5° | 2.1 nm |

## 3.7 References


[1] CAMECA, Duoplasmatron illustratration, IMS 6-F USER'S GUIDE**,** 1-64 (1996).

[2] CAMECA, IMS 6F Instrument Specifications & Aceptance Tests**,** 5 (1996).

[3] F. A. Stevie, P. M. Kahora, D. S. Simons, and P. Chi, Journal of Vacuum Science & Technology A (Vacuum, Surfaces, and Films) **6,** 76-80 (1988).

[4] E. Chason, J. Erlebacherb, M. J. Azizb, J. A. Floroc, and M. B. Sinclairc, Nuclear Instruments and Methods in Physics Research Section B: Beam Interactions with Materials and Atoms **178,** 55-61 (2001).

[5] CAMECA, "Application Note:ACCEL/DECEL SYSTEM," (2000).

[6] M. Schuhmacher, B. Rasser, and F. Desse, Journal of Vacuum Science & Technology B **18,** 529-532 (2000).

[7] G. D. Alton, R. F. Welton, B. Cui, S. N. Murray, and G. D. Mills, Nuclear Instruments & Methods in Physics Research Section B-Beam Interactions with Materials and Atoms **142,** 578-591 (1998).

[8] M. G. Inghram and W. A. Chupka, Review of Scientific Instruments **24,** 518-520 (1953).

[9] CAMECA, Microbeam Cesium Source Principle, IMS 6-F USER'S GUIDE**,** 1-65 (1996).

[10] CAMECA, Illustration of mass spectrometer, IMS 6-F USER'S GUIDE (1996).

[11] CAMECA, Illustration of Faraday Cup, IMS 6-F USER'S GUIDE**,** 1-77 (1996).

[12] R. Fleming, Secondary Ion Mass Spectrometry Instrumentation Tutorial, http://www.cea.com/cai/simsinst/detector.htm (1995).

[13] CAMECA, "Application Note: Post acceleration system," (1996).

[14] CAMECA, Dead tims, IMS 6-F USER'S GUIDE**,** 1-79 (1996).

[15] J. B. Williamson, Proc. Inst. Mech. Eng. **182,** 21 (1967).

[16] Tencor KLA Profilometer, http://grover.mirc.gatech.edu/equipment/equipview.phtml?id=119.

[17] Tencor, P-2-h Long Scan Profiler Reference Manual**,** 4-2.

[18] Cree Inc., www.cree.com.

[19] A. Roshko, K. Bertness, and J. Armstrong, Phys. Stat. Sol. (c) **0,** 992-997 (2003).

[20] C. Hombourger, R. Staub, M. Schuhmacher, F. Desse, E. de Chambost, and C. Hitzman, Applied Surface Science **203,** 383-386 (2003).

[21] S. J. B. Reed, Mikrochimica Acta Supplementum **15,** 39 (1998).

[22] P. F. Staub, C. Hombourger, and M. Schuhmacher, Journal of Vacuum Science & Technology B **20,** 436-440 (2002).

[23] Y. F. Wu, B. P. Keller, P. Fini, S. Keller, T. J. Jenkins, L. T. Kehias, S. P. Denbaars, and U. K. Mishra, Ieee Electron Device Letters **19,** 50-53 (1998).

[24] H. Hirayama, Y. Enomoto, A. Kinoshita, A. Hirata, and Y. Aoyagi, Applied Physics Letters **80,** 37-39 (2002).

[25] K. B. Nam, J. Li, M. L. Nakarmi, J. Y. Lin, and H. X. Jiang, Applied Physics Letters **81,** 1809-1811 (2002).

[26] M. L. Nakarmi, K. H. Kim, M. Khizar, Z. Y. Fan, J. Y. Lin, and H. X. Jiang, Applied Physics Letters **86,** - (2005).

[27] J. Li, K. B. Nam, J. Y. Lin, and H. X. Jiang, Applied Physics Letters **79,** 3245-3247 (2001).

[28] K. B. Nam, J. Li, M. L. Nakarmi, J. Y. Lin, and H. X. Jiang, Applied Physics Letters **81,** 1038-1040 (2002).

[29] Rashmi, A. Kranti, S. Haldar, M. Gupta, and R. S. Gupta, Ieee Transactions on Microwave Theory and Techniques **51,** 607-617 (2003).

[30] K. G. Grigorov, I. Nedkov, G. Beshkov, C. Angelov, H. S. Maciel, W. Matz, R. Groetzchel, and N. Velchev, Journal of Optoelectronics and Advanced Materials **7,** 381-384 (2005).

[31] B. Rauschenbach, A. Kolitsch, and E. Richter, Thin Solid Films **109,** 37-45 (1983).

[32] H. Ryssel and I. Huge, *Ion Implantation* (Wiley, New York, 1986).

[33] S. N. Mohammad, A. A. Salvador, and H. Morkoc, Proceedings of the Ieee **83,** 1306-1355 (1995).

[34] H. Morkoc, S. Strite, G. B. Gao, M. E. Lin, B. Sverdlov, and M. Burns, Journal of Applied Physics **76,** 1363-1398 (1994).

[35] H. W. Werner and A. E. Morgan, Journal of Applied Physics **47,** 1232 (1976).

[36] C. A. Anderson, H. J. Roden, and C. F. Robinson, Journal of Applied Physics **40,** 3419 (1969).

[37] I. A. Abroyan, V. P. Lavrov, and I. G. Fedora, Sov. Phys. Solid State **7,** 2954 (1966).

[38] J. I. Goldstein and D. E. Newbury, *Scanning Electron Microscopy and X-ray Mocroanalysis, Second Edition, p.89* (Plenum Press, New York and London, 1992).

[39] A. L. Pivovarov, F. A. Stevie, and D. P. Griffis, Applied Surface Science **231-2,** 786-790 (2004).

[40] A. Pivovarov, C. Gu, F. Stevie, and D. Griffis, Applied Surface Science **231-2,** 781-785 (2004).

# 4 Quantification of Matrix and Impurity Species in $Al_xGa_{1-x}N$ under $O_2^+$ Bombardment with Positive Ion Detection

## 4.1 Introduction

Quantitative SIMS analysis using an $O_2^+$ primary ion beam and detection of positive secondary ions is commonly used because of the large positive ion yield enhancement obtained when using $O_2^+$ for many elements. However, due to the large matrix effect introduced, the quantification of matrix level in III-nitride materials using oxygen primary beam and detection of positive secondary ions has not been widely studied. Nevertheless, in the AlGaN material system, this approach should be investigated because it has the advantage of quantifying both matrix (Al, Ga) and the most common n-type (Si) and p-type (Mg) impurities simultaneously and with high sensitivity.

Using $O_2^+$ primary ion beam bombardment, Griffis et al.[1] studied $Al^+/Ga^+$ ion intensity ratio and $Mg^+$ RSF (normalized to $Ga^+$) as a function of x in $Al_xGa_{1-x}N$, with x ranging from 0 to 0.31. The results showed a near linear relationship between $Al^+/Ga^+$ ion intensity ratio and x, and an $Mg^+$ RSF (normalized to $Ga^+$) which decreased with the increasing of x in the range of $0 \leq x \leq 0.22$. In Lefforge's work,[2] $Mg^+$ RSF (normalized to $Ga^+$) is also plotted as a function of x with $x \leq 0.33$. In his work, the RSF showed no significant variation with x.

With the wide interest in high Al content AlGaN for deep UV emitters used in bio-chemical detection, and for solar blind UV sensors with superior sensitivity used in threat recognition aimed against aircraft,[3-5] the quantification of matrix and impurity species in high Al content $Al_xGa_{1-x}N$ ($x>0.4$) is important. In the work described in this chapter, the quantification of matrix and impurity species in $Al_xGa_{1-x}N$ will be investigated in the range of $0 \leq x \leq 1$ and calibration curves will be determined. The calibration curves can then be used for accurate quantification of matrix and impurity species in samples with varying Al content.

In this chapter the oxygen incorporation and its secondary ion yield enhancement mechanism will be reviewed briefly. The experimental method and results in $Al_xGa_{1-x}N$ quantification will be discussed. Based on the results, the mechanisms influencing secondary ion yields in $Al_xGa_{1-x}N$ under $O_2^+$ primary beam will be rationalized.

## 4.2 Oxygen Incorporation and Positive Secondary Ion Emission Enhancement

The secondary ion yield enhancement due to oxygen gas flooding was first studied in detail in 1966 by Slodzian and Hennequin.[6] The presence of oxygen was found to enhance the yield of positive atomic ions by several orders of magnitude, and to enhance the yield of atomic negative ions slightly.[7] Based on the yield enhancement of oxygen, a SIMS instrument using an oxygen primary ion beam was proposed to increase the analytical sensitivity of electropositive elements. Although the effects of oxygen have been known and studied for over 40 years, there is still little consensus on the mechanism of the effects. The secondary ion formation and emission mechanisms are reviewed in section 2.2.

Anderson[8] proposed that oxygen increases the surface work function which increases positive ionization probability. However, it is found that the surface work functions of Mg,[9] Mo(100),[10] and Nb(110) [11] metals are actually decreased by oxygen adsorption while the yield of the corresponding positive ions is simultaneously enhanced. Besides, if the work function is increased, the negative ion yield should be reduced in the presence of oxygen which is not the case. To explain the yield enhancement of oxygen for both positive and negative ions as well as the controversy for Mg, Mo and Nb metal, Williams[7,12] proposed a surface polarization model. Oxygen can be adsorbed onto or incorporated beneath the surface, which creates localized electron-retentive and electron-emissive sites. For a substrate which is less electronegative than oxygen, an electron transfers to the oxygen from the sample surface. Adsorbed oxygen on the surface creates a dipole with electric field pointing to the surface which increases the barrier for electron emission. Oxygen incorporated beneath the surface layer creates a dipole with electronic field pointing from the surface which reduces the barrier for electron emission. Atom-surface interactions are extremely short-range effects with the result that the sputtered atom or ion interacts only with its immediate neighbors at the sputtering site. The surface work function is not a measure of the local potential barrier, but rather an average property of the surface.

In the bond-breaking model (section 2.2.1), it is assumed that oxygen atoms create a local ionic lattice in metals, which has lower potential energy than neutral dissociation.[12] The ionic character of the metal-oxygen bonds promotes direct emission of ions. In the case of a semiconductor such as Si, the presence of oxygen generates oxidation states with 1 to 4 oxygen atoms at nearest neighbor sites.[13] The energy of the Coulombic curve of $SiO_x$

decreases with x and the crossing distance with the neutral dissociate ($R_C$) increases, which results in the enhancement of positive ion yield of $Si^+$.

In the electron-tunneling model (section 2.2.2), the adsorbed oxygen on the surface creates local dipole layer which increase the work function of the sample. The increase of the work function increases the separation distance of crossing point ($Z_C$) where the energy level of sputtered atom coincides with the occupied electronic levels in the metal (below Fermi level) and where the electron can tunnel between the levels via a resonant electron transfer process.[14] When the crossing point is increased, the probability that an electron will tunnel from the metal to neutralize the departing excited atom is reduced, thus the atoms have higher probability to escape as positive ions.

In the band structure model, the excited atom moving away from a metal surface could de-excite through resonant detachment, when the excited electron tunneled into a vacant state above the Fermi level in the metal.[15] When the surface is oxidized, the electrons are removed to the valence band where they are at too low an energy to undergo resonant transitions to neutralize most departing ion species.

There are also other models to rationalize the yield enhancement of oxygen. Although the oxygen secondary ion yield enhancement mechanism is still not established, oxygen ion beam have been used experimentally for elemental compositional analysis with very high sensitivity for electropositive elements. In this chapter, the quantification of matrix and impurity species in $Al_xGa_{1-x}N$ under $O_2^+$ bombardment is discussed, and the ionization mechanism will be rationalized.

## 4.3 Experimental Method

Three sets of samples were used (see section 3.3). SS1 (sample set number one) consists of $Al_xGa_{1-x}N$ films grown on a SiC substrate with a GaN buffer layer. These samples have an AlN mole fraction of $0 \leq x \leq 0.21$ as determined by LEXES (Low energy Electron induced X-ray Emission Spectrometry). SS2 ((sample set number two) consists of $Al_xGa_{1-x}N$ films grown on a sapphire substrate with an AlN buffer layer, having an AlN mole fraction of $0.23 \leq x \leq 0.58$, also determined by LEXES. The films were grown by Metal Organic Chemical Vapor Deposition (MOCVD) in both cases. All samples in SS1 and SS2 were

implanted with $^{16}O$, $^{24}Mg$ and $^{29}Si$ with energy and dose shown in table 3-1. The samples in SS3 (sample set number three) were fabricated using high dose ion implantation of Al into GaN or Ga into AlN, with low x (0.02, 0.22) and high x (0.81, 0.98) in the ion implant peak position. All the samples in all sample sets were sputter coated with ~10nm of Au.

SIMS analyses were performed using an $O_2^+$ primary ion beam extracted from the duoplasmatron of the CAMECA IMS-6F. High energy and low energy $O_2^+$ primary beams were used for the analysis. Table 4-1 lists the analysis conditions. Angles of incidence were calculated using a program written by Schumacher[16] which compensates for the IMS-6F primary ion column deflector voltages used for positioning the beam onto the secondary ion column optical axis of the IMS-6f mass spectrometer. Practical primary beam impact energies commonly used in our laboratory were selected for these analyses.

**Table 4-1 Analysis conditions under $O_2^+$ primary ion bombardment**

| Primary Ion Species | Primary Ion Acceleration Voltage (kV) | Sample Potential (kV) | Impact Energy (keV) | Angle of Incidenc e (degrees) | Ion Current (nA) | Raster Size ($um^2$) | Beam Density ($\mu A/um^2$) |
|---|---|---|---|---|---|---|---|
| $O_2^+$ | 10 | 4.5 | 5.5 | 41.3 | 80 | 180x180 | 2.47 |
| $O_2^+$ | 3 | 1.75 | 1.25 | 48.5 | 50 | 200x200 | 1.25 |

Secondary ions were collected from a 60µm diameter optically gated area (750µm field aperture, 150µm image field, 400µm contrast aperture). The collection area is centered on a square raster area of 180 x 180 $\mu m^2$ or 200 x 200 $\mu m^2$. Entrance slits and exit slits were adjusted to obtain a mass resolution of 1600 m/Δm to separate $^{24}Mg$ and $^{12}C_2$. The depth of sputtered craters was measured using a KLA-Tencor P-20 profilometer.

Electron beam charge neutralization was performed using the Normal Incidence Electron Gun (NEG) provided with the CAMECA IMS-6F. For positive SIMS, the electron beam was aligned to the left side of the primary ion raster area (see section 3.5.1).[17] The energy of the electron beam was chosen such that the NEG electron beam diameter was less than 1000µm. If the electron beam is too large in size, it cannot be deflected to the left side of the primary ion beam rastered area due to the limitation of the excitation strength in magnetic sector deflector. The electron beam size is affected by the setting of the immersion lens. For positive secondary ion detection, a higher sample bias requires a higher immersion lens

setting resulting in a larger the electron beam size reaching the sample. For a reasonable electron beam size, an electron high voltage (HV) of -2 kV was used for a +4.5 kV sample potential and electron HV of -1 kV was used for a +1.75 kV sample potential. The criterion detailed in eq. (3-6) was used to determine the proper electron HV.

For matrix element analyses, depth profiles were acquired until the matrix ion counts reach a steady state. For implanted impurity analyses, depth profiles were acquired until the impurity ion counts dropped to the background level. Matrix ions monitored are $Al^+$ and $Ga^+$, and impurity ions monitored are $Si^+$ and $Mg^+$. A typical depth profile under $O_2^+$ primary beam with positive SIMS is shown in figure 4-1.

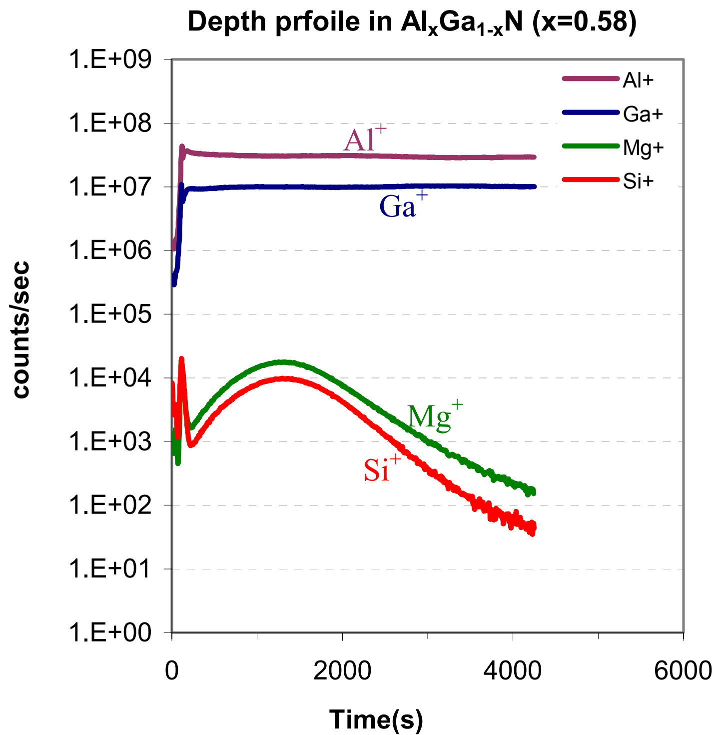


**Figure 4-1. Depth profile of matrix and impurity species in $Al_xGa_{1-x}N$ where x= 0.58 under $O_2^+$ with positive ion detection**

$Al^+/Ga^+$ ion intensity ratios, the RSF's of $Si^+$ and $Mg^+$ normalized to $Ga^+$, and the sputter yields ($um^3/(s.nA)$) were calculated after the depth profiles for all samples analyzed in this study. The relationships of these parameters with respect to AlN mole fraction were studied.

## 4.4 Results and Discussion

### 4.4.1 Sputter Rate

The sputter rates were normalized to primary beam density which is proportional to sputter yield (The number of particles sputtered from the surface of a target per primary ion). The normalized sputter rates using $O_2^+$ bombardment are plotted as a function of AlN mole fraction (x) as shown in figure 4-2. Figure 4-2a is the sputter rate at 5.5 keV impact energy; figure 4-2b is at 1.25 keV impact energy. The two figures show a similar relationship of the sputter rate to the AlN mole fraction (x) in the range $0 \le x \le 0.58$ for these primary ion impact energies. As the AlN mole fraction x increases, the sputter rate decreases for both these primary ion impact energy conditions, but the rate of decrease in the sputter rate versus x declines as the AlN mole fraction increases.

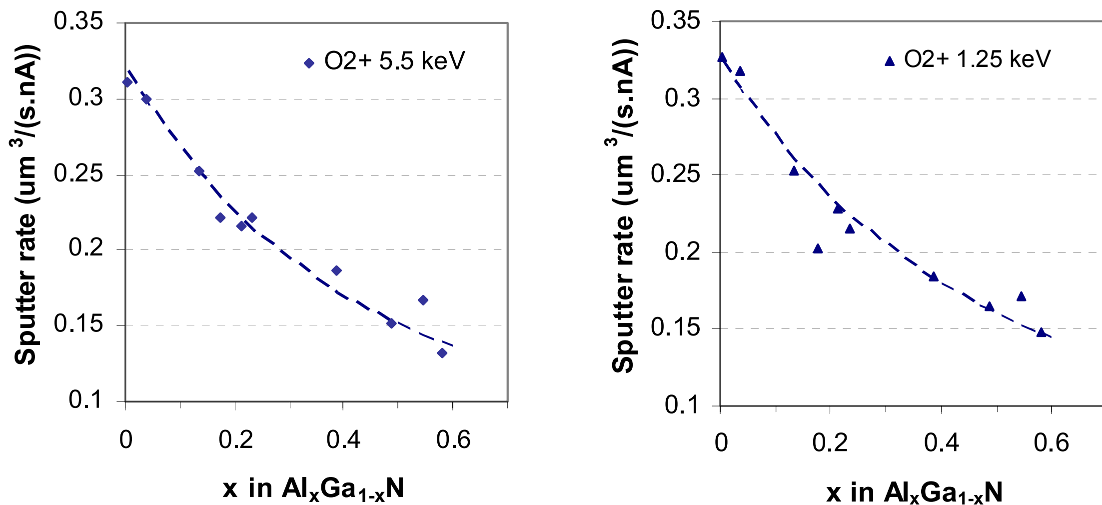


(a) Sputter rate at high impact energy (b) Sputter rate at low pact energy

**Figure 4-2. Sputter rate of $Al_xGa_{1-x}N$ as a function of AlN mole fraction under $O_2^+$ bombardment**

Figure 4-3 shows the comparison of sputter rate at 1.25 keV and 5.5 keV impact energies. Within measurement error, the sputter rates at both energies are the same. It is believed that this results from the fact that sputter rate is inversely affected by decreasing primary ion energy (sputter rate decreases) and increasing angle of incidence (sputter rate increases). The angle of incidence for 5.5 keV impact energy (10/4.5 kV bias) is 41.3° from

normal, for 1.25 keV (3/1.75 kV bias) is 48.3° from normal. For the sputter rate at 1.25 keV, it seems that the effect from lower energy (which reduces sputter rate) and from higher angle of incidence from normal (which increases sputter rate) counteracts, thus the sputter yields with 5.5 and 1.25 keV impact energies are close.

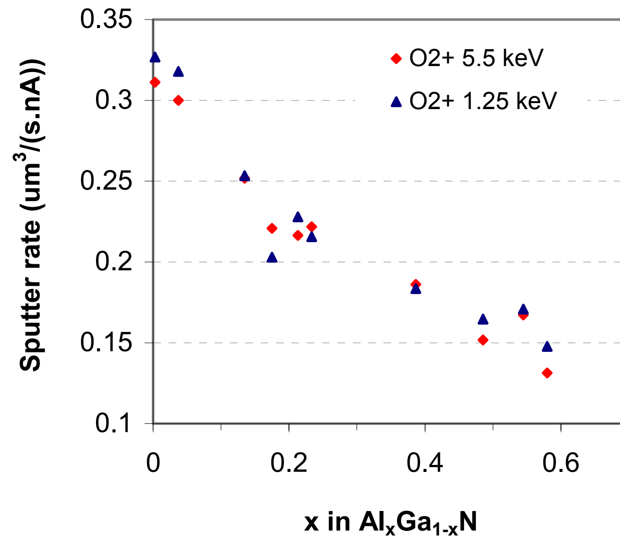


**Figure 4-3. Comparison of sputter rate of $Al_xGa_{1-x}N$ as a function of AlN mole fraction (x) at high and low impact energies under $O_2^+$ primary ion bombardment**

### 4.4.2 Matrix Ion Intensity Ratio

The matrix ion intensity ratios of $Al^+/Ga^+$ at 5.5 keV impact energy under $O_2^+$ bombardment were first plotted as a function of x in $Al_xGa_{1-x}N$. Figure 4-4 shows that at low Al concentration the relationship appears linear up to x=0.4. As x increases beyond 0.4, $Al^+/Ga^+$ increases at a non linear rate.

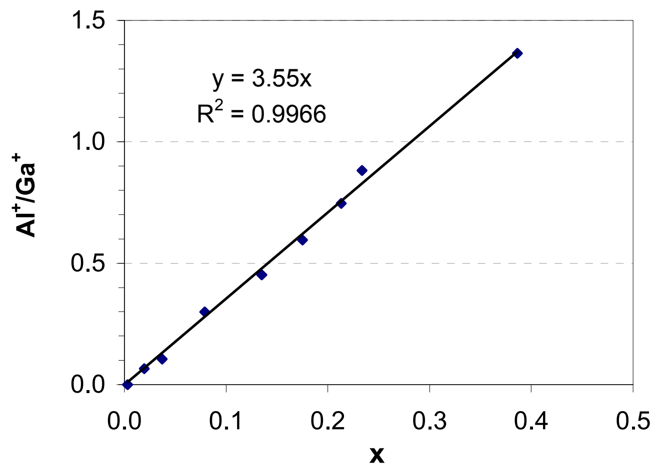


**Figure 4-4. Matrix ion intensity ratio $Al^+/Ga^+$ ratio as a function of AlN mole fraction (x) with x<0.4 ($O_2^+$ ion impact energy 5.5 keV)**

Figure 4-5 displays the matrix ion intensity ratio as a function of x over the whole range of AlN mole fractions under 5.5 keV $O_2^+$ ion bombardment. Note that the $Al^+/Ga^+$ ratio in Figure 4-5a is plotted using a log scale, while the Al/Ga in Figure 4-5b is plotted using a linear scale. The red data points were obtained from the ion implantation generated samples (SS3; section 3.3). The ion implanted samples at low AlN mole fraction (x) fit the curve well supporting the validity of this method of sample fabrication. The ion implanted samples at high AlN mole fraction x follow the same trend as that of the high AlN mole fraction samples. Note that the data from SS3 are represented in red symbols in the following figures in this section. They will not be differentiated in later chapters.

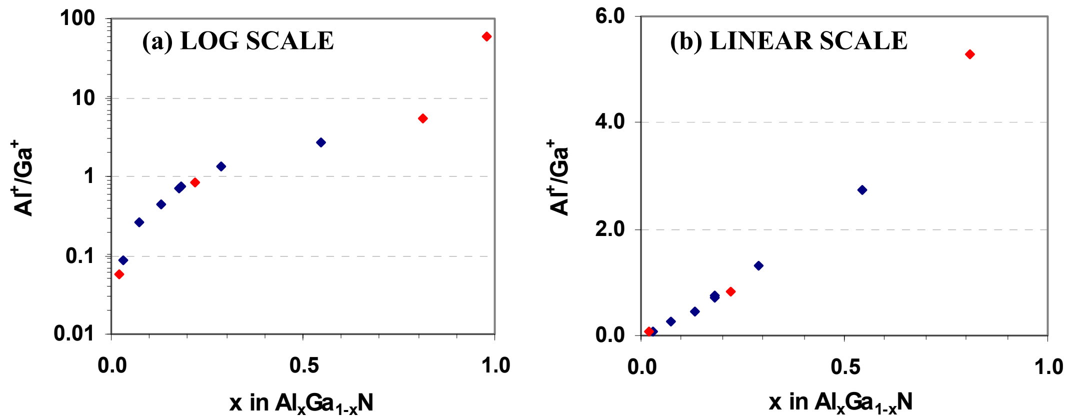


**Figure 4-5. Matrix ion intensity ratio $Al^+/Ga^+$ ratio as a function of AlN mole fraction (x) with wide range of x ($0 \leq x < 1$) with $O_2^+$ ion impact energy 5.5 keV; the left figure is in log scale, the right one is in linear scale. The red data points are data from ion implantation fabricated samples.**

As x increases to larger than 0.4, the curve of $Al^+/Ga^+$ ratio as a function of AlN mole fraction (x) does not appear linear. However, if the matrix ion intensity ratio is plotted as a function of x/(1-x) which is Al and Ga atomic concentration ratio in the materials, the curve is linear up to x=0.58, or x/(1-x)=1.38. Thus for $0 \leq x \leq 0.58$, the matrix ion intensity ratio appears linearly proportional to the atomic concentration ratio giving a slope of 2.34 for 5.5 $O_2^+$ impact energy (see figure 4-6). This indicates that the $Al^+$ yield is approximately 2.34 times higher than the $Ga^+$ yield over this range of x.

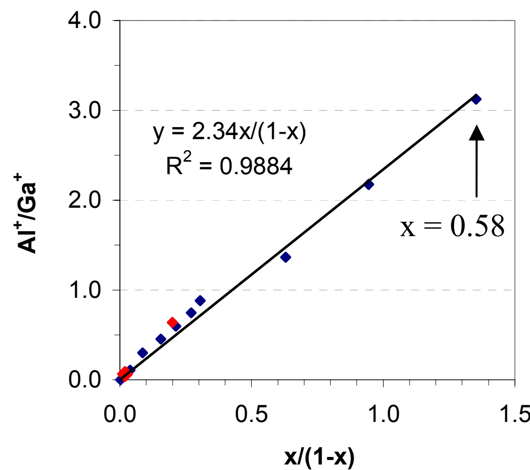


**Figure 4-6. Matrix ion intensity ratio $Al^+/Ga^+$ ratio as a function of AlN and GaN mole fraction ratio x/(1-x); The red points are data from ion implantation fabricated samples.**

The apparent linear relationship of the $Ga^+/Al^+$ ratio with the mole fraction ratio is important experimentally in the quantification of $Al_xGa_{1-x}N$. This apparent linear relationship of matrix ion intensity with mole fraction allows the use of a single standard for determination of the AlN mole fraction in an unknown sample simplifying matrix element quantification. When x is larger than 0.58, the relationship of $Al^+/Ga^+$ ion intensity ratio as a function of mole fraction ratio no longer appears linear. However, if plotted inversely, i.e. $Ga^+/Al^+$ as a function of (1-x)/x, then the relationship does appear linear for $0 \leq (1-x) \leq 0.86$, as shown in figure 4-7. Replotting the data in this fashion allows simplified quantification of high AlN mole fraction matrix species.

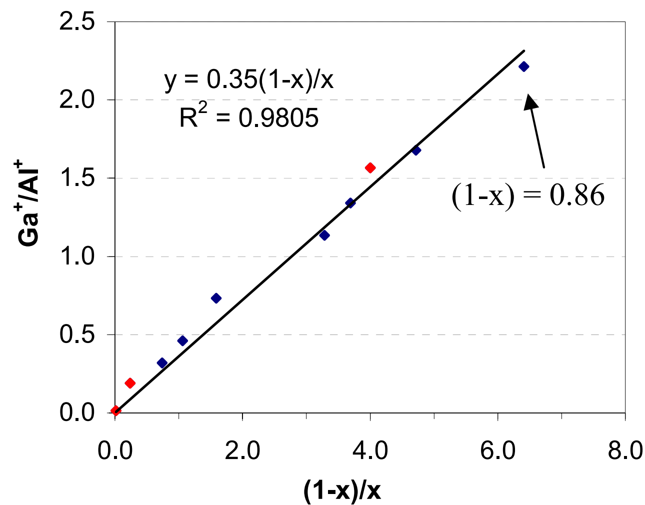


**Figure 4-7. Inverse plot of figure 4-6: Matrix ion intensity ratio $Ga^+/Al^+$ ratio as a function of GaN and AlN mole fraction ratio (1-x)/x; The red points are data from ion implantation fabricated samples.**

Figure 4-8 compares the $Al^+/Ga^+$ ion intensity ratio as a function of Al and Ga atomic concentration ratio for high (5.5 keV) and low (1.25 keV) impact energies. In both cases, the relationship appears linear up to $x \leq 0.58$ or $x/(1-x) \leq 1.38$. However the $Al^+/Ga^+$ ratio is higher with higher impact energy, which indicated that $Al^+$ ion yield is higher than $Ga^+$ ion yield at higher impact energy. The possible reason is the more efficient oxygen incorporation into the sample with high impact energy and low angle of incident with respect to sample normal.[18]

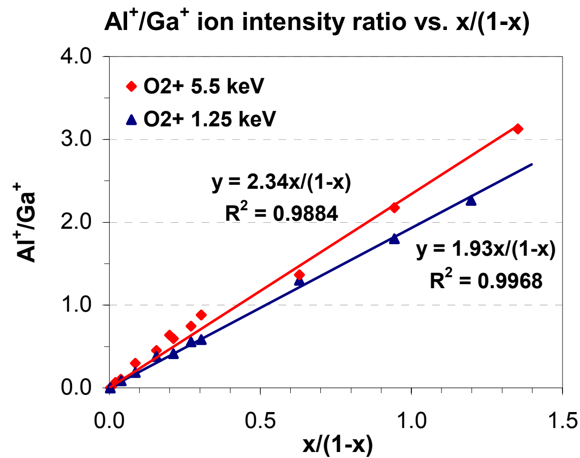


**Figure 4-8. Comparison of matrix ion intensity ratio with high and low impact energies**

### 4.4.3 Impurity RSF's

Figure 4-9 presents the relative sensitivity factors (RSF) for $Mg^+$ normalized to $Ga^+$ at high and low $O_2^+$ beam impact energy for AlN mole fraction x up to x=0.58. The $Mg^+$ RSF appears to decrease exponentially over this range. At the higher impact energy, the RSF's are lower indicating a higher $Mg^+$ secondary ion yield relative to that of $Ga^+$. The reason for the RSF change is not well understood. One possible reason is the more efficient oxygen incorporation at high energy and low angle of incident.[18] The impurity and matrix ion yields are affected differently by the more efficient oxygen incorporation. The detail mechanism on the change of impurity RSF with respect to matrix ions needs further investigation.

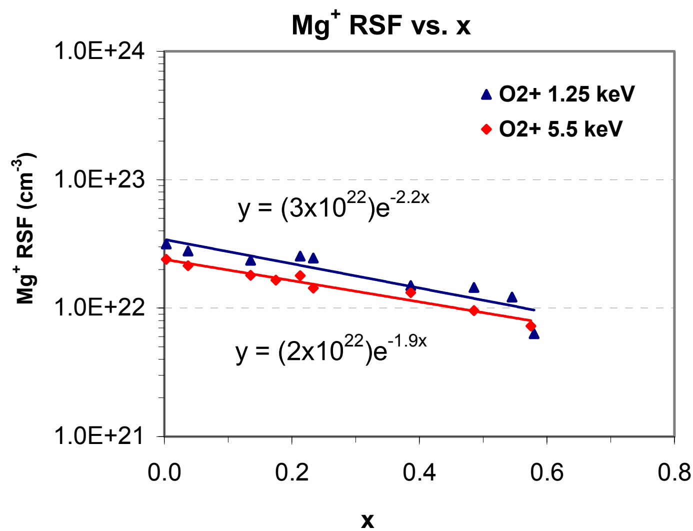


**Figure 4-9. $Mg^+$ RSF (normalized to $Ga^+$) as a function of AlN mole fraction (x) at high and low impact energies**

Figure 4-10 shows the relative sensitivity factor (RSF) of $Si^+$ normalized to $Ga^+$ at high and low $O_2^+$ primary ion beam impact energy. Similarly to the $Mg^+$ RSF's, the $Si^+$ RSF's are lower at higher impact energy, which indicate an increase of $Si^+$ ion yield relative to that of $Ga^+$ with the higher primary beam impact energy.

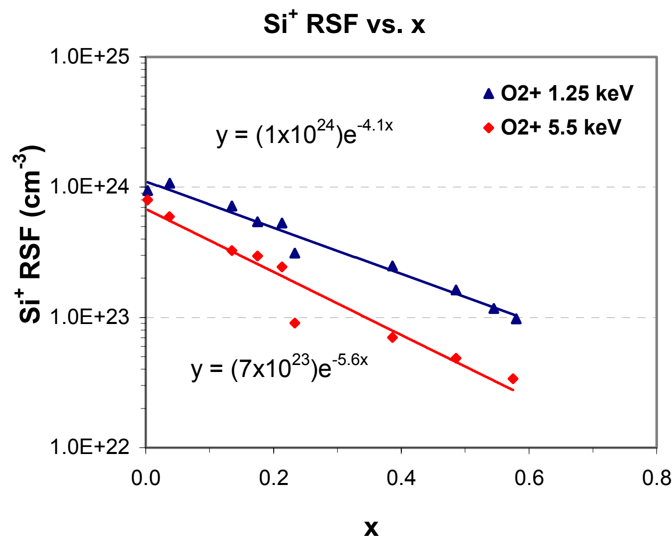


**Figure 4-10. $Si^+$ RSF (normalized to $Ga^+$) as a function of AlN mole fraction (x) at high and low impact energies**

The exponential relationship of RSF's with the AlN mole fraction is consistent with the exponential relationship of ionization probability with the surface work function. When AlN mole fraction increases, the sputter yield is reduced. The surface concentration of oxygen then increases which changes the local surface work function and increases the positive ion yields.[19]

## 4.5 Secondary Ion Emission Mechanism in $Al_xGa_{1-x}N$ under $O_2^+$ Primary Beam

### 4.5.1 Trend of the Secondary Ion Yield of Matrix and Impurity Species

It is well known that the formation of positively charged secondary ions is dramatically enhanced by the presence of oxygen at the surface of the sputtered sample. In the samples used in this study, there are three sources of oxygen. One source is the residual oxygen contamination during material growth. It has been reported that the bulk oxygen concentration in $Al_xGa_{1-x}N$ increases as Al concentration increases.[20] In MOCVD, the source of oxygen is often the $NH_3$ precursor or oxygen impurities leached from the quartz containment vessel usually employed in $N_2$ plasma sources. The typical oxygen concentration varies from $10^{16}$ to $10^{19}$ atoms/cm$^3$. A second source of oxygen in these samples is implanted oxygen. The samples were implanted with $^{16}O$ with 5E14 atoms/cm$^2$ in the low AlN mole fraction x sample set (SS1) and with 5E15 atoms/cm$^2$ in the higher AlN mole fraction x sample set (SS2). A third source of oxygen is from oxygen primary beam bombardment. The sputter yield of the sample is related to the AlN mole fraction x. As x increases, the sputter yield decreases resulting in a higher steady state surface concentration of oxygen. The sticking coefficients for oxygen also increase with x because of stronger Al-O bonding energy as compared to Ga-O bonding.

Under oxygen bombardment, the sputter rate is typically several tenths of nanometers per second in a 180x180 μm$^2$ raster area using 30nA primary ion current. For a 0.2nm/sec linear sputter rate, the volumetric sputter rate is:

$$S = \frac{0.2/1E-3}{30/180^2} = 0.216 \ \text{um}^3/(\text{nA}\cdot\text{s}) = 2.16E-13\,\text{cm}^3/(\text{nA}\cdot\text{s})$$

Suppose the primary ions are singly charged, then one ion is equal to 1.602x10$^{-19}$ Coulomb, so 1nA=6.24x10$^9$ ions/s. The atom sputter yield (Y) is:

$$Y = \frac{2.16E-13}{6.24E9} \frac{cm^3/s}{atoms/s} * 1E23 \ \ atoms/cm^3 = 3.46$$

Here 1E23 atoms/$cm^3$ is approximately the AlGaN atomic density. The steady state surface concentration of primary species (atom fraction) can be calculated as: [21]

$$[O] = \frac{1}{1+Y} = 0.22$$

The surface concentration of primary species is determined by the primary bombarding conditions, mainly the primary species, the impact energy and the angle of incidence. In Sobers' work[22] of sputtering of Si using oxygen primary ions in a CAMECA IMS-3f, the O/Si ratio at sample surface is 1.1 at 8 keV impact energy. The surface oxygen fraction is then 0.52, which is larger that that occurring in this study since the sputter yield of Si is less than that of GaN. In the case of Cs bombardment, the surface concentration of Cs is lower than that of oxygen since $Cs^+$ usually sputters faster than oxygen for similar analysis conditions. Wirtz's work[21] showed that by bombarding the Si sample surface with a $Cs^+$ primary ion in a CAMECA IMS 4-f, the surface concentration of Cs (atom fraction) is 0.12 at 5.5 keV impact energy and 42° angle of incidence.

With atomic density of 1E23 atoms/$cm^3$ in $Al_xGa_{1-x}N$, the surface atomic concentration of oxygen in this case is 2.24E22 atoms/$cm^3$, which is much higher than the oxygen contamination ($10^{16}$-$10^{19}$ $cm^{-3}$) and oxygen implantation (peak concentration is <5E20 $cm^{-3}$). It is thus concluded that the yield change of the secondary ions under $O_2^+$ bombardment is mainly caused by the sputter rate change.

As x in $Al_xGa_{1-x}N$ increases, the sputter yield decreases while the surface concentration of oxygen increases. Thus the yield of positive secondary ions should increases. First let's consider the useful ion yield of matrix ion $Ga^+$, which can be calculated from eq. (4-1) [23]

$$\tau_{Ga} = \frac{I_{Ga} t}{C_{Ga} d A_{detect}} \qquad \textbf{(Equation 4-1)}$$

where $I_{Ga}$ and $C_{Ga}$ are the secondary ion intensity (in counts/sec) of $Ga^+$ and the concentration of Ga respectively, t is the sputtering time, d is the crater depth and $A_{detect}$ is the area from which secondary ions are collected. Figure 4-11 shows the useful ion yield of

$Ga^+$ as a function of x in $Al_xGa_{1-x}N$ obtained using $O_2^+$ at 5.5keV primary ion impact energy. The useful ion yield increases with x ranging from 0 to 0.21 and from 0.23 to 0.58.

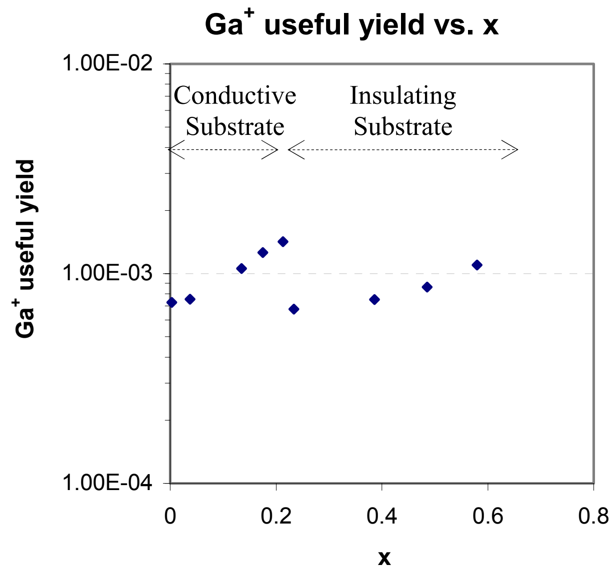


**Figure 4-11. Useful ion yield of $Ga^+$ as a function of x using $O_2^+$ bombardment and detecting positive secondary ions with impact energy 5.5 keV**

Note the discontinuity between the yield at x=0.21 and x=0.23. The data set for x≤0.21 is from samples with SiC substrate (SS1), while the data set for x>0.23 is from samples with Sapphire substrate (SS2). In this analysis performed using $O_2^+$ at 5.5 keV impact energy, the set of samples with SiC substrate did not charge while those with Sapphire substrate charged severely. It was suspected that the electron beam charge neutralization changed the energy distribution of ions and thus the ion transmission efficiency resulting in a decrease of secondary ions reaching the detector for the sample set with AlN mole fraction x>0.23. To test the hypothesis, the energy distribution of $Ga^+$ and $Al^+$ was acquired from the $Al_xGa_{1-x}N$ samples with x=0.21 and x=0.23 using the same analysis conditions. Electron beam charge neutralization was performed by aligning the electron beam adjacent to the raster area (described in Chapter 3, Section 3.5.1). Figure 4-12 shows the result of $Al^+$ and $Ga^+$ energy distribution from conductive (x=0.21) and non-conductive (x=0.23) samples. It is seen that the energy of the secondary ions was increased by the charging effect. During normal mass spectrometer tuning, the energy slit of the IMS-6f is adjusted such that the maximum number of secondary ions from a conductive sample

are transmitted to the detector. The "energy window" provided by the fully open energy slit is approximately 130 eV wide. The normal adjustment position with respect to an atomic secondary ion energy distribution is depicted as the blue shaded region in Figure 4-12. An $Al^+$ or $Ga^+$ secondary ion leaving a non-charged sample will have an energy distribution that is distributes as seen in the “$Ga^+$ and $Al^+$ no charging” sample energy spectra in Figure 4-12.. An $Al^+$ or $Ga^+$ secondary ion leaving a charged sample will have an energy distribution that is shifted partially out of the "energy window" as seen in the “$Ga^+$ and $Al^+$ with charging” sample energy spectra in Figure 4-12. The data in Figure 4-12 clearly illustrates that charges samples will have more of their secondary ion energy distribution outside the "energy window" (blue area). Thus the transmitted secondary ions from samples with charging effects have reduced intensity.

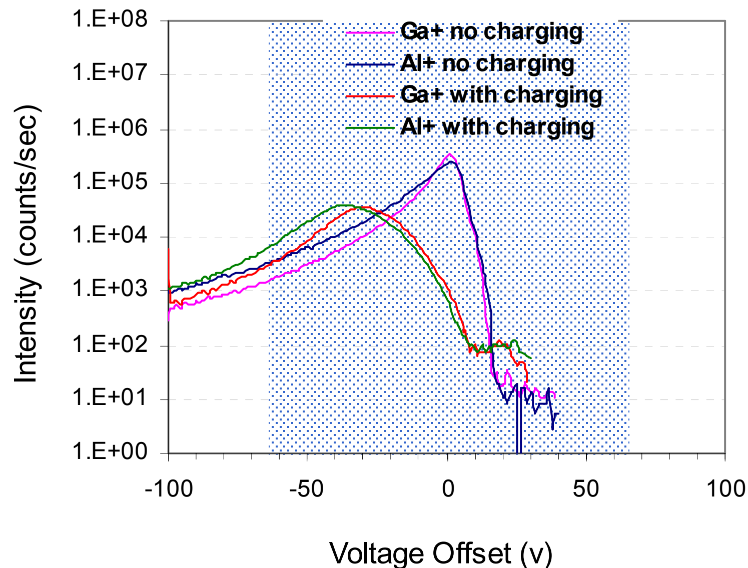


**Figure 4-12. The energy distribution of $Al^+$ and $Ga^+$ from conductive and non-conductive samples. The electron beam charge neutralization was performed by aligning electron beam adjacent to the raster area.**

Although the matrix ion intensity was constant during the depth profile, sample charging was not well compensated. While constant matrix ion intensity is often used as an indicator of good charge compensation, better criteria for determination of the quality of charge compensation is a secondary on energy distribution of secondary ions which has its peak at near zero eV.

In cases where differences in secondary ion transmission exist, but stable signals are obtained as in the example presented above and as is the case for the data presented in this study, normalization to a matrix species in the case of impurities or ratioing of matrix species to each other e.g. $Al^+/Ga^+$ can remove much of this artifact resulting from sample charging. If the ion transmission efficiency is corrected for the sample with charging effect, then the useful ion yield of $Ga^+$ would increase with the increase of AlN mole fraction. Due to the charging induced ion transmission differences in the samples used in this study, the relative ion yield of impurity species references the ion yield of $Ga^+$ will be discussed.

The relative secondary ion yield of impurity species to the yield of the matrix ion $Ga^+$ can be calculated from the RSF's which are normalized to $Ga^+$ ion intensity. In SIMS analysis, RSF is defined in eq. (4-2).

$$RSF = C_m RSF_i = \frac{I_m}{I_i} C_i \qquad \textbf{(Equation 4-2)}$$

Where $C_m$ and $I_m$ are matrix concentration and matrix ion intensity, $C_i$ and $I_i$ are impurity concentration and impurity ion intensity. In $Al_xGa_{1-x}N$, the matrix concentration ($C_{Ga}$) is not a constant, so the sensitivity factor $RSF_i$ can be used as defined in eq. (4-3)

$$RSF_i = \frac{RSF}{C_{Ga}} \qquad \textbf{(Equation 4-3)}$$

where

$$C_{Ga} = (1-x) * \frac{N_{AlGaN}}{2} \qquad \textbf{(Equation 4-4)}$$

where $N_{AlGaN}$ is the atomic density of $Al_xGa_{1-x}N$ which is approximated as 1E23 atoms/cm$^3$.

The $RSF_i$ is inversely proportional to the ion yield. The useful ion yield is defined as the total ions of species detected divided by the number of sputtered atoms from the same sampling volume. For an ion implanted standard sample, the useful ion yield can be calculated using eq. (4-5)[23]

$$\tau_i = \frac{\int I_i}{\Phi A_{detect}} \qquad \textbf{(Equation 4-5)}$$

where $\int I_i$ is the integrated number of detected secondary ions over the depth profile, Φ is implant dose in standards, and $A_{detect}$ is the ion collected area. For matrix ions which have a constant concentration, the useful ion yield can be written as

$$\tau_m = \frac{I_m t}{C_m d A_{detect}} \quad . \qquad \textbf{(Equation 4-6)}$$

where d is the crater depth, $I_m$ is the average matrix ion intensity in counts/sec, and t is total sputter time. Combining eq. (4-5) and (4-6) and considering the RSF calculation in eq. (2-22), the useful ion yield ratio of impurity and matrix can be expressed as:

$$\frac{\tau_i}{\tau_m} = \frac{\int I_i}{\Phi A_{detect}} / \frac{I_m t}{C_m d A_{detect}} = \frac{d * \int I_i}{\Phi I_m t} * C_m = \frac{C_m}{RSF} \qquad \textbf{(Equation 4-7)}$$

Combining eq. (4-1) and (4-6), we obtain

$$\frac{1}{RSF_i} = \frac{C_m}{RSF} = \frac{\tau_i}{\tau_m} \qquad \textbf{(Equation 4-8)}$$

Thus $1/RSF_i$ represents the normalized ion yield of impurity element to ion yield of matrix. Figure 4-14 is the relative $Al^+$ yield to $Ga^+$ yield as a function of x. $Al^+$ yield is always about two times higher than $Ga^+$ yield independent of the AlN mole fraction.

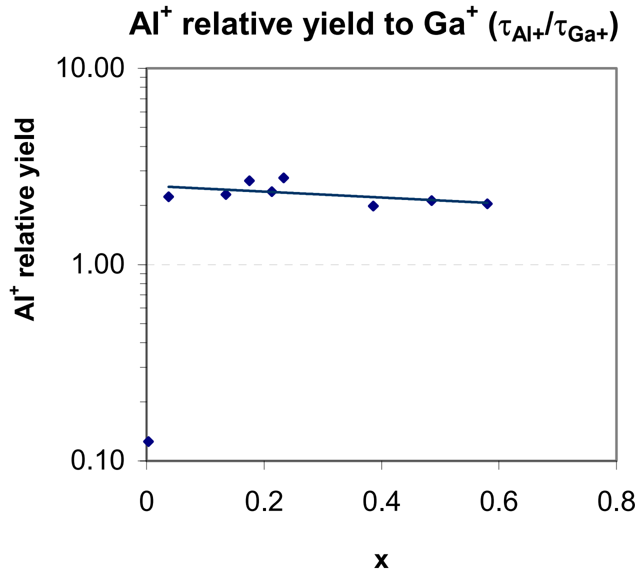


**Figure 4-13. Relative ion yield of $Al^+$ ($1/RSF_{Al}$) to that of $Ga^+$ as a function of x in $Al_xGa_{1-x}N$ under $O_2^+$ primary beam with 5.5 keV impact energy**

Figure 4-15 shows the relative ion yield of $Si^+$ and $Mg^+$ to that of $Ga^+$. The relative yield of $Si^+$ increases exponentially with AlN mole fraction x, but the relative yield of $Mg^+$ increases only slightly with x. Despite the lower yield of $Si^+$ due to the higher ionization potential of Si as compared with that of Al, Ga and Mg, $Si^+$ is most strongly affected by the surface concentration of oxygen.

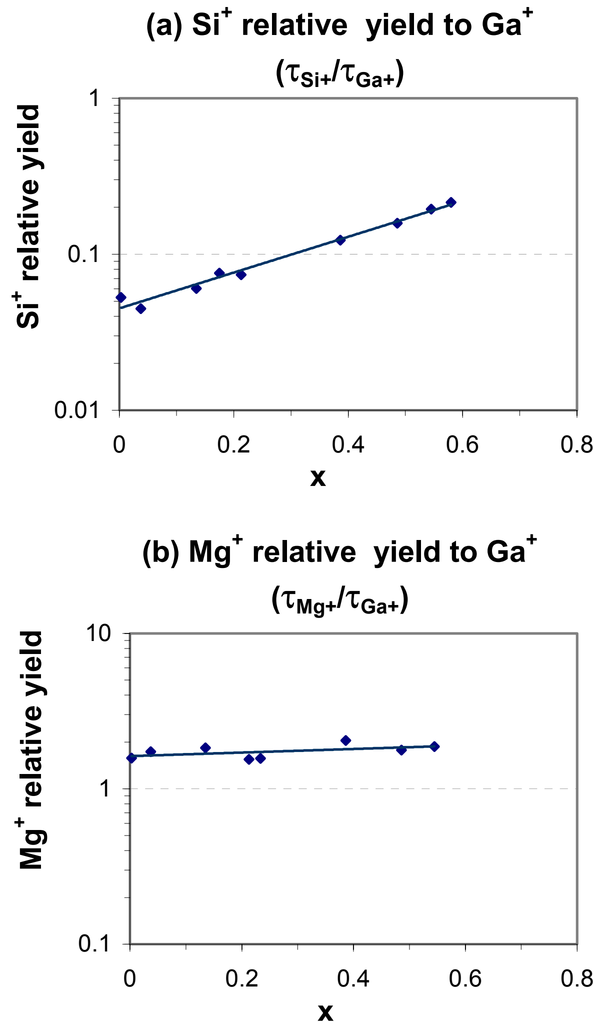


**Figure 4-14 Relative ion yield of $Si^+$ and $Mg^+$ to that of $Ga^+$ as a function of x in $Al_xGa_{1-x}N$ under $O_2^+$ primary beam with 5.5 keV impact energy**

In summary, the useful ion yield of $Ga^+$, $Al^+$, $Si^+$ and $Mg^+$ in $Al_xGa_{1-x}N$ increases with x in the range of $0 \leq x \leq 0.58$ due to the sputter yield reduction which leads to the increase of surface oxygen concentration. $Al^+$ yield is always about two times higher than $Ga^+$ yield. The relative yield of $Si^+$ increases exponentially with x and that of $Mg^+$ increases only

slightly with x. Although the ion yield of $Si^+$ is low due to silicon's high ionization potential, it is significantly more responsive to the surface oxygen concentration than that of $Mg^+$. It is interesting that the $Si^+$ and $Al^+$ yield with surface oxygen concentration in AlGaN has a trend similar to these elements ion yields in Si with O/Si flux ratio.[13] In silicon, $Al^+$ yield was always high regardless of bulk oxygen concentration, while the $Si^+$ yield is more responsive to the oxygen concentration change. This earlier study[13] explained the phenomena using a local oxidation model.

### 4.5.2 Secondary Ion Emission Mechanism in $Al_xGa_{1-x}N$ under $O_2^+$ Primary Beam

The data shown above can be explained by a local bond-breaking model (see review in section 2.2.1). In the local bond-breaking model, the ion yield is only affected by its nearest neighbor conditions (microscopic) unlike in ion yield effects that would be present in phenomenological models. When x in $Al_xGa_{1-x}N$ increases, the reduction in sputter yield causes an increase in surface oxygen concentration. The oxygen atoms form bonds with the atoms in the sample surface which often have a partial ionic character. The ionic character of the metal-oxygen bonds promotes direct emission of ions.[12,24,25] The increase of the surface oxygen concentration increases the formation of these ionic bonds thus increasing positive ion yields.

However, oxidation of the atoms in the sample resulting from oxygen primary ion beam bombardment is not uniform. In this experiment, it was found that the secondary ion yield of $Si^+$ is strongly enhanced by [O] while the secondary ion yields of $Al^+$, $Ga^+$ and $Mg^+$ are less responsive to [O]. One possible explanation for the phenomena is the strong Si-O bond. The bond enthalpies (KJ/mol) with O in gaseous diatomic species for Al, Ga, Si, Mg are listed in table 4-2.[26] Among the four elements studied, Si has the strongest bond enthalpy with O. It is speculated that Si always adsorbs more oxygen and can form local bonds of $SiO_x$ with x=0-4. If $SiO_4$ were formed, the Si would be in a more ionic environment resulting in the enhancement of the positive ion yield of $Si^+$.

**Table 4-2. Bond enthalpies in gaseous diatomic species [26]**

| Bond | Bond Enthalpies (KJ/mol) | Uncertainties (KJ/mol) |
|---|---|---|
| Si-O | 799.6 | ±13.4 |
| Al-O | 511 | ±3 |
| Mg-O | 363.2 | ±12.6 |
| Ga-O | 353.5 | ±41.8 |

## 4.6 Summary

The most common dopants in $Al_xGa_{1-x}N$ (Si and Mg) and the matrix elements (Al and Ga) can be quantitatively analyzed simultaneously with high detectability using $O_2^+$ beam with positive secondary ion detection due to the positive ion yield enhancement of oxygen. Using dynamic SIMS, depth profiling of matrix and impurity species in $Al_xGa_{1-x}N$ was performed; the sputter rate, matrix ion intensity ratio, impurity RSF and ion yield variation as a function of AlN mole fraction were studied.

Under the same sputtering conditions, sputter yield decreases as AlN mole fraction (x) in $Al_xGa_{1-x}N$ increases showing a trend that is similar to that previously observed for $Al_xGa_{1-x}As$. The matrix ion intensity ratio $Al^+/Ga^+$ appears to increase linearly with AlN mole fraction (x) up to x=0.4. As x increases further, the relationship between $Al^+/Ga^+$ and x no longer appears linear. However the ion intensity ratio as a function of Al and Ga atomic concentration ratio (x/(1-x)) is linear in the range of $0\leq x\leq 0.58$. By plotting this data inversely, i.e., $Ga^+/Al^+$ as a function of Ga and Al atomic concentration ratio, the data appears linear over the range of GaN mole fraction of $0<(1-x)<0.86$. This result indicates that, for a wide range of AlN mole fraction in $Al_xGa_{1-x}N$, the ion intensity ratio of Al and Ga is proportional to their atomic concentration ratio. The relative sensitivity factors (RSF) of $Si^+$ and $Mg^+$ with respect to $Ga^+$ seem to decrease exponentially with x in the range of $0\leq x\leq 0.58$. This is consistent with the exponential relationship of ion yield with the surface work function.

The yields of $Ga^+$, $Al^+$, $Mg^+$ and $Si^+$ all increase as AlN mole fraction increases due to the increase of surface oxygen concentration. The ion yield of $Al^+$ is always about twice that

of $Ga^+$. $Si^+$ relative yield to $Ga^+$ increases 5 times when x changes from 0 to 0.58, while $Mg^+$ relative yield to $Ga^+$ only increases slightly.

The secondary ion yield emission mechanism for positive secondary ions can be explained using a local bond breaking model. The incorporation of oxygen atoms forms M-O bonds where M is the element on the sample surface. These bonds often have a partial ionic character which promotes direct emission of ions. When AlN mole fraction x is increased, the reduction in the sputter yield causes an increase in the surface oxygen concentration resulting in an increase of positive ion yields. $Si^+$ yields are more strongly enhanced by the surface oxygen concentration possibly due to the strong Si-O bond.

The electron beam charge neutralization was performed by aligning the electron beam adjacent to the ion raster area. In this technique, sample charging was not well compensated, as evidenced by the useful ion yield differences between uncharged and charged sample sets. In order to avoid this problem, the secondary ion energy distributions must be measured to insure that charge compensation is complete.

## 4.7 References


[1] D. P. Griffis, R. Loesing, D. A. Ricks, M. D. Bremser, and R. F. Davis, Secondary Ion Mass Spectrometry SIMS XI, edited by G. Gillen, R. Lareau, J. Bennett and F. Stevie, John Wiley & Sons**,** 201-204 (1997).

[2] D. L. Lefforge, Y. L. Chang, M. Ludowise, and E. L. Allen, Mat. Res. Soc. Symp. Proc. **510,** 155-161 (1998).

[3] J. C. Carrano, T. Li, D. L. Brown, P. A. Grudowski, C. J. Eiting, R. D. Dupuis, and J. C. Campbell, Electronics Letters **34,** 1779-1781 (1998).

[4] J. C. Carrano, T. Li, P. A. Grudowski, C. J. Eiting, D. Lambert, J. D. Schaub, R. D. Dupuis, and J. C. Campbell, Electronics Letters **34,** 692-694 (1998).

[5] M. Razeghi and A. Rogalski, Journal of Applied Physics **79,** 7433-7473 (1996).

[6] G. Slodzian and J. F. Hennequin, Compt. Rend. Acad. Sci. B **263,** 1246 (1966).

[7] P. Williams and J. C.A Evans, Surface Science **78,** 324 (1978).

[8] C. A. Anderson, Int. J. Mass Spectrom. Ion Phys. **3,** 413 (1970).

[9] G. Blaise and G. Slodzian, Surface Science **40,** 708 (1973).

[10] E. Bauer and H. Poppa, Surface Science **88,** 31 (1979).

[11] R. Pantel, M. Bujor, and J. Bardolle, Surface Science **62,** 589 (1977).

[12] P. Williams, Surface Science **90,** 588-634 (1979).

[13] K. Franzreb, J. Lorincik, and P. Williams, Surface Science **573,** 291-309 (2004).

[14] M. L. Yu and N. D. Lang, Nucl. Instrum. Methods Phys. Res. Sect. **B14,** 403 (1986).

[15] R. Kelly and C. B. Kerkdijk, Surface Science **46,** 537 (1974).

[16] M. Schumacher, CAMECA Instruments, computer program.

[17] A. L. Pivovarov, F. A. Stevie, and D. P. Griffis, Applied Surface Science **231-2,** 786-790 (2004).

[18] N. Menzel and K. Wittmaack, Materials Science and Engineering B **12,** 91-95 (1992).

[19] V. R. Deline, C. A. Evans, and P. Williams, Applied Physics Letters **33,** 578-580 (1978).

[20] S. P. Grabowski, M.Schneider, H. Nienhause, and W. Monch, Applied Physics Letters **78,** 2503-2505 (2001).

[21] T. Wirtz, B. Duez, H. N. Migeon, and H. Scherrer, International Journal of Mass Spectrometry **209,** 57-67 (2001).

[22] R. C. Sobers, K. Franzreb, and P. Williams, Applied Surface Science **231-2,** 729-733 (2004).

[23] R. G. Wilson, F. A. Stevie, and C. W. Magee, *Secondary Ion Mass Spectrometry : a Practical Handbook for Depth Profiling and Bulk Iimpurity Analysis* (1989).

[24] M. L. Yu, Nuclear Instruments and Methods in Physics Research B **18,** 542-548 (1987).

[25] J. L. Alay and W. Vandervorst, Physical Review B **50,** 15015-15025 (1994).

[26] *CRC handbook of chemistry and physics*, 83th ed. (Chemical Rubber Company Press, Cleveland, Ohio, 2004-2005).

# 5 Quantification of Matrix and Impurity Species in $Al_xGa_{1-x}N$ under $Cs^+$ Bombardment with Negative Ion Detection

## 5.1 Introduction

For electronegative impurities such as O and Si in $Al_xGa_{1-x}N$, SIMS analysis using $Cs^+$ primary ion bombardment with negative secondary ions detection is required because the presence of Cs on the ion bombardment solid surface can promote the emission of negative secondary ions.

In earlier studies of $Al_xGa_{1-x}N$ using $Cs^+$ primary beam with negative secondary ion detection, the work by Griffis et al.[1] showed a linear relationship between $Al^-$ and $Ga^-$ ion intensity ratio and AlN mole fraction in the range of $0<x<0.2$. $C^-$, $O^-$, $Si^-$ were monitored and their RSF's with respect to $Ga^-$ were plotted as a function of AlN mole fraction. The trend of the RSF's in the range of $x<0.05$ is not clear; while in the range of $0.05<x<0.21$, RSF's of $C^-$ do not change, those of $O^-$ increase and $Si^-$ decrease. Work by Lefforge et al.[2] showed exponentially decreasing of $O^-$ and $Si^-$ RSF's with respect to $GaN^-$ or $Ga^-$ with $x<0.31$. Chu[3] suggested that the calibration with respect to the matrix ion $MN^-$ (where M is Ga or Al in AlGaN) is preferable to the use of $M^-$ because the $M^-$ ion intensity is more sensitive to the instrumental tuning conditions and produces a wider spread in the RSF's.

As discussed in the previous chapter, the quantification in high Al content AlGaN has become important. In this chapter, Cs incorporation and its secondary ion yield enhancement mechanism will be described. The experimental method using $Cs^+$ with negative secondary ion detection and results in AlGaN quantification in the range of $0\leq x\leq 1$ will be discussed. Based on the results, the ionization mechanism in $Al_xGa_{1-x}N$ under $Cs^+$ primary beam with negative secondary ion detection will be rationalized.

## 5.2 Cs Incorporation and Negative Secondary Ion Yield Enhancement

It is well known that the presence of cesium (Cs) and other electropositive atoms of ion bombarded solid surfaces can promote the emission of negative atomic ions in secondary ion mass spectrometry by several orders of magnitude.[4] This finding is widely utilized in

SIMS for sensitive detection of electronegative elements by the use of Cs primary ions and by monitoring negative secondary ions. In contrast to the controversy with regard to the effect of oxygen on positive secondary ion yields, the effect of Cs on the negative secondary ionization process seems to be intuitively correct i.e. the Cs on a surface lowers the surface work function, enhances negative ion yield and suppresses positive ion yield.[5-7] The reduction of surface work function results from an electric dipole layer generated by the presence of $Cs^+$ on the surface. It has been shown in many cases that ionization probability $P^-$ increases exponentially with the lowering of the surface work function $\phi$.[8] In the first approximation, the relationship between $P^-$ and $\phi$ is shown in eq. (5-1) for a large range of $\phi$.[9]

$$P^- \propto \exp[(A - \phi)/\varepsilon_0] \qquad \textbf{(Equation 5-1)}$$

Here A is the electron affinity of the sputtered atom outside the surface, $\phi$ is the surface work function, and $\varepsilon_0$ is a parameter anticipated to vary with the normal component of the emission velocity of the sputtered atom ($v_\perp$). There have been debates on the velocity dependence of ion yields. Yu[10] found that for $O^-$ in both V and Nb surfaces, the ion yield is directly proportional to the normal component of the emission velocity for $V_\perp$>1E6 cm/s (or $V_\perp$>8.3 eV). At lower velocities, which include the majority of the $O^-$ ions, $P^-$ is relatively independent of velocity.

The validity of work function dependence in eq. (5-1) has been verified in several static alkali-metal adsorption experiments[11, 12] and a dynamic $Cs^+$ bombardment experiment.[7] In static alkali-metal adsorption experiments, Li or Cs thin layers were deposited on a metal surface to alter the surface work function. Secondary ion yields were then monitored as a function of alkali coverage and work function.[11, 12] In the dynamic experiment, a focused 14.5 keV $Cs^+$ ion beam bombarded sample surface with varying area, and the negative ion intensity was monitored as a function of $Cs^+$ fluence and work function variation.[7] In both cases, the sputtered negative ion yields scale exponentially with the work function change.

## 5.3 Experimental Method

The same sets of samples were used as previously discussed (section 4.3). Set one (SS1) consists of $Al_xGa_{1-x}N$ films grown on SiC substrate with $0 \leq x \leq 0.21$. Set two (SS2)

consists of $Al_xGa_{1-x}N$ films grown on sapphire substrate with 0.23≤x≤0.58. These films were implanted with $^{16}O$, $^{24}Mg$ and $^{29}Si$ with energy and dose listed in table 3-1. Set three (SS3) was produced using high dose ion implantation of Ga into AlN to obtain high Al content at the ion implant peak position (x=0.81, 0.98). All the samples were sputter coated with ~10 nanometers of Au.

Analyses were performed using a $Cs^+$ primary ion beam extracted from the Cs microbeam source of the CAMECA IMS-6F. A focused 30nA $Cs^+$ primary ion beam having 14.5 keV impact energy and 20nA $Cs^+$ primary ion beam having 6.0 keV impact energy were rastered over a 180x180 $\mu m^2$ area in the analyses. Table 5-1 lists the analysis conditions. Angles of incidence was calculated using a program written by Schumacher[13] which includes the IMS-6F primary ion column deflector voltages used for positioning the beam onto the primary column optical axis of the IMS-6f mass spectrometer.

**Table 5-1 Analysis conditions using $Cs^+$ primary ion with negative secondary ions detection**

| Primary Ion Species | Primary Ion Acceleration Voltage (kV) | Sample Potential (kV) | Impact Energy (keV) | Angle of Incidence (degree) | Ion Current (nA) | Raster Size ($um^2$) | Beam Density ($\mu A/um^2$) |
|---|---|---|---|---|---|---|---|
| $Cs^+$ | 10 | -4.5 | 14.5 | 24.8 | 30 | 180x180 | 0.926 |
| $Cs^+$ | 5 | -1.0 | 6.0 | 27.3 | 20 | 180x180 | 0.617 |

Secondary ions were collected from a 60µm diameter optically gated area (750µm field aperture, 150µm image field, 400µm contrast aperture). The collection area is centered on the rastered area. Entrance slits and exit slits were adjusted to obtain a mass resolution of 1320 m/Δm to separate mass $^{27}AlH_2$ and $^{29}Si$. Depth of sputtered craters was measured using a KLA-Tencor P-20 profilometer.

Electron beam charge neutralization was implemented using the Normal Incidence Electron Gun (NEG) provided with the CAMECA IMS-6F. For negative secondary ion detection, the NEG accelerating voltage was chosen to match the sample potential so that electrons were attracted to the sample only if the sample charged. The NEG was adjusted using the procedure described previously (section 3.5.2).[14]

Depth profiles were acquired until the matrix secondary ion counts reached a steady state and the implanted impurity ion counts dropped to the background level. Matrix ions

monitored were $AlN^-$ and $GaN^-$, and impurity ions monitored were $Si^-$, $O^-$ and $GaN^-$. $Ga^-$ and $ON^-$ were also monitored; however, their yields are about two orders of magnitude less than corresponding $GaN^-$ and $O^-$ ions. The species having the highest ion yields were chosen for the analyses. $^{29}Si^{14}N$ was not used in these analyses since this secondary ion has a strong mass interference from $^{27}Al^{16}O$. Mass separation of these two secondary ions requires a mass resolution of $m/\Delta m$=14,000. $AlN^-/GaN^-$ ion intensity ratios, the RSF's of $Si^-$ , $MgN^-$ and $O^-$ normalized to $GaN^-$, and sputter rates normalized to primary beam density were calculated after depth profiles were obtained for the all of the sample sets. The trends of these parameters with respect to AlN mole fraction were studied.

In order to minimize the effect on oxygen measurements of any residual gas in the IMS-6f analysis chamber, the analysis chamber pressure was reduced to less than 2E-10 Torr prior to any analysis by using a Ti sublimator pump and an $LN_2$ cold trap.

## 5.4 Results and Discussion

### 5.4.1 Sputter Rate

Sputter rates were normalized to primary ion beam density and plotted as a function of AlN mole fraction (x). Figure 5-1 shows sputter rates of $Al_xGa_{1-x}N$ obtained using 14.5 keV and 6.0 keV $Cs^+$ impact energy. The two curves show a similar relationship of sputter rate to AlN mole fraction (x) in the range of $0 \leq x \leq 0.58$. The sputter rate decreases with increasing AlN mole fraction x, but the rate of decrease in the sputter rate versus x declines as the AlN mole fraction increases.

It can be seen that the sputter rate at 14.5 keV is higher. Although the angle of incidence at 14.5 keV (24.8° from normal) is a little lower than that at 6.0 keV (27.3° from normal) which results in the decrease of sputter yield, the higher energy dominates in this case and the sputter yield at 14.5 keV is higher.

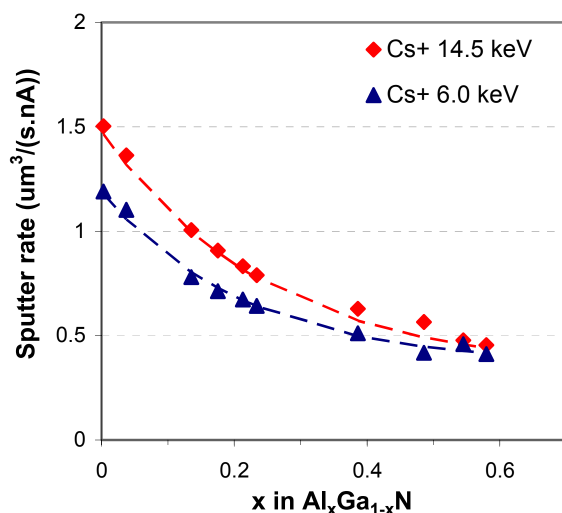


**Figure 5-1. Comparison of sputter rate of $Al_xGa_{1-x}N$ under $Cs^+$ bombardment with negative ion extraction at high and low impact energies.**

### 5.4.2 Matrix Ion Intensity Ratio

Figure 5-2 displays the matrix ion intensity ratio of $AlN^-/GaN^-$ as a function of x for high (14.5 keV) and low (6.0 keV) primary ion impact energies. Although the data for 6.0 keV impact energy is more scattered , the relationship of the $AlN^-/GaN^-$ ratio with AlN mole fraction x for both primary ion impact energies suggests a linear increase for $0 \leq x \leq 0.58$. The slopes of both primary ion impact energies are similar.

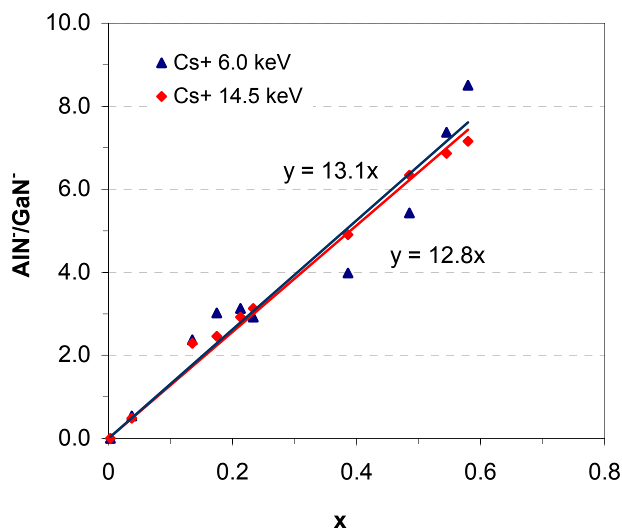


**Figure 5-2. Matrix ion intensity ratio $AlN^-/GaN^-$ as a function of AlN mole fraction (x) with $x \leq 0.58$ at impact energy of 6.0 keV and 14.5 keV**

When x is larger than 0.58, the relationship no longer appears linear. However if plotted inversely, i.e. $GaN^-/AlN^-$ as a function of GaN mole fraction (1-x), then the relationship appears linear for 0≤(1-x)≤0.61, as shown in figure 5-3. The overlap of the apparently linear ranges of x in the in Figures 5-2 and 5-3 provides the information necessary to quantify the matrix elements Al and Ga in $Al_xGa_{1-x}N$ over the entire range of AlN mole fractions from 0≤x≤1.

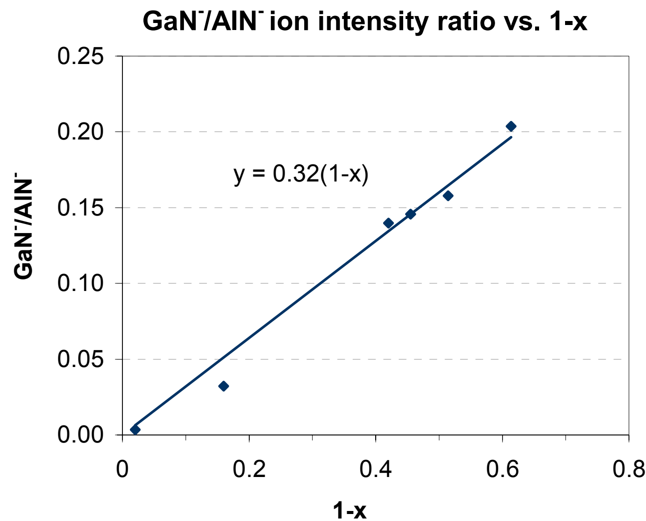


**Figure 5-3. Inverse plot of figure 5-3: Matrix ion intensity ratio $GaN^-/AlN^-$ ratio as a function of GaN mole fraction (1-x) in $Al_xGa_{1-x}N$ at 14.5 keV impact energy**

### 5.4.3 Impurity RSF's

Figure 5-4 shows the relative sensitivity factors (RSF's) of $MgN^-$ normalized to $GaN^-$ for the high and low $Cs^+$ primary ion beam impact energies used in this study. The $MgN^-$ RSF decreases exponentially with x in the range of x≤0.58. While the slopes of the two RSF data sets is almost identical, the RSF's at higher impact energy are higher than those at lower impact energy indicating somewhat decreased sensitivity for Mg using the higher primary ion beam impact energy.

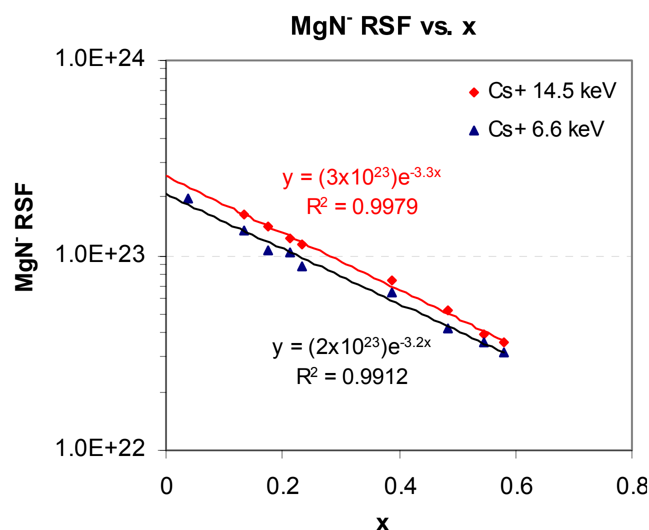


**Figure 5-4. $MgN^-$ RSF (normalized to $GaN^-$) as a function of AlN mole fraction (x) at high and low impact energies**

Figure 5-5 shows the relative sensitivity factors (RSF's) for $Si^-$ normalized to $GaN^-$ at the high and low $Cs^+$ beam impact energies used in this study. The $Si^-$ RSF seems to decrease exponentially with x, although the data is more scattered than that of the $MgN^-$ RSF's due to the variations of the relative ion intensities of the atomic impurity ion ($Si^-$) with respect to the molecular matrix ion ($GaN^-$) resulting from differences in the extraction efficiency of molecular versus atomic ions at different positions on the IMS-6f sample holder (see section 7.3.3). Both the slopes and magnitudes of the RSF's of $Si^-$ obtained at the higher and lower primary ion impact energies are similar.

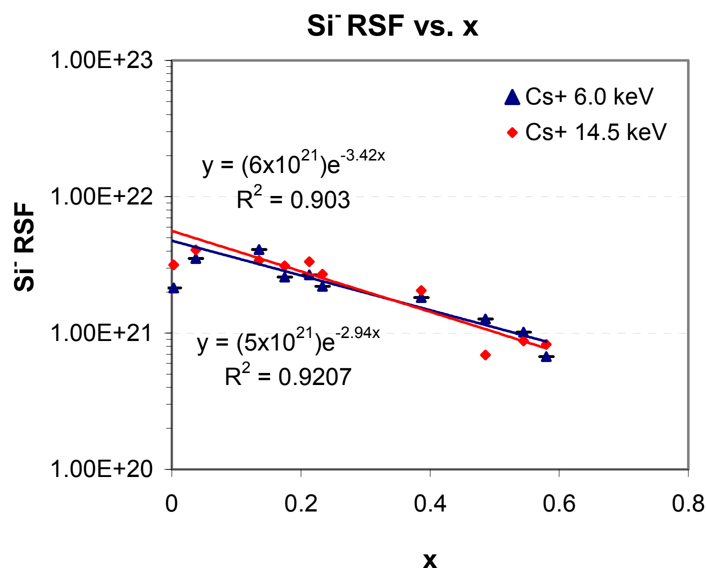


**Figure 5-5. $Si^-$ RSF (normalized to $GaN^-$) as a function of AlN mole fraction (x) at high and low impact energy**

Similar to the discussion of quantification using $O_2^+$ primary ion with positive secondary ion detection in the previous chapter, the exponential relationship of RSF's with the AlN mole fraction is consistent with the exponential relationship of ionization probability with the surface work function. Under the bombardment of $Cs^+$, the steady state surface concentration of Cs atoms is affected by the sputter yield of the samples. When AlN mole fraction is increased, the sputter yield is decreased. The surface concentration of Cs then increases which reduces the local surface work function and increases negative ion yields.[15] Since the yield enhancement effect may not be the same for impurity and matrix ions, the resulting variations of ion yield may result in a change of the RSF's of the impurity species normalized to a matrix ion. When a Ga-containing ion is used as the matrix ion ($GaN^-$ in this case), the reduction of Ga concentration in $Al_xGa_{1-x}N$ causes the reduction of the RSF's as x is increased.

With regard to $O^-$ secondary ion generation, both the surface oxygen contamination and bulk contamination for the samples in this study are high resulting in significant variations in the RSF data obtained. The RSF's $O^-$ RSF's generated by normalizing $O^-$ secondary ion intensity to $GaN^-$ do not show a downward trend with the increase of AlN

mole fraction (figure 5-6) as seen for $Si^-$. In contrast, it can be seen that the RSF's do not change dramatically from AlN mole fraction x=0 to x=0.58.

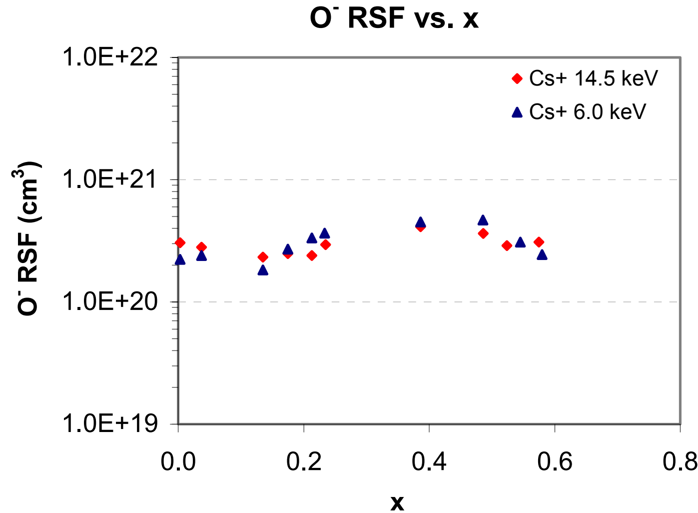


**Figure 5-6. $O^-$ RSF (normalized to $GaN^-$) as a function of AlN mole fraction (x) in $Al_xGa_{1-x}N$ at 14.5 keV and 6.0 keV impact energies**

## 5.5 Secondary Ion Emission Mechanism in $Al_xGa_{1-x}N$ under $Cs^+$ Primary Beam

### 5.5.1 Trend of the Secondary Ion Yield of Matrix and Impurity Species

It is well known that the presence of Cs enhances the negative ion yield. In this study, the source of the Cs is the primary ion bombardment. From calculations of the steady state surface concentration of Cs, the surface Cs concentration under the conditions used in this work (Section 5.3) is on the order of 1E21 to 1E22 atoms/$cm^3$.

The useful ion yields of $GaN^-$, $AlN^-$, $Si^-$ and $MgN^-$ were computed as a function of AlN mole fraction in $Al_xGa_{1-x}N$. Figure 5-7 shows the useful ion yields at 14.5 keV and 6.0 keV Cs primary ion impact energies. The useful ion yields increase as AlN mole fraction is increased, and the slopes of the increase are similar for the four secondary ion species.

The trends of the plotted useful ion yield data versus AlN mole fraction x in $Al_xGa_{1-x}N$ appear to be inverse to the trends obtained for sputter rate versus AlN mole fraction x (See figure 5-1 above). At lower x, the sputter yields decrease rapidly while secondary ion yields increase rapidly as a function of AlN mole fraction x. As x becomes higher, the rate of

decrease for sputter yields declines while the rate of increase for secondary ion yields also declines. These facts lend support to the theory that negative secondary ion yields are directly related to sputter yield i.e. that increased Cs surface concentrations resulting from reduced sputter rates result in increased negative secondary ion yields.

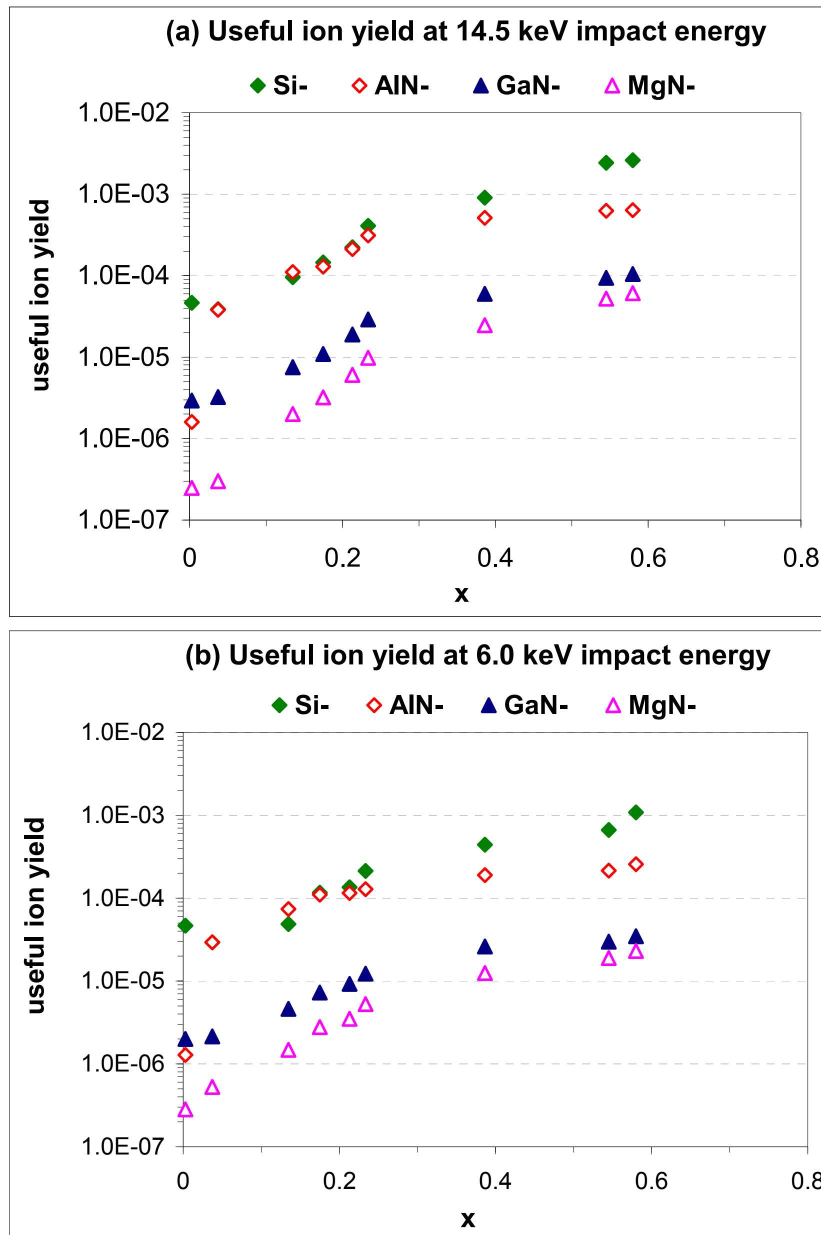


**Figure 5-7. Useful ion yield of negative ions in $Al_xGa_{1-x}N$ under $Cs^+$ primary ion bombardment. (a) at high impact energy (14.5 keV); (b) at lower impact energy (6.0 keV)**

### 5.5.2 Negative Secondary Ion Emission Mechanism in $Al_xGa_{1-x}N$ under $Cs^+$ Primary Ion Beam Bombardment

As can be seen in eq. (5-1), the negative ion ionization probability is exponentially related to the electron affinity of the sputtered atoms A and the surface work function $\phi$.[9]

$$P^- \propto \exp[(A - \phi)/\varepsilon_0] \qquad \text{(Recall of eq. 5-1)}$$

Here $\varepsilon_0$ is is a parameter anticipated to vary with the normal component of the emission velocity of the sputtered atom ($v_\perp$)(see Reference 9). The electron affinity of an element is the energy released when a neutral atom in the gas phase gains an electron to form a negatively charged ion. The electron affinity of molecular species $MN^-$ can be calculated using eq. (5-2), where $A_M$ and $A_N$ are the electron affinity values of element M and N.[16]

$$A_{MN} = \mathrm{Ln}[\mathrm{Exp}(A_M) + \mathrm{Exp}(A_N)] \qquad \textbf{(Equation 5-2)}$$

The electron affinities of the monitored species are listed in table 5-2. The trend in the relative magnitudes of the secondary ion yields of the monitored species is in agreement with the trend in their electron affinities. Si has the highest electron affinity and the highest negative secondary ion yield while MgN has the lowest electron affinity and the lowest negative secondary ion yield.

**Table 5-2. Electron affinity of Si, AlN, GaN, and MgN (data are from reference 17)**

| Elements/Molecules | Electron Affinity (KJ/mol) |
|---|---|
| Si | 133.6 |
| AlN | 42.5 |
| GaN | 28.9 |
| MgN | 7.0 |

For semiconductors, the work function in the relationship of eq. (5-1) is defined as the energy needed to move an electron in the solid atom from the Fermi level to vacuum level. A schematic of the energy band structure of a semiconductor is shown in figure 5-8. The work function is the sum of electron affinity of the surface $\chi$ and energy difference of conduction band minimum and Fermi energy ($E_c$-$E_F$), as shown in eq. 5-3.

$$\phi = \chi + (E_c - E_F) \qquad \textbf{(Equation 5-3)}$$

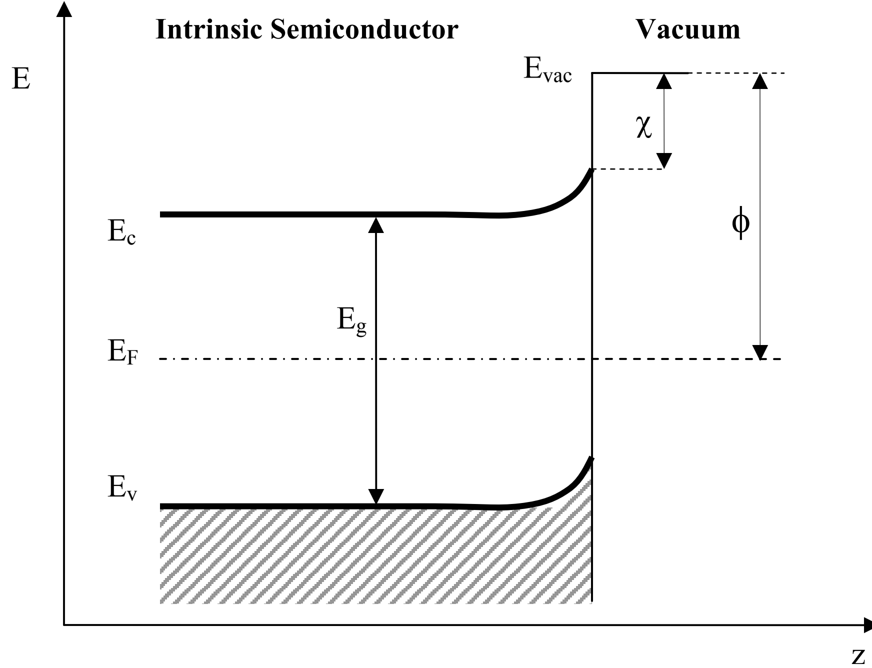


**Figure 5-8. Schematic drawing of the energy band gap of semiconductor showing the conduction band minimum ($E_c$), valence band maximum ($E_v$), the vacuum level $E_{vac}$, the Fermi energy $E_F$, the electron affinity $\chi$ and the work function $\phi$.**

In an intrinsic semiconductor, $E_F$ can be assumed to be in the center of the energy band gap if one ignores the different effective masses of an electron and a hole. Thus,

$$\phi = \chi + \frac{E_g}{2} \qquad \textbf{(Equation 5-4)}$$

For $Al_xGa_{1-x}N$, the electron affinity decreases linearly with x from 3.1±0.2 eV in GaN to 0.25±0.3 eV in AlN,[18] while the energy band gap increases with x from 3.4 eV in GaN to 6.2 eV in AlN.[19] Thus the work function in $Al_xGa_{1-x}N$ is from 4.8±0.2 eV in GaN to 3.35±0.3 eV in AlN. For a clean intrinsic $Al_xGa_{1-x}N$ surface, the work function decreases as AlN mole fraction (x) is increased.

When the Cs atoms are adsorbed on the surface, surface dipoles are formed. Cs is much more electropositive than Al, Ga or N, so the Cs-induced surface dipoles are oriented such that the bond charge is displaced from the Cs in the surface toward the electronegative substrate atoms. As a result, the surface barrier for electrons is lowered.

Figure 5-9 shows the work function change of n-type and p-type GaN as a function of Cs evaporation time to the GaN surface.[20] The work function of cesiated GaN surface first decreases, then passes through a minimum, and eventually reaches a value of 2.1 eV which is the work function of metallic Cs samples. The minimum work function is reached when the first continuous layer of covalently bonded Cs atoms is completed.

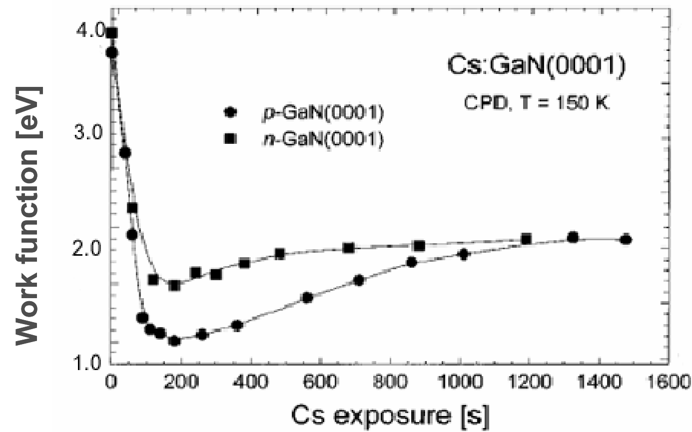


**Figure 5-9. Work function of n-type and p-type GaN as a function of Cs evaporation time at 130K (adapted from reference 20)**

In dynamic bombardment using a $Cs^+$ primary ion beam on the CAMECA IMS-6f SIMS instrument, the surface concentration of Cs atoms does not reach the concentration at which the first continuous layer of covalently bonded Cs atoms is completed, or at which the work function minimum is reached.[21] In the range of steady state surface concentration of Cs obtained during Cs sputtering using the IMS-6F, the work function decreases as surface Cs atom concentration is increased. In $Al_xGa_{1-x}N$, the sputter yield is decreased when x is increased, thus the surface concentration of Cs atoms is increased. This increase in Cs surface concentration results in the reduction of the surface work function and the enhancement of negative ion yields. From figure 5-9, it can be seen that the work function of n-type and p-type GaN is different at the same surface concentration of Cs atoms. This work function difference can possibly cause differences in negative ion yields and RSF's. In this study, there is no p-type $Al_xGa_{1-x}N$ in the sample set. Further study is needed to investigate the RSF dependence on the n-type and p-type behavior of the material. The surface concentration of Cs atoms can be calculated from the sputter yield. Under $Cs^+$ bombardment, the volume sputter rate is:

$$S = \frac{\text{linear sputter rate (nm/sec)}}{\text{sputter area } (\mu m^2)} * 1E-3\,(\mu m/nm) \qquad \textbf{(Equation 5-5)}$$

The units of S from this expression are $\mu m^3$/sec. Since the primary ions are singly charged, then one 1nA consists of $6.24 \times 10^9$ ions/s. For a given primary ion current Ip (nA), the sputter yield (Y) is:

$$Y = \frac{S\,(\mu m^3/s)}{I_p * 6.24E9 \text{ atoms/s}} * N_{AlGaN}\,(\text{atoms/cm}^3) * 1E\text{-}12(\text{cm}^3/\mu m^3) \qquad \textbf{(Equation 5-6)}$$

where $N_{AlGaN}$ is the atomic density of AlGaN in atoms/cm$^3$. The steady state surface concentration of primary species can be calculated as:

$$[Cs] = \frac{1}{1+Y} * N_{AlGaN}. \qquad \textbf{(Equation 5-7)}$$

The surface concentration of Cs atoms and the corresponding $GaN^-$ yield change with x in $Al_xGa_{1-x}N$ is shown in figure 5-10. Both have the same increasing trend as AlN mole fraction is increased.

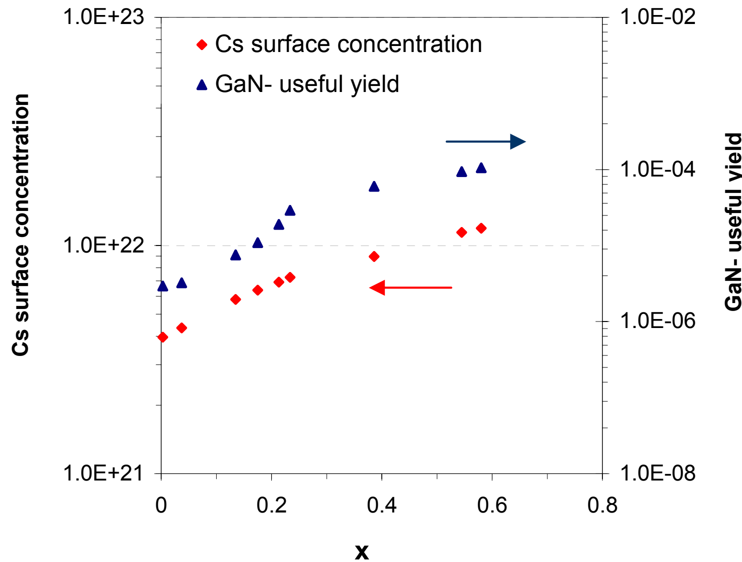


**Figure 5-10. The surface concentration of Cs atoms and the corresponding $GaN^-$ yield change with x in $Al_xGa_{1-x}N$ at 14.5 keV impact energy.**

The increase in negative secondary ion yields with a decrease in surface work can be explained as follows. From the theoretical review of secondary atomic ion emission, the effect of Cs on the negative ion yield enhancement in $Al_xGa_{1-x}N$ can be explained using an

electron tunneling model (section 2.2.2). As a negative ion leaves the solid surface, the electron affinity (A) of the leaving ion is shifted down by an image potential on the surface which is inversely proportional to the separation between the ion and the surface.[22] When the energy level of the sputtered atom coincides with the occupied electronic levels in the sample surface (below Fermi level), an electron can tunnel between them via a resonant electron transfer process, hence neutralization of the outgoing ion can occur.[23] This process is illustrated in the schematic drawing of the energy diagram of a sputtered atom leaving the solid surface in Figure 5-11. In the figure, A is the electron affinity of the sputtered atom at an infinite distance from the sample surface, $\phi$ is the work function of sample surface, $E_F$ is the Fermi level in the sample surface, $E_{vac}$ is the vacuum energy, and $Z_C$ is the crossing distance between the sputtered atom and solid surface when $Ea = E_F$ and a resonant electron transfer occurs.

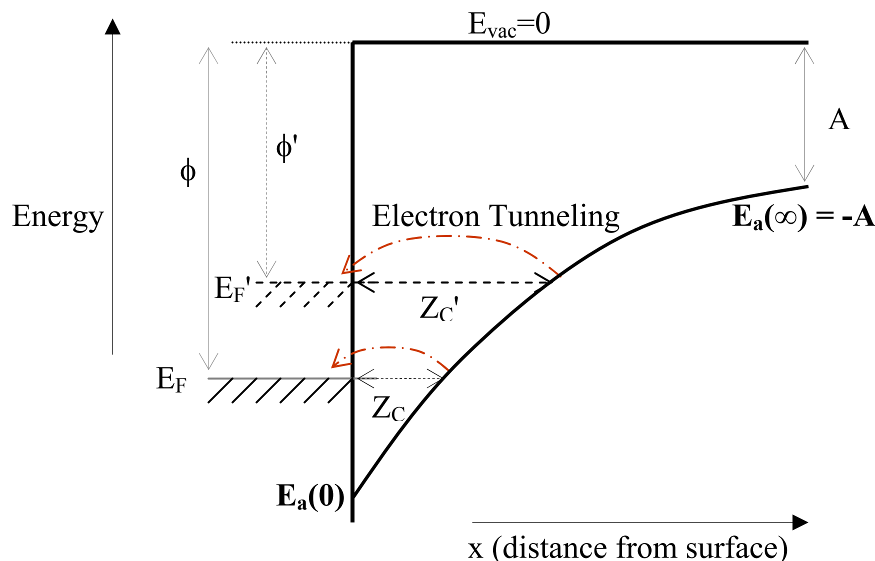


**Figure 5-11. Schematic energy diagram for a sputtered atom leaving solid surface. $Z_c$ is the separation between the atom and solid surface at the cross point where $Ea = E_F$, A is the electron affinity of the sputtered atoms, $E_F$ and $\phi$ and $\phi$' are the Fermi energy and work function prior to surface cesiation, $E_F$' and $\phi$' are the Fermi energy and work function after surface cesiation. The vacuum level $E_{vac}$ is kept constant in the drawing.**

After the solid surface is cesiated, the Fermi energy is raised (from $E_F$ to $E_F'$) which implies that, by definition, the work function is reduced (from $\phi$ to $\phi'$).[24] As a result the

crossing distance $Z_C$ is increased, and the probability of negative ions leaving without being neutralized is increased resulting in an increase in negative ion yield.

## 5.6 Summary

Quantification of impurities and matrix species in $Al_xGa_{1-x}N$ using $Cs^+$ primary ions and negative secondary detection was studied, and the mechanism of ion emission in $Al_xGa_{1-x}N$ was discussed. The ionization mechanism was used to explain the trends in the secondary ion yield data obtained in the quantification of matrix and impurity species in $Al_xGa_{1-x}N$.

Under $Cs^+$ bombardment, the sputter yield decreases with increasing AlN mole fraction x. As a result, the steady state surface concentration of Cs atoms is increased, which reduces the surface work function and increases the negative ion yield.

Matrix quantification in $Al_xGa_{1-x}N$ can be realized using calibration curves of matrix ion intensity ratio as a function of AlN mole fraction. The matrix ion intensity ratio of $AlN^-$/$GaN^-$ appears to increase linearly with the increase of x in $Al_xGa_{1-x}N$ in the range of $0 \leq x \leq 0.58$. For higher Al content $Al_xGa_{1-x}N$, the matrix ion ratios can be plotted as a function of GaN mole fraction, i.e. $GaN^-/AlN^-$ vs. (1-x). This relationship appears linear over the range of $0 \leq (1-x) \leq 0.6$ GaN mole fraction, or $0.4 \leq x \leq 1$ AlN mole fraction. With the apparently linear relationship of these two plots, the matrix elements in $Al_xGa_{1-x}N$ can be quantified over the entire AlN mole fraction range of $0 \leq x \leq 1$ using $Cs^+$ primary ions with negative secondary ion detection.

Impurity elements in $Al_xGa_{1-x}N$ can be quantified using RSF method. The RSF's of $Si^-$ and $MgN^-$ normalized to $GaN^-$ seem to decrease exponentially with the increase of x in $Al_xGa_{1-x}N$. The decrease of the RSF's is mainly the result of the decrease of Ga atomic concentration when x is increased. The exponential relationship is consistent with the exponential relationship of ion yield with the surface work function. With the calibration curves of RSF's as a function of x in $Al_xGa_{1-x}N$, the impurity species can be quantified over $0 \leq x \leq 0.58$. Samples were not available at the time of this study to extend quantification beyond an AlN mole fraction of $x > 0.58$.

The useful ion yields are increased when x is increased in $Al_xGa_{1-x}N$, due mainly to the increase of steady state surface concentration of primary species (Cs) resulting from the reduced sputter rates as x is increased. When Cs concentration is increased, the surface work

function is decreased, and the probability of sputtered negative ions leaving the surface is increased. This trend in negative secondary ion yield is consistent with trends in ion emission versus surface work function given by the electron tunneling model.

## 5.7 References


[1] D. P. Griffis, R. Loesing, D. A. Ricks, et al., Secondary Ion Mass Spectrometry SIMS XI, edited by G. Gillen, R. Lareau, J. Bennett and F. Stevie, John Wiley & Sons, 201 (1997).

[2] D. L. Lefforge, Y. L. Chang, M. Ludowise, et al., Mat. Res. Soc. Symp. Proc. **510**, 155 (1998).

[3] D. P. Chu, M. G. Dowsett, and G. A. Cooke, Journal of Applied Physics **80**, 7104 (1996).

[4] M. L. Yu, Surface Science **90**, 442 (1979).

[5] M. L. Yu, phys. Rev. Lett. **50**, 127 (1983).

[6] H. Gnaser, Phys. Rev. B **54**, 17141 (1996).

[7] H. Gnaser, Phys. Rev. B **54**, 16456 (1996).

[8] M. L. Yu, J. Vac. Sci. Technol. A **1**, 500 (1982).

[9] J. K. Norskov and B. L. Lundquist, Phys. Rev. B **19**, 5661 (1979).

[10] M. L. Yu, J. Vac. Sci. Technol. **20**, 417 (1982).

[11] M. L. Yu, in *Sputtering by Particle Bombardment III*, edited by R. Behrisch and K. Wittmaack (Springer, Berlin, 1991), p. 91.

[12] M. L. Yu, Phys. Rev. B **26**, 4731 (1982).

[13] M. Schumacher, CAMECA Instruments, computer program.

[14] A. Pivovarov, C. Gu, F. Stevie, et al., Applied Surface Science **231-2**, 781 (2004).

[15] V. R. Deline, C. A. Evans, and P. Williams, Applied Physics Letters **33**, 578 (1978).

[16] R. G. Wilson, F. A. Stevie, and C. W. Magee, *Secondary Ion Mass Spectrometry : a Practical Handbook for Depth Profiling and Bulk Impurity Analysis*, 1989).

[17] A. M. James and M. P. Lord, *Macmillan's Chemical and Physical Data* (Macmillan, London, UK, 1992).

[18] S. P. Grabowski, M.Schneider, H. Nienhause, et al., Applied Physics Letters **78**, 2503 (2001).

[19] H. Morkoc, *Nitride Semiconductors and Devices* (Springer-Verlag Berlin Heidelberg, 1999).

[20] M. Eyckeler, W. Monch, T. U. Kampen, et al., Journal of Vacuum Science & Technology B **16**, 2224 (1998).

[21] T. Wirtz, B. Duez, H. N. Migeon, et al., International Journal of Mass Spectrometry **209**, 57 (2001).

[22] M. L. Yu and N. D. Lang, Nucl. Instrum. Methods Phys. Res. Sect. **B14**, 403 (1986).

[23] J. L. Alay and W. Vandervorst, Physical Review B **50**, 15015 (1994).

[24] P. Kambhampati, M. C. Foster, and A. Campion, Journal of Chemical Physics **110**, 551 (1999).

# 6 Quantification of Matrix and Impurity Species in $Al_xGa_{1-x}N$ using the $MCs^+$ Technique

## 6.1 $MCs^+$ Technique

The $MCs^+$ technique is the detection of $MCs_x$ clusters (where x=1 or 2) under $Cs^+$ primary ion bombardment where M is the element to be analyzed. This technique has historically been used in the analysis of some impurities and rare gases to obtain better detection sensitivity.[1, 2] Gao[3] proposed utilizing this technique to reduce matrix effects for matrix element quantification in III-V compound semiconductor.

In III-V semiconductors, quantitative analyses for matrix elements are hampered because variations in matrix composition change the secondary ion yields (matrix effect) of both matrix and impurity elements. The $MCs^+$ technique has been used to minimize the matrix effects in SIMS analysis and has enabled quantification of impurities.[3-9] $MCs_2^+$ ions are also employed to suppress matrix effects and to obtain a sufficiently high useful secondary ion yield for analysis of electronegative elements.[7, 10] It was found that for electropositive elements, the yield of $MCs^+$ is higher than that of $MCs_2^+$, while for electronegative elements, the yield of $MCs_2^+$ is higher. By detecting both $MCs^+$ and $MCs_2^+$ cluster ions, the electropositive and electronegative elements can be measured simultaneously.[7] The $MCs^+$ technique is also found to provide better depth resolution than using $O_2^+$ beam at similar potentials due to the greater mass of Cs.[11] With the capability of suppressing matrix effect, of measuring electropositive and electronegative elements simultaneously, and of providing better depth resolution, the $MCs^+$ technique is a valuable approach for quantitative analysis in secondary ion mass spectrometry.

In this chapter, the formation mechanisms of $MCs^+$ and $MCs_2^+$ cluster ions are discussed, the experimental method and results of quantification in $Al_xGa_{1-x}N$ using $MCs^+$ technique are described, and the formation of $MCs^+$ in $Al_xGa_{1-x}N$ is rationalized in terms of $MCs_x^+$ useful ion yield as a function of AlN mole fraction.

## 6.2 $MCs^+$ and $MCs_2^+$ Secondary Ion Formation

$MCs^+$ ion formation was proposed to occur via the atomic combination of sputtered neutral $M^0$ atoms and $Cs^+$ ions above the sample surface as shown in eq. (6-1).[12-15]

$$M^0 + Cs^+ \rightarrow MCs^+ \quad \textbf{(Equation 6-1)}$$

In this case, emission and ionization processes are decoupled in analogy to secondary ion neutral mass spectrometry (SNMS).[13] Since most sputtered particles in SIMS analysis are electronically neutral, SIMS analysis of $MCs^+$ is almost matrix independent.

For $MCs_2^+$ clusters, several possible formation processes were proposed as shown in eq. (6-2) to (6-4).[16]

$$M^0 + Cs_2^+ \rightarrow MCs_2^+ \quad \textbf{(Equation 6-2)}$$

$$MCs^0 + Cs^+ \rightarrow MCs_2^+ \quad \textbf{(Equation 6-3)}$$

$$M^- + Cs^+ + Cs^+ \rightarrow MCs_2^+ \quad \textbf{(Equation 6-4)}$$

It has postulated in the literature that the first mechanism (eq. 6-2) dominates in the case of electropositive elements M and that the last two mechanisms (equations 6-3 and 6-4) become important for electronegative elements.[16, 17] The $MCs^0$ neutral in the formation process of eq. (6-3) results from the neutralization of an $MCs^+$ ion by electron capture.[13] For electronegative elements, work by Sarkar and Chakraborty[18] showed that the intensity of $MCs_2^+$ is higher than $MCs^+$ while the intensity of $Cs_2^+$ is lower than that of $Cs^+$. This calls into question the formation process in eq. (6-2). The author argued that the formation process of eq. (6-4) is the dominate one.

Other studies have also found that the process of eq. (6-2) is not the dominant one in the formation of $MCs_2^+$ for either electropositive or electronegative elements.[13, 18] Mootz and coworkers[13] found that the energy distribution of $Cs_2^+$ is broader than $Cs^+$ while that of $MCs_2^+$ is smaller than the corresponding $MCs^+$ for all the elements investigated (Zn, Cu, Ge, Ni, Mo). This calls into question the $MCs_2^+$ formation process in eq. (6-2) with the $MCs^+$ formation process in eq. (6-1).

It has been shown that the $MCs^+$ and $MCs_2^+$ yields strongly depend on the steady state cesium surface concentration incorporated in the specimen during the primary bombardment. However, too high a Cs surface concentration can lower the surface work function below a

critical value, the magnitude of which is situated slightly below the ionization energy of Cs. If this occurs, according to the electron tunneling model for secondary ion formation, the probability of secondary $Cs^+$ ionization and consequently the probability of $MCs^+$ and $MCs_2^+$ cluster formation strongly decreases.[5, 17, 19]

$MCs^+$ yields depend on the density of $Cs^+$ ions and neutral $M^0$ atoms available above the surface as well as the ionization probability of $MCs^+$. The measured intensity of $MCs^+$ clusters can be expressed by eq. (6-5) [20]

$$I(MCs^+) = I_P \cdot Y^2 \cdot C_M \cdot C_{Cs} \cdot P_{Cs^+} \cdot \gamma_{M^0-Cs^+} \cdot \eta_{MCs^+} \qquad \textbf{(Equation 6-5)}$$

where $I_P$ is the primary current, Y is the sputter yield, $C_M$ and $C_{Cs}$ are the surface concentration of sputtered neutral $M^0$ and the steady state Cs, $P_{Cs^+}$ represents the ionization probability of sputtered Cs atom, $\gamma_{M0\text{-}Cs^+}$ is a factor describing the combination probability between the independently sputtered $M^0$ neutral and $Cs^+$ ions, and $\eta_{MCs^+}$ is the instrumentation transmission and detection factor of $MCs^+$ clusters.

The useful yield of an element M is defined as eq. (6-6).[21]

$$\tau = \frac{\text{number of detected ions}}{\text{number of sputted atoms}} \qquad \textbf{(Equation 6-6)}$$

The number of sputtered atoms of an element M can be expressed as:

$$n(M) = \int_0^{t_{final}} \frac{I_P}{e} \cdot Y \cdot C_M(t)dt = \frac{I_P}{e} \cdot Y \cdot \int_0^{t_{final}} C_M dt \qquad \textbf{(Equation 6-7)}$$

where $t_{final}$ is the total sputtering time, e is the elementary charge, and $C_M(t)$ is the concentration of element M.

Considering eq. (6-5) to (6-7), the useful ion yield of $MCs^+$ can be expressed as:[20]

$$\tau(MCs^+) = k_1 \cdot Y \cdot C_{Cs} \cdot P_{Cs^+} \qquad \textbf{(Equation 6-8)}$$

The factor $k_1$ is a factor related to the combination probability and the efficiency factors, and a factor that is independent of the Cs surface concentration.

The factors governing the useful ion yield of $MCs^+$ are sputtering yield Y, the steady state surface concentration of Cs ($C_{Cs}$) and the ionization probability of sputtered Cs atoms $P_{Cs^+}$. As the sputtering yield increases, the surface concentration of Cs decreases. The change of the steady state surface concentration of Cs alters the surface work function.

When Cs concentration is reduced, the surface work function increases and the positive ionization probability of Cs atom increases. Thus an optimum value of surface concentration of Cs exists when the useful yield of $MCs^+$ is the highest.

Similarly the useful ion yield of $MCs_2^+$ from formation process of (6-2), (6-3) and (6-4) can be expressed as (6-9), (6-10) and (6-11), respectively.[20]

$$\tau(MCs_2^+) = k_2 \cdot Y^2 \cdot C_{Cs}^2 \cdot P_{Cs^+} \qquad \textbf{(Equation 6-9)}$$

$$\tau(MCs_2^+) = k_3 \cdot Y^2 \cdot C_{Cs}^2 \cdot P_{Cs^+}^2 \cdot \varepsilon \qquad \textbf{(Equation 6-10)}$$

$$\tau(MCs_2^+) = k_4 \cdot Y^2 \cdot C_{Cs}^2 \cdot P_{Cs^+}^2 \cdot \beta_{M^-} \qquad \textbf{(Equation 6-11)}$$

The factor ε in eq. (6-10) denotes the probability of a neutralization of a $MCs^+$ cluster by electronic capture. $\beta_{M^-}$ is the ionization probability of $M^-$.

Wirtz et al.[20] found that in CAMECA IMS-4f system, the useful ion yield of $MCs_x^+$ can not be maximized because of the sputtering yield limitation and the fact that the optimum surface Cs concentration cannot be reached. A new SIMS instrument called Cation Mass Spectrometer (CMS) was designed to reach high $MCs_x^+$ useful yields by allowing the optimization of $C_{Cs}$.[20] Figure 6-1 shows the useful ion yield of $MCs_x^+$ for six analyzed species versus the corresponding sputtering yield. Sputtering yields that can be obtained using the CAMECA IMS-4F (similar in geometry to the IMS-6f) are below the value resulting in maximum $MCs_x^+$ useful ion yield. The higher the sputtering rate, the higher the useful ion yields.

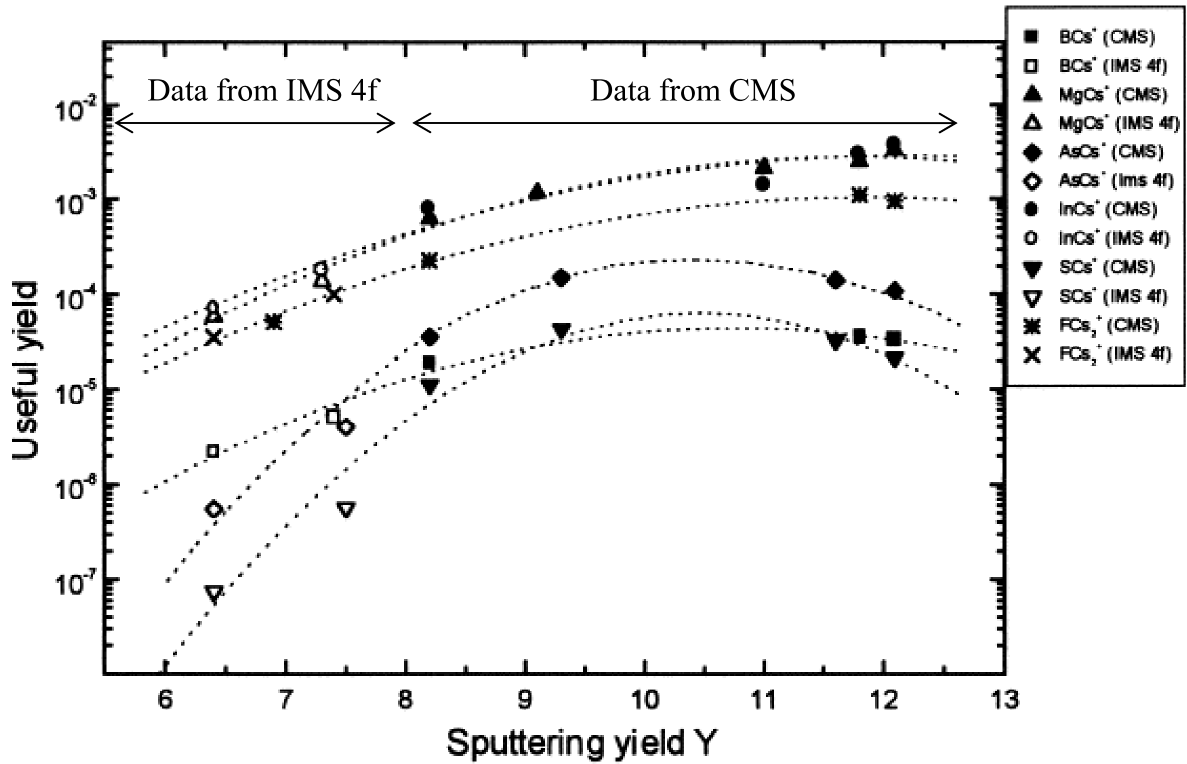


**Figure 6-1. Compilation of the useful yields determined for the six analyzed species versus the corresponding sputtering yield. (Adapted from reference 20)**

### 6.3 Previous Studies on III-nitrides using $MCs^+$ Technique

Gao and Chu[9, 22] characterized III-nitride materials and generated the calibration curves of matrix ion intensity ratio as a function of matrix concentration ratio in the range of $0 \leq x \leq 0.2$, where x is AlN mole fraction in $Al_xGa_{1-x}N$ or InN mole fraction in $In_xGa_{1-x}N$. The value of x was determined by RBS (Rutherford Backscattering Spectrometry). In this range ($0 \leq x \leq 0.2$), the authors stated that the matrix $AlCs^+/GaCs^+$ ion intensity ratios and $InCs^+/GaCs^+$ versus composition ratios x/(1-x) show a linear relationship. The authors claimed that the linear relationship indicates that matrix effects are negligible.

Lefforge et al.[23] studied $Al_xGa_{1-x}N$ with Al concentrations using the $MCs^+$ method. Calibration curves of matrix ion intensity ratio, sputter rate and $MgCs^+$ RSF versus AlN mole fraction were established. The matrix $AlCs^+/GaCs^+$ ion intensity ratios versus Al composition x showed a non-linear relationship. The sputter rate was shown to decreased linearly with AlN mole fraction for x up to 0.32 after which sputter rate appears to be

independent of AlN mole fraction for x>0.32. The RSF's of $MgCs^+$ were compared by normalizing to $GaCs^+$, $Ga^+$, $NCs^+$ and $N^+$. In the range of $0 \leq x \leq 0.31$, the RSF's generated using $GaCs^+$ as the reference decrease with x while those using $Ga^+$, $NCs^+$ or $N^+$ as reference increase with x.

Putting these studies together, it is clear that matrix and impurity quantification using the MCs method for quantification of low Al content AlGaN is reasonably well understood. For high Al content AlGaN (x>0.4), however, the relationship between the matrix ion intensity ratios and AlN mole fraction has not been well established, and the apparent constant sputter rates at AlN mole fractions x>0.32 is not well understood. In this work, the intended goal is to establish the quantification of matrix and impurities in AlGaN with low and high Al content and to understand the ion formation mechanism under $MCs^+$ method.

## 6.4 Experimental

The same sets of samples as previously discussed were used in this experiment (section 4.3). Set one (SS1) is $Al_xGa_{1-x}N$ films grown on SiC substrate with AlN mole fraction ranging from $0 \leq x \leq 0.21$. Set two (SS2) is $Al_xGa_{1-x}N$ films grown on sapphire substrate with AlN mole fraction ranging from $0.23 \leq x \leq 0.58$. These films were implanted with $^{16}O$, $^{24}Mg$ and $^{29}Si$ with energy and dose listed in table 3-1. Set three (SS3) was produced using high dose ion implantation of Ga into AlN to obtain high Al content at the ion implant peak position (x=0.81, 0.98). All the samples were sputter coated with ~10nm of Au.

The analysis was performed using a $Cs^+$ primary ion beam extracted from the Cs microbeam source of the CAMECA IMS-6F and positive secondary extraction potential. High energy and low energy $Cs^+$ beam were used for the analysis. Table 6-1 lists the analysis conditions. The angles of incidence were calculated using a program written by Schumacher[24] which includes the IMS-6F primary ion column deflector voltages used for positioning the beam onto the primary column optical axis of the IMS-6f mass spectrometer.

**Table 6-1. Analysis conditions under $Cs^+$ primary ion bombardment with positive secondary ion ($MCs^+$) detection**

| Primary Ion Species | Primary Ion Acceleration Voltage (kV) | Sample Potential (kV) | Impact Energy (keV) | Angle of Incidence (degrees) | Ion Current (nA) | Raster Size ($\mu m^2$) | Beam Density ($\mu A/um^2$) |
|---|---|---|---|---|---|---|---|
| $Cs^+$ | 10 | +4.5 | 5.5 | 41.3 | 40 | 200x200 | 1 |
| $Cs^+$ | 3 | +1.75 | 1.25 | 48.5 | 10 | 220x220 | 0.21 |

Secondary ions were collected from a 60µm diameter optically gated area (750µm field aperture, 150µm image field, 750µm contrast aperture). The collection area is centered on a square raster area of 200 x 200 $\mu m^2$. Due to the low yield of $MCs_x^+$ ions, the entrance and exit slits were kept open to obtain the best possible secondary ion transmission. With the detection of $MCs_x^+$ ions, very high mass resolution is needed to separate mass interferences due to the high masses of the secondary ions, e.g. 7900 m/Δm to separate $^{29}SiCs^+$ from $AlH2Cs^+$ which is not practical in this analysis. The energy slit was adjusted to be fully open to allow a 130 eV energy band pass at 4.5 kV sample potential and a 50 eV energy band pass at 1.75 kV sample potential.[25] The depths of sputtered craters were measured using a KLA-Tencor P-20 profilometer.

At the low impact energy of 1.75 keV, the samples with Sapphire substrate (insulator) showed significant charging effects. Electron beam charge neutralization using the Normal Incidence Electron Gun (NEG) equipped with the CAMECA IMS-6F was required. The electron beam was aligned on the left side of the ion raster area as described in section 4.3. An electron gun accelerating voltage (HV) of -1 kV was used for a +1.75 kV sample potential.

To evaluate the effectiveness of electron beam charge neutralization, the energy distribution of $GaCs^+$ was acquired as shown in figure 6-2. The energy slit was centered so that the maximum secondary ion intensity was positioned at zero volts offset using a conductive sample (Al grid on Si). For a charging sample, if charge neutralization is successful, the maximum of the secondary ion intensity energy distribution is at zero volts offset. When the NEG is operated at a low accelerating potential such as -1keV, the electron beam current achieved is limited due to inefficient electron extraction from the electron

source. The data in figure 6-2 was acquired from the sample exhibiting the most severe charging effect in the sample set ($Al_xGa_{1-x}N$ on Sapphire substrate with x=0.58). It can be seen that although it was not possible to shift the electron energy distribution maximum to 0 volt offset, the entire secondary ion intensity distribution is contained within the energy window with the energy slit wide open, which is illustrated with the red highlighted area in figure 6-2. Since the entire intensity distribution is contained within the energy window, the slight amount of residual charging does not affect the measured secondary ion intensity.

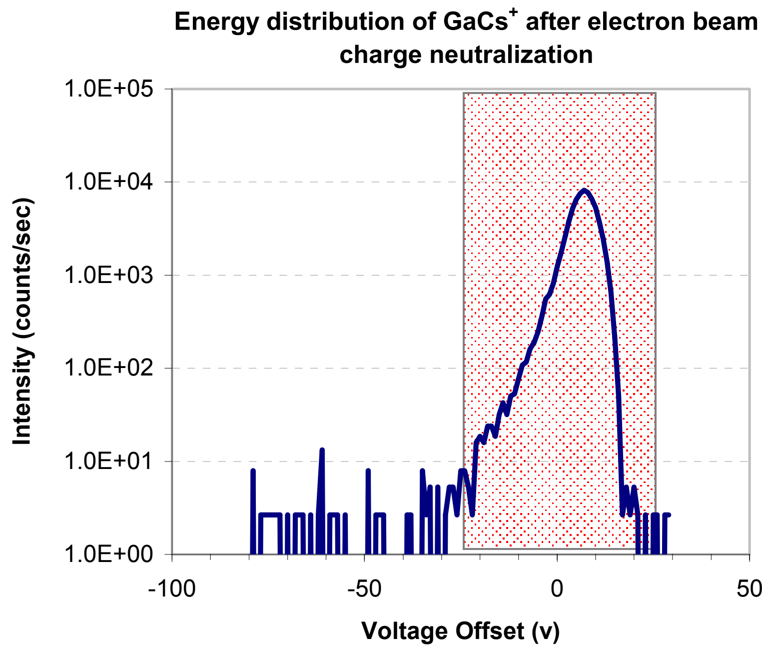


**Figure 6-2. Energy distribution of $GaCs^+$ after electron beam charge neutralization from the sample with the worst charging effect ($Al_xGa_{1-x}N$ on Sapphire substrate with x=0.58). Analysis conditions are $Cs^+$ with 1.25 keV impact energy and -1 kV electron beam energy. The highlighted window is the energy pass band (50 eV) at 1.75 kV secondary ion extraction potential.**

For matrix element analyses, depth profiles were acquired until the matrix ion counts reach a steady state. For implanted impurity analyses, depth profiles were acquired until the impurity ion counts dropped to the background level (see figure 6-3). It is very important to choose a suitable secondary ion for analysis of impurities in order to minimize matrix effects, to obtain the maximum useful secondary ion yield, and to avoid mass interferences between the secondary ion peaks. It can be seen in figure 6-3 that although the intensity of $SiCs^+$ in $Al_{0.21}Ga_{0.79}N$ is higher than that of $SiCs_2^+$, the detection limit using $SiCs^+$ is higher by a factor of 100 than if $SiCs_2^+$ is used. The reason for the poor $SiCs^+$ detection limit is not well

understood. The high secondary ion background for $SiCs^+$ is probably due to a mass interference by $AlH_2Cs^+$. Although $SiCs_2^+$ also has a mass interference from $AlH_2Cs_2^+$, the intensity of $AlH_2Cs_2^+$ is much lower than that of $AlH_2Cs^+$. The low intensity of this mass interference is a result of the lower secondary ion intensity of $AlCs_2^+$ than that of $AlCs^+$, since Al is an electropositive element. To separate $^{29}SiCs^+$ from $AlH_2Cs^+$, a mass resolution of m/Δm=7900 is needed, which is not practical in this analysis. If the slits were adjusted to obtain a mass resolution of 7900, the impurity ion intensity would be too low to be analyzed with good precision. The detection of $SiCs_2^+$ for Si impurity ensures a dynamic range of two orders magnitude, even at low mass resolution, as shown in figure 6-3.

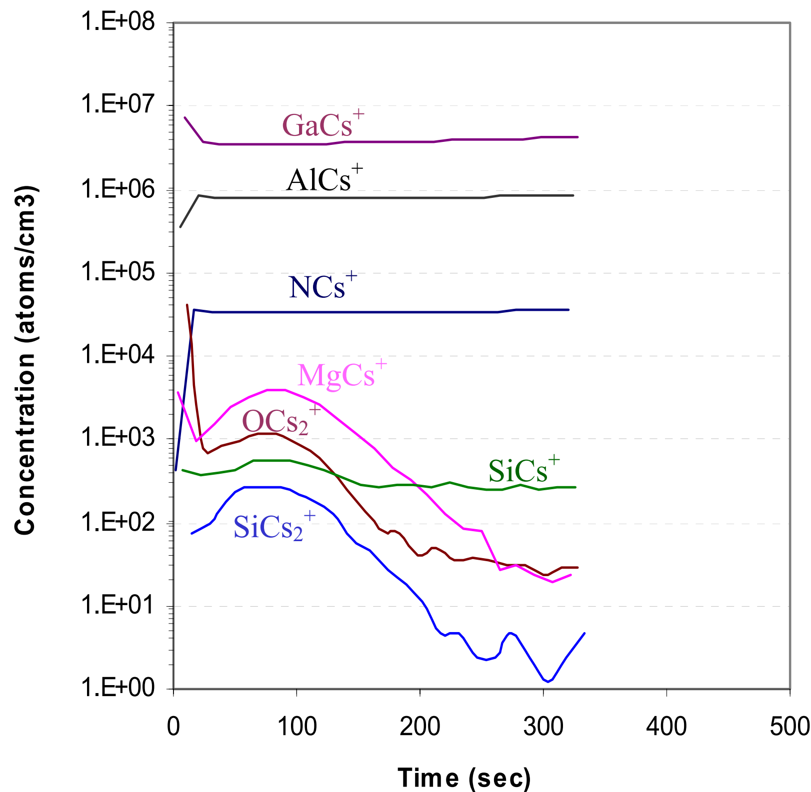


**Figure 6-3. Depth profile of matrix and impurity species in $Al_xGa_{1-x}N$ with x=0.21 at 5.5 keV impact energy using $MCs^+$ technique**

Using the $MCs^+$ technique, the secondary ion intensities of the $MCs^+$ or, in other cases, the $MCs_2^+$ peaks are higher than the respective $M^+$ ion intensities, and the ion intensities of $Cs^+$ and $Cs_2^+$ are the highest in the spectrum as shown in the mass spectrum in figure 6-4. In this experiment, the matrix ions monitored were $AlCs^+$, $GaCs^+$, $NCs^+$, and

$NCs_2^+$. Impurity ions monitored were $MgCs^+$, $SiCs_2^+$ and $OCs_2^+$. $GaCs_2^+$, $Cs^+$ and $Cs_2^+$ were also monitored in order to understand the formation mechanisms of $MCs_x^+$ secondary ions sputtered from AlGaN. $AlCs^+$/ $GaCs^+$ ion intensity ratios, the RSF's of $MgCs^+$, $SiCs_2^+$ and $OCs_2^+$ normalized to different matrix signal, and the sputter rates were calculated after the depth profiles are obtained for the entire sample set. The trends of these parameters with respect to AlN mole fraction were studied.

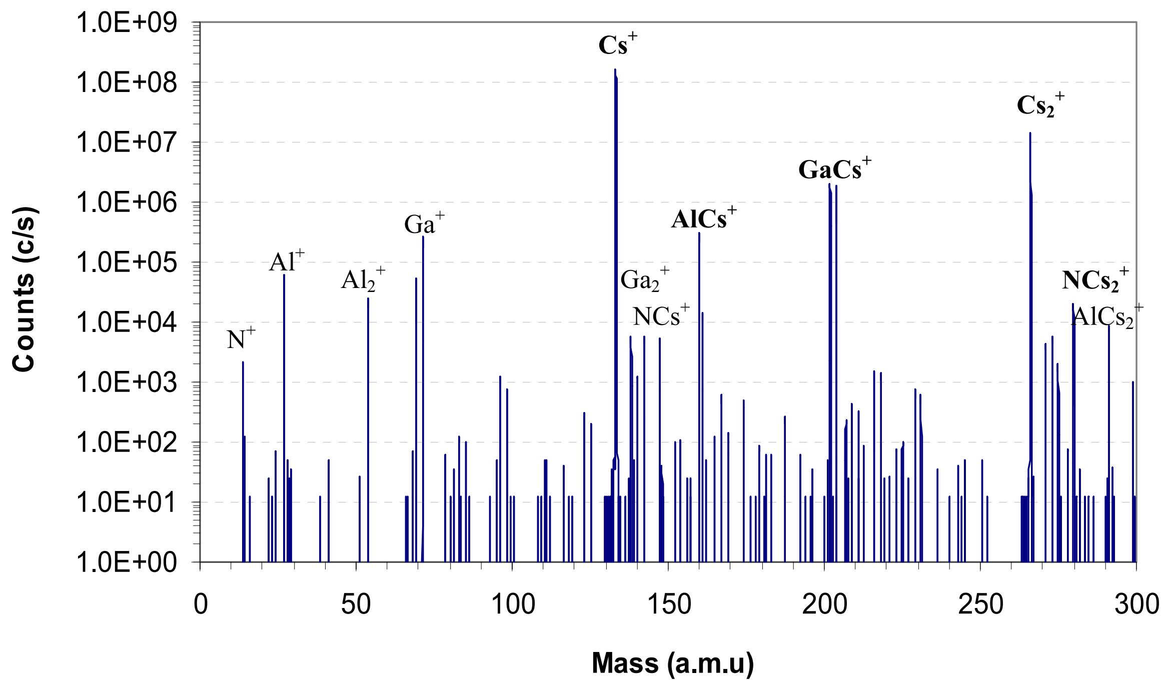


**Figure 6-4. Mass Spectrum of $Al_xGa_{1-x}N$ (x=0.21) at 5.5 keV energy using $MCs^+$ Technique**

## 6.5 Results and Discussion

### 6.5.1 Sputter Rate

The sputter rates given below were calculated by normalizing the sputter rates obtained from crater depth measurements to primary beam density resulting in a value which is proportional to sputter yield. The sputter rates at 5.5 keV and 1.25 keV $Cs^+$ primary ion impact energy are plotted as a function of AlN mole fraction (x) in figure 6-5. Note the similar trends as compared to the sputter rates obtained using other analysis conditions (See

Figures 4-2 and 5-1). The sputter rate decreases with increasing AlN mole fraction x, but the rate of decrease in the sputter rate versus x declines as the AlN mole fraction increases.

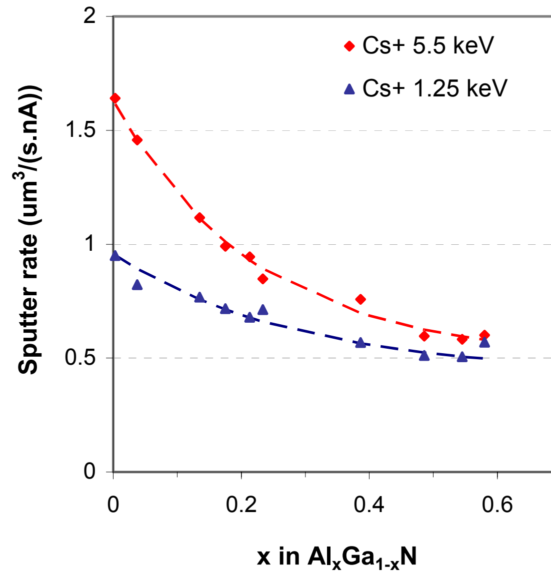


**Figure 6-5. Sputter rate (normalized to beam density) of $Al_xGa_{1-x}N$ as a function of AlN mole fraction (x) using $MCs^+$ at 5.5 keV and 1.25 keV impact energy**

Comparing the sputter rates obtained for the two primary ion impact energies used in figure 6-5, the sputter rate at 5.5 keV impact energy is higher. Although the angle of incidence for 5.5 keV impact energy (41.3° from normal) is slightly lower than for 1.25 keV (48.3° from normal), the energy dependence of the sputter rate outweighs any increase in sputter rate due to increased angle of incidence.

### 6.5.2 Matrix Ion Intensity Ratio

The matrix ion intensity ratio $AlCs^+/GaCs^+$ as a function of AlN/GaN mole fraction ratio x/(1-x) shows an apparently linear trend over the AlN mole fraction $0 \le x \le 0.58$ (figure 6-6). The slope of the curve is less than 1, i.e. $AlCs^+$ yield decreases with increasing AlN mole fraction.

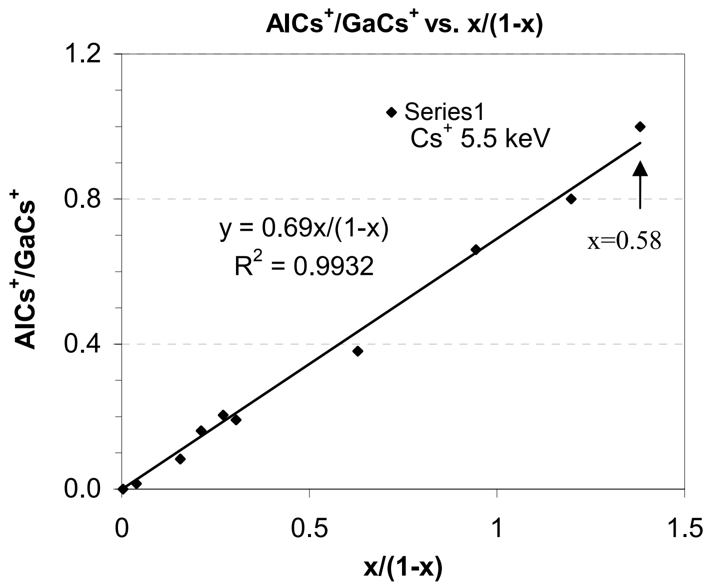


**Figure 6-6. Matrix ion intensity ratio versus the matrix mole fraction ratio at 5.5 keV impact energies using $MCs^+$ technique**

When x is larger than 0.58, the trend in the $AlCs^+/GaCs^+$ ion intensity ratio versus the Al/Ga mole fraction ratio appears to become non linear. However, if plotted inversely, i.e. $GaCs^+/AlCs^+$ as a function of (1-x)/x, then the relationship appears linear for $0 \leq (1-x) \leq 0.92$, as shown in figure 6-7.

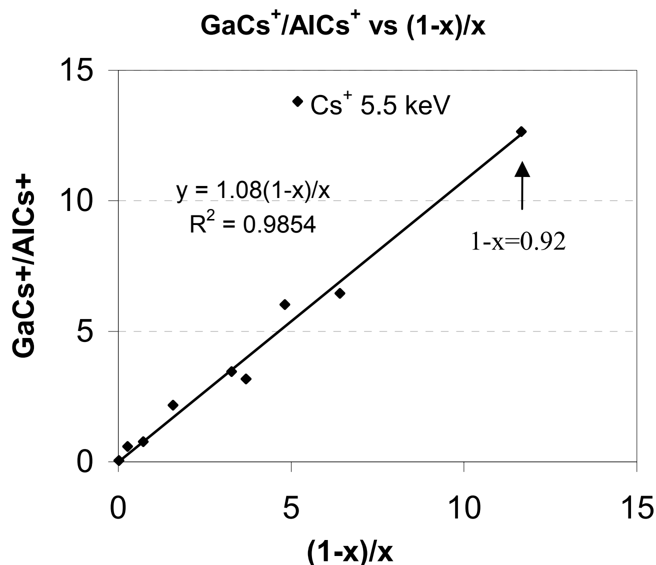


**Figure 6-7. Inverse plot of matrix ion intensity ratio versus the matrix mole fraction ratio at 5.5 keV impact energies using $MCs^+$ technique**

Figure 6-8 shows the $AlCs^+/GaCs^+$ ion intensity ratio as a function of Al and Ga atomic concentration ratio for high impact energy (5.5 keV) and low impact energy (1.25 keV). At both high and low impact energies, the correlation appears linear up to $x \leq 0.6$ or $x/(1-x) \leq 1.5$. The $AlCs^+/GaCs^+$ intensity ratio with 5.5 keV and 1.25 keV impact energies appear the same within error.

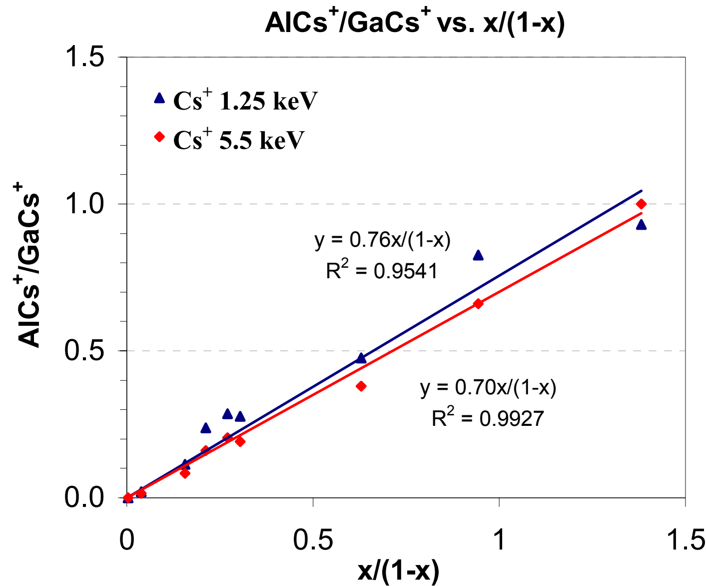


**Figure 6-8. Comparison of matrix ion intensity ratio with high and low impact energy using $MCs^+$ technique**

### 6.5.3 Impurity RSF's

$MgCs^+$, $SiCs_2^+$ and $OCs_2^+$ were monitored in order to measure impurity concentrations of Mg, Si and O. The RSF's for these impurity species were computed by normalizing their respective secondary ion intensities to $GaCs^+$, $NCs^+$ or $NCs_2^+$. In general, the impurity ions and matrix ions should have similar atomic or molecular configurations, since ions with similar types have similar energy distributions and thus similar secondary ion transmission variations from different holder positions. In AlGaN, normally Ga-containing ions are used for matrix ions, e.g. $Ga^+$, $GaN^-$ and $GaCs^+$. However, neither the Al nor the Ga concentrations in $Al_xGa_{1-x}N$ with differing AlN mole fraction are constant, while the concentration of N does remain constant. Although $N^+$ and $N^-$ yields are low, $NCs^+$ and

$NCs_2^+$ yields are sufficiently high to be used as matrix reference ions. By using $NCs^+$ or $NCs_2^+$ as the matrix reference ion, quantification in $Al_xGa_{1-x}N$ over the entire range of x from $0 \leq x \leq 1$ can be achieved without the artifacts that would be introduced as a result using a matrix reference with varying concentration.

Figure 6-9 shows the relative sensitivity factor (RSF) of $MgCs^+$ normalized to $GaCs^+$ and $NCs^+$ acquired using the high and low $Cs^+$ beam impact energies used in this study. RSF's normalized to $NCs_2^+$ were not computed since $MgCs^+$ and $NCs_2^+$ do not have the same configuration. The $Mg^+$ RSF seems to change exponentially with x for x=0 ~ 0.58. At higher impact energy, the RSF's are higher, which indicate a lower $Mg^+$ ion yield relative to the matrix ion yield.

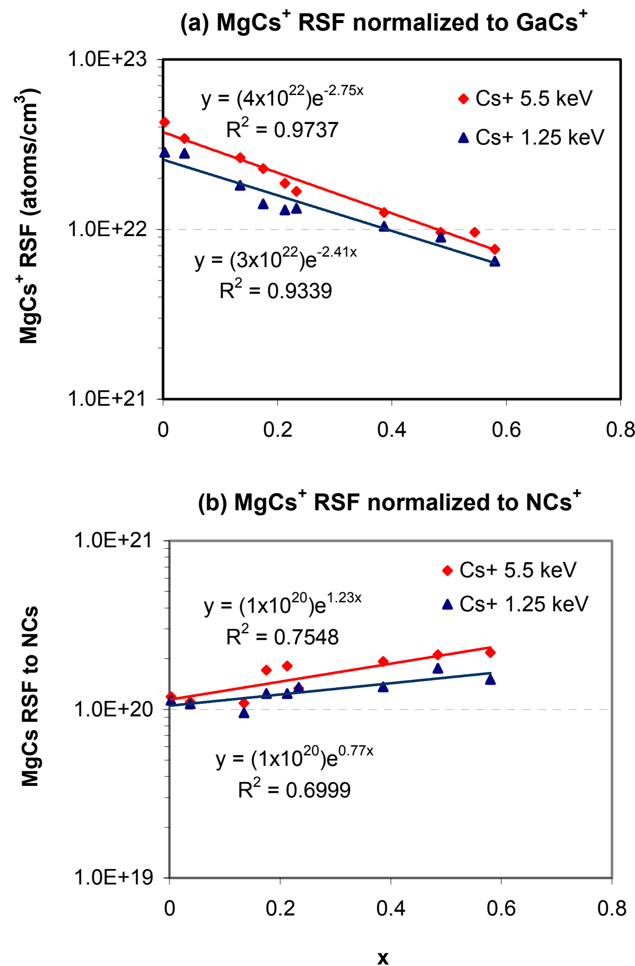


**Figure 6-9. $MgCs^+$ RSF as a function of AlN mole fraction (x) at 1.25 and 5.5 keV impact energies. Figure (a) is normalized to $GaCs^+$, (b) is normalized to $NCs^+$**

Comparing the $MgCs^+$ RSF's normalized to $GaCs^+$ and to $NCs^+$, the RSF's normalized to $GaCs^+$ show a relatively large decrease with increasing AlN mole fraction x mainly due to the reduction of $Ga^+$ ion intensity caused by the decrease of Ga concentration as the AlN mole fraction x increases from 0 to 0.58. In contrast, the RSF's normalized to $NCs^+$ increase slightly with x, and the RSF variation with x is within the factor of 2. The normalization of $NCs^+$ provides a valuable quantification method because a) N concentration is constant from GaN to AlN and b) the RSF does not change significantly, especially in the case of 1.25 keV impact energy where the RSF is from 1E20 to 1.5E20 for $0 \le x \le 0.58$.

Figure 6-10 shows the relative sensitivity factor (RSF) of $SiCs_2^+$ normalized to $GaCs^+$, $NCs^+$ and $NCs_2^+$ at high and low impact energies. Similar to the $Mg^+$ RSF, the $SiCs^+$ RSF's are higher at higher impact energy

Comparing the $SiCs_2^+$ RSF's normalized to different matrix ions in figure 6-10, the RSF's normalized to $GaCs^+$ (figure 6-10a) decrease with x mainly due to the reduction of $Ga^+$ ion intensity caused by the decrease of Ga concentration as AlN mole fraction increases. The variation of the RSF's is large when x changes from x to 0.58. The RSF's normalized to $NCs^+$ (figure 6-10b) decreases slightly with x, and their variation with x is less than the ones normalized to $GaCs^+$. The RSF's normalized to $NCs_2^+$ (figure 6-10c) seem to remain constant in the range of $0 \le x \le 0.58$. In the case of $SiCs_2^+$, the normalization to $NCs_2^+$ provides a valuable quantification method because of the constant N concentration from GaN to AlN and the small variation of RSF when the AlN mole fraction x varies from $0 \le x \le 0.58$.

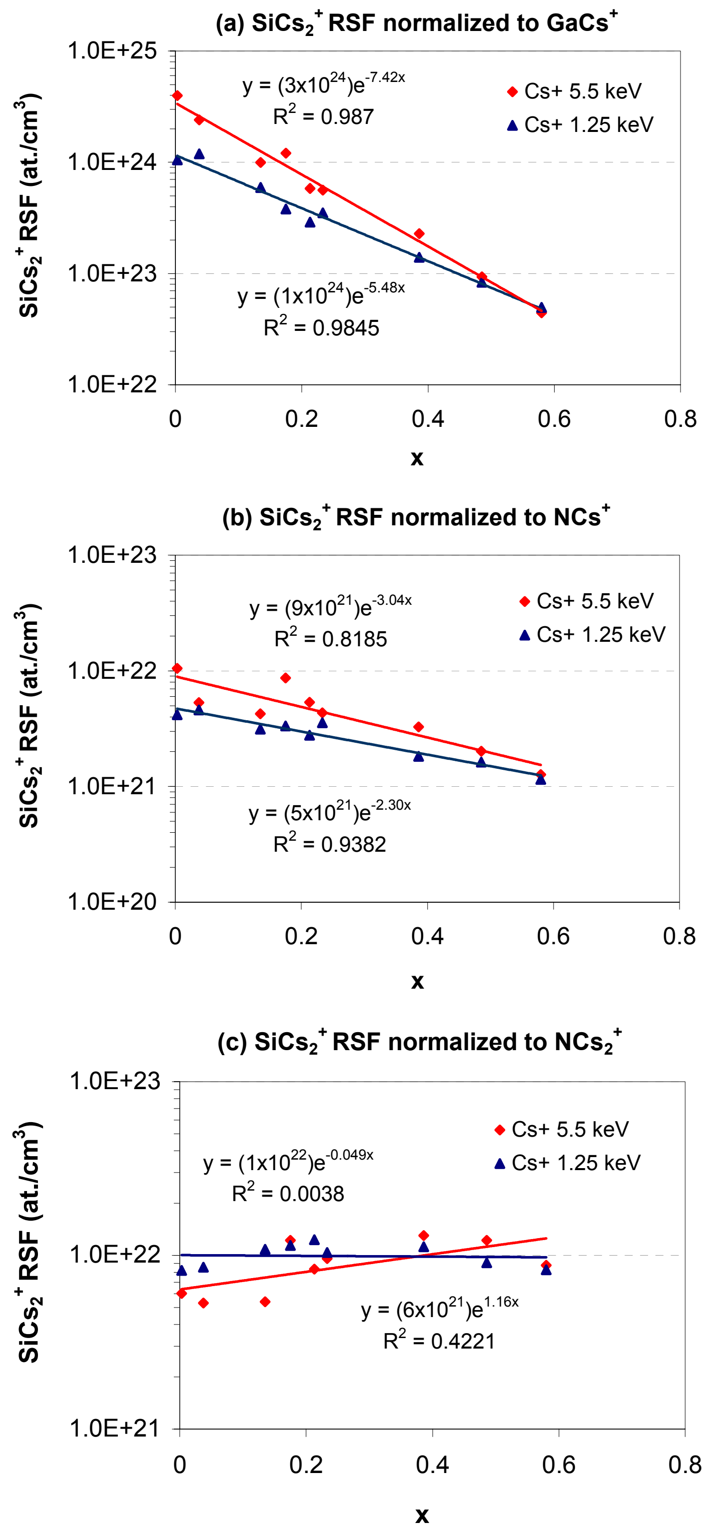


**Figure 6-10.** $SiCs_2^+$ **RSF as a function of AlN mole fraction (x) at high and low impact energies. Figure (a) is** $SiCs_2^+$ **RSF normalized to** $GaCs^+$**, (b) to** $NCs^+$ **and (c) to** $NCs_2^+$**.**

Figure 6-11 shows the relative sensitivity factors (RSF's) generated for $OCs_2^+$ normalized to $GaCs^+$, $NCs^+$ and $NCs_2^+$ at high impact energy. The detection limit of $OCs_2^+$ at low impact energy is too poor to allow acquisition of useful data. As with the $SiCs_2^+$ RSF obtained by normalizing to $GaCs^+$ as seen in figure 6-14a, the RSF's obtained by normalization of $OCs_2^+$ to $GaCs^+$ (figure 6-11a) decrease with increasing AlN mole fraction x due to the reduction of $Ga^+$ ion intensity resulting from the decrease of Ga concentration. The variation of the RSF's is large as x covers the range from x to 0.58. The $OCs_2^+$ RSF's normalized to $NCs^+$ (figure 6-11b) show a much reduced change with x, while the $OCs_2^+$ RSF's normalized to $NCs_2^+$ (figure 6-11c) increase with x. In the case of $OCs_2^+$, the normalization to $NCs^+$ provides the minimum variation in the RSF over the range of $0 \leq x \leq 0.58$, but the data are noisy (large error). The RSF's normalized $NCs_2^+$ should be the best choice for oxygen quantification in $Al_xGa_{1-x}N$ using calibration curves method due to the same configuration of $OSi_2^+$ and $NCs_2^+$.

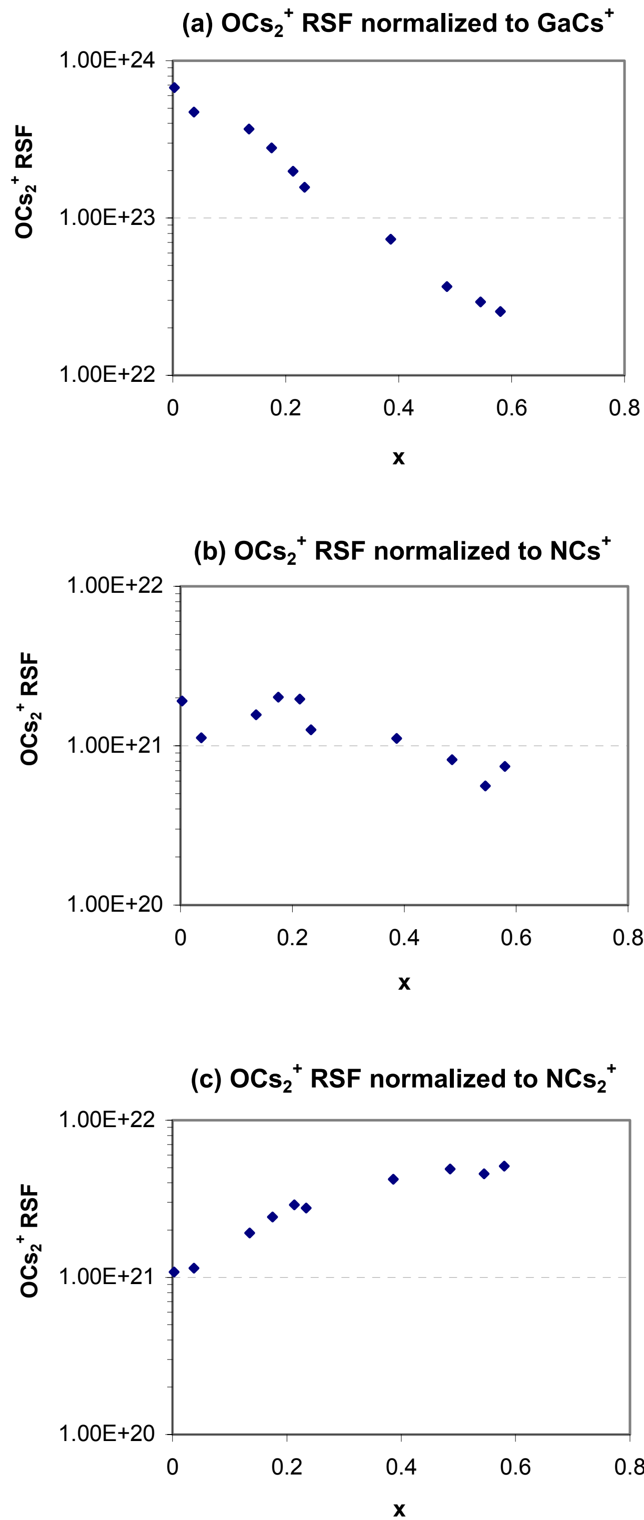


**Figure 6-11.** $OCs_2^+$ RSF as a function of AlN mole fraction (x). $OCs_2^+$ RSF generated by normalization to (a) $GaCs^+$, (b) $NCs^+$ and (c) $NCs_2^+$ .

### 6.5.4 Secondary Ion Formation Mechanism in $Al_xGa_{1-x}N$ Using $MCs^+$ Method

In order to understand the formation mechanism of $MCs^+$ and $MCs_2^+$ ions in $Al_xGa_{1-x}N$, the useful ion yields of some $MCs_x^+$ secondary ions are computed. With regard to understanding the formation mechanism of $MCs_x^+$ secondary ions, the magnitude of the $Cs^+$ and $Cs_2^+$ ions available for combination is of more interest than their useful ion yields. The measured $Cs_x^+$ ions can be computed using eq. 6-12 where x is 1 or 2.

$$C_{Cs_x^+} = \frac{I_{Cs_x^+} * t}{d * A_{detect}}$$ **(Equation 6-12)**

where $I_{Csx+}$ is the detected ion intensity of $Cs_x^+$ in ions/sec, t is the total sputtering time, d is the crater depth and $A_{detect}$ is the detected area. Note that the $Cs^+$ ion production computed in this manner reflects the number of $Cs^+$ secondary ions detected, not the actual number of $Cs^+$ ions available for combination. The number of $Cs^+$ secondary ions detected should be related to the number $Cs^+$ ions created by the instrument transmission factor and detection efficiency factor. Based on the above, the number of $Cs^+$ and $Cs_2^+$ secondary ions available for combination is significantly greater than the number of these ions detected. The relative number of $Cs^+$ and $Cs_2^+$ ions available near the sample surface as a function of x are shown in figure 6-12 a and b. When x increases, the $Cs^+$ ion production shows a slight decreasing trend while the $Cs_2^+$ ion production does not show an apparent trend.

As x in $Al_xGa_{1-x}N$ increases, the sputter rate of the material decreases and the surface concentration of Cs atoms increases, however the positive ionization probability decreases caused by the decrease of the local surface work function. The ion production of $Cs^+$ depends on both the surface concentration of Cs atoms and the ionization probability of $Cs^+$. In the CAMECA IMS series magnetic sector SIMS, the reduction of ionization probability dominates with the result that the $Cs^+$ ion production decreases with x due the reduction of $Cs^+$ ionization probability caused by increasing surface concentration of Cs atoms. The increase of $Cs^+$ ions detected with 5.5 keV impact energy compared with that with 1.25 keV can be attributed to the closer-to-normal angular distribution of the emitted particles. Under ion bombardment, the angular distribution of emitted atoms is related to the energy and angle of incidence of primary ions. Higher energy and lower angles of incidence with respect to

normal yield secondary ions with closer-to-normal angular distribution.[26] The secondary ion transmission system in CAMECA IMS SIMS changes with the angle of secondary ion emission, i.e. only secondary ions emitted within certain angular range are transmitted and detected. Secondary ions having angular distributions which are near normal to the sample surface have higher transmissions. As is evident of figure 6-12b, the intensity distribution of $Cs_2^+$ secondary ions is more scattered with x, and it does not have a strong increasing or decreasing trend. The formation of $Cs_2^+$ is believed to through the combination of $Cs^0$ neutral and $Cs^+$. Since the concentration of $Cs^0$ neutral increases as x increases, the trend of $Cs_2^+$ ions versus x does not follow the obvious decreasing trend of $Cs^+$ versus x.

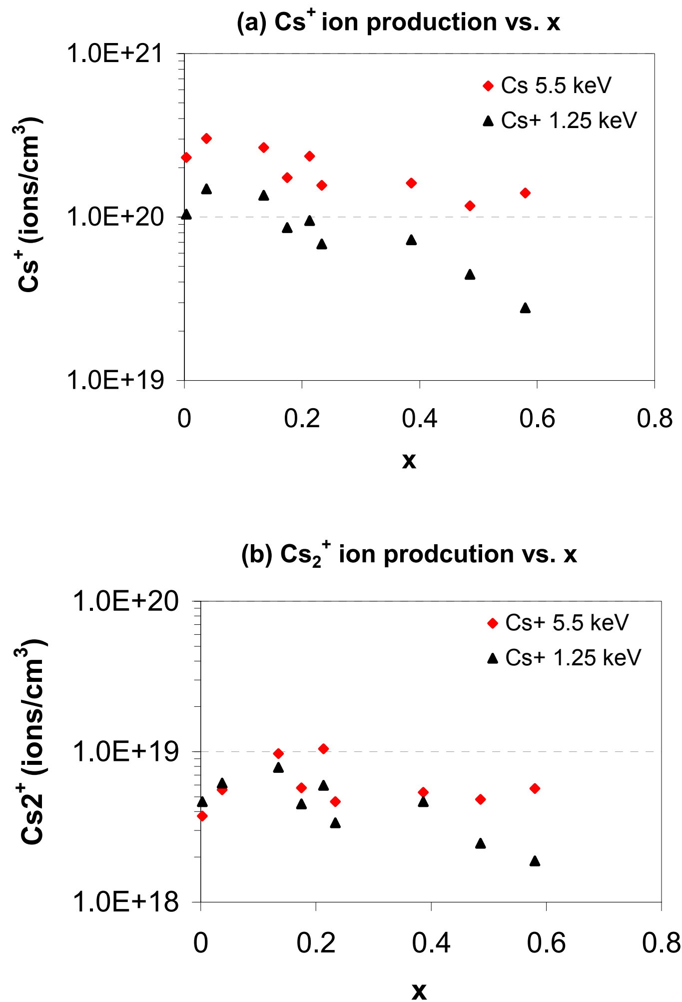


**Figure 6-12. Ion production of $Cs^+$ and $Cs_2^+$ ions at 5.5 keV and 1.25 keV impact energies**

Figure 6-13 shows the useful ion yield of the $MCs^+$ secondary ions , i.e. $GaCs^+$, $AlCs^+$, $MgCs^+$ and $NCs^+$, as a function of AlN mole fraction (x) in $Al_xGa_{1-x}N$. Other than $NCs^+$, the data of useful ion yield of $MCs^+$ suggests an obvious decreasing trend with the increase of x, which is the similar trend as the ion production of $Cs^+$. This suggests that the formation of $MCs^+$ is through the combination of $M^0$ neutral and $Cs^+$ ion, as illustrated in eq. (6-1).

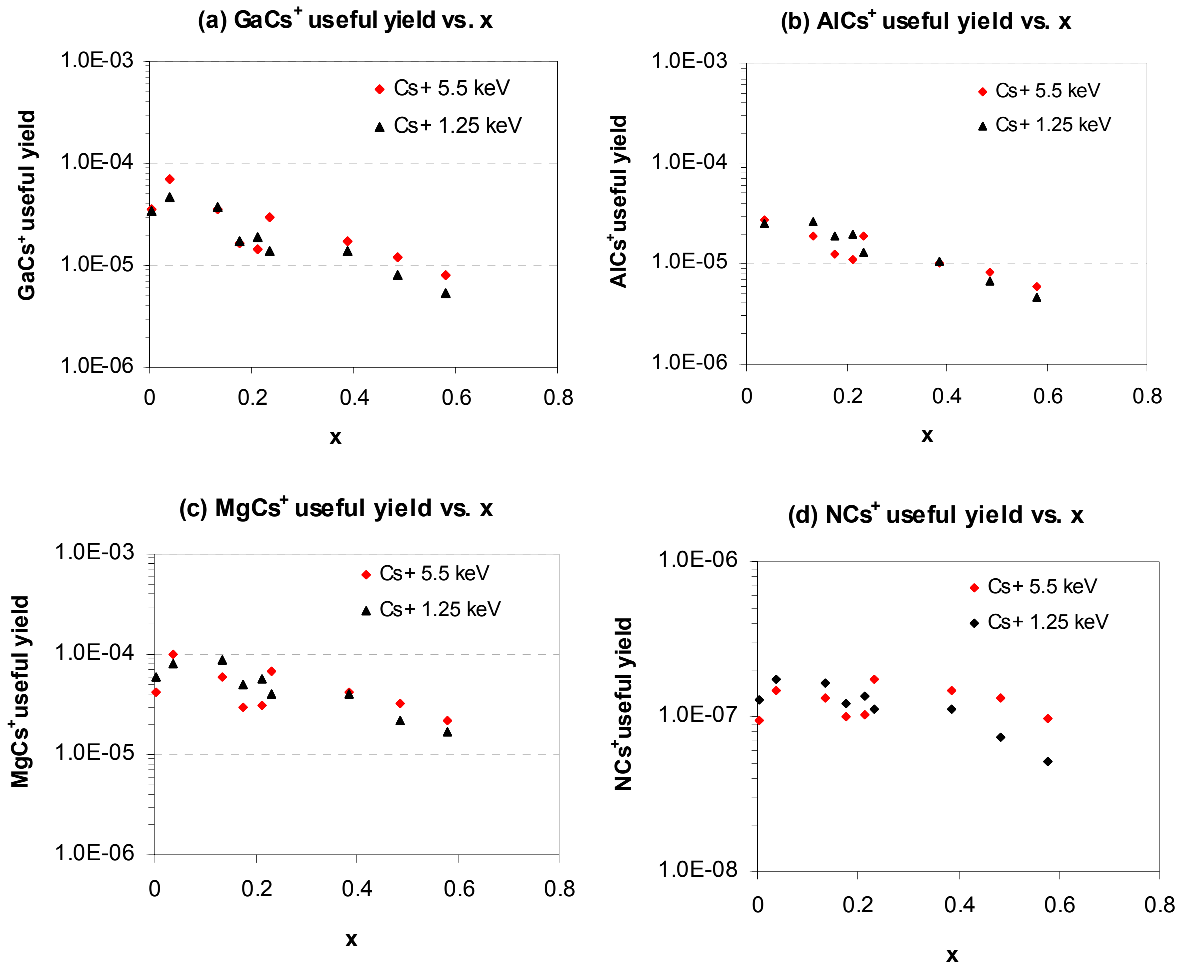


**Figure 6-13. The useful ion yield of $MCs^+$ versus AlN mole fraction (x) in $Al_xGa_{1-x}N$. (a) $GaCs^+$; (b) $AlCs^+$; (c) $MgCs^+$ and (d) $NCs^+$**

Figure 6-14 shows the useful ion yield of $MCs_2^+$ secondary ions, $GaCs_2^+$, $SiCs_2^+$ and $NCs_2^+$, as a function of AlN mole fraction in $Al_xGa_{1-x}N$. For electropositive elements such as Ga, the pattern of the secondary ion yield of $GaCs_2^+$ resembles that of the $Cs_2^+$ secondary ion yield (comparing Figures 6-12b and 6-14a). Thus the most probable formation process for $GaCs_2^+$ is the combination of $Ga^0$ and $Cs_2^+$.

For electronegative elements such as Si and N, the ion yield of $MCs_2^+$ suggests a slight increasing trend as AlN mole fraction increases, especially in the case of 5.5 keV impact energy. The trend does not resemble that of $Cs_2^+$ concentration, which suggests that the combination of neutral and $Cs_2^+$ is not the dominant formation process. On the other hand, the combination of $M^-$ and two $Cs^+$ ions is the probable dominating formation process since the ionization probability of $M^-$ ($\beta_{M-}$ in eq. (6-11)) increases with the increase of AlN mole fraction due to the increase of Cs surface concentration.

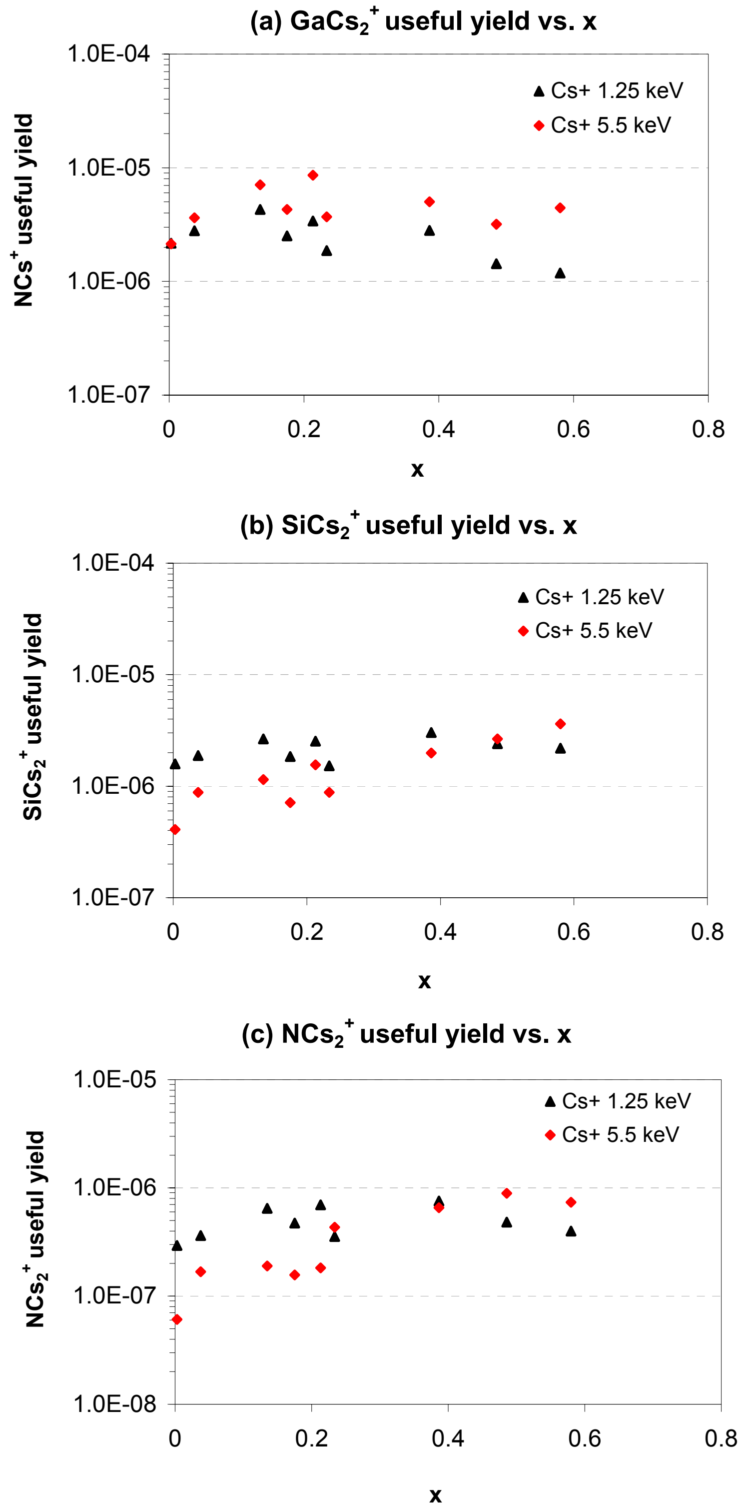


**Figure 6-14. The useful ion yield of $MCs_2^+$ versus AlN mole fraction (x) in $Al_xGa_{1-x}N$. (a) $GaCs_2^+$; (b) $SiCs_2^+$ and (c) $NCs_2^+$**

In summary, when using $Cs^+$ primary ion bombardment and positive secondary ion detection, the production of $Cs^+$ secondary ions decreases with increasing AlN mole fraction in $Al_xGa_{1-x}N$ due to the reduction of positive ionization probability resulting from the increase in Cs surface concentration. The production of $Cs_2^+$ secondary ions does not suggest an obvious increasing or decreasing trend during the sputtering of $Al_xGa_{1-x}N$ with increasing AlN mole fraction, because the increase of the surface Cs atom concentration counteracts the decrease of the positive $Cs^+$. The ion yields of $MCs^+$ secondary ions decrease with the increase of AlN mole fraction, which appears to follow the trend of $Cs^+$ secondary ion production. The trends of $MCs_2^+$ ion yields and AlN mole fraction are dependent on the electronegativity of the analyte M. From the ion yield point of view, it appears probable that the formation of $MCs^+$ is the result of the combination of neutral $M^0$ and $Cs^+$ while the formation of $MCs_2^+$ secondary ions are apparently related to the combination of $M^0$ and $Cs_2^+$ for electropositive elements and to the combination of $M^-$ and two $Cs^+$ secondary ions for electronegative elements.

## 6.6 Summary

$Al_xGa_{1-x}N$ with x from 0 to 1 was studied using $Cs^+$ primary ion bombardment by detecting positive $MCs_x^+$ cluster ions. $MCs^+$ analysis is valuable for quantification of III-nitrides due to the reduced matrix affects inherent in this technique, the capability of measuring electropositive and electronegative elements during the same analysis, and the improved depth resolution resulting from the use of a high mass primary ion and the low primary ion impact energies available on the IMS-6f when using like polarity primary and secondary ions.

Using the $MCs^+$ technique, the sputter yield decreases with increasing AlN mole fraction x, but the rate of decrease in the sputter rate versus x declines as the AlN mole fraction increases. The matrix ion intensity ratio of $AlCs^+/GaCs^+$ versus their mole fraction ratio x/(1-x) appears linear for $0 \leq x \leq 0.58$, and the inverse plot of $GaCs^+/AlCs^+$ versus (1-x)/x appears linear for $0 \leq (1-x) \leq 0.92$. This apparent linearity provides a valuable approach for the quantification of matrix element concentration in $Al_xGa_{1-x}N$ from x=0 to x=1. The RSF's of impurity species vary with AlN mole fraction depending on the matrix ions used. For $MgCs^+$ and $OCs_2^+$, normalizing to $NCs^+$ gives RSFs with small variation in the range of $0 \leq x \leq 0.58$.

For $SiCs_2^+$, normalizing to $NCs_2^+$ provides a nearly constant RSF. Normalizing to $NCs^+$ or $NCs_2^+$ provides a valuable quantification method because a) N concentration is constant over the entire range of AlN mole fraction from GaN to AlN and b) the RSF variation is small in the range of $0 \leq x \leq 0.58$.

With decreasing sputter yield, the surface concentration of Cs atoms increases which results in the reduction of positive ionization probability. The effect of this decrease in positive ionization probability is the decrease of $MCs^+$ yield and slight increase or no change in the $MCs_2^+$ yield as AlN mole fraction increases. Based on trends observed in changes of useful ion yields with AlN mole fraction in $Al_xGa_{1-x}N$, it appears probable that the formation of $MCs^+$ in $Al_xGa_{1-x}N$ is the result of the combination of $M^0$ neutral and $Cs^+$ ions. For electropositive elements, the formation of $MCs_2^+$ appears to be related to the combination of $M^0$ neutral and $Cs_2^+$; while for electronegative elements, the formation of $MCs_2^+$ is related to the combination of $M^-$ and two $Cs^+$ ions.

## 6.7 References

[1] M. R. Ray, J. E. Baker, C. M. Loxton, et al., J. Vac. Sci. Technol. A **6**, 44 (1988).

[2] M. Gauneau, R. Chaplain, and A. Rupert, J. Microsc. Spectrosc. Electron. **9**, 451 (1984).

[3] Y. Gao, Journal of Applied Physics **64**, 3760 (1988).

[4] M. Tomita, Y. Homma, and M. Inaba, Anal. Sci. **7**, 447 (1991).

[5] K. Wittmaak, Nuclear Instruments and Methods in Physics Research B **64**, 621 (1992).

[6] Y. Gao, Surface and Interface Analysis **14**, 552 (1989).

[7] C. Hongo, M. Tomita, and M. Suzuki, Applied Surface Science **144-145**, 306 (1999).

[8] G. H., J. Vac. Sci. Technol. A **12**, 452 (1994).

[9] P. K. Chu, Y. Gao, and J. W. Erickson, J. Vac. Sci. Technol. B **16**, 197 (1998).

[10] Y. Gao, Y. Marie, F. Saldi, et al., Secondary Ion Mass Spectrometry, SIMS IX, edited by A. Benninghoven et al., Wiley, Chichester, p.406 (1994).

[11] M. Kachan, J. Hunter, D. Kouzminov, et al., Applied Surface Science **231-2**, 684 (2004).

[12] T. Mootz and F. Adams, International Journal of Mass Spectrometry and Ion Processes **152**, 209 (1996).

[13] T. Mootz, A. Adriaens, and F. Adams, International Journal of Mass Spectrometry and Ion Processes **156**, 1 (1996).

[14] C. W. Magee, W. L. Harrington, and E. M. Botnick, International Journal of Mass Spectrometry and Ion Processes **103**, 45 (1990).

[15] H. Gnaser and H. Oechsner, Fresenius Journal of Analytical Chemistry **341**, 54 (1991).

[16] Y. Gao, Y. Marie, F. Saldi, et al., Secondary Ion Mass Spectrometry, SIMS IX, edited by A. Benninghoven et al., Wiley, Chichester, p.382 (1994).

[17] Y. Marie, Y. Gao, F. Saldi, et al., Surface and Interface Analysis **23**, 38 (1995).

[18] S. Sarkar and P. Chakraborty, Nuclear Instruments & Methods in Physics Research Section B-Beam Interactions with Materials and Atoms **212**, 364 (2003).

[19] K. Wittmaak, Nuclear Instruments and Methods in Physics Research Section B: Beam Interactions with Materials and Atoms **85**, 374 (1994).

[20] T. Wirtz, B. Duez, H. N. Migeon, et al., International Journal of Mass Spectrometry **209**, 57 (2001).

[21] R. G. Wilson, F. A. Stevie, and C. W. Magee, *Secondary Ion Mass Spectrometry: a Practical Handbook for Depth Profiling and Bulk Iimpurity Analysis*, 1989).

[22] Y. Gao, S. Mitha, C. Chung, et al., Secondary Ion Mass Spectrometry, SIMS XI, edited by G. Gillen, R. Lareau, J. Bennett and F. Stevie, John Wiley & Sons, Chichester, p.193 (1997).

[23] D. L. Lefforge, Y. L. Chang, M. Ludowise, et al., Mat. Res. Soc. Symp. Proc. **510**, 155 (1998).

[24] M. Schumacher, CAMECA Instruments, computer program.

[25] CAMECA, IMS-6F User's Manual: Energy Slit, 2-14 (1996).

[26] B. M. Gurmin, Y. A. Ryzhov, and I. I. Shkarban, Bulletin of the Academy of Sciences of the USSR **33**, 752 (1970).

# 7 Comparison of SIMS Quantification Techniques for $Al_xGa_{1-x}N$

## 7.1 Introduction

Three different SIMS analytical techniques were discussed in previous chapters for quantitative characterization of both matrix and impurity elements in $Al_xGa_{1-x}N$, i.e. using an $O_2^+$ primary beam with positive secondary ion detection and a $Cs^+$ primary beam with negative and $MCs^+$ secondary ion detection.

The $O_2^+$ primary beam with positive secondary ion detection is used when high sensitivity of electropositive elements is required. $O_2^+$ has the advantage of providing sufficient sensitivity for the quantification of both matrix (Al, Ga) and the most common n-type (Si) and p-type (Mg) impurities during the same analysis with good sensitivity. The $Cs^+$ primary beam with negative secondary ion detection is used when high sensitivity of electronegative elements such as O is required. The $MCs^+$ method, the detection of positive $MCs_x^+$ (where x=1 or 2) clusters using $Cs^+$ as the primary ion beam, has the advantage of detecting both electropositive and electronegative elements simultaneously with reasonable detection limits.

In this chapter, the quantification in $Al_xGa_{1-x}N$ using these three techniques will be compared, and the uncertainty of the measured parameters will be discussed. The analyses discussed in the previous chapters were performed using primary ions with both high and low energies. The high primary ion beam energy provided higher sputter rates while the low energy ions provided higher depth resolution. For matrix ion intensity ratios and impurity RSF's as a function of x in $Al_xGa_{1-x}N$, the trend with high and low energies was similar. In this chapter, matrix ion intensity ratio and impurity RSF data obtained using high energy (5.5 keV and 14.5 keV impact energy) primary ions are compared for the three techniques.

## 7.2 Quantification in $Al_xGa_{1-x}N$

### 7.2.1 Sputter Yield

The investigation of sputter yields of the materials is important not only for film thickness determination and elemental quantification, but also to aid in the understanding of

the ionization mechanisms of the sputtered secondary ions, since the sputter yield affects the steady state surface concentration of primary species. The higher the sputter yield, the lower the surface concentration of the primary ion species. A change in the surface concentration of primary species alters secondary ion yields.

Sputter yields obtained for the SIMS analytical conditions described in the previous chapters for the $Al_xGa_{1-x}N$ samples are presented in figure 7-1, where the sputter rate is normalized to the primary ion current and sputter area with units of $\mu m^3/(s.nA)$. Figure 7-1a is in linear scale, and figure 7-1b is in log scale. Note that the normalized sputter rate is proportional to the sputter yield Y by the factor of 14.68, as shown in eq. (7-1)

$$1\,\mu m^3/(s.nA) = \frac{1E-12\,cm^3}{6.24E19\,ions} * N_{AlGaN} = 14.68\ \text{atoms/ion} \qquad \textbf{(Equation 7-1)}$$

where $N_{AlGaN}$ is the atomic intensity of AlGaN in atoms/cm$^3$.

As can be seen in Figure 7-1, sputter yields decrease as the AlN mole fraction (x) is increased but the rate of decrease in the sputter rate versus x declines as the AlN mole fraction increases.

Using the log scale in figure 7-1b the variation of the sputter rates with the change of x in $Al_xGa_{1-x}N$ can be seen more clearly. Sputter rate variations over the range of $0 \le x \le 0.58$ are similar for similar primary ion energies (e.g. $Cs^+$ 5.5 keV and $Cs^+$ 6.0 keV). Bombardment with primary ions having high energy results in larger variation of the sputter rate over the range of $0 \le x \le 0.58$ (e.g. $Cs^+$ 14.5 keV); Bombardment with primary ions having low energy and high angle of incidence results in smaller variation (e.g. $Cs^+$ and $O_2^+$ at 1.25 keV and 48.5°).

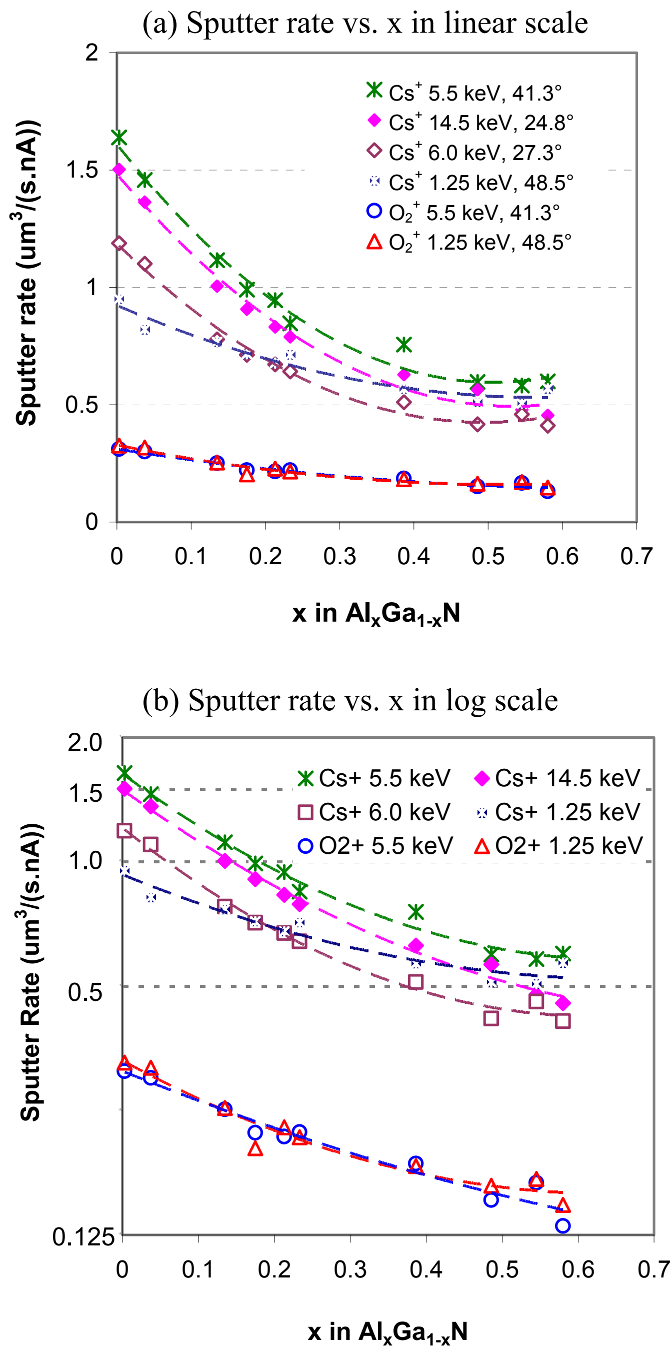


**Figure 7-1. Sputter rate as a function of x in $Al_xGa_{1-x}N$ using $Cs^+$ and $O_2^+$ at different energies and different angle of incidence. Figure (a) is in linear scale and (b) in log scale.**

It has been known that sputter yield depends on the bombardment parameters, i.e. the mass, the energy and the angle of incidence of the primary ions.[1] From figure 7-1, it can be seen that $Cs^+$ sputters faster than $O_2^+$ at the investigated impact energies, due to the higher

mass of Cs. Although the increase in the $Cs^+$ sputter yield for the 5.5keV (10 kV primary ion/4.5 kV sample bias) versus the 14.5keV (10 kV primary ion/-4.5 kV sample bias) impact energy may appear counter intuitive, the difference in sputter yields can be attributed to the 41.3° (with respect to sample normal) impact angle of the 5.5 keV $Cs^+$ versus the 24.8° impact angle of the 14.5keV $Cs^+$. Sputter yield generally increases nearly linearly with energy of primary ions at low energies (from tens of eV to a few hundred eV). Sputter yield continues to rise above the linear portion but with decreasing slope, finally reaching either a maximum or a plateau. The plateau region is generally from around 10 keV to 30 keV.[2] Above the plateau region, or peak, the sputter yield begins to decline. The sputter yield also increases with the angle of incidence until reaching a maximum at around 60° from normal, and then the yield decreases until reaching zero at 90° from normal. In the range of energies investigated (1.25 keV to 14.5 keV), sputter yield behavior is in either the region of yield increase with the energy of primary ions or in the low slope or plateau region. Angles of incidence used are in the range of angles where yield increases rapidly with angle (24.8° to 48.5°).

The sputter yield also depends on sample characteristics such as mass, density and surface binding energy.[1] It has been found that the sputter yields of elemental targets show a periodicity effect over the periodic table, lower yield for the most open electronic arrangements and higher yields for elements which have filled d-shells.[2] Although Al and Ga have the same outer shell arrangement, the sputter yield of Ga is always higher than that of Al probably due to the smaller binding energy of the Ga-Ga bond (112.1±7 KJ/mol at 298K) compared with the Al-Al bond (133±6 KJ/mol).[3,4] For alloys and compounds, the total sputter yield $Y_t$ of a multi-component sample can be expressed as the sum of the partial sputter yields $Y_i$ of the constituents:[1]

$$Y_t = \sum Y_i \qquad \textbf{(Equation 7-2)}$$

Although there is no simple relation between the sputter yield of a pure elemental target and the sputter yield of the same element in a multi-component target, qualitatively the partial sputter yield of an element in a multi-component sample is higher if its sputter yield is as a pure element target is higher. Thus, in the compounds with varying Al and Ga concentration, higher the Al concentration should result in lower the sputter yields. In

$Al_xGa_{1-x}N$, the sputter yield decreases when x is increased similar to results previously reported for $Al_xGa_{1-x}As$.[5] Note that at low energy and high angle of incidence from normal (e.g. $Cs^+$ 1.25 keV at 48.5°) the sputter yield change from x=0~0.58 is smaller than at high energy and low angle of incidence from normal.

### 7.2.2 Quantification of Matrix Species

Quantification of matrix species in $Al_xGa_{1-x}N$ can be achieved using calibration curves of matrix ion intensity ratio as a function of AlN mole fraction. In the range of $0 \le x \le 0.58$, the matrix ion intensity ratios of $Al^+/Ga^+$ obtained using $O_2^+$ and the matrix ion intensity ratios of $AlCs^+/GaCs^+$ obtained using $MCs^+$ both appear to increase linearly with matrix mole fraction ratio (x/(1-x)), as shown in figure 7-2a. However, the ratios of $AlN^-/GaN^-$ using $Cs^+$ and $AlN^+/GaN^+$ using $O_2^+$ appear to increase linearly with AlN mole fraction x instead of mole fraction ratio (figure 7-2b). Future work is needed to understand the cause of this difference in behavior for $AlN^{\pm}/GaN^{\pm}$.

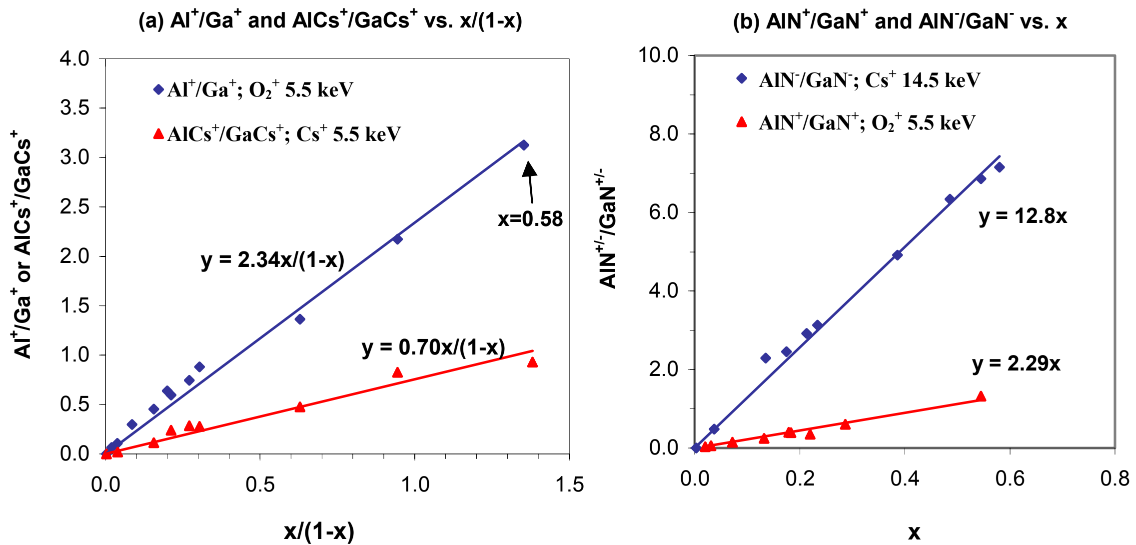


**Figure 7-2. Matrix ion intensity ratio versus mole fraction ratio or AlN mole fraction in $Al_xGa_{1-x}N$ under different analysis conditions**

The apparently linear relationship of matrix intensity with mole fraction allows the use of a single standard for determination of the AlN mole fraction in an unknown sample simplifying matrix element quantification. When x is greater than 0.58, the matrix ion

intensity ratios of Al-containing ions and Ga-containing ions increase faster and the curves no longer have a linear correlation with x or x/(1-x). However, if plotted inversely, i.e. the ratio of Ga-containing ions over Al-containing ions as a function of GaN mole fraction (1-x) or mole fraction ratio (1-x)/x, the linear range can be extended to x=1. The relationship of $Ga^+/Al^+$ or $GaCs^+/AlCs^+$ versus (1-x)/x appears linear over the range of $0 \le (1-x) \le 0.86$ GaN mole fraction, or $0.14 \le x \le 1$ AlN mole fraction (see figure 7-3). The relationship of $GaN^{\pm}/AlN^{\pm}$ versus (1-x) appears linear in the range of $0 \le (1-x) \le 0.61$, or $0.39 \le x \le 1$ (see figure 5-4).

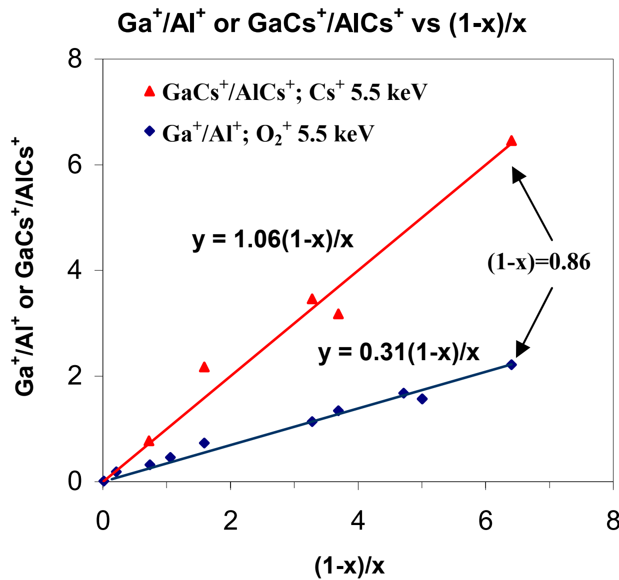


**Figure 7-3. The reverse plot of matrix ion intensity ratios vs. atomic concentration ratios**

The overlap of these apparently linear ranges allows quantification of matrix over the entire range of $Al_xGa_{1-x}N$, i.e. from $0 \le x \le 1$, under these analytical conditions using single standard sample.

### 7.2.3 Quantification of Impurity Species

The relative sensitivity factor (RSF) method is normally used for quantitative analysis of trace impurity species in SIMS. The quantification of impurity species in $Al_xGa_{1-x}N$ can be achieved using the calibration curves of impurity RSF's as a function of AlN mole fraction. The RSF's for Mg and Si were computed by normalizing the intensities of the

various secondary ion species to selected matrix ions. The matrix and impurity secondary ions monitored for different analysis conditions are listed in table 7-1.

**Table 7-1. List of impurity and matrix secondary ions for the analysis conditions**

| Primary Beam | Secondary Polarity | Impurity Secondary Ions | Matrix Secondary Ions |
|---|---|---|---|
| $O_2^+$ | positive | $Mg^+$ and $Si^+$ | $Ga^+$ |
| $Cs^+$ | negative | $MgN^-$ and $Si^-$ | $GaN^-$ |
| $Cs^+$ | positive | $MgCs^+$ and $SiCs_2^+$ | $GaCs^+$, $NCs^+$, $NCs_2^+$ |

The comparison of the respective RSF's versus AlN mole fraction obtained using the SIMS analytical conditions described in previous chapters is presented in Figure 7-4. All RSF's appear to have an exponential correlation with AlN mole fraction. The RSF data for $Mg^+$ and $Si^-$ are in agreement with results previously reported for AlN mole fraction of $0 \leq x \leq 0.21$.[6, 7]

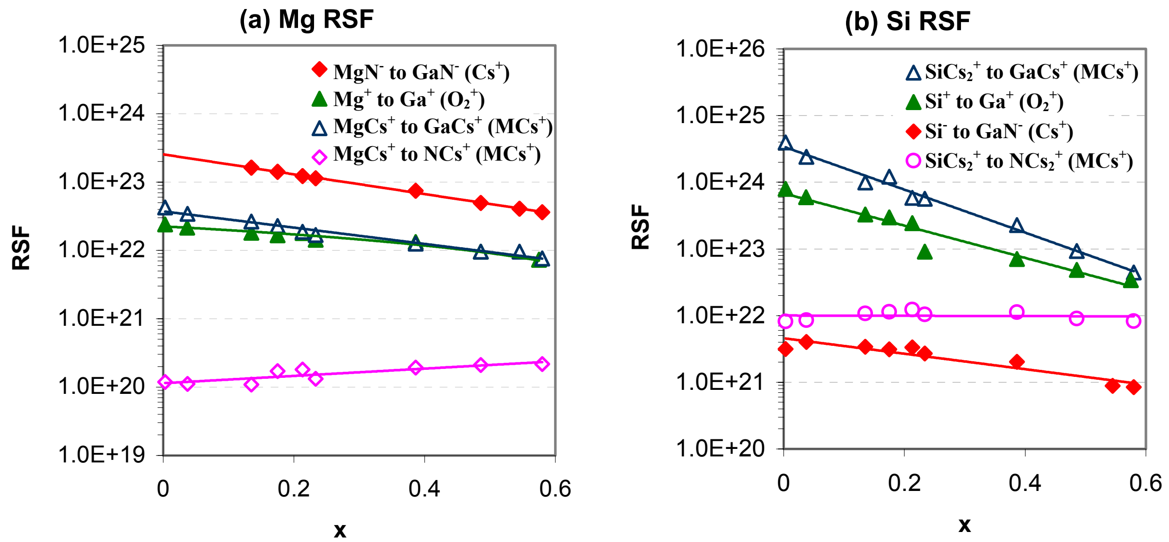


**Figure 7-4. RSF's of Mg (a) and Si (b) under $O_2^+$ and $Cs^+$ beam versus AlN mole fraction**

RSF's normalized to Ga-containing matrix ions decrease when x is increased, mainly because the decrease in matrix ion intensity resulting from the reduction of Ga concentration as the AlN mole fraction x increases. In $Al_xGa_{1-x}N$, the concentration of N is independent of

x, and RSF's normalized to N-containing matrix ions show significantly less change with x. For example, RSF's of $MgCs^+$ normalized to $NCs^+$ increase slightly when x is increased (figure 7-4a), and those of $SiCs_2^+$ normalized to $NCs_2^+$ show no measurable change with x (figure 7-4b). The normalization to N-containing matrix ions provides a valuable quantification method in $Al_xGa_{1-x}N$ with x from 0 to 1.

The exponential correlation of other RSF's, calculated via normalizing to Ga-containing matrix species, with the AlN mole fraction is consistent with the exponential correlation of ionization probability with the local surface work function.[8] When AlN mole fraction is increased, the increase in the surface concentration of primary species resulting from sputter yield reduction alters the local surface work function and the ion yields.[9] The effect of surface concentration of primary species on the ion yield enhancement of different species varies, which causes the RSF variation with x. If the ion yields of impurity and matrix species are affected similarly by the surface concentration of primary species, e.g. $SiCs_2^+$ and $NCs_2^+$, then the RSF's do not change with x. In this case, a standard sample with any AlN mole fraction can be used for quantification of Si in $Al_xGa_{1-x}N$.

## 7.3 Uncertainty Analysis

The data presented in the previous sections have uncertainties resulting from sample composition uncertainty, measurement errors, and system errors generally associated with SIMS instrument performance such as primary ion beam instability, secondary ion transmission efficiency, etc. The uncertainties related to sample matrix composition, sputter rate, matrix ion intensity ratio and impurity RSF will be analyzed.

### 7.3.1 Sample Composition Measurement

Sample matrix compositions were measured by LEXES (Low Energy X-Ray Emission Spectroscopy). LEXES is a modified version of a multiple-spectrometer WDS (Wavelength Dispersive Spectrometer) X-Ray analysis. The accuracy of the measurement depends on the accuracy of the standard and the repeatability of the technique. For a LEXES instrument with three Wavelength Dispersive Spectrometers, a typical accuracy of better than 5% in compositional measurement and a 1-5% precision for a measurement time of 1 min can be achieved.[10] For this particular measurement of AlN mole fraction in $Al_xGa_{1-x}N$, pure

Al and AlN compound (Ga implanted) standard samples were used, and correction was made by an IntriX model based on $\phi(\rho z)$ correction. The LEXES analyst estimated that the accuracy of the measurement is better than a few percent. It is reasonable to assume the accuracy of the AlN mole fraction in the samples for this work measured by LEXES is within ±5%.

### 7.3.2 Sputter Rate Error Analysis

The main error sources for sputter rate determination are primary beam instability and crater depth measurements. The primary beam current density affects the sputter rate in a directly proportional manner. The primary beam is often not completely stable during the long times required for some of the experiments. Generally speaking, the $O_2^+$ beam is less stable that the Cs primary ion beam. Although the excitation strength of lenses in primary column were varied to keep the primary beam current (measured by a FC in primary column) the same during analysis, the beam density may change.

The Tencor P-20 stylus profilometer specification indicates that this instrument has a repeatability of 8 Angstroms maximum standard deviation ($1\sigma$).[11] Accuracy of depth measurement by a P-20 is about 1 nm for a flat and smooth sample.[12] Based on this specification, the repeatability and accuracy of the profilometer with respect to the sputter rate measurement should not be a limiting factor of the sputter rate calculations.

Although Au coating affects sputter rate calibration because Au has higher sputter yield than the $Al_xGa_{1-x}N$ sample,[13] the calibration error is small since the Au coating is around 10 nm compared to more than 500 nm total sputtered depth. Assume that Au sputters two times faster than $Al_xGa_{1-x}N$, the error caused by the 10nm Au coating is less than 1%.

To estimate the precision of sputter rate, samples with the same composition were sputtered to similar depth (judging from the ion implantation depth profile) and the sputter rates were computed from the measured crater depth. The largest variation were found when using $O_2^+$ bombardment with low impact energy (1.25 keV) since $O_2^+$ beam is less stable than $Cs^+$ beam, especially at low energy. One sample was sputtered using $O_2^+$ at 1.25 keV and 50 nA beam current with rastered area of 200μm by 200μm. The first two craters were sputtered one after another, the third one 20 hours later (the $O_2^+$ was on all the time to sputter other samples). Sputter rates obtained were illustrated in table 7-2. Although the sputter rate

varied only 2% with two consequent sputtering, the overall variation with the whole 20 hours of sputtering was 7%.

**Table 7-2. Estimation of the error of sputtering rate of $Al_xGa_{1-x}N$ with x=0.58 using $O_2^+$ beam at 1.25 keV and 50 nA beam current with raster area of 200µm by 200µm**

| Sample ID (x=0.58) | Sputter Rate 1 (nm/s) | Sputter Rate 2 (nm/s) | Sputter Rate 3 (nm/s) | Average Sputter Rate | Error |
|---|---|---|---|---|---|
| M1082 | 0.127 | 0.130 | 0.114 | 0.123 | ±7% |

Note that the above data are for the worst case i.e. using many hours of low energy $O_2^+$ beam. For $Cs^+$ beam with high energy, sputter rates should be very stable since the beam density is stable. Five pieces from the same sample were loaded and three sites were sputtered in each piece with $Cs^+$ at 14.5 keV and 30 nA beam current with raster area of 180µm by 180µm. The sputter rate variation was 1.3% as shown in table 7-3.

**Table 7-3. Estimation of the error of sputtering rate of $Al_xGa_{1-x}N$ with x=0.18 using $Cs^+$ beam at 14.5 keV and 30 nA beam current with raster area of 180µm by 180µm**

| Sample ID (x=0.18) | Mean Sputter Rate (nm/sec) | Standard Deviation (STDEV) | Relative Standard Deviation (RSD) |
|---|---|---|---|
| GaN-4 | 1.02 | 1.33E-2 | ±1.3% |

### 7.3.3 Matrix Ion Intensity Ratio and RSF Error Analysis

The measurement of matrix ion intensity was performed by using the "CURVE PROCESSING" program in CAMECA IMS-6F software. The mean values of matrix ion intensities are obtained by the SURFACE function in the program.[14] Within the lower and higher limits of the X (time) interval on the depth profile defined by the operator, this function computes the "*mean*" of the selected Y (ion intensity) values. Once the mean values of ion intensity for the two matrix species in the steady state region were obtained, their ratio can be calculated.

The calculation of RSF of impurity species is also performed by using the "CURVE PROCESSING" program in CAMECA IMS-6F software. The RSF's are computed from the dose of the species of interest and the integrated number of detected ions by specifying the

minimum depth, maximum depth and background intensity to integrate.[15] The relationship of RSF can be computed using the following relationship: [15]

$$RSF = Dose / \int_{depth\,\min}^{depth\,\max} (I_i / I_m), \quad \text{(integral} \int \text{over [depth minimum, depth maximum])}$$

One error of matrix ion intensity ratio and RSF results from incomplete charge neutralization during the depth profile (see section 3.5 for charge neutralization). For insulating samples, the electron beam from the normal incidence electron gun (NEG, See section 3.2.1.4) was used to neutralize the positive charge buildup on the sample. For positive secondary ion charge neutralization, the electron beam is directed to an area adjacent to but not touching the area over which the primary on beam is rastered. However, the NEG beam position is affected by the strong magnetic field of the mass spectrometer which varies with mass and thus varies cyclically during a depth profile of multiple elements. When elements with a wide range of mass are monitored in one profile, the degree of neutralization the various elements in a depth profile may change slightly, particularly if the NEG is tuned to relatively low energy (e.g. 2.75 keV). Incomplete charge neutralization can reduce the measured secondary ion intensities of the elements (See section 4.5.1). Figure 7-4 shows the depth profile of $^{27}Al^+$ and $^{69}Ga^+$ under $O_2^+$ bombardment with 1.25 keV impact energy. In this experiment, the electron current to the sample ($I_{sample}$) was intentionally reduced by varying the bias of the NEG source (e-Wehnelt). As the electron current is reduced, the intensity of secondary ions decreases and the ratio of $^{27}Al^+$ and $^{69}Ga^+$ also changes due to incomplete charge neutralization. When the electron density is reduced, the excess charge in the sample may not be completely compensated. The excess charges alter the potential of the sputtered surface, which reduces the transmission of the various secondary ions.

Although the error caused by the charge neutralization can be significant, the magnitude of the error is difficult to estimate. In the experiments for this work, the electron beam intensity and position are aligned such that the intensity of both the highest and lowest mass is maximized to minimize the effect of incomplete or over charge compensation in an effort to minimize this error.

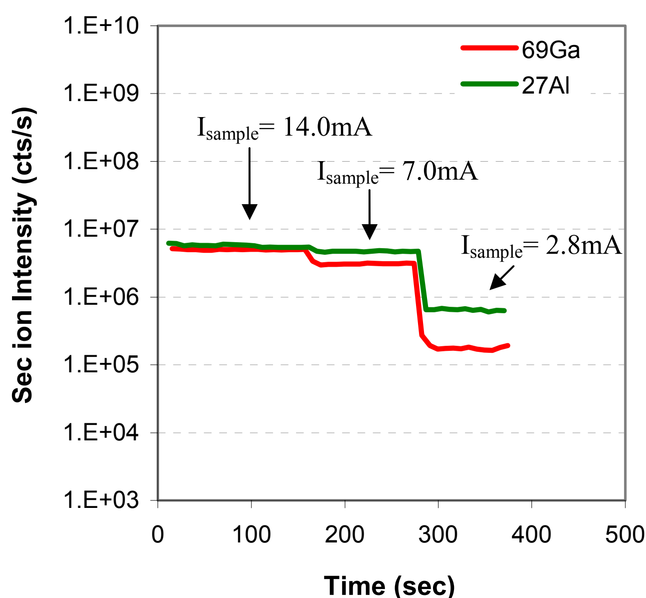


**Figure 7-4. The effect of electron beam intensity on the matrix ion intensity ratio in $Al_xGa_{1-x}N$ with x=0.39 using $O_2^+$ bombardment and positive secondary ion detection at 1.25 keV impact energy. $I_{sample}$ is the electron current to the sample which is the algebraic sum of the electrons impinged to the sample and any secondary/backscattered electrons emitted.**

Another important possible source of error affecting the calculation of impurity RSF's is from implant dose uncertainty. All impurity RSF's were calculated using the implants in the various AlGaN samples. Implant doses are measured during the implantation process and thus provided by the ion implanter. A typical implantation dose with error of 10% is commonly accepted in a dose measurement.[16] Table 7-3 gives the results of the comparison of dose reported by the implanter and measured dose as compared to an SIMS lab internal standard (an implanted sample having the same sample matrix and which is routinely used in the SIMS laboratory for comparison).

**Table 7-4. Comparison of nominal and measured dose after ion implantation**

| Implanted Species | Nominal Dose (atoms/cm$^2$) | Measured dose (atoms/cm$^2$) | Error comparing to our laboratory standard |
|---|---|---|---|
| 24 Mg | 2E14 | 2.20e14 | 10% |
| 16 O | 5E15 | 5.15e15 | 3% |
| 29 Si | 1E15 | 1.23e15 | 23% |

The background level of an impurity element present in a sample matrix prior to implantation is also a source of error for RSF computation. The back ground levels of $^{16}O$ and $^{28}Si$ present in many of the samples implanted for use as standards are in the $10^{17}$ to $10^{18}$ atoms/cm$^3$ range and they vary with depth in general having higher contamination levels near the sample surface and near the buffer layer or substrate. In the worst case, the background of O is one order less than the peak concentration. In figure 7-5, $O^-$ profiles in $Al_xGa_{1-x}N$ film with x=0.49 are compared before and after $^{16}O$ implantation using $Cs^+$ primary ion and negative secondary ion detection at 14.5 keV impact energy. The red curve is O contamination before ion implantation; the green curve is O profile after 5E15 atoms/cm$^2$ ion implantation with 150 keV energy. The green shaded area is the area integrated for dose calculation when computing RSF. The red shaded area is not included in the calculation which, in this case can introduce an error of up to 5%.

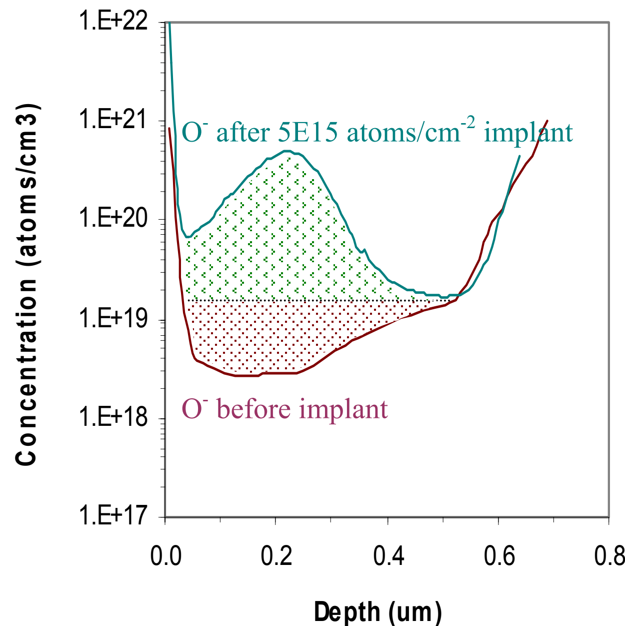


**Figure 7-5. Comparison of O profile in $Al_xGa_{1-x}N$ film with x=0.49 before and after $^{16}O$ implantation using $Cs^+$ primary ion and negative secondary ion detection at 14.5 keV impact energy. Red curve is O contamination before ion implantation; green curve is O profile after 5E15 atoms/cm$^3$ ion implantation with 150 keV energy. The green shaded area is the area integrated for dose calculation when computing RSF.**

The analysis location in the CAMECA IMS-6f sample holder can significantly affect the collection efficiency for secondary ions. These changes in secondary ion collection efficiency result form differences in secondary ion extraction efficiency resulting from inhomogeneities in the electric field produced by the biased sample holder. In the CAMECA IMS-type SIMS instrument, a high extraction field, typically 1.0 kV/mm, is used between the sample and a grounded extraction plate (immersion lens cover plate). These extraction fields differ as a function of position of the sample with respect to the windows in the sample holder mask and with respect to the edge of the sample holder itself. These differences in surface potential alter the secondary ion energy distribution and thus the extraction efficiency. In the 5-window holder typically used for SIMS analysis with the window size 2 mm x 10mm, as shown in figure 7-6, it was determined that variation of the extraction efficiency in the different sample positions can be large. Five samples with the same composition were loaded in the 5-window holder and depth profiles of matrix and impurity elements from 15 locations were acquired using $Cs^+$ and negative secondary ion detection at 14.5 keV impact energy. The results are shown in table 7-4 and figure 7-7.

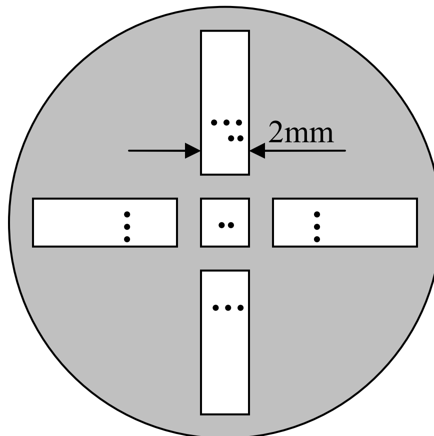


**Figure 7-6. A typical 5-window holder for SIMS analysis. Dots represent the locations of analysis.**

Although the absolute matrix ion intensities vary by as much as 31%, the matrix ion intensity ratio of $AlN^-/GaN^-$ varies only 4.5%. RSF's were calculated by normalizing to $GaN^-$ matrix ion. The RSF's of impurity molecular ions, such as $MgN^-$ which has similar configuration with the matrix ion, have variation less than 6%; however the RSF's of impurity atomic ions, such as $O^-$ and $Si^-$, have variations of 23.7% and 19.4% (see table 7-4).

These large differences in relative error are results from the different energy distributions of atomic and molecular ions. The sputtering process produces secondary ions with a range of kinetic energies. The energy distributions are distinctly different for atomic and molecular ions. Molecular ions have relatively narrow energy distributions because they have kinetic energy in internal vibrational and rotational modes whereas atomic ions have all kinetic energy in translational modes.[17] In the quantitative SIMS analyses, if RSF's were generated using atomic secondary ion normalized to atomic matrix reference secondary ion or molecular secondary ions normalized to molecular matrix reference ions, the error from this source can be reduced to less than 5%.

**Table 7-5. The variation of secondary ion intensity and the calculated RSF's using 5-window holder and bombarded with $Cs^+$ at 14.5 keV impact energy**

| Secondary Ions | $AlN^-$ | $GaN^-$ | $AlN/GaN^-$ | $Si^-$ RSF | $O^-$ RSF | $MgN^-$ RSF |
|---|---|---|---|---|---|---|
| RSD | 30.9% | 31.0% | 4.5% | 19.4% | 23.7% | 4.8% |

Note: The RSF's are computed by normalizing to matrix ion $GaN^-$. RSD is relative standard deviation.

In this experiment, $^{29}SiN^-$ has a strong mass interference from $AlO^-$ which needs mass resolution of m/Δm=14,333 to separate. This resolution is not practical using the IMS-6f due to the resulting very low mass spectrometer transmission forcing use of $^{29}Si^-$ rather than $^{29}SiN^-$. For electronegative elements such as Si and O, the atomic ion yield ($Si^-$ and $O^-$) is one to two orders magnitude higher than the corresponding molecular ion yield ($SiN^-$ and $ON^-$), so the detection of atomic ions yields high detection sensitivity. Matrix ion of $GaN^-$ was used instead of $Ga^-$ because $GaN^-$ has higher yield and the $Ga^-$ ion intensity is more sensitive to the instrumental tuning conditions and produces a wider spread in the RSF's.[18]

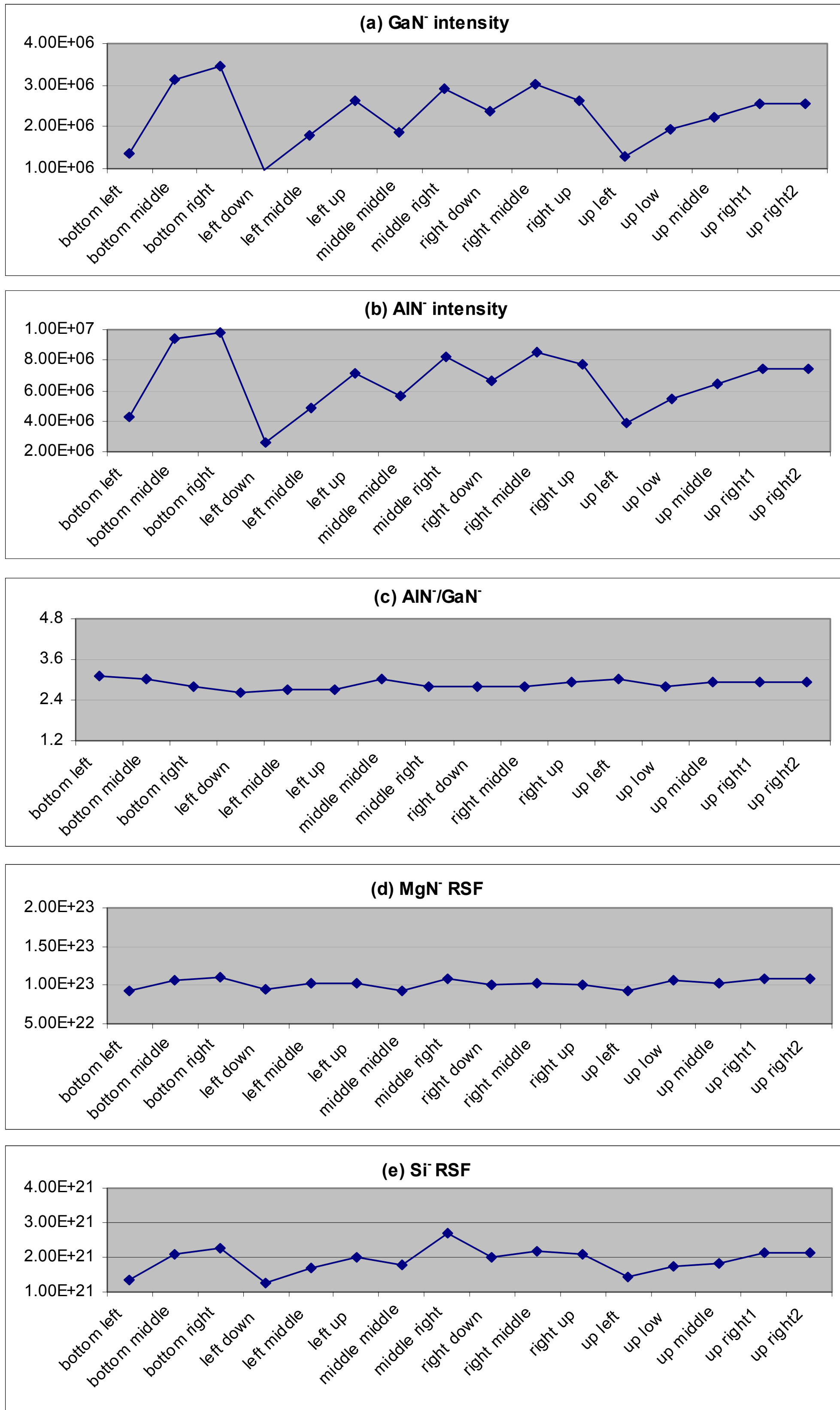


**Figure 7-7. The variation of secondary ion intensities and the calculated RSF's**

After determination of the errors due to secondary ion extraction efficiency variations with respect to sample holder position presented above, an effort was made to determine if there were instrument adjustments or modifications that would reduce these errors. It was determined that careful adjustment of the immersion lens strip with respect to the IMS-6f mass spectrometer optical axis reduced the extraction efficiency error. In addition, the use of sample holders configured as shown in figure 7-8 also reduced this variation. In this holder design, there is only one window in the center with larger open area so the analyzed location can be further away the edge of the window. With the adjusted immersion lens strip position and the holder design shown in figure 7-8, a Si sample was loaded and depth profiles of atomic ion ($Si^-$) and molecular ion ($Si_2^+$) from multiple locations were acquired using $Cs^+$ and negative secondary ion detection at 14.5 keV impact energy. It was shown that an atomic ion intensity variation of 5% can be achieved across the holder within the area 2 mm away from the window edge, as shown in the shaded area in figure 7-8. The variation of atomic and molecular ion intensity ratio is also 5%.

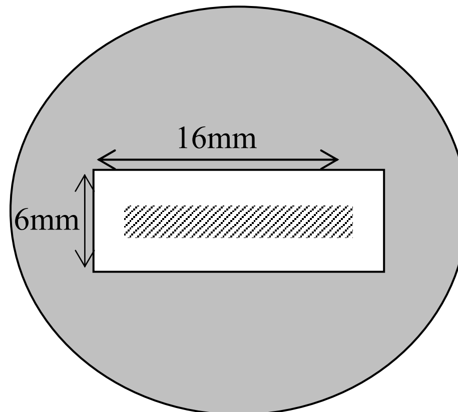


**Figure 7-8. A modified 1-window holder for SIMS analysis. The ion intensity variation is less than 5% in the shaded area which is 2 mm away from the window edge.**

Note that the sample size required for the 1-window holder is larger than for the 5-window holder. In the case that the available sample size is limited, the 5-window holder is still often used. In this project, some of the experiments were performed using the 1-window holder, others were performed using the 5-window holder and the immersion lens cover plate position with the variation of table 7-4.

### 7.3.4 Ion Yield Error Analysis

Ion yield is the secondary ion yield obtained for an element with respect to all species of that element sputtered from the sample over the region from which secondary ions are extracted. Useful ion yield is a measure of the number of detected secondary ions for a species under a specified set of sputtering conditions so it is greatly affected by the sample position. As shown in table 3-7 and figure 3-17, the variation resulting from differences in secondary ion extraction efficiency with respect to position of the sample on the sample holder is 31% by using the 5- window holder. Other factors that affect the useful ion yield are charge neutralization, dose measurement, etc. as discussed above. Since the ion yield data is only used qualitatively to understand the ionization mechanism, errors in ion yield measurements do not affect quantification.

### 7.3.5 Summary of Experimental Uncertainty

In summary, the AlN mole fraction in $Al_xGa_{1-x}N$ measured by LEXES is estimated to be within 5%. The error sources for sputter rate are mainly primary beam instability and crater measurement which is estimated to be within 7% in the worst case. For matrix ion intensity ratio, impurity RSF and useful ion yield, the errors mainly from secondary ion intensity variations resulting from incomplete charge neutralization and from changes in secondary ion extraction efficiency resulting from sample position variations. Although incomplete or over charge neutralization affects these parameters, it is hard to estimate the error. In the experiments in this project, efforts are made to fully neutralize the excess charge. Different sample positions have different surface potential depending on the distance from the edge of the sample holder, which affects the ion extraction of atomic or molecular secondary ions differently due to differences in their secondary ion energy distribution. In an experiment using a 5-window holder under 14.5 keV $Cs^+$ with negative ion detection, the ion transmission varies as much as 31%. However the matrix ion intensity ratio varies less than 5%, and the RSF's of similar molecular impurity ion normalized to the molecular matrix vary less than 5%, while the RSF's of atomic impurity ion normalized to the molecular matrix vary from 12% to 26%. The estimated errors are summarized in table 7-5, where the total error is the square root of the sum of squares of the individual errors from every source.[19, 20]

**Table 7-6. Summary of experimental uncertainty**

<table>
<tr><th></th><th colspan="2">Error Sources</th><th>Error in Worst Case</th><th>Total Error</th></tr>
<tr><td>Matrix composition</td><td colspan="2">LEXES measurement</td><td>±5%</td><td>±5%</td></tr>
<tr><td rowspan="2">Sputter rate</td><td colspan="2">Primary beam instability</td><td rowspan="2">±7%</td><td rowspan="2">±7%</td></tr>
<tr><td colspan="2">Crater measurement</td></tr>
<tr><td rowspan="3">Matrix ion intensity ratio</td><td colspan="2">Charge neutralization</td><td>Uncertain</td><td rowspan="3">±5%</td></tr>
<tr><td rowspan="2">Sample position</td><td>1-window holder</td><td>±5%</td></tr>
<tr><td>5-window holder</td><td>±5%</td></tr>
<tr><td rowspan="5">RSF</td><td colspan="2">Charge neutralization</td><td>Uncertain</td><td rowspan="5">±12% ~ ±26%</td></tr>
<tr><td colspan="2">Implanted dose</td><td>±10%</td></tr>
<tr><td colspan="2">Background level of impurities</td><td>+5%</td></tr>
<tr><td rowspan="2">Sample position</td><td>1-window holder</td><td>±5%</td></tr>
<tr><td>5-window holder</td><td>±24%</td></tr>
<tr><td colspan="3">Matrix element quantification</td><td colspan="2">±10%</td></tr>
<tr><td colspan="3">Impurity element quantification</td><td colspan="2">±15% ~ ±27%</td></tr>
</table>

The uncertainties of these parameters are not independent. For example, the uncertainty of matrix species quantification in $Al_xGa_{1-x}N$ is affected by the uncertainty of matrix ion intensity ratio, matrix composition and sputter rate. In the simplest estimation, the combined error is the square root of the sum of squares of the individual errors. The error of matrix quantification is then 10%, while that of impurity quantification is 15%-27% in the worst case.

To minimize the error in SIMS analysis using the IMS-6f, it is recommended that the 1- window holder similar to that shown in figure 7-8 is used to reduce ion transmission variation from different position. The immersion lens strip must also be carefully positioned to minimize the secondary ion extraction variations from different holder position. The impurity and matrix species should be chosen to be of the same ion type i.e. atomic species should be normalized to atomic species and molecular species to molecular species.

## 7.4 References

[1] K. Wittmaack, in *Practical Surface Analysis*, edited by D. Briggs and M. P. Seah (JOHN WILEY & SONS, 1992), Vol. 2, p. 105.

[2] R. G. Wilson and G. R. Brewer, *Ion Beams: With Applications to Ion Implantation, p320* (JOHN WILEY & SONS, 1973).

[3] J. E. Mahan and A. Vantomme, Physical Review B **61**, 8516 (2000).

[4] J. A. Kerr, in *CRC Handbook of Chemistry and Physics*, edited by D. R. Lide (CRC Press, Boca Raton, Florida, USA, 2000).

[5] M. Meuris, W. Vandervorst, G. Borghs, et al., Secondary Ion Mass Spectrometry SIMS VI, edited by A. Benninghoven, A.M. Huber, and H.W. Werner, John Wiley & Sons, 277 (1988).

[6] D. P. Griffis, R. Loesing, D. A. Ricks, et al., Secondary ion Mass Spectrometry SIMS XI, edited by G. Gillen, R. Lareau, J. Bennett and F. Stevie, John Wiley & Sons, 201 (1997).

[7] D. L. Lefforge, Y. L. Chang, M. Ludowise, et al., Mat. Res. Soc. Symp. Proc. **510**, 155 (1998).

[8] M. L. Yu, J. Vac. Sci. Technol. A **1**, 500 (1983).

[9] V. R. Deline, C. A. Evans, and P. Williams, Applied Physics Letters **33**, 578 (1978).

[10] C. Hombourger, R. Staub, M. Schuhmacher, et al., Applied Surface Science **203**, 383 (2003).

[11] Tencor, P-20h Long Scan Profiler Rererence Manual, A.

[12] R. Loesing, in *Materials Science and Engineering* (North Carolina State University, Raleign, 2001), p. 47.

[13] R. G. Wilson and G. R. Brewer, *Ion Beams: With Applications to Ion Implantation, p324* (JOHN WILEY & SONS, 1973).

[14] CAMECA, SURFACE function in CURVE PROCESSING, IMS CAMECA SOFTWARE USER'S GUIDE Release 3.1, 9.35 (1995).

[15] CAMECA, CONCENTRATION function in CURVE PROCESSING, IMS CAMECA SOFTWARE USER'S GUIDE, Release 3.1, 9.54 (1995).

[16] R. G. Wilson, F. A. Stevie, and C. W. Magee, *Secondary Ion Mass Spectrometry : a Practical Handbook for Depth Profiling and Bulk Iimpurity Analysis, p3.2-1*, 1989).

[17] R. Fleming, Secondary Ion Mass Spectrometry Instrumentation Tutorial, http://www.cea.com/cai/simsinst/detector.htm (1995).

[18] D. P. Chu, M. G. Dowsett, and G. A. Cooke, Journal of Applied Physics **80**, 7104 (1996).

[19] *Guide to the expression of uncertainty in measurement* (ISO, Geneva, Switzerland, 1993).

[20] I. A. Abroyan, V. P. Lavrov, and I. G. Fedora, Sov. Phys. Solid State **7**, 2954 (1966).

# 8 Conclusions and Future Work

## 8.1 The Contribution

The quantification of impurities and matrix species in $Al_xGa_{1-x}N$ over the range of AlN mole fraction (x) is challenging because of matrix effects and charging effects. For quantitative characterization of both matrix and impurity elements in $Al_xGa_{1-x}N$, novel charge neutralization methods were employed and calibration curves were created using an $O_2^+$ primary beam with positive secondary ion detection and a $Cs^+$ primary beam with negative and $MCs^+$ secondary ion detection. The data were interpreted using secondary ion emission models.

Using the sputtering conditions presented in this study, the sputter yield decreases when AlN mole fraction in $Al_xGa_{1-x}N$ is increased which is similar to the trend previously observed for $Al_xGa_{1-x}As$.[1]

In the range of $0 \le x \le 0.58$, the matrix ion intensity ratios of $Al^+/Ga^+$ obtained using $O_2^+$ and $AlCs^+/GaCs^+$ obtained using $Cs^+$ appear to increase linearly with matrix mole fraction ratio of x/(1-x) in $Al_xGa_{1-x}N$. However, the ratios of $AlN^-/GaN^-$ and $AlN^+/GaN^+$ appear to increase linearly with the AlN mole fraction x instead of the mole fraction ratio. If plotted inversely, the apparent linear correlation range increases. For example, the ratios of $Ga^+/Al^+$ or $GaCs^+/AlCs^+$ versus (1-x)/x appear linear for $0 \le (1-x) \le 0.86$ GaN mole fraction, while the ratio of $GaN^{\pm}/AlN^{\pm}$ versus (1-x) appears linear for $0 \le (1-x) \le 0.61$ GaN mole fraction. The overlap of these apparently linear ranges allows quantification of matrix over the entire range of $Al_xGa_{1-x}N$'s i.e. from $0 \le x \le 1$ under these analytical conditions.

The RSF's for Si and Mg generated via normalization to the appropriate Ga-containing matrix ions appear to decrease exponentially with x in the range of $0 \le x \le 0.58$. RSF's generated using $MCs^+$ method and via normalization to N-containing matrix ions vary less in the range of $0 \le x \le 0.58$. The normalization of $MCs_x^+$ secondary ions to N-containing matrix ions provides a valuable quantification approach since variations in RSF's generated via normalization to $NCs_x^+$ show only a small variation over the range of AlN mole fraction x presumably because of the constant concentration of N in $Al_xGa_{1-x}N$ from GaN to AlN. The larger exponential variations of other RSF’s with respect to x is consistent with variations of ion yields with the surface work function.

Based on the calibration curves developed in this work for multiple analysis conditions, the matrix elements in $Al_xGa_{1-x}N$ can be quantified in the range of $0 \leq x \leq 1$, and the impurity species can be quantified over AlN mole fraction $0 \leq x \leq 0.58$. These SIMS analytical techniques can be employed for impurity control, composition and growth rate determination, as well as structural analysis of the finished optoelectronic and electronic devices.

Changes in the ionization yields of both positive and negative ions were studied versus AlN mole fractions x in $Al_xGa_{1-x}N$. Yield variations were found to be directly related to increases of the surface concentrations of the primary species i.e. reduction of sputter yields with increasing AlN mole fraction x resulting in increased primary ion surface concentrations. Under $O_2^+$ primary ion bombardment, the positive secondary ion yields increase as x is increased due to the increase of surface O concentration. However the amount of increase differs for Mg and Si impurities. $Si^+$ is more responsive to the change of surface concentration of oxygen. This response is thought to be due to the strong Si-O bonds which form during oxygen primary ion beam sputtering. The ion yield enhancement provided by $O_2^+$ can be explained using a local bond-breaking model.

Under $Cs^+$ bombardment, negative ion yields increase as AlN mole fraction x increases, and the effect of Cs surface concentration on different negative ions is similar. The negative ionization mechanism under $Cs^+$ can be explained using an electron-tunneling model.

The ionization mechanism of $MCs^+$ is more complex. From secondary ion useful yield changes with changes in the AlN mole fraction in $Al_xGa_{1-x}N$, it is probable that the formation of $MCs^+$ in $Al_xGa_{1-x}N$ is through the combination of $M^0$ neutral and $Cs^+$ ions. For electropositive elements, it is probable that the formation of $MCs_2^+$ occurs via the combination of $M^0$ neutral and $Cs_2^+$. For electronegative elements, it is probable that the formation of $MCs_2^+$ occurs via the combination of $M^-$ and two $Cs^+$ ions.

## 8.2 Recommendations for Future Work

### 8.2.1 Further Study using Better Quality $Al_xGa_{1-x}N$ Samples

The samples for this study have significant variation in structure, in native impurity species, and in ion implantation conditions. The samples were grown using different

MOCVD systems on different substrates with different buffer layers. One set of samples (SS2) has a high level of O and Si contamination forcing the use of significantly higher implant doses for O and Si. The high Al content (x>0.6 and other than AlN) samples were fabricated using high dose Ga implantation into AlN.

These variation of the samples caused high measurement errors on the calibration curves discussed in precious chapters, and made it difficult to determine overall trends of certain characteristic parameters in $Al_xGa_{1-x}N$ such as the RSF and ion yield of oxygen impurity. For better understanding and quantification in $Al_xGa_{1-x}N$, films grown on the same substrates, with x ranging from 0 to 1 would be ideal. In addition, these films should have similar impurity contamination levels and should be implanted with the various impurity species with the same dose and same energy. Study of such a high quality set of samples should provide calibration curves with reduced errors for quantification and provide more insights in the ionization mechanisms in $Al_xGa_{1-x}N$ for the range of $0 \leq x \leq 1$.

$NCs^+$ and $NCs_2^+$ are used as the matrix ions for computing RSF's in the quantification of impurity species in $Al_xGa_{1-x}N$ using $MCs^+$ method, which provides a valuable approach because N is constant in $Al_xGa_{1-x}N$ independent on x. For quantification using $O_2^+$ with positive ion detection and $Cs^+$ with negative ion detection, it may be useful to evaluate the possibility to use $N^+$ or $N^-$ as matrix ions since N is constant over the entire range of AlN mole fraction x in $Al_xGa_{1-x}N$.

### 8.2.2 Study of InGaN

Due to the lack of samples, quantification in $In_xGa_{1-x}N$ was not studied in this project. As one of the most important members of III-nitride family, $In_xGa_{1-x}N$ is a key material in the GaN-based blue/UV light emitters/lasers and high-power electronic devices.[2-5]

The literature on quantification of $In_xGa_{1-x}N$ only addresses matrix level quantification using $MCs^+$ techniques. A linear correlation was proposed for $InCs^+/GaCs^+$ ion intensity ratio as a function of the mole fraction ratio x/(1-x) in the range of $x \leq 0.2$.[6, 7] No literature was found on the quantification of impurity or matrix species with InN mole fraction (x>0.3).

Similar to the SIMS analysis in $Al_xGa_{1-x}N$, secondary ion yields in $In_xGa_{1-x}N$ are will almost certainly be affected by the surface concentration of primary species due to the sputter

yield changes. It has been determined that the sputter yield of indium material is slightly higher than that of gallium[8] probably due to the lower In-In bond strength (100±8 kJ/mol) than Ga-Ga (112.1±7 KJ/mol at 298K).[9] Using the same reasoning as in section 7.2.1, the incorporation of indium will increase the sputtering rate of $In_xGa_{1-x}N$. It has been reported that the sputter yield of $In_xGa_{1-x}As$ has a linear correlation with the InN mole fraction in the range of $0 \le x \le 1$.[10] Thus, it is expected the sputter yield of $In_xGa_{1-x}N$ will also a have linear correlation with the InN mole fraction.

When the sputter yield is increased, the surface concentration of primary species is decreased. As a result, the positive ion yields under $O_2^+$ bombardment and the negative ion yields under $Cs^+$ bombardment will be decreased. The ion yield of $MCs_x^+$ depends on the electronegativity of the elements M.

Similar to the quantification issues found for $Al_xGa_{1-x}N$, the calibration curves of sputter yield, matrix ion intensity ratios, and impurity RSF's as a function of InN mole fraction x in $In_xGa_{1-x}N$ will be needed.

### 8.2.3 Thin Layer Quantification

InGaN/GaN or AlGaN/GaN multiple quantum well (MQW) structures are commonly used as the active region for III-Nitride light emitting diodes (LED's) and laser diodes (LD's). In the MQW structures, the QW thickness can be less than one nanometer which is beyond the depth resolution of current magnetic sector SIMS analysis. Quantification in the thin layers can be complex, because SIMS matrix effects and sputtering yields change from matrix to the thin layer and to subsequent layers. Furthermore, it is very difficult to make thin layer standards, both for matrix and impurity species.

For quantitative analysis in a thin layer, several approaches have been proposed. One of them is to use a delta profile as a response function to decompose a chemical profile from the measured data.[11] This involves deriving a SIMS resolution function S(z) from the analysis of one delta plane, then simulating the expected profile M(z) from a given input profile R(z) by the convolution of R(z) with S(z). Another approach for thin layer quantification uses a high energy primary ion beam to spread the thin layer constituents by ion beam mixing.[12] As shown in figure 8-2, the quantity of a constituent of the layer can then

be obtained from expression $Q_I = Q.I_I/I_Q$, where Q is the dose of standard, $I_I$ and $I_Q$ are integration of standard and unknown sample, respectively.

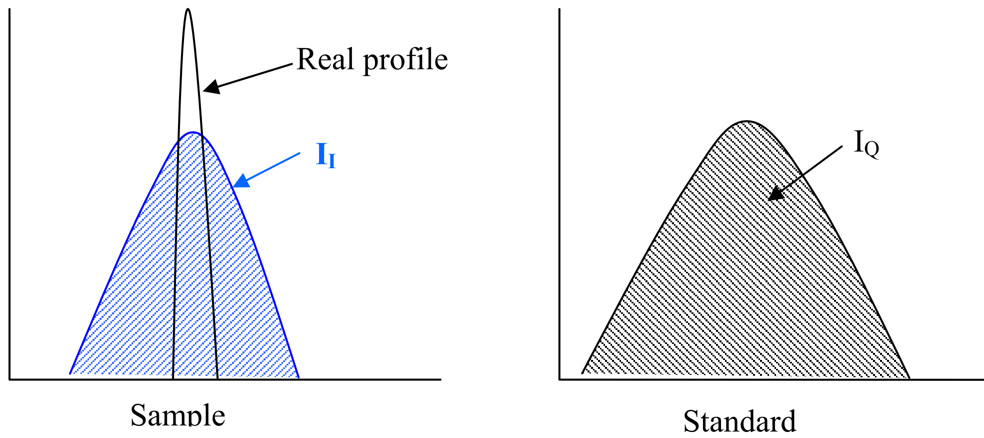


**Figure 8-1. Illustration of thin layer quantification with profile spreading by ion mixing**

For a thin layer in nanometer thickness, depth profiling with low energy quadrupole SIMS can yield good results.

## 8.3 References


[1] M. Meuris, W. Vandervorst, G. Borghs, et al., Secondary Ion Mass Spectrometry SIMS VI, edited by A. Benninghoven, A.M. Huber, and H.W. Werner, John Wiley & Sons, 277 (1988).

[2] O. Manasreh, (Elsevier Press, Oxford, 2000).

[3] H. Morkoc, *Nitride semiconductors and devices,* (Springer Press, Berlin, 1999).

[4] S. Nakamura and G. Fasol, *The blue laser diode* (Springer Press, Berlin, 1997).

[5] J. I. Pankove and T. D. Moustakas, in *Semiconductors and semimetals*, edited by W. R.K. and W. R. (Academic Press, San Diego, 1998), Vol. 50.

[6] Y. Gao, S. Mitha, C. Chung, et al., Secondary Ion Mass Spectrometry, SIMS XI, edited by G. Gillen, R. Lareau, J. Bennett and F. Stevie, John Wiley & Sons, Chichester, p.193 (1997).

[7] P. K. Chu, Y. Gao, and J. W. Erickson, J. Vac. Sci. Technol. B **16**, 197 (1998).

[8] J. E. Mahan and A. Vantomme, Physical Review B **61**, 8516 (2000).

[9] J. A. Kerr, in *CRC Handbook of Chemistry and Physics*, edited by D. R. Lide (CRC Press, Boca Raton, Florida, USA, 2000).

[10] M. Maier, D. Serries, T. Geppert, et al., Applied Surface Science **203**, 486 (2003).

[11] M. G. Dowsett, R. D. Barlow, and P. N. Allen, Journal of Vacuum Science & Technology B **12**, 186 (1994).

[12] P. Williams, Secondary Ion Mass Spectrometry, SIMS VI, edited by A. Benninghoven et al., John Wiley & Sons, p.261 (1987).